



**Design and modeling of optical fibers
for spatial division multiplexing
using the orbital angular momentum of light**

Thèse

Charles Brunet

Doctorat en génie électrique
Philosophiæ doctor (Ph.D.)

Québec, Canada

© Charles Brunet, 2016

**Design and modeling of optical fibers
for spatial division multiplexing
using the orbital angular momentum of light**

Thèse

Charles Brunet

Sous la direction de:

Leslie A. Rusch, directrice de recherche

Résumé

Les besoins toujours croissants en terme de transfert de données numériques poussent au développement de nouvelles technologies pour accroître la capacité des réseaux, notamment en ce qui concerne les réseaux de fibre optique. Parmi ces nouvelles technologies, le multiplexage spatial permet de multiplier la capacité des liens optiques actuels. Nous nous intéressons particulièrement à une forme de multiplexage spatial utilisant le moment cinétique orbital de la lumière comme base orthogonale pour séparer un certain nombre de canaux.

Nous présentons d'abord les notions d'électromagnétisme et de physique nécessaires à la compréhension des développements ultérieurs. Les équations de Maxwell sont dérivées afin d'expliquer les modes scalaires et vectoriels de la fibre optique. Nous présentons également d'autres propriétés modales, soit la coupure des modes, et les indices de groupe et de dispersion. La notion de moment cinétique orbital est ensuite introduite, avec plus particulièrement ses applications dans le domaine des télécommunications.

Dans une seconde partie, nous proposons la carte modale comme un outil pour aider au design des fibres optiques à quelques modes. Nous développons la solution vectorielle des équations de coupure des modes pour les fibres en anneau, puis nous généralisons ces équations pour tous les profils de fibres à trois couches. Enfin, nous donnons quelques exemples d'application de la carte modale.

Dans la troisième partie, nous présentons des designs de fibres pour la transmission des modes avec un moment cinétique orbital. Les outils développés dans la seconde partie sont utilisés pour effectuer ces designs. Un premier design de fibre, caractérisé par un centre creux, est étudié et démontré. Puis un second design, une famille de fibres avec un profil en anneau, est étudié. Des mesures d'indice effectif et d'indice de groupe sont effectuées sur ces fibres.

Les outils et les fibres développés auront permis une meilleure compréhension de la transmission dans la fibre optique des modes ayant un moment cinétique orbital. Nous espérons que ces avancements aideront à développer prochainement des systèmes de communications performants utilisant le multiplexage spatial.

Abstract

The always increasing need for digital data bandwidth pushes the development of emerging technologies to increase network capacity, especially for optical fiber infrastructures. Among those technologies, spatial multiplexing is a promising way to multiply the capacity of current optical links. In this thesis, we are particularly interested in current spatial multiplexing using the orbital angular momentum of light as an orthogonal basis to distinguish between a few optical channels.

We first introduce notions from electromagnetism and physics needed for the understanding of the later developments. We derive Maxwell's equations describing scalar and vector modes of optical fiber. We also present other modal properties like mode cutoff, group index, and dispersion. Orbital angular momentum is briefly explained, with emphasis on its applications to optical communications.

In the second part, we propose the modal map as a tool that can help in the design of few mode fibers. We develop the vectorial solution of the ring-core fiber cutoff equation, then we extend those equations to all varieties of three-layer fiber profiles. Finally, we give some examples of the use of the modal map.

In the third part of this thesis, we propose few fiber designs for the transmission of modes with an orbital angular momentum. The tools that were developed in the second part of this thesis are now used in the design process of those fibers. A first fiber design, characterized by a hollow center, is studied and demonstrated. Then a second design, a family of ring-core fibers, is studied. Effective indexes and group indexes are measured on the fabricated fibers, and compared to numerical simulations.

The tools and the fibers developed in this thesis allowed a deeper comprehension of the transmission of orbital angular momentum modes in fiber. We hope that those achievements will help in the development of next generation optical communication systems using spatial multiplexing.

Contents

Résumé	iii
Abstract	iv
Contents	v
List of Tables	viii
List of Figures	x
List of Algorithms	xii
List of Symbols	xiii
List of Acronyms	xvi
Remerciements	xix
Foreword	xx
Introduction	1
0.1 The need for new multiplexing schemes	1
0.2 Thesis outline	5
0.3 List of contributions	6
I Background	8
1 Guided modes of optical fiber	9
1.1 Derivation of Maxwell's equations	9
1.2 Optical fiber modes	11
1.3 Modes in step-index fibers	13
1.4 Modes of standard step-index fiber	14
1.5 Scalar modes	17
1.6 Cutoff of standard step-index fibers	18
1.7 Group index and dispersion	19
2 The orbital angular momentum of light	21
2.1 Linear and angular momentum	21

2.2	The angular momentum of light	21
2.3	Generation of OAM beams	23
2.4	Detecting OAM modes	25
2.5	OAM in free-space telecommunications	26
2.6	OAM fiber modes	27
2.7	OAM modes in optical fibers	29
3	Solving for modes using numerical methods	32
3.1	The simulation software	32
3.2	The transfer matrix method	32
3.3	Optimizing the search for n_{eff}	37
3.4	Computing the electromagnetic fields	42
II	The modal map: a design tool	45
4	Cutoff of ring-core fibers	46
4.1	Definition of ring-core fiber	46
4.2	Derivation of the characteristic equation for vector modes	47
4.3	Cutoffs of RCF	49
4.4	Numerical validation	54
4.5	Asymptotic limits	58
4.6	Approximation for cutoff of $\text{HE}_{1,m}$ modes	62
5	Cutoff of three-layer fibers	64
5.1	The family of three-layer fibers	64
5.2	Derivation of the characteristic equation for vector modes	65
5.3	Cutoffs of 3LSIF	68
5.4	Numerical validation	76
5.5	Continuity between fiber profiles	76
6	The modal map	85
6.1	Counting the number of dimensions	85
6.2	Selecting number of modes	86
6.3	Targeting mode separation	90
III	Fibers designed for OAM transmission	96
7	Air-core annular fiber	97
7.1	Design of an OAM fiber	97
7.2	Modeling and simulation	99
7.3	Fiber fabrication	100
7.4	Exciting OAM modes in ACF	103
8	A family of ring-core fibers	110
8.1	Choice of fiber parameters	111
8.2	Simulation of modal properties	114
8.3	Fiber fabrication	115

8.4	Effective index measurement	118
8.5	Group index measurement	122
8.6	Discussion	126
Conclusion		128
8.7	Openings for future work	129
8.8	Closing remarks	131
A	Formulas	132
A.1	Vector operators and identities	132
A.2	The Bessel functions	133
A.3	Selected trigonometric identities	137
A.4	Stencil method for numerical estimation of the derivatives	137
B	Refractive index calculation	138
B.1	Refractive index of Air	138
B.2	Refractive index of silica	138
B.3	Refractive index of doped silica	138
Bibliography		140

List of Tables

1.1	Cutoff conditions for standard step-index fibers	18
1.2	Cutoffs of the first modes in standard step-index fiber.	19
4.1	Cutoff conditions for ring-core fibers	54
5.1	Cutoff equations for fiber profile (a) (W-type fiber)	79
5.2	Cutoff equations for fiber profile (b)	80
5.3	Cutoff equations for fiber profile (c)	81
5.4	Cutoff equations for fiber profile (d)	82
5.5	Dimensions and indexes of test profiles	82
6.1	Normalized fiber parameter equivalences in 3LSIF.	86
6.2	Fiber parameters, as function of fiber profile.	86
7.1	Index constraints for air-core annular fiber	98
7.2	Parameters of designed air-core annular fiber	100
7.3	Effective indexes and effective index separations, at 1550 nm, for designed ACF.	101
7.4	Parameters of air-core annular fiber model.	103
7.5	Effective indexes and effective index separations, at 1550 nm, for ACF model.	105
8.1	List of design criteria for RCF family.	112
8.2	RCF fiber index parameters.	112
8.3	Geometry of the designed RCF fibers.	114
8.4	Effective indexes of the modes in RCFs (at 1550 nm).	114
8.5	Effective index separation within mode groups (at 1550 nm).	115
8.6	Group indexes of the modes in RCFs (at 1550 nm).	117
8.7	Δn_{eff} measured values (using FBG), compared to calculated values.	122
8.8	Lengths of ring-core fibers used for time-of-flight experiment.	123
8.9	Measured values for TOF experiment in RCF1	124
8.10	Measured values for TOF experiment in RCF2	125
8.11	Measured values for TOF experiment in RCF3	125
8.12	Measured values for TOF experiment in RCF4	125
8.13	Measured values for TOF experiment in RCF5	125
8.14	Relative group indexes ($\Delta n_g \cdot 10^3$) of the modes in RCFs (at 1550 nm).	126
8.15	Group index difference between simulation and measurement ($\cdot 10^3$)	126
A.1	Coefficients for five-point stencil ($m = 4$)	137
B.1	Sellmeier coefficients, for silica and germania.	139

B.2 Coefficients for Claussius-Mossotti interpolation	139
---	-----

List of Figures

0.1	North American Internet traffic.	1
0.2	Data transmission capacity of fiber transmission systems as a function of year.	2
0.3	Nonlinear capacity curves for a range of transmission distances.	3
0.4	Different approaches for realizing SDM.	4
0.5	The evolution of transmission capacity in optical fibers.	4
1.1	Standard step-index fiber geometry (top view, and profile).	14
2.1	Spiral phase plate.	23
2.2	Some examples of fork grating patterns.	24
2.3	The four OAM mode degeneracies.	29
3.1	Example of a characteristic function.	38
3.2	Optimization and parallelization of the algorithm.	43
4.1	Ring-core fiber geometry (top view, and profile).	47
4.2	Normalized $e_z^2(r)$ of some modes, near cutoff.	50
4.3	Cutoffs of a ring-core fiber with weak index contrast.	56
4.4	Cutoffs of a ring-core fiber with a relatively high index contrast.	57
4.5	Cutoffs of a silica tube surrounded by air.	58
4.6	Approximated and exact cutoffs for $HE_{1,m}$ modes	63
5.1	The five possible three-layer fiber profiles.	65
5.2	Cutoffs of first modes for fiber profile (a).	77
5.3	Cutoffs of first modes for fiber profile (b).	77
5.4	Cutoffs of first modes for fiber profile (c).	78
5.5	Cutoffs of first modes for fiber profile (d).	78
5.6	V at cutoff as a function of the index of the center layer, in 3LSIF.	83
5.7	V at cutoff as a function of the index of the intermediate layer, in 3LSIF.	83
6.1	Mode cutoffs as function of NA , for SSIF.	87
6.2	Modal map of LP modes in RCF.	88
6.3	Modal map of vector modes in RCF (fixed indexes).	89
6.4	Modal map of vector modes in RCF (fixed ρ).	90
6.5	Contour plot of cutoff frequency of $HE_{2,1}$ mode in RCF.	91
6.6	Effective index separation between modes in a RCF.	92
6.7	Smallest effective index separation between modes in a RCF.	93
6.8	Minimal effective index separation in a RCF.	93
6.9	Augmented modal map for RCF.	94

7.1	Air-core annular fiber geometry (top view, and profile).	99
7.2	Effective index as function of wavelength, for designed ACF.	101
7.3	Optical microscope photograph of the end of the air-core annular fiber.	102
7.4	Refractive index measurement of the air-core annular fiber.	103
7.5	Comparison between ACF design and realized fiber profiles.	104
7.6	Comparison between realized fiber profiles and ACF model.	104
7.7	Effective index as function of wavelength, for ACF model.	105
7.8	Experimental setup for the transmission of OAM through ACF	106
7.9	OAM beam interference, after transmission in fiber ($\ell = 0$ to 5).	107
7.10	OAM beam interference, after transmission in fiber ($\ell = 6$ to 9).	108
8.1	Augmented modal map for RCF family design.	113
8.2	Normalized propagation constant as function of normalized frequency, in RCF.	115
8.3	Effective index separation, in RCF.	116
8.4	Group index of RCF, as function of outer radius of the ring-core (r_2).	116
8.5	Optical microscope photographs of RCFs.	117
8.6	Refractive index measurement of RCF.	119
8.7	Intensity profile after transmission in RCF 2	120
8.8	FBG reflectogram for RCF 2 (sample 2).	121
8.9	Superimposed FBG reflectogram for all RCFs.	121
8.10	Experimental setup for TOF using fork-grating.	123
8.11	Time-of-flight experiment results, using linear polarization, for all RCFs.	124
A.1	Ordinary Bessel functions of first (a) and second (b) kind.	134
A.2	Modified Bessel functions of first (a) and second (b) kind.	134

List of Algorithms

3.1	Finding n_{eff} of a given mode (simplified version)	33
3.2	Layer-by-layer method	37
3.3	Roots of the characteristic function	39

List of Symbols

\mathbf{B}	Magnetic flux density vector
b	Normalized propagation constant
β	Propagation constant (for a given mode)
β_i	i^{th} coefficient of the Taylor series expansion of the propagation constant
c	Speed of light in a vacuum ($299\,792\,458\text{ m s}^{-1}$)
\mathbf{D}	Electric flux density vector
D	Dispersion parameter (in $\text{ps nm}^{-1}\text{ km}^{-1}$)
Δ	Fiber parameter (for SSIF), given by $1 - 2\Delta = n_{\text{cl}}^2/n_{\text{co}}^2$
Δn_{eff}	Difference between the effective indexes of two modes
Δ^{\pm}	Variable used to simplify notation for cutoff expressions of three-layer step-index fibers
\mathbf{E}	Electric field vector
\mathbf{e}	Envelope of electric field
e_{ϕ}	Azimuthal component of the envelope of the electric field
e_r	Radial component of the envelope of the electric field
e_z	Longitudinal component of the envelope of the electric field
ε_0	Vacuum permittivity ($8.854\,187\,82 \times 10^{-12}\text{ F m}^{-1}$)
η_0	Free-space (vacuum) impedance ($\eta_0 = \mu_0/\varepsilon_0$)
$\mathcal{F}_{\nu}(ur)$	Function defined as $\mathcal{F}_{\nu}(ur_2) = J_{\nu}(ur_2) - \gamma N_{\nu}(ur_2)$, used to simplify notation of three-layer step-index fiber modal equations
$f_{\nu}(\phi)$	Azimuthal dependency of e_z component
$g_{\nu}(\phi)$	Azimuthal dependency of h_z component
γ	Variable used in $\mathcal{F}_{\nu}(ur)$ function, used to simplify notation of three-layer step-index fiber modal equations
\mathbf{H}	Magnetic field vector
\mathbf{h}	Envelope of magnetic field

h	Plank constant ($6.626\,069\,57 \times 10^{-34}$ J s)
h_ϕ	Azimuthal component of the envelope of the magnetic field
h_r	Radial component of the envelope of the magnetic field
h_z	Longitudinal component of the envelope of the magnetic field
\hbar	Reduced Plank constant ($\hbar = h/2\pi = 1.054\,571\,73 \times 10^{-34}$ J s)
\mathbf{J}	Current density vector
j	Imaginary unit ($j = \sqrt{-1}$)
k_0	Wavenumber ($k_0 = 2\pi/\lambda$)
\mathbf{L}	Angular momentum
ℓ	Mode parameter, related to the number of symmetry axes in Cartesian coordinates (for LP modes) or to the topological charge (for OAM modes) For OAM, ℓ is the topological charge
λ	Wavelength (in m)
\mathbf{M}	Induced magnetic polarization
M	Mass (in kg)
m	Mode parameter related to the number of zeros in the radial component of the fields
μ	Vacuum permeability ($4\pi \times 10^{-7}$ H m ⁻¹)
N	Number of layers in a fiber
n	Refractive index
n_{eff}	Effective index (for a given mode)
n_g	Group index (of a mode)
ν	Mode parameter related to the number of azimuthal symmetry axes in the fields
ω	Angular frequency ($\omega = 2\pi c/\lambda$ rad/sec)
ω_0	Central angular frequency of a pulse
\mathbf{P}	Induced electric polarization
\mathbf{p}	Linear momentum (in kg m s ⁻¹ or in N s)
ϕ	Azimuthal component (in cylindrical coordinates)
ϕ_0	Arbitrary phase
$\hat{\phi}$	Azimuthal unit vector
φ	Phase component of a vector field
\mathbf{r}	Position vector
r	Radial component (in polar or cylindrical coordinates)

r_i	Radius of the i^{th} layer in a step-index fiber
$\hat{\mathbf{r}}$	Radial unit vector
ρ	Ratio between inner and outer radius, in ring-core fiber ($\rho = r_1/r_2$)
ρ_f	Charge density
\mathbf{S}	Poynting vector (energy flux density, in W m^{-2})
S	Dispersion slope (in $\text{ps nm}^{-2} \text{km}^{-1}$)
σ	Spin (polarization) of light
t	Time (in seconds)
u	Mode parameter, given by $u = (k_0^2 n^2 - \beta^2)^{1/2}$
\hat{u}_i	Modal parameter (real or imaginary) defined by $\hat{u}_i^2 = n_i^2 k_0^2 - \beta^2$, where n_i is the refractive index of the i^{th} layer
V	Normalized frequency
\mathbf{v}	Velocity (in m s^{-1})
v_g	Group velocity (of a mode)
v_p	Phase velocity (of a mode)
w	Mode parameter, given by $w = (\beta^2 - k_0^2 n^2)^{1/2}$
z	Longitudinal component (in Cartesian or cylindrical coordinates)
$\hat{\mathbf{z}}$	Longitudinal unit vector

List of Acronyms

ACF	Air-core fiber
AWGN	Additive white Gaussian noise
CVB	Cylindrical vector beam
COPL	<i>Centre d'optique, photonique et laser</i>
DPSK	Differential phase-shift keying
DGD	Differential group delay
EDFA	Erbium doped fiber amplifier
FBG	Fiber Bragg grating
FEM	Finite element method
FMF	Few-mode fiber
GPU	Graphical processing unit
GPGPU	General purpose graphical processing unit
HG	Hermite-Gaussian
IPGIF	Inverse parabolic graded-index fiber
LDPC	Low-density parity-check
LG	Laguerre-Gaussian
LP	Linearly polarized
MCF	Multicore fiber
MCVD	Modified chemical vapor deposition
MDM	Mode division multiplexing

MIMO	Multiple input multiple output
MMF	Multimode fiber
OAM	Orbital angular momentum
OOK	On off keying
PCF	Photonic crystal fiber
PDM	Polarization division multiplexing
QAM	Quadrature amplitude modulation
QPSK	Quadrature phase-shift keying
RCF	Ring-core fiber
RIP	Refractive index profile
SAM	Spin angular momentum
SDM	Space division multiplexing
SIF	Step-index fiber
SLM	Spacial light modulator
SMF	Single mode fiber
SNR	Signal to noise ratio
SSIF	Standard step-index fiber
TDM	Time division multiplexing
TEM	Transverse electro-magnetic
TOF	Time of flight
WDM	Wavelength division multiplexing
3LSIF	Three layer step-index fiber

Beautiful is better than ugly.
Explicit is better than implicit.
Simple is better than complex.
Complex is better than complicated.
Flat is better than nested.
Sparse is better than dense.
Readability counts.
Special cases aren't special enough to break the rules.
Although practicality beats purity.
Errors should never pass silently.
Unless explicitly silenced.
In the face of ambiguity, refuse the temptation to guess.
There should be one— and preferably only one —obvious way to do it.
Although that way may not be obvious at first unless you're Dutch.
Now is better than never.
Although never is often better than **right** now.
If the implementation is hard to explain, it's a bad idea.
If the implementation is easy to explain, it may be a good idea.
Namespaces are one honking great idea – let's do more of those!

The Zen of Python, by Tim Peters

Remerciements

Merci à *Valérie*, mon épouse, qui a accepté bien patiemment que mes études se prolongent, même si elle a très hâte que j'aie un *vrai* travail. Merci de m'avoir permis de poursuivre cette passion que j'ai pour apprendre de nouvelles choses. Merci d'être à mes côtés.

Merci à mes enfants, *Marie-Thérèse* et *Timothée*, qui ont vu le jour durant mes études, et pour qui cela semble tout naturel que papa aille travailler à l'université chaque matin.

Merci à *Leslie*, ma directrice, qui m'a accompagné tout au long de ma maîtrise et de mon doctorat. Merci de m'avoir encouragé à poursuivre aux études graduées. Merci de m'avoir enseigné ce domaine des communications optiques, qui était totalement nouveau pour moi. Merci pour toute la confiance qui m'a été faite. Merci de m'avoir montré à devenir un chercheur ; à pousser jusqu'au bout ma curiosité, et à développer ma rigueur scientifique. Merci surtout pour cette grande liberté dont j'ai pu bénéficier dans les orientations que j'ai pu donner à ma recherche. Merci enfin pour les horaires flexibles, qui m'ont permis de concilier les études et ma vie familiale.

Merci à *Pierre-André*, rencontré presque par hasard, mais qui m'a permis de développer tout un aspect de cette thèse. Maintenant je sais que je ne suis pas le seul sur terre à être passionné par les fonctions de Bessel !

Merci à *Sophie*, merci à *Réal*, qui m'ont enseigné un aspect ou l'autre de la fibre optique, et ont contribué à alimenter ma passion.

Merci à *Bora*, pour tous ces échanges fructueux, et pour tes commentaires judicieux sur mes articles. Thank you, *Pravin*, for all the hours spent at the lab for realizing the experiments. Thank you, *Lixian*, for the fruitful discussions and the great ideas you shared.

Foreword

Most of the work contained in this thesis was previously published in contributed papers, or presented at conferences. I give here the list of relevant publications, along with the contribution of each co-author. I am the main contributor for all these publications.

“Design of an Optical Fiber Supporting 16 OAM Modes” [1] was submitted to *Optical Fiber Communication Conference 2014*, and presented as a poster on March 13, 2014. “Design, fabrication and validation of an OAM fiber supporting 36 states” [2] contains similar material, but provides more details and contains updated results. It was submitted to *Optics Express* on September 25, 2014, accepted on October 6, 2014, and published on October 16, 2014. “System and Method for Optical Fiber” [3] is a US patent filed on October 14, 2014 and published on April 16, 2015. It is related to the same fiber design presented in [1, 2]. Bora Ung is mentioned for fruitful discussions about the fiber design. Pravin Vaity performed all the experimentation on the fiber, and developed the perfect OAM beam generation. Younès Messaddeq is the supervisor of the fiber fabrication facilities. Eric Bernier, from Huawei technologies, is mentioned as a contributor on commercial exploitation and market factors in the fabrication and performance of fibers for spatial division multiplexing. Sophie LaRochelle and Leslie Rusch are mentioned as supervisors. I was responsible for fiber design, simulations, and all other works. Chapter 7 presents the fiber mentioned in those papers.

“Design of a Family of Ring-Core Fiber for OAM” [4] was submitted to *Optical Fiber Communication Conference 2015*, and presented as a technical presentation on March 23, 2015. “Design of a family of ring-core fibers for OAM transmission studies” [5] is a longer version, related to the same work, submitted to *Optics Express* on February 17, 2015, accepted on April 9, 2015, and published on April 15, 2015. The idea of designing a family of fibers from a single preform is the result of discussions with Bora Ung. We also worked together for choosing the design parameters. Finally, Bora performed some simulations using COMSOL Multiphysics[®]. Pravin Vaity performed experimental transmission of OAM through the fibers. Lixian Wang performed the measurements using Bragg grating. Younès Messaddeq is the supervisor of the fiber fabrication facilities. Sophie LaRochelle and Leslie Rusch are mentioned as supervisors. Chapter 8 presents the fibers mentioned in those papers.

“Vector mode analysis of ring-core fibers: design tools for spatial division multiplexing” [6] was submitted to *Journal of Lightwave Technologies* on September 12, 2014, and published on October 2, 2014. The initial idea of finding cutoff in ring-core fibers is from Pr. Pierre-André Bélanger. Bora Ung helped by performing some numerical simulations on COMSOL Multiphysics[®], and by fruitful discussions. Sophie LaRochelle, Younès Messaddeq, and Leslie Rusch are mentioned as supervisors. The development of cutoff equations is a joint work of Pr. Bélanger and me. All other simulations and development are my work. Mathematical development of the cutoff equations is reproduced in Chapter 4, but with more details than in the paper. Discussion about the modal map is presented in Chapter 6.

“Exact expressions for vector mode cutoff in three-layer step-index fibers” [7] was submitted to *Journal of Lightwave Technology* on Dec 8, 2015, and is, at the time of writing, under revision. Pierre-André Bélanger reviewed the equations. Leslie Rusch is mentioned as supervisor. All other work is mine. Equations and results are presented in Chapter 5.

I am mentioned as co-author in [8], because it uses a fiber I designed, and because I helped in the understanding OAM modes in optical fiber. I am mentioned as co-author in [9], for the fruitful discussions about the transmission of OAM modes in optical fiber.

Introduction

0.1 The need for new multiplexing schemes

During the last decades, global network traffic increased exponentially, mainly due to the rapid Internet evolution. For example, [10] plots the American Internet traffic as function of years, and shows a growth rate of 50% to 60% a year (see Fig. 0.1). With the increasingly use of voice over IP, video on demand, cloud storage and computing, and the emerging Internet of things, the trends show no sign of decline.

Most of this data traffic is now supported by optical fiber systems. Fortunately, the capacity of fiber transmission systems also increased exponentially during the last decades, following the Internet traffic demand. This capacity increase was caused by successive technology improvements: low losses single-mode fibers, fiber amplifiers (EDFAs), wavelength multiplexing (WDM), and high-efficiency spectral coding (see Fig. 0.2). The trend is for systems capacity increasing ten times every four years. However, current systems are reaching a capacity limit, that would lead to a capacity crunch in a few years, if no new technologies are developed [11].

Typically, the capacity of a channel [12] is limited by the noise, usually modeled as additive white Gaussian noise (AWGN). It is convenient to characterize a channel by its spectral

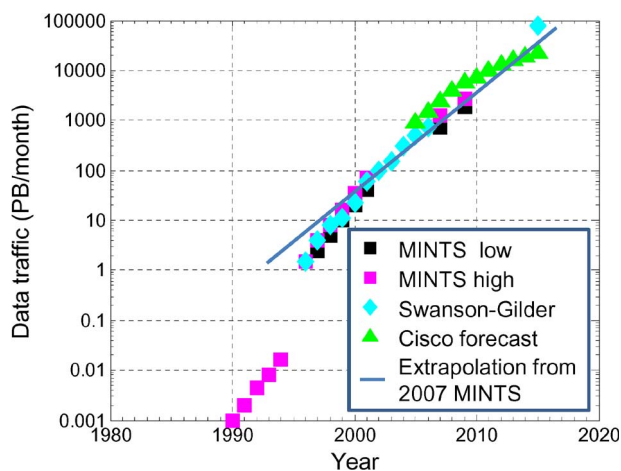


Figure 0.1: North American Internet traffic (reproduced from [10, Fig. 1]).

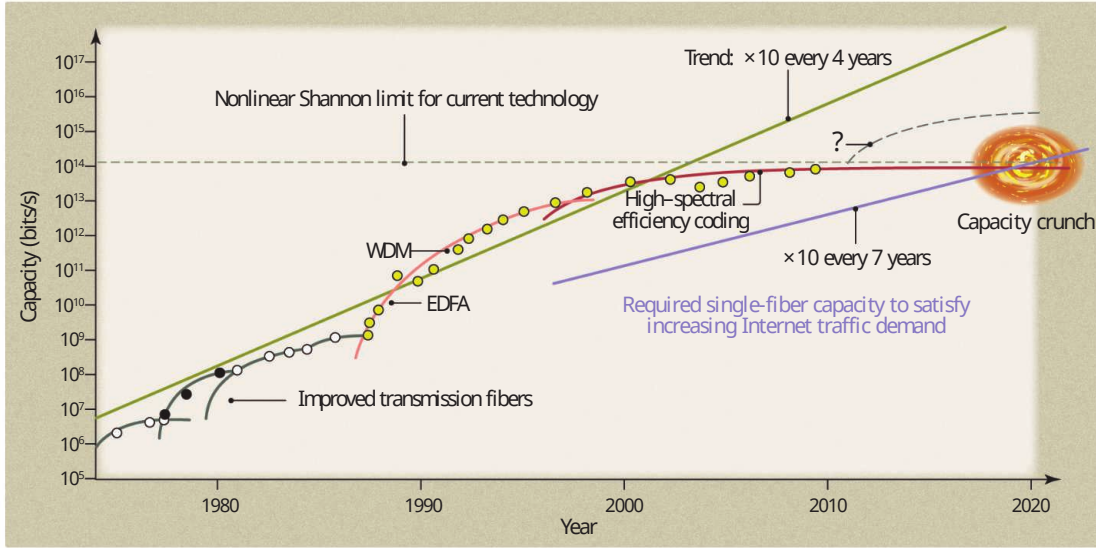


Figure 0.2: Data transmission capacity of fiber transmission systems as a function of year (reproduced from [11]).

efficiency, defined as the capacity per unit of bandwidth. To increase the spectral efficiency, one must increase the signal to noise ratio (SNR). For a fixed noise level, higher signal power will result in higher spectral efficiency. The maximum spectral efficiency we can achieve for a given SNR is called the Shannon limit.

However, it is not that simple with optical fiber channels, because optical fibers are nonlinear medium. Therefore, as the signal power increases, nonlinear effects occur that decrease the spectral efficiency. This becomes especially important as the fiber length increases. A new theoretical limit appears on spectral efficiency: the nonlinear Shannon limit [10]. This limit is a function of fiber parameters, such as loss coefficient, and effective area. An example of capacity curves, for different lengths of standard single-mode fiber, is given in Fig. 0.3. We can see that, as SNR increases, the nonlinear effects dominate on the fiber capacity limit.

As we can see on Fig. 0.2, we are now reaching system capacities that are very close to this nonlinear capacity limit. We can fabricate systems with spectral efficiency almost reaching the theoretical limit. The only way to increase capacity would be to use multiple optical fibers, or to use a new dimension for multiplexing.

We currently are able to multiplex optical data, not only in wavelength (WDM), but also in polarization (PDM), in time (TDM), and in phase (quadrature). Those are all orthogonal dimensions, meaning that the number of channels in one dimension is multiplied by the number of channels in the other dimensions. One dimension remains: space. Space division multiplexing (SDM) [13–15] can be achieved either by using multicore fibers (MCF), by using the different modes of few-mode fibers (FMF), or by a combination of both multiple cores and

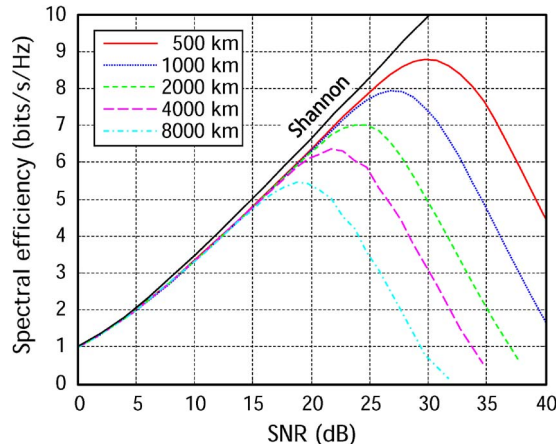


Figure 0.3: Nonlinear capacity curves for a range of transmission distances (reproduced from [10, Fig. 10]).

mode multiplexing. Figure 0.4 shows *different approaches for realizing SDM*:

(a) Fiber bundles composed of physically independent SMFs with reduced cladding thickness could provide increased core packing densities relative to current fiber cables. However, ‘in-fiber’ SDM is required to achieve the higher core densities and integration levels ultimately desired. (b) MCF containing multiple independent cores with sufficiently large spacing to limit crosstalk. Fibers with up to 19 cores have been demonstrated for long-haul transmission – higher core counts are possible for short-haul applications (for example, data communications) for which higher levels of crosstalk per unit length can be tolerated. (c) FMF with a core dimension/numerical aperture set to guide a restricted number of modes (typically 6–12 distinct modes, including all degeneracies and polarizations). (d) Coupled-core fibers support supermodes that allow higher spatial mode densities than isolated-core fibers. MIMO processing is essential to address the inherent mode coupling. (e) Photonic bandgap fibers guide light in an air core and thus offer ultralow optical nonlinearity and potentially lower losses than solid-core fibers. Work is currently being conducted to determine whether such fibers can support MDM. [14, Fig. 2]

Using SDM allows us to surpass the previously encountered capacity limit, as some experiments already demonstrated. This is illustrated in Fig. 0.5, where we clearly see how SDM is needed for communication systems to support all Internet data traffic during the following years. In this figure:

the data points represent the highest capacity transmission numbers (all transmission distances considered) reported at the postdeadline sessions of the annual

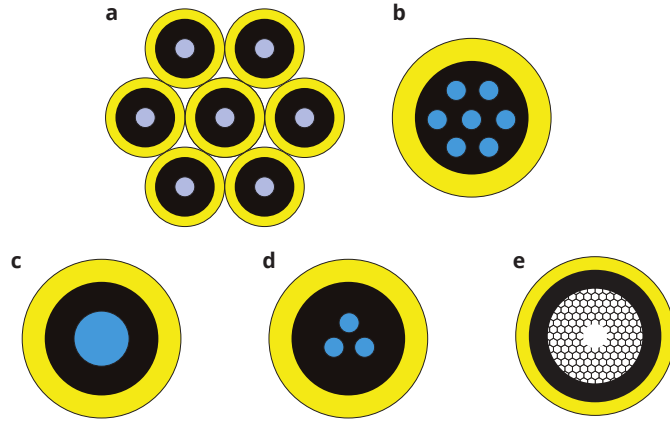


Figure 0.4: Different approaches for realizing SDM (reproduced from [14, Fig. 2]).

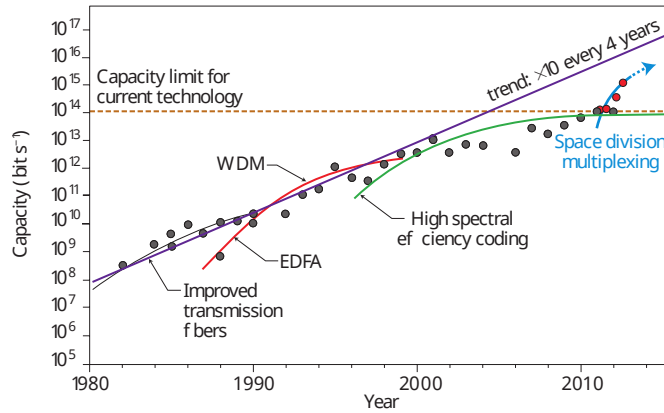


Figure 0.5: The evolution of transmission capacity in optical fibers as evidenced by state-of-the-art laboratory transmission demonstrations (reproduced from [14, Fig. 1]).

Optical Fiber Communications Conference over the period 1982 to the present. The transmission capacity of a single fiber increases by a factor of approximately 10 every four years. Key previous technological breakthroughs include the development of low-loss SMFs, the EDFA, WDM and high-spectral-efficiency coding through DSP-enabled coherent transmission. The data points for SDM also include results from the postdeadline session of the annual European Conference on Optical Communications in 2011 and 2012. SDM seems poised to provide the next big jump in transmission capacity. [14, Fig. 1]

This motivates the subject of this thesis, where we will study the design of few-mode fibers for SDM, using a special kind of modes called OAM modes.

0.2 Thesis outline

The thesis is divided in three parts, each containing several chapters. The first part, *Background*, contains no original contribution, but rather gives an introduction to concepts needed elsewhere in the thesis. It also acts as a review of the state-of-the-art. The second part, *The modal map: a design tool*, is about fiber cutoffs and design techniques for OAM fibers. Finally, the third part, *Fibers designed for OAM transmission*, presents different fibers designed for the transmission of OAM modes, that we fabricated and we tested. The following describes the chapters within each part of the thesis.

0.2.1 Part I: Background

Chapter 1 is about the modal equations for optical fibers. Starting from Maxwell's equations, we derive the wave equation and find the modes for standard step-index fibers, composed of a central core and a cladding. The goal of this chapter is to introduce the notation we will use elsewhere in the document, and to introduce some equations we will need in further developments.

Chapter 2 is about the orbital angular momentum (OAM) of light. It introduces OAM, how it works, and gives a review of the use of OAM in telecommunications. Finally, it presents the problematic of OAM in optical fibers.

Chapter 3 gives details about the numerical methods used to solve for fiber modes elsewhere in this document. It can be considered as the continuation and the application of notions introduced in Chapter 1.

0.2.2 Part II: The modal map: a design tool

Chapter 4 is about the cutoff equations of ring-core fibers. We give the complete development of those equations, and prove their accuracy using asymptotic developments and numerical simulations.

Chapter 5 is about the cutoff equations of three-layers fibers. It is a generalization of what was developed in the previous chapter.

Chapter 6 is about the modal map, a graphical representation developed to help in the design of few-modes fibers. We present this tool, and we explain how to use it and why it is useful.

0.2.3 Part III: Fibers designed for OAM transmission

Chapter 7 presents a fiber with a hollow center, designed to support OAM modes. Numerical simulations are performed to predict the fiber characteristics, and OAM support is confirmed in the lab.

Chapter 8 presents a family of ring-core fibers, especially designed to study how OAM is supported in optical fibers. We compare simulation and measurements of effective index and group index of the supported modes.

0.2.4 Appendices

Appendix A contains common formulas used throughout this thesis. It first introduces vector operators notation and definitions, and gives some related identities for these operators. Then it introduces the Bessel functions, and lists some Bessel function identities. Finally, it presents the five points stencil method used for the numerical estimation of the derivatives.

Appendix B gives the formulas, the parameters, and the references for the wavelength dependent refractive index calculation of the different materials we used for the design of our OAM fibers.

0.3 List of contributions

In Chapter 3:

1. I proposed an algorithm to find the roots of the modal characteristic function;
2. I proposed optimizations to increase the speed of the mode solver;

In Chapter 4:

3. I found the cutoff equations for vector modes in ring-core fibers;
4. I found an asymptotic expression for radial order of a ring-core fiber;
5. I proposed a generalized version of the V number for any fiber profile;

In Chapter 5:

6. I found the cutoff equations for vector and scalar modes in an arbitrary three-layer fiber;
7. I qualitatively explained the influence of the refractive index of each layer in three-layer fibers;

In Chapter 6:

8. I proposed a graphical representation called the modal map;

In Chapter 7:

9. I proposed a new air-core fiber design for OAM transmission;
10. I confirmed this design supports the highest ever reported number of OAM modes transmitted through an optical fiber;

In Chapter 8:

11. I proposed a set of five ring-core fibers for OAM transmission;
12. I proposed a way to fabricate a family of ring-core fibers from a single preform.

Part I

Background

Chapter 1

Guided modes of optical fiber

1.1 Derivation of Maxwell's equations

The development in the current section can be found in many reference books, for instance [16, chapter 30] or [17, chapter 1]. However, it is useful to repeat it here, as we use slightly different notation.

Electro-magnetic fields are governed by Maxwell's equations:

$$\nabla \times \mathbf{E} = -\frac{\partial \mathbf{B}}{\partial t} \quad (1.1a)$$

$$\nabla \times \mathbf{H} = \mathbf{J} + \frac{\partial \mathbf{D}}{\partial t} \quad (1.1b)$$

$$\nabla \cdot \mathbf{D} = \rho_f \quad (1.1c)$$

$$\nabla \cdot \mathbf{B} = 0 \quad (1.1d)$$

where \mathbf{E} and \mathbf{H} are respectively electric and magnetic field vectors, \mathbf{D} and \mathbf{B} are electric and magnetic flux densities, \mathbf{J} is the current density vector, ρ_f is the charge density, $\nabla \times$ is the curl operator, and $\nabla \cdot$ is the divergence. See Appendix A.1 for more details about the vector operators.

The flux densities \mathbf{D} and \mathbf{B} are related to field vectors \mathbf{E} and \mathbf{H} through the constitutive relations:

$$\mathbf{D} = \varepsilon_0 \mathbf{E} + \mathbf{P} \quad (1.2a)$$

$$\mathbf{B} = \mu_0 \mathbf{H} + \mathbf{M} \quad (1.2b)$$

where $\varepsilon_0 = 8.85 \times 10^{-12} \text{ F m}^{-1}$ is the vacuum permittivity, $\mu_0 = 4\pi \times 10^{-7} \text{ H m}^{-1}$ is the vacuum permeability, and \mathbf{P} and \mathbf{M} are the induced electric and magnetic polarizations.

Those equations can be simplified, assuming light is propagating through glass, a non-magnetic, dielectric material. Therefore, there are no charges ($\rho_f = 0$), no currents ($\mathbf{J} = 0$), and no

induced magnetic polarization ($\mathbf{M} = 0$). The evaluation of induced polarization \mathbf{P} can be complex. However, in the case of silica fibers, within telecommunication wavelengths, we can neglect nonlinear effects and material absorption, without lose of accuracy [18]. Therefore, we assume:

$$\mathbf{D} = \varepsilon_0 n^2 \mathbf{E} \quad (1.3)$$

where n is the frequency dependent refractive index of the material. If the material is not uniform, n is also dependent on the position in space.

The time dependency of the fields is given by:

$$\mathbf{E} = \mathbf{E}(\mathbf{r}, t) = \mathbf{e}(\mathbf{r}) \exp(-j\omega t) \quad (1.4a)$$

$$\mathbf{H} = \mathbf{H}(\mathbf{r}, t) = \mathbf{h}(\mathbf{r}) \exp(-j\omega t) \quad (1.4b)$$

where \mathbf{r} is the position in space, t is time, \mathbf{e} and \mathbf{h} are the envelopes of a rapidly oscillating signal, and ω is the angular frequency.

We can now rewrite the equations as functions of \mathbf{E} and \mathbf{H} only. We substitute (1.2b) into (1.1a), and (1.3) into (1.1b), and we evaluate the partial derivatives. By definition, $\mu_0 \varepsilon_0 = 1/c^2$. Free-space impedance is given by $\eta_0 = \sqrt{\mu_0/\varepsilon_0}$. We also define the wavenumber as $k_0 = \omega/c = 2\pi/\lambda$.

$$\nabla \times \mathbf{E} = j\omega\mu_0 \mathbf{H} = jk_0\eta_0 \mathbf{H} \quad (1.5a)$$

$$\nabla \times \mathbf{H} = -j\omega\varepsilon_0 n^2 \mathbf{E} = -j\frac{k_0}{\eta_0} n^2 \mathbf{E} \quad (1.5b)$$

We take the curl of each equation, apply identity (A.1) on the left-hand part, and identity (A.2) on the right-hand part:

$$\nabla(\nabla \cdot \mathbf{E}) - \nabla^2 \mathbf{E} = \nabla(jk_0\eta_0) \times \mathbf{H} + jk_0\eta_0 \nabla \times \mathbf{H} \quad (1.6a)$$

$$\nabla(\nabla \cdot \mathbf{H}) - \nabla^2 \mathbf{H} = \nabla(-j\frac{k_0}{\eta_0} n^2) \times \mathbf{E} - j\frac{k_0}{\eta_0} n^2 \nabla \times \mathbf{E} \quad (1.6b)$$

The gradient of $jk_0\eta_0$ is zero since it does not vary over space. However, n can vary in space (for instance, in a graded index fiber). From (1.1c) and (1.3), we know that $\nabla \cdot (\varepsilon_0 n^2 \mathbf{E}) = 0$. Therefore, using identity (A.3), we find: $\nabla \cdot \mathbf{E} = -\mathbf{E} \cdot \nabla n^2/n^2$. Similarly, from (1.1d) and (1.2b), we know that $\nabla \cdot \mathbf{H} = 0$. Maxwell's equations reduce to:

$$\nabla^2 \mathbf{E} + \nabla(\mathbf{E} \cdot \frac{\nabla n^2}{n^2}) = -jk_0\eta_0(\nabla \times \mathbf{H}) \quad (1.7a)$$

$$\nabla^2 \mathbf{H} = j\frac{k_0}{\eta_0}(\nabla n^2 \times \mathbf{E} + n^2(\nabla \times \mathbf{E})) \quad (1.7b)$$

We substitute (1.5a) and (1.5b) into (1.7b) and (1.7a) respectively, and we replace the remaining \mathbf{E} in (1.7b) by isolating it in (1.5b). This gives us the wave equations:

$$\nabla^2 \mathbf{E} + \nabla \left(\mathbf{E} \cdot \frac{\nabla n^2}{n^2} \right) + k_0^2 n^2 \mathbf{E} = 0 \quad (1.8a)$$

$$\nabla^2 \mathbf{H} + \frac{\nabla n^2}{n^2} \times \nabla \times \mathbf{H} + k_0^2 n^2 \mathbf{H} = 0 \quad (1.8b)$$

1.2 Optical fiber modes

When we study propagation of light in optical fiber, we can make further simplifications. We assume fiber is perfectly circular, infinitely long, and that the cladding is infinitely thick. Solution under those conditions are called *modal* solutions.

By convention, the fiber is aligned in length along the z axis. It is convenient to use cylindrical coordinates (r, ϕ, z) , because in that case, refractive index is only dependent on the r coordinate. Vector fields, in cylindrical coordinates, are given by:

$$\mathbf{E} = \mathbf{E}(r, \phi, z, t) = \mathbf{e}(r, \phi) \exp\{j(\beta z - \omega t)\} \quad (1.9a)$$

$$\mathbf{H} = \mathbf{H}(r, \phi, z, t) = \mathbf{h}(r, \phi) \exp\{j(\beta z - \omega t)\} \quad (1.9b)$$

where β is the propagation constant. With that definition of the fields, the $\partial/\partial z$ operator is equivalent to multiplication by $j\beta$.

We can rewrite (1.5) explicitly with the determinant operator as:

$$\mathbf{E} = j\eta_0 \frac{1}{k_0 n^2} \begin{vmatrix} \hat{\mathbf{r}} & \hat{\phi} & \hat{\mathbf{z}} \\ \partial/\partial r & 1/r(\partial/\partial\phi) & j\beta \\ h_r & h_\phi & h_z \end{vmatrix} \quad (1.10a)$$

$$\mathbf{H} = -j \frac{1}{\eta_0 k_0} \begin{vmatrix} \hat{\mathbf{r}} & \hat{\phi} & \hat{\mathbf{z}} \\ \partial/\partial r & 1/r(\partial/\partial\phi) & j\beta \\ e_r & e_\phi & e_z \end{vmatrix} \quad (1.10b)$$

Separating the components, this gives:

$$e_r = \eta_0 \frac{1}{k_0 n^2} \left(\frac{1}{r} \frac{\partial j h_z}{\partial \phi} + \beta h_\phi \right) \quad (1.11a)$$

$$e_\phi = -\eta_0 \frac{1}{k_0 n^2} \left(\beta h_r + \frac{\partial j h_z}{\partial r} \right) \quad (1.11b)$$

$$j e_z = -\eta_0 \frac{1}{k_0 n^2 r} \left(\frac{\partial(r h_\phi)}{\partial r} - \frac{\partial h_r}{\partial \phi} \right) \quad (1.11c)$$

$$h_r = -\frac{1}{\eta_0} \frac{1}{k_0} \left(\frac{1}{r} \frac{\partial j e_z}{\partial \phi} + \beta e_\phi \right) \quad (1.11d)$$

$$h_\phi = \frac{1}{\eta_0} \frac{1}{k_0} \left(\beta e_r + \frac{\partial j e_z}{\partial r} \right) \quad (1.11e)$$

$$j h_z = \frac{1}{\eta_0} \frac{1}{k_0 r} \left(\frac{\partial(r e_\phi)}{\partial r} - \frac{\partial e_r}{\partial \phi} \right) \quad (1.11f)$$

It is then possible to rewrite all transverse components as functions of longitudinal components [16, 17]:

$$e_r = \frac{1}{n^2 k_0^2 - \beta^2} \left[\beta \frac{\partial j e_z}{\partial r} + \eta_0 \frac{k_0}{r} \frac{\partial j h_z}{\partial \phi} \right] \quad (1.12a)$$

$$e_\phi = \frac{1}{n^2 k_0^2 - \beta^2} \left[\frac{\beta}{r} \frac{\partial j e_z}{\partial \phi} - \eta_0 k_0 \frac{\partial j h_z}{\partial r} \right] \quad (1.12b)$$

$$h_r = \frac{1}{n^2 k_0^2 - \beta^2} \left[\beta \frac{\partial j h_z}{\partial r} - \frac{1}{\eta_0} \frac{k_0 n^2}{r} \frac{\partial j e_z}{\partial \phi} \right] \quad (1.12c)$$

$$h_\phi = \frac{1}{n^2 k_0^2 - \beta^2} \left[\frac{\beta}{r} \frac{\partial j h_z}{\partial \phi} + \frac{1}{\eta_0} k_0 n^2 \frac{\partial j e_z}{\partial r} \right] \quad (1.12d)$$

In those equations, we see that longitudinal components e_z and h_z are purely imaginary, while transverse components are real. This is a convention that comes from the definition of the propagation constant in (1.9). It shows that longitudinal and transverse components are expressed on an orthogonal basis.

Modes are eigensolutions of the optical waveguide. They are parametrized by two quantities: ν , a non-negative integer that is the mode order, and m , a positive integer that is the radial order. ν is related to the number of symmetry axes in the azimuthal dependency of the fields, and m is related to the number of zeros in the radial dependency of the fields. When the mode is purely radial, or purely azimuthal, ν is zero, and we call the mode either TE (azimuthal \mathbf{E} and radial \mathbf{H} field) or TM (radial \mathbf{E} and azimuthal \mathbf{H} field). In other cases ($\nu > 0$), modes are called either EH or HE, determined by whether the e_z or h_z component is dominant.

1.3 Modes in step-index fibers

If we consider step-index fibers, (1.8) simplifies further, because the refractive index does not vary as a function of position. Therefore, $\nabla n^2 = 0$, and the wave equations take the form of Helmholtz equations:

$$(\nabla^2 + k_0^2 n^2) \mathbf{E} = 0 \quad (1.13)$$

that we can write explicitly as:

$$\frac{\partial^2 \mathbf{E}}{\partial r^2} + \frac{1}{r} \frac{\partial \mathbf{E}}{\partial r} + \frac{1}{r^2} \frac{\partial^2 \mathbf{E}}{\partial \phi^2} + (k_0^2 n^2 - \beta^2) \mathbf{E} = 0 \quad (1.14)$$

Because of (1.12), we only need to solve for longitudinal components e_z and h_z to get the complete solution for the \mathbf{E} and \mathbf{H} fields. \mathbf{e} and \mathbf{h} , per (1.9), are invariant in z . Furthermore, because of the circular symmetry, the field must keep the same value after a full 2π azimuthal rotation. Therefore, it has the following separable form:

$$e_z(r, \phi, z) = e_z(r) \cos(\nu\phi + \phi_0) \exp(j\beta z) \quad (1.15)$$

where ν is a non-negative integer, and ϕ_0 is an arbitrary phase. The second partial derivative of e_z with respect to ϕ is given by $\partial^2 e_z / \partial \phi^2 = -\nu^2 e_z$. The differential equation for e_z is now:

$$\frac{\partial^2 e_z}{\partial r^2} + \frac{1}{r} \frac{\partial e_z}{\partial r} + \left(k_0^2 n^2 - \beta^2 - \frac{\nu^2}{r^2} \right) e_z = 0 \quad (1.16)$$

which is the Bessel differential equation (see Appendix A.2.1), with $u = (k_0^2 n^2 - \beta^2)^{1/2}$. Therefore, the solution for $e_z(r)$ is formed from the linear combination of ordinary Bessel functions J and N :

$$e_z(r) = AJ_\nu(ur) + BN_\nu(ur) \quad (1.17)$$

where A and B are appropriate constants. Solution for h_z is similar, but takes different values for the constants.

In a medium of refractive index n , the light travels at speed c/n . However, in a waveguide, the material index is not uniform, and light does not travel in a straight line. For a given mode in a given waveguide, the equivalent index of a material where light would travel in a straight line at the same speed as that mode within the waveguide is called the effective index (n_{eff}). Effective index for each mode is related to the propagation constant by the following relation:

$$\beta = k_0 n_{\text{eff}} \quad (1.18)$$

In an optical fiber, each n_{eff} is located somewhere between the highest material index of the fiber (n_{max}), and the index of the cladding (n_{cl}):

$$n_{\text{cl}} < n_{\text{eff}} < n_{\text{max}} \quad (1.19)$$

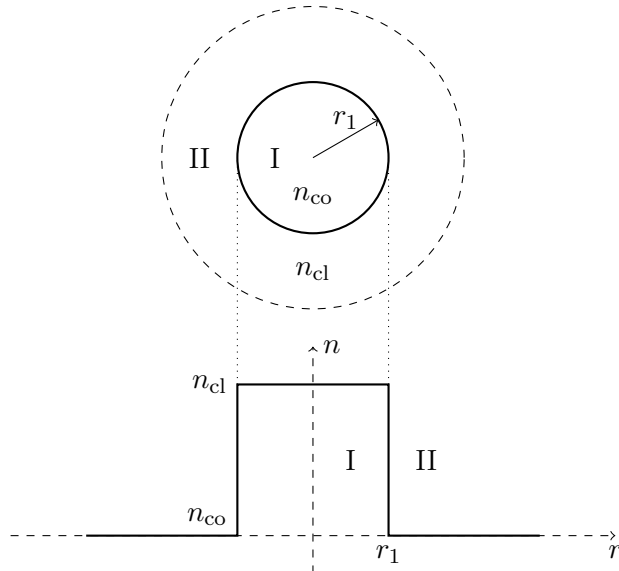


Figure 1.1: Standard step-index fiber geometry (top view, and profile).

This implies that, in cladding, and possibly in some other fiber layers, refractive index can be lower than effective index, thus $k_0 n < \beta$. In that case, (1.16) becomes

$$\frac{\partial^2 e_z}{\partial r^2} + \frac{1}{r} \frac{\partial e_z}{\partial r} - \left(\beta^2 - k_0^2 n^2 + \frac{\nu^2}{r^2} \right) e_z = 0 \quad (1.20)$$

which is the modified Bessel differential equation, and solutions are given by the linear combination of modified Bessel functions I and K :

$$e_z(r) = AI_\nu(wr) + BK_\nu(wr) \quad (1.21)$$

where $w = (\beta^2 - k_0^2 n^2)^{1/2}$.

1.4 Modes of standard step-index fiber

The simplest optical fiber is illustrated in Fig. 1.1. It is composed of two step-index layers: a core (I) and the cladding (II). The radius of the core is r_1 , the refractive index of the core is n_{co} , and the refractive index of the cladding is n_{cl} . This is what we call *standard step-index fiber* (SSIF).

In SSIF, we have $u = (k_0^2 n_{co}^2 - \beta^2)^{1/2}$ and $w = (\beta^2 - k_0^2 n_{cl}^2)^{1/2}$. It is also convenient to define the *normalized frequency* as:

$$V = r_1(u^2 + w^2)^{1/2} = k_0 r_1(n_{co}^2 - n_{cl}^2)^{1/2} \quad (1.22)$$

Longitudinal solutions in the core are formed by ordinary Bessel functions, because $n_{\text{co}} > n_{\text{eff}}$. Furthermore, we must reject solutions containing $N_\nu(ur)$, because this function goes to infinity when $r \rightarrow 0$. Longitudinal solutions in the cladding are formed by modified Bessel functions, because $n_{\text{co}} < n_{\text{eff}}$, and we need to reject solutions containing $I_\nu(wr)$, because this function increases to infinity when $r \rightarrow \infty$.

$$e_z = f_\nu(\phi) \begin{cases} AJ_\nu(ur) & r < r_1 \\ BK_\nu(wr) & r > r_1 \end{cases} \quad (1.23a)$$

$$h_z = g_\nu(\phi) \begin{cases} CJ_\nu(ur) & r < r_1 \\ DK_\nu(wr) & r > r_1 \end{cases} \quad (1.23b)$$

A , B , C , and D are appropriate constants, and functions $f_\nu(\phi)$ and $g_\nu(\phi)$ are azimuthal dependencies of the fields, and are of the form $\cos(\nu\phi + \phi_0)$. To satisfy (1.12), we must ensure that

$$\frac{df_\nu(\phi)}{d\phi} = \nu g_\nu(\phi) \quad \text{and} \quad \frac{dg_\nu(\phi)}{d\phi} = -\nu f_\nu(\phi) \quad (1.24)$$

By convention, and for simplicity, we usually choose

$$f_\nu(\phi) = \cos(\nu\phi) \quad g_\nu(\phi) = -\sin(\nu\phi) \quad (1.25)$$

for modes we call *even*, and

$$f_\nu(\phi) = \sin(\nu\phi) \quad g_\nu(\phi) = \cos(\nu\phi) \quad (1.26)$$

for modes we call *odd*. We now need to ensure continuity of the fields at $r = r_1$. From (1.23), we evaluate the partial derivatives of e_z and h_z , at $r = r_1$:

$$\left. \frac{\partial e_z}{\partial \phi} \right|_{r=r_1} = A\nu g_\nu(\phi) J_\nu(ur_1) = B\nu g_\nu(\phi) K_\nu(wr_1) \quad (1.27a)$$

$$\left. \frac{\partial e_z}{\partial r} \right|_{r=r_1} = Au f_\nu(\phi) J'_\nu(ur_1) = Bw f_\nu(\phi) K'_\nu(wr_1) \quad (1.27b)$$

$$\left. \frac{\partial h_z}{\partial \phi} \right|_{r=r_1} = -C\nu f_\nu(\phi) J_\nu(ur_1) = -D\nu f_\nu(\phi) K_\nu(wr_1) \quad (1.27c)$$

$$\left. \frac{\partial h_z}{\partial r} \right|_{r=r_1} = Cug_\nu(\phi) J'_\nu(ur_1) = Dw g_\nu(\phi) K'_\nu(wr_1) \quad (1.27d)$$

where the prime denotes the derivative of the Bessel function with respect to the argument. We substitute (1.27) into (1.12b) and (1.12d), and evaluate the equalities at $r = r_1$ to obtain continuity of the azimuthal fields:

$$\frac{1}{u^2} \left[\frac{\beta}{r_1} A\nu J_\nu(ur_1) - \eta_0 k_0 C u J'_\nu(ur_1) \right] = -\frac{1}{w^2} \left[\frac{\beta}{r_1} B\nu K_\nu(wr_1) - \eta_0 k_0 D w K'_\nu(wr_1) \right] \quad (1.28a)$$

$$\frac{1}{u^2} \left[-\frac{\beta}{r_1} C\nu J_\nu(ur_1) + \frac{1}{\eta_0} k_0 n_{\text{co}}^2 A u J'_\nu(ur_1) \right] = -\frac{1}{w^2} \left[-\frac{\beta}{r_1} D\nu K_\nu(wr_1) + \frac{1}{\eta_0} k_0 n_{\text{cl}}^2 B w K'_\nu(wr_1) \right] \quad (1.28b)$$

From (1.23), due to the continuity of the longitudinal fields, we have

$$B = A \frac{J_\nu(ur_1)}{K_\nu(wr_1)} \quad D = C \frac{J_\nu(ur_1)}{K_\nu(wr_1)} \quad (1.29)$$

that we can substitute into (1.28). We divide both equations by $J_\nu(ur_1)$, and we write the system in matrix form:

$$\begin{bmatrix} \left(\frac{1}{u^2} + \frac{1}{w^2}\right) \frac{\beta}{r_1} \nu & -\eta_0 k_0 \left(\frac{J'_\nu(ur_1)}{uJ_\nu(ur_1)} + \frac{K'_\nu(wr_1)}{wK_\nu(wr_1)}\right) \\ \frac{1}{\eta_0} k_0 \left(n_{\text{co}}^2 \frac{J'_\nu(ur_1)}{uJ_\nu(ur_1)} + n_{\text{cl}}^2 \frac{K'_\nu(wr_1)}{wK_\nu(wr_1)}\right) & -\left(\frac{1}{u^2} + \frac{1}{w^2}\right) \frac{\beta}{r_1} \nu \end{bmatrix} \begin{bmatrix} A \\ C \end{bmatrix} = 0 \quad (1.30)$$

To get a non-trivial solution, the determinant of the matrix must be zero. Therefore:

$$\left(\frac{1}{u^2} + \frac{1}{w^2}\right)^2 \frac{\beta^2}{r_1^2} \nu^2 = k_0^2 \left(\frac{J'_\nu(ur_1)}{uJ_\nu(ur_1)} + \frac{K'_\nu(wr_1)}{wK_\nu(wr_1)}\right) \left(n_{\text{co}}^2 \frac{J'_\nu(ur_1)}{uJ_\nu(ur_1)} + n_{\text{cl}}^2 \frac{K'_\nu(wr_1)}{wK_\nu(wr_1)}\right) \quad (1.31)$$

This is the *eigenvalue* (or characteristic) equation of SSIF guided modes. It depends on ν , on k_0 (related to wavelength), and on fiber parameters (r_1 , n_{co} , and n_{cl}), and gives discrete solutions for β (u and w parameters being directly related to β).

For TE and TM modes, $\nu = 0$, thus the left-hand part of (1.31) is zero. By definition, $e_z = 0$ for TE modes, therefore the eigenvalue equation for TE modes is

$$\left(\frac{J_1(ur_1)}{uJ_0(ur_1)} + \frac{K_1(wr_1)}{wK_0(wr_1)}\right) = 0 \quad (1.32)$$

Similarly, $h_z = 0$ for TM modes, and eigenvalue equation becomes:

$$\left(n_{\text{co}}^2 \frac{J_1(ur_1)}{uJ_0(ur_1)} + n_{\text{cl}}^2 \frac{K_1(wr_1)}{wK_0(wr_1)}\right) = 0 \quad (1.33)$$

For EH and HE modes, we substitute

$$x = \frac{J'_\nu(ur_1)}{uJ_\nu(ur_1)} \quad b = \frac{K'_\nu(wr_1)}{wK_\nu(wr_1)} \quad \text{and} \quad c = \left(\frac{1}{u^2} + \frac{1}{w^2}\right)^2 \frac{n_{\text{eff}}^2}{r_1^2} \nu^2 \quad (1.34)$$

into (1.31). We find the quadratic form:

$$n_{\text{co}}^2 x^2 + (n_{\text{co}}^2 + n_{\text{cl}}^2)bx + (n_{\text{cl}}^2 b^2 - c) = 0 \quad (1.35)$$

Solutions are given by

$$x = -b(1 - \Delta) \pm \sqrt{b^2 \Delta^2 + c/n_{\text{co}}^2} \quad (1.36)$$

where $1 - 2\Delta = n_{\text{cl}}^2/n_{\text{co}}^2$. One can show that solutions with a plus sign are EH modes, and solutions with a minus sign are HE modes.

1.5 Scalar modes

Frequently, the refractive index difference between core and cladding in optical fiber is very small. We are then under the *weakly guiding condition*, and some approximations can be applied.

From a qualitative point of view, the refractive index is almost uniform over all the space; thus the waveguide looks like a planar waveguide. Therefore, guided modes become quasi-TEM, and have negligible e_z and h_z components.

Having $e_z = h_z = 0$, and assuming $\beta = n_{\text{eff}}k_0 \approx n_{\text{co}}k_0 \approx n_{\text{cl}}k_0$, we get from (1.11):

$$e_r = \frac{\eta_0}{n} h_\phi \qquad e_\phi = -\frac{\eta_0}{n} h_r \qquad (1.37)$$

where n can be assumed to be n_{eff} , as suggested in [17]. Equivalently, we get, in Cartesian coordinates:

$$e_x = \frac{\eta_0}{n} h_y \qquad e_y = -\frac{\eta_0}{n} h_x \qquad (1.38)$$

Under the weakly guiding approximation, modes are linearly polarized. Therefore, they only have one component in the \mathbf{E} field, and one component in the \mathbf{H} field (by convention, either e_x and h_y , or e_y and h_x). This is why we call them *scalar* modes.

Under the weakly guiding approximation, the characteristic equation of standard step-index fiber (1.31) simplifies to:

$$\pm \frac{\nu}{r_1} = \left(\frac{J'_\nu(ur_1)}{uJ_\nu(ur_1)} + \frac{K'_\nu(wr_1)}{wK_\nu(wr_1)} \right) \qquad (1.39)$$

The plus sign in (1.39) relates to EH modes, while the minus sign relates to HE modes. Using Bessel derivative functions (A.14) and (A.17), this simplifies to either

$$\frac{J_{\nu+1}(ur_1)}{uJ_\nu(ur_1)} + \frac{K_{\nu+1}(wr_1)}{wK_\nu(wr_1)} = 0 \qquad (1.40a)$$

or

$$\frac{J_{\nu-1}(ur_1)}{uJ_\nu(ur_1)} - \frac{K_{\nu-1}(wr_1)}{wK_\nu(wr_1)} = 0 \qquad (1.40b)$$

It is possible, using Bessel recurrence relationships, to show that (1.40a) and (1.40b) are equivalent, and can be written as [19]:

$$\frac{uJ_{\ell-1}(ur_1)}{J_\ell(ur_1)} = -\frac{wK_{\ell-1}(wr_1)}{K_\ell(wr_1)} \qquad (1.41)$$

where

$$\ell = \begin{cases} 1 & \text{for TE and TM modes} \\ \nu + 1 & \text{for EH modes} \\ \nu - 1 & \text{for HE modes} \end{cases} \qquad (1.42)$$

This is the characteristic equation of LP modes.

From this development, we can see that, under the weakly guiding approximation, EH modes with parameter $\ell - 1$ are similar to HE modes with parameter $\ell + 1$, and lead to LP modes with parameter ℓ . Similarly, HE modes with parameter $\nu = 2$ are similar to TE and to TM modes ($\nu = 0$), and lead to LP modes with parameter $\ell = 1$. Finally, HE modes with $\nu = 1$ lead to LP modes with $\ell = 0$.

1.6 Cutoff of standard step-index fibers

In an optical fiber, effective index (n_{eff}) of a given mode is a function of the wavelength. The condition for a fiber mode to be guided is to have its effective index greater than the effective index of the cladding ($n_{\text{eff}} > n_{\text{cl}}$). When wavelength increases, effective index decreases. The fundamental mode ($\text{HE}_{1,1}$) is always guided. For other modes, there exists a critical wavelength where $n_{\text{eff}} = n_{\text{cl}}$; beyond this point, the mode is no longer guided. This critical point is what we call the *cutoff* of the mode.

For standard step-index fibers, at cutoff, we have $u = k_0(n_{\text{co}}^2 - n_{\text{cl}}^2)^{1/2}$ and $w = 0$, because $n_{\text{eff}} = n_{\text{cl}}$, causing $K_\nu(wr_1) \rightarrow \infty$. Substituting $K_\nu(wr_1)$ in (1.31) (or in (1.41) for scalar modes) by its asymptotic expansion, using $V = ur_1$, and evaluating the limits, we get the cutoff conditions found in Table 1.1.

Table 1.1: Cutoff conditions for standard step-index fibers

Mode	cutoff	
$\text{LP}_{\ell,m}$	$J_{\ell-1}(V) = 0$	(1.43)
$\text{TE}_{0,m}, \text{TM}_{0,m}$	$J_0(V) = 0$	(1.44)
$\text{HE}_{1,m}$	$J_1(V) = 0$	(1.45)
$\text{HE}_{\nu,m}$	$\left(\frac{n_{\text{co}}^2}{n_{\text{cl}}^2} + 1\right) J_{\nu-1}(V) = \frac{V}{\nu-1} J_\nu(V)$	(1.46)
$\text{EH}_{\nu,m}$	$J_\nu(V) = 0$	(1.47)

Because cutoffs of $\text{HE}_{\nu,m}$ modes depends on the refractive index ratio between core and cladding, we choose $n_{\text{co}} = 1.474$ and $n_{\text{cl}} = 1.444$ as typical values to make cutoff calculations. The cutoff for the first mode group ($V = 2.405$) is called the *single mode condition*. If the V number of a given fiber is below that value, the fiber will only guide the fundamental mode ($\text{HE}_{1,1}$ or $\text{LP}_{0,1}$). Table 1.2 gives the cutoffs (expressed as V number) for the first modes in a standard step-index fiber.

Table 1.2: Cutoffs of the first modes in standard step-index fiber ($n_{\text{co}} = 1.474$, $n_{\text{cl}} = 1.444$).

	$m = 1$	$m = 2$	$m = 3$	$m = 4$	$m = 5$
LP _{0,m} , HE _{1,m}	0	3.832	7.016	10.173	13.324
LP _{1,m} , TE _{0,m} , TM _{0,m}	2.405	5.520	8.654	11.792	14.931
HE _{2,m}	2.422	5.528	8.659	11.795	14.934
LP _{2,m} , EH _{1,m}	3.832	7.016	10.173	13.324	16.471
HE _{3,m}	3.853	7.028	10.182	13.330	16.476
LP _{3,m} , EH _{2,m}	5.136	8.417	11.620	14.796	17.960

1.7 Group index and dispersion

The effective index (n_{eff}) is related to the *phase velocity* (v_p) of the mode:

$$v_p = \frac{c}{n_{\text{eff}}} = \frac{\omega}{\beta} \quad (1.48)$$

The phase velocity is the speed at which the light – a rapidly oscillating signal – travels in the propagation direction of the fiber.

However, the effective index varies as a function of the wavelength, for two reasons. First, the refractive index of a medium is a function of the wavelength (see Appendix B); we call this effect the *material dispersion*. Second, the characteristic equation of the modes is a function of the wavelength (because of the k_0 parameter, included in u and w parameters); we call that the *waveguide dispersion*. Because of this wavelength dependency, a pulse sent through an optical fiber – the envelope of a rapidly oscillating signal – travels at a speed that is different from the phase velocity. We call this the *group velocity* (v_g), and it is related to the first derivative of the effective index of the mode:

$$v_g = c \left(n_{\text{eff}} - \lambda \frac{dn_{\text{eff}}}{d\lambda} \right)^{-1} = \frac{d\omega}{d\beta} \quad (1.49)$$

If n_{eff} was not varying with the wavelength, the derivative of n_{eff} would be zero, and v_g would be equal to v_p .

Similarly to the effective index, we can define a *group index*, which relates the group velocity to the speed of light:

$$n_g = \frac{c}{v_g} \quad (1.50)$$

A pulse of light never is composed of a single wavelength; it always has a spectral bandwidth, that can be more or less narrow, depending on the laser source. Therefore, because of material and waveguide dispersion, the bluish part of the pulse does not travel at the exact same velocity as the reddish part of the pulse. This causes the pulse to broaden during the transmission over a length of fiber. This broadening of the pulse is a linear effect that we

call the dispersion. It is characterized by what we call the dispersion parameter (D), usually expressed in $\text{ps nm}^{-1} \text{km}^{-1}$, and related to the second derivative of the effective index:

$$D = -\frac{\lambda}{c} \frac{d^2 n_{\text{eff}}}{d\lambda^2} = -\frac{\omega^2}{2\pi c} \frac{d^2 \beta}{d\omega^2} \quad (1.51)$$

Since the dispersion is a linear effect, it can easily be compensated. However, on WDM systems, where signals with many different wavelength travel alongside, the dispersion is not exactly the same for every wavelength, and it can be necessary to take into account the slope of the dispersion (S), expressed in $\text{ps nm}^{-2} \text{km}^{-1}$, and related to the third derivative of the effective index:

$$S = \frac{dD}{d\lambda} \quad (1.52)$$

A convenient way to describe the propagation of a mode through an optical fiber is to develop the propagation constant β as a Taylor series, around the central frequency of the pulse ω_0 :

$$\beta(\omega) = \beta_0 + \beta_1(\omega - \omega_0) + \frac{1}{2}\beta_2(\omega - \omega_0)^2 + \frac{1}{6}\beta_3(\omega - \omega_0)^3 + \dots \quad (1.53)$$

where β_0 is the propagation constant at the central frequency, and:

$$\beta_i = \left. \frac{d^i \beta}{d\omega^i} \right|_{\omega_0} \quad (1.54)$$

Chapter 2

The orbital angular momentum of light

2.1 Linear and angular momentum

In classical mechanics, *linear momentum* (\mathbf{p}) is defined as the product of the mass (M) and velocity (\mathbf{v}) of an object. Therefore, this is a vector quantity, expressed in kg m s^{-1} (or in N s):

$$\mathbf{p} = M\mathbf{v} \quad (2.1)$$

An interesting property of linear momentum is that it is a conserved quantity. A classical demonstration of this is the Newton's cradle, where a series of pendulums are aligned, and the movement of the first sphere is transmitted to the last one, while intermediate spheres remain stationary. Another illustration is in the game of pool, where all balls included in a collision will carry a portion of the momentum of the ball that initiated the collision.

A related property exists in a rotating system, which is the *angular momentum* (\mathbf{L}), expressed in $\text{kg m}^2 \text{s}^{-1}$ (or in N m s), and defined as:

$$\mathbf{L} = \mathbf{r} \times \mathbf{p} \quad (2.2)$$

where \mathbf{r} is the position vector of the object, relative to the origin, and \mathbf{p} is the linear momentum of that object. Because of the cross product, \mathbf{L} is perpendicular to both \mathbf{r} and \mathbf{p} . There also is a conservation law of angular momentum, which is typically illustrated with the gyroscope, whose orientation is maintained, regardless of the orientation of the mounting frame.

2.2 The angular momentum of light

Light, as an electromagnetic wave, carries energy. The energy flux density (in W m^{-2}) is given by the Poynting vector

$$\mathbf{S} = \mathbf{E} \times \mathbf{H} \quad (2.3)$$

A more surprising property of electromagnetic wave is that it also carries momentum. The consequence of the linear momentum of light is exertion of a small pressure on a target surface, that we call the radiation pressure. While effects of this pressure are usually too small to be observed (the linear momentum of light is equivalent to $k_0\hbar$ per photon, where $\hbar = h/2\pi = 1.055 \times 10^{-34}$ J s is the reduced Plank constant), it has major effects on the development of the cosmos, and can also be observed at the atomic level.

Light also carries an angular momentum, meaning it can rotate around the propagation direction. In fact, there are two forms of angular momentum: the *spin angular momentum* (SAM), and the *orbital angular momentum* (OAM).

The spin angular momentum occurs when light is circularly or elliptically polarized. In that case, the direction of the transverse electrical field (the polarization) is rotating around an axis, and each photon carries a spin angular momentum of $\sigma\hbar$, where $-1 \leq \sigma \leq +1$. For circular polarization, $\sigma = \pm 1$, depending on whether it is left- or right-handed. When $\sigma = 0$, there is no SAM, and the polarization is linear. Intermediate values denote elliptical polarization.

With orbital angular momentum, the phase front of the light beam rotates around an axis. This means that OAM is related to the spatial distribution of the field, and not to the polarization. Mathematically, it means that the phase of an OAM carrying beam, on the transverse plane, is given by:

$$\varphi(r, \phi) = \exp(j\ell\phi) \tag{2.4}$$

where the ℓ parameter, an integer, is called the *topological charge*, or the OAM order. While the OAM of light was theoretically known, it is only in 1992 that Allen et al. demonstrated it, showing that any helically phased beam carries an OAM equivalent to $\ell\hbar$ per photon [20]. Because ℓ can be any integer, the value of OAM can be much higher than the value of SAM.

The azimuthal dependency of the phase, given by (2.4), implies that the phase is undefined at $r = 0$. Therefore, the intensity always is zero at the center of an OAM beam. This is why OAM beams often are called *vortex beams*, and sometime *cylindrical vector beams* (CVB) [21, 22]. The most common form of a vortex beam is the Laguerre-Gaussian (LG) beam. However, not all vortex beams necessarily carry OAM; it depends on the phase front of the beam.

Under the paraxial approximation, when the beam only varies slowly with respect to the z axis (as is the case with a collimated beam), it can be shown that SAM and OAM can be separated [23]. Therefore, OAM is independent of SAM, and vice-versa, and the total angular momentum of a beam is the sum of the contributions of the SAM and OAM. However, for a non-paraxial beam, SAM and OAM are not completely separable, and a correction term must be added when we calculate the total angular momentum [24]. Conry et al. studied the

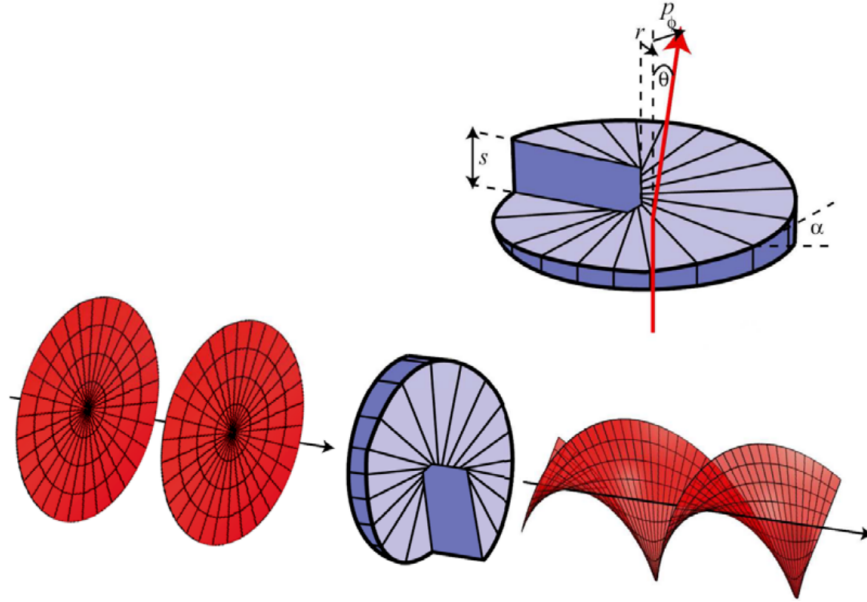


Figure 2.1: A spiral phase plate can generate a helically phased beam from a Gaussian. In this case $\ell = 0 \rightarrow \ell = 2$ (reproduced from [28, Figure 5]).

polarization dependency in OAM-carrying LG beams [25].

The OAM of light rapidly found many applications [26–28], including, but not limited to, the ability to spin microscopic objects and to drive micromachines, trapping, guiding and rotating atoms, advanced optical manipulations, microscopy, applications in space physics studies, and higher-levels quantum information systems.

2.3 Generation of OAM beams

There are a few different techniques to generate OAM beams. The most common techniques are reported in [28, Section 2].

Probably the most obvious method is to use a spiral phase plate, as illustrated in Fig. 2.1, where the thickness of the plate is defined as a function of the azimuthal position by: $\ell\lambda\phi/2\pi(n-1)$, where ℓ is the OAM order, λ is the incident beam wavelength, ϕ is the azimuthal position, and n is the refractive index of the plate. This device is very efficient, and allows the conversion of beams with relatively high power. However, it needs extreme precision in manufacturing, it is wavelength dependent, and you need a different plate for each kind of OAM mode you want to generate. An adjustable spiral phase plate was proposed in [29].

OAM can be generated using diffractive optical elements. A common technique is to use a *fork grating*, generated by the superposition of the OAM phase mask and a linear phase ramp, modulo 2π . This fork pattern could, for example, be etched in a glass plate, or printed

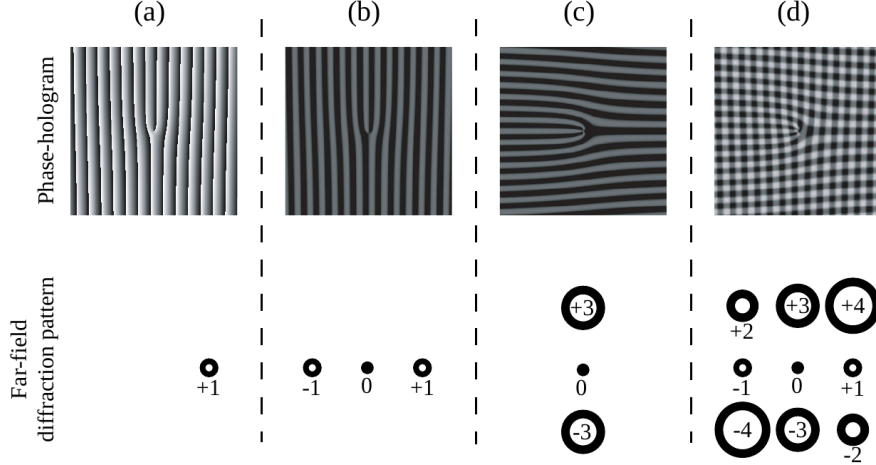


Figure 2.2: Some examples of fork grating patterns. (a) pattern for horizontally shifted $\ell = 1$ beam. (b) discretized pattern (to 0 or π) for $\ell = -1, 0, 1$ beams. (c) discretized pattern for vertically shifted $\ell = -3, 3$ beams. (d) sum of the two phase patterns that create a 3×3 array of beams. (reproduced from [30, Figure 2]).

on transparent material. When illuminating the center of the grating, most of the light is transmitted with no alteration, but part of it is diffracted and carries a $+\ell$ topological charge to one side of the output, and a $-\ell$ topological charge to the other side. It is also possible to superimpose two different fork gratings, for example one horizontally and one vertically, to generate multiple topological charges simultaneously [30]. This is the main advantage of this technique. Depending on the material used for supporting the grating, it can also accept potentially high power. The quality of the generated beam highly depends on the precision of the grating. The main disadvantage of this technique is its poor efficiency. Some example of fork grating patterns are illustrated on Fig. 2.2. A variation of this technique was proposed to improve efficiency, using forked polarization grating [31].

In the original experiment from Allen et al. in 1992 [20], OAM was generated by transforming Hermite-Gaussian (HG) modes to LG modes using cylindrical lens. The principles of that conversion are explained in [32].

Multi-plane light conversion, while typically used for the multiplexing of LP modes [33, 34], could potentially be used for OAM multiplexing, if designed accordingly. At the time of writing, we are currently testing such a device, designed and fabricated by CAILabs. The principle is to use a multipass cavity, where the input beams, spatially separated, are transformed and combined by successive reflections on a specially designed phase plate.

A very convenient way to generate OAM is to use a spatial light modulator (SLM). The SLM is a device, made of liquid crystals, that is programmable using a computer [35]. It is composed of a matrix of pixels, just like a computer screen, and each pixel can be programmed

to generate a given phase (there also exists SLMs that act on amplitude instead of phase). The programming of the SLM is made by displaying a grayscale image on it, which is automatically converted to a phase pattern. Most SLMs work in reflection – we send a beam with a given angle, and the reflected beam has its phase modified per the pattern programmed on the SLM – but some SLMs work in transmission. To generate the OAM beam, we can either program the SLM with the OAM phase mask, or program it with a diffractive pattern. The main advantage of the SLM is its versatility; it can be reconfigured as needed. It is even possible to send different beams on different sections of the SLM, to modulate several beams simultaneously. However, the SLM is a polarization dependent device, and it accepts only limited power.

It is also possible to use optical fiber for the generation of OAM. This can be done using the fiber as a mode selector [21] or a mode converter [36, 37], by the conversion of acoustic waves to optical waves [38], using a fiber coupler [39], using a mechanical grating [40, 41], a tilted optical grating [42], a helical grating [43], multicore fibers [44–47], or using liquid core optical fiber [48].

The use of thermally tuned q-plates seems a very promising and efficient way of generating OAM beams [49].

Finally, the recent trend is to use silicon photonic integrated devices for the generation of OAM. In [50–52], a star coupler is used to generate the phase pattern, and a circular grating coupler vertically couples the OAM mode to an optical fiber, or in free-space. A similar approach is described in [53–55], but using a 3D waveguide. A different approach, using a grated microring resonator, is proposed in [56]. Another proposition is integrating a spiral phase plate directly on the top of a VCSEL [57].

2.4 Detecting OAM modes

An OAM beam never has intensity at its center, and thus is always doughnut shaped, as we already explained in Section 2.2. This characteristic, however, is not sufficient to identify OAM beams and their topological charge, because we need to confirm phase information as well. But the phase of an optical signal cannot be measured directly; hence we need techniques to confirm the helical phase front of OAM beams.

A common way to identify OAM is to interfere the incident beam with a Gaussian beam, and to visualize the resulting interference pattern on a camera. If the incident beam is Gaussian, the interference pattern will look like a series of concentric circles. However, if the incident beam has a helical phase front, the interference pattern will be a spiral, where the number of arms is the topological charge, and the direction of the spiral is linked with the handedness of the phase rotation (i.e., the sign of ℓ).

While the interference pattern is useful to validate the presence of an OAM beam, it cannot really be used for demultiplexing. A better way is to convert the incident beam back to Gaussian, using a phase pattern or a fork grating, on a glass plate or a SLM, for instance. It works because the resulting operation is to add (or subtract) to the topological charge. Therefore, if you send an incident beam with $\ell = +1$ through a fork grating, the output will be a $\ell = 0$, i.e. Gaussian, beam to the left or right side, and $\ell = 2$ OAM beam to the other side. Similarly, sending an OAM beam on a spiral phase plate would increase or decrease the topological charge, depending on the direction of the helical structure. After the conversion, an iris can be used to remove potential doughnut shape intensity of OAM modes, and to detect the intensity of the resulting Gaussian beam.

A mode sorter was proposed to identify OAM modes, where the lateral position of the resulting beam tells the topological charge of the incident beam [58].

2.5 OAM in free-space telecommunications

OAM states are orthogonal to each other in a free-space beam. Thus it is possible to use OAM states to encode different information channels on a single optical beam. Furthermore, the OAM state is independent of wavelength, quadrature, and polarization. Therefore, it provides an additional dimension for encoding information, the spatial dimension, potentially enabling a dramatic improvement in the capacity of optical links.

This idea was first proposed by Bouchal and Čelechovský in 2004 [59]. Four bits of information were encoded on four OAM channels, with topological charges of respectively $\ell = 1, 3, 5, 7$. Soon after, a real data transmission experiment was performed by Gibson et al., where 8 OAM states ($\ell = \pm 4, \pm 8, \pm 12, \pm 16$) were transmitted over 15 m in free-space [30]. The signal was encoded using a phase mask on a SLM, and decoded using two superimposed fork grating, on a second SLM, resulting in nine possible spot positions on the CCD camera, one per channel (the central Gaussian spot being used for alignment).

In those setups, the OAM signal was dynamically modulated using the SLM. The problem is that in such setup, the data rate is limited by the slow refresh rate of the SLM. In 2007, Čelechovský and Bouchal proposed and demonstrated an alternative setup where data was modulated onto each mode separately, and then the modes were multiplexed for transmission. The modulation rate was independent of the mode generation technique [60]. They fully encoded and decoded four information channels using four OAM modes ($\ell = \pm 4, \pm 8$) over 6 m.

In 2010, a system in C-band was demonstrated, carrying 20 Gbit s^{-1} signal over 2 OAM states [61]. The year after, a system using 4 OAM channels ($\ell = -8, +10, +12, -14$) and 16-QAM encoding was demonstrated, proving the compatibility of quadrature encoding with OAM [62–

64]. The same team also demonstrated a setup with 2 OAM states ($\ell = 8, 16$) and 25 WDM channels, using OOK, DPSK, or QPSK coherent encoding, and reaching up to 2 Tbit s^{-1} , showing the compatibility of WDM with OAM [65]. Another team demonstrated the transmission of 16 different OAM channels ($\ell = \pm 1, \pm 2, \dots, \pm 8$) [66]. In 2013, another demonstration was made, using 24 OAM channels and 42 WDM channels, for a total of 1008 channels; adding polarization multiplexing and QPSK encoding, a theoretical $100.8 \text{ Tbit s}^{-1}$ was achieved [67, 68]. Finally, we should mention a recent review paper on free-space communications using OAM links [69].

One motivation for using OAM in free-space is the security advantage it offers, since OAM states cannot be recovered if the detector is not exactly positioned in the path of the beam [70]. OAM states can be used to perform quantum cryptography. While SAM already permitted the encoding of (2 levels) qubits, OAM allows the realization of quantum systems with a higher number of levels [71, 72].

One problem with the free-space transmission of OAM is that atmospheric turbulence randomly affects the phase of the transmitted signal, which can affect the OAM state. This is one reason why all free-space experiments are on very short distances, or at very low transmission rates [73]. Effects of turbulences were studied in several papers [74–77]. LDPC codes were proposed to compensate for those impairments [78].

To complete our review of the use of OAM in telecommunications, we should also mention some experiments on OAM in radio-communications [79–82].

2.6 OAM fiber modes

We saw in Chapter 1 that, in circular optical fiber, the electrical field can be expressed as:

$$\mathbf{E}(r, \phi, z, t) = \mathbf{e}(r) \begin{Bmatrix} f_\nu(\phi) \\ g_\nu(\phi) \\ f_\nu(\phi) \end{Bmatrix} \exp(j\beta z - j\omega t) \quad (2.5)$$

where $\mathbf{e}(r)$ is the radial dependency of the field, and $f_\nu(\phi)$ and $g_\nu(\phi)$, defined in (1.25) and (1.26), is the azimuthal dependency of the field. The three lines inside the curly braces are for the r , ϕ , and z components of the electrical field, respectively. In this expression, ν and β are given by modal solutions. $\mathbf{E}(r, \phi, z, t)$ is a complex field; its modulus gives the envelope of a rapidly oscillating signal, while the angle gives the phase of the signal. The azimuthal orientation of the field is arbitrary, and defined by $f_\nu(\phi)$ and $g_\nu(\phi)$ functions. Usually, we assign them sin and cos functions, and qualify the mode to be *even* or *odd*, in relation with the symmetry of the underlying trigonometric function.

If we take an even and an odd mode, with a $\pi/2$ phase difference, and we sum the fields, we

get, as a resulting field:

$$\mathbf{E}(r, \phi, z, t) = \mathbf{e}(r) \left\{ \begin{array}{l} f_{\nu}^{\text{even}}(\phi) + j f_{\nu}^{\text{odd}}(\phi) \\ g_{\nu}^{\text{even}}(\phi) + j g_{\nu}^{\text{odd}}(\phi) \\ f_{\nu}^{\text{even}}(\phi) + j f_{\nu}^{\text{odd}}(\phi) \end{array} \right\} \exp(j\beta z - j\omega t) \quad (2.6)$$

Because $f_{\nu}(\phi)$ and $g_{\nu}(\phi)$ are trigonometric functions, we have, using the Euler formula (A.35), this equivalent form:

$$\mathbf{E}(r, \phi, z, t) = \mathbf{e}(r) \left\{ \begin{array}{l} \exp(j\nu\phi) \\ -\exp(j\nu\phi) \\ \exp(j\nu\phi) \end{array} \right\} \exp(j\beta z - j\omega t) \quad (2.7)$$

This is precisely the azimuthal dependency of the phase, defined for OAM modes in (2.4). Therefore, the addition of even and odd vector modes with a $\pi/2$ phase difference leads to an OAM mode. In other words, guided OAM modes in optical fiber are made of a combination of vector eigenmodes.

We can rewrite (2.7) as:

$$\mathbf{E}(r, \phi, z, t) = \mathbf{e}(r) \left\{ \begin{array}{l} \exp(j\sigma\phi) \exp(j\ell\phi) \\ -\exp(j\sigma\phi) \exp(j\ell\phi) \\ \exp(j\nu\phi) \end{array} \right\} \exp(j\beta z - j\omega t) \quad (2.8)$$

where $\sigma = \pm 1$ and $\sigma + \ell = \nu$. In this expression, ν is the total angular momentum order, σ is the spin, and is related to the polarization of the transverse field, and ℓ is the orbital angular momentum order. The $\exp(j\sigma\phi)$ term indicates that the polarization has an azimuthal dependency; therefore, polarization of OAM modes in an optical fiber is circular, i.e., is rotating.

We can summarize the relation between vector and OAM modes by the following relation:

$$\text{OAM}_{\pm\ell, m}^{\pm} = \text{HE}_{\ell+1, m}^{\text{even}} \pm j \text{HE}_{\ell+1, m}^{\text{odd}} \quad (2.9a)$$

$$\text{OAM}_{\pm\ell, m}^{\mp} = \text{EH}_{\ell-1, m}^{\text{even}} \pm j \text{EH}_{\ell-1, m}^{\text{odd}} \quad (2.9b)$$

where the superscript denotes the direction of the circular polarization, and ℓ is the topological charge. It means that OAM modes made from $\text{HE}_{\nu, m}$ modes are rotating in the same direction as the spin (spin aligned), and OAM modes made from $\text{EH}_{\nu, m}$ modes are rotating in the opposite direction as the spin (spin anti-aligned) [83, 84].

OAM modes made from $\text{HE}_{1, m}$ modes would have a spin, but no topological charge ($\ell = 0$). Therefore, this is not a true OAM mode, but simply a vector mode with circular polarization. However, we will consider it as $\text{OAM}_{0, m}$, in a more general definition.

In theory, we could also have OAM modes made from $\text{TE}_{0, m}$ and $\text{TM}_{0, m}$, like this:

$$\text{OAM}_{\pm 1, m}^{\mp} = \text{TE}_{0, m} \pm j \text{TM}_{0, m} \quad (2.10)$$

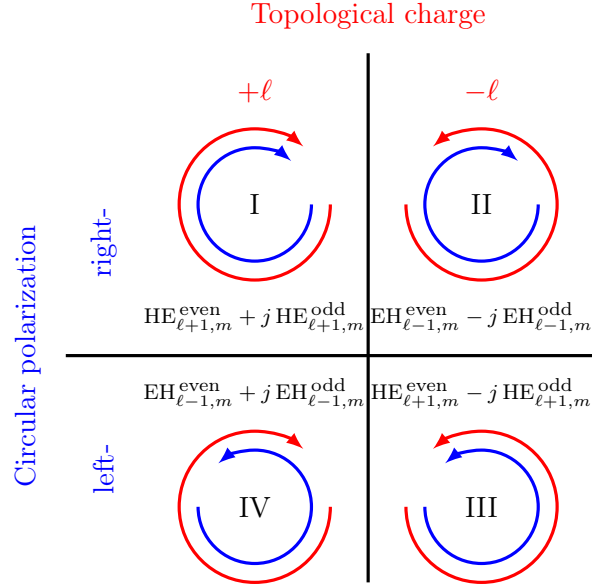


Figure 2.3: The four OAM mode degeneracies.

However, this mode is not stable and cannot propagate, because the β propagation constants of $\text{TE}_{0,m}$ and $\text{TM}_{0,m}$ modes are different. Therefore, we call this an unstable vortex (IV) [38].

To summarize, for a given topological charge ℓ , there are four possible OAM modes: two different spin rotation, and two different phase rotation. This is illustrated in Fig. 2.3. The only exceptions are for $\text{OAM}_{\pm 1,m}$, where spin and topological charge always have the same sign, and for $\text{OAM}_{0,m}$, where there is no topological charge (only spin).

2.7 OAM modes in optical fibers

2.7.1 Transmission of OAM modes

The first paper we are aware of that mentions the possibility of transmitting OAM modes through optical fiber is from Alexeyev et al. in 1998 [85]. They showed, from the wave equations, that the solution for OAM modes can exist in multimode fibers. However, for a long time, optical fibers were only used for the generation or the transformation of OAM modes, and not for their transmission [21, 36–39].

The first real demonstration of the transmission of OAM modes through optical fiber is from Ramachandran et al. in 2009 [40]. They designed a special fiber, they called *vortex fiber*, which has a central core able to transmit the fundamental mode, surrounded by a lower trench, and an outer ring able to transmit the first OAM mode group. In this first paper, they reported a transmission through more than 20 m fiber. Two years later, transmission of OAM through a 1 km fiber was reported [86–88].

Data transmission using OAM through optical fiber begins with a 2011 paper, that describes theoretically the components of a multidimensional optical fiber communication system using OAM modes [89]. Then a first data transmission experiment was reported, using the vortex fiber, with four OAM channels ($\ell = \pm 1$, and fundamental mode with both polarizations) [90]. Other experiments followed, using QPSK encoding and LDPC codes [91], and using 16-QAM and 10 channels WDM [92]. Finally, all the experiments on the vortex fiber were summarized in a *Science* paper [93].

Because having a high index contrast is a desirable feature for an OAM transmitting fiber, a fiber with a ring core and air in the middle was proposed [94]. The fiber was fabricated, and 12 OAM modes were transmitted through 2 m of that fiber, and 2 OAM modes over 1 km [95]. Using that fiber, they demonstrated that OAM modes with higher ℓ value are less sensitive to perturbations like bends and twists [96, 97].

An inverse parabolic graded index fiber, supporting 4 OAM modes, was demonstrated [9, 98]. A dual-guided ring-core fiber, very similar to the original vortex fiber, was proposed and simulated [99].

We proposed and fabricated a fiber with an air-core, and achieved the world record number of OAM modes transmitted through an optical fiber [1, 2]. More details about this fiber will be given in Chapter 7. We also designed a family of five ring core fibers, to study propagation effects of OAM modes [4, 5]. More details about those fibers are given in Chapter 8.

To increase even further the capacity of the fiber link, OAM based multiplexing can be combined with multi-core fibers. A first demonstration was achieved with 2 OAM modes and 7 cores fiber, on a 80 cm long fiber [100, 101], then on a 500 m fiber [102]. Li and Wang presented a similar concept, with 7 cores and 22 OAM modes [103, 104], then 19 cores and 22 OAM modes [105]. It was also proposed to use a multicore structure to propagate OAM modes as supermodes [106].

2.7.2 SDM using OAM in a different way

A related but different way to use OAM with optical fibers is to launch an OAM mode in a standard multimode fiber, and to detect the resulting mode at the end of the fiber, even if it is no longer an OAM mode. This was first proposed by Carpenter [107], to increase the conversion efficiency between free-space and fiber modes. Similar idea was reintroduced, to enhance the transmission in short-range MMF [108].

There also are a few papers by Murshid, where different OAM ring sizes are used to multiplex the information [13, 109–111].

2.7.3 OAM components and functions

Being able to multiplex, transmit, and demultiplex information using OAM modes is not sufficient by itself to justify that the use of OAM multiplexing could increase fiber capacity and reduce costs, compared to the use of a bunch of fibers. Other common functions need to be performed directly on the OAM modes, like amplification, mode conversion, and add/drop multiplexing. While a complete review on this topic exceed the scope of this thesis, we can nevertheless mention some contributions.

Most of the proposed systems work in free-space. It includes multicasting OAM modes [112], add/drop multiplexers [113, 114], and amplification using light-acoustic interaction [115].

A few fiber-based devices begin to emerge, like fiber based mode converter using mechanical stresses on the fiber [116], and OAM erbium-doped fiber amplifier [117].

Chapter 3

Solving for modes using numerical methods

3.1 The simulation software

While commercial softwares exist to numerically solve for modes in optical fibers, we choose to develop our own in-house software. The goal was two-fold: first, implementing the algorithms by ourself is the best way to deeply understand them; second, using our own software, we have no limitations on the customizations that can be done to solve for particular problems. Furthermore, this gives to the community a free to use implementation of the algorithms, that could be used and improved by other researcher*. We do not pretend to have a faster or a more accurate simulation software than what is commercially available, but we believe is accurate, usable, and mostly customizable.

3.2 The transfer matrix method

The transfer matrix method [17, 118] is an algorithm used to solve for effective index of step-index optical fiber. The advantages of this method, compared to other numerical methods such as finite element methods (FEM), is that it is faster, it is more accurate, it lessen the chances failing to identify modes, and it allows an easier identification of modes found. However, it applies only to step-index fibers, while FEM allows to solve for arbitrary fiber profiles.

The principle is to ensure the continuity of the fields at each layer interface. This gives us an eigenvalue problem, where only specific combinations of ν and n_{eff} allow solutions. Each combination of ν and n_{eff} that allows the fields to be continuous across layers is called a fiber mode. Algorithm 3.1 gives the generic idea of the algorithm used to find the effective index of a given mode (defined by ν , m , and the mode family) at a given wavelength (λ), for a given

*<https://github.com/cbrunet/fibermodes>

step index fiber (defined by the vector of refractive indexes \mathbf{n} and the vector of layer radii \mathbf{r} , starting from the center of the fiber). This is a simplified version, as it is written for shortness and explicitness over performance. The FINDNEFF function finds the m^{th} root of CHARFUNC, starting from highest possible n_{eff} (the highest refractive index of the fiber) to the lowest (the refractive index of the cladding). The characteristic function CHARFUNC, that we will detail in the following sections, returns zero if the given parameters are the parameter of a existing fiber mode. As we will see later, the simple **for** loop hides more complex optimizations, needed to accurately find all the characteristic function roots, in a reasonable time.

Algorithm 3.1 Finding n_{eff} of a given mode (simplified version)

```

1: function FINDNEFF( $\nu, m$ , family,  $\lambda, \mathbf{n}, \mathbf{r}$ )
2:    $k_0 \leftarrow 2\pi/\lambda$ 
3:   for  $n_{\text{eff}} \leftarrow \max \mathbf{n}, n_N$  do                                     ▷ From highest  $n$  to  $n_{\text{cladding}}$ 
4:      $r \leftarrow \text{CHARFUNC}(n_{\text{eff}}, \nu, \text{family}, k_0, \mathbf{n}, \mathbf{r})$ 
5:     if  $r = 0$  then                                                         ▷ We found a root
6:        $m \leftarrow m - 1$                                                  ▷ Count the number of roots
7:     end if
8:     if  $m = 0$  then                                                         ▷ This was the  $m^{\text{th}}$  root
9:       return  $n_{\text{eff}}$ 
10:    end if
11:  end for
12:  return Mode not found
13: end function

```

Modes are ordered in a given order (as function of n_{eff}) [17]. For vector modes, we have:

$$\begin{cases} \text{HE}_{\nu,1} > \text{EH}_{\nu,1} > \text{HE}_{\nu,2} > \text{EH}_{\nu,2} > \dots > \text{HE}_{\nu,m} > \text{EH}_{\nu,m} \\ \text{TE}_{0,1} > \text{TE}_{0,2} > \dots > \text{TE}_{0,m} \\ \text{TM}_{0,1} > \text{TM}_{0,2} > \dots > \text{TM}_{0,m} \end{cases} \quad (3.1)$$

and for scalar modes:

$$\text{LP}_{\ell,1} > \text{LP}_{\ell,2} > \dots > \text{LP}_{\ell,m} \quad (3.2)$$

Once we found the m^{th} root of the characteristic function, we can tag the mode. The ν parameter was already chosen. For LP, TE, and TM modes, the mode family is determined by the characteristic function we used (that is different for each family of modes), and the m parameter is the number of roots, from the highest n_{eff} . For HE and EH modes, the characteristic function is the same for both families, hence the family and the m parameter are determined from the mode order given in (3.1).

3.2.1 The matrix method

As we saw in Section 1.3, the azimuthal component of the electrical and the magnetic fields, for layer i , are given by:

$$e_z(r, \phi) = f_\nu(\phi) \begin{cases} A_i J_\nu(u_i r) + B_i N_\nu(u_i r) & n_{\text{eff}} < n_i \\ A_i I_\nu(w_i r) + B_i K_\nu(w_i r) & n_{\text{eff}} > n_i \end{cases} \quad (3.3a)$$

$$h_z(r, \phi) = g_\nu(\phi) \begin{cases} C_i J_\nu(u_i r) + D_i N_\nu(u_i r) & n_{\text{eff}} < n_i \\ C_i I_\nu(w_i r) + D_i K_\nu(w_i r) & n_{\text{eff}} > n_i \end{cases} \quad (3.3b)$$

where $f_\nu(\phi)$ and $g_\nu(\phi)$ are trigonometric functions defined in (1.25) and (1.26), $u_i = k_0(n_i^2 - n_{\text{eff}}^2)^{1/2}$, $w_i = k_0(n_{\text{eff}}^2 - n_i^2)^{1/2}$, n_i is the refractive index of the fiber layer, and A_i , B_i , C_i , and D_i are appropriate constants to be found. From (1.12), we know that the transverse components of the fields are all dependent of the azimuthal components. Substituting (3.3) into (1.12), we have:

$$e_r(r, \phi) = f_\nu(\phi) \frac{1}{k_0 r (n_i^2 - n_{\text{eff}}^2)} \begin{cases} k_0 r n_{\text{eff}} u_i [A_i J'_\nu(u_i r) + B_i N'_\nu(u_i r)] - \\ \quad \eta_0 \nu [C_i J_\nu(u_i r) + D_i N_\nu(u_i r)] & n_i > n_{\text{eff}} \\ k_0 r n_{\text{eff}} w_i [A_i I_\nu(w_i r) + B_i K_\nu(w_i r)] - \\ \quad \eta_0 \nu [C_i I_\nu(w_i r) + D_i K_\nu(w_i r)] & n_i < n_{\text{eff}} \end{cases} \quad (3.4a)$$

$$e_\phi(r, \phi) = g_\nu(\phi) \frac{1}{k_0 r (n_i^2 - n_{\text{eff}}^2)} \begin{cases} k_0 n_{\text{eff}} \nu [A_i J_\nu(u_i r) + B_i N_\nu(u_i r)] - \\ \quad \eta_0 u_i r [C_i J'_\nu(u_i r) + D_i N'_\nu(u_i r)] & n_i > n_{\text{eff}} \\ k_0 n_{\text{eff}} \nu [A_i I_\nu(w_i r) + B_i K_\nu(w_i r)] - \\ \quad \eta_0 w_i r [C_i I'_\nu(w_i r) + D_i K'_\nu(w_i r)] & n_i < n_{\text{eff}} \end{cases} \quad (3.4b)$$

$$h_r(r, \phi) = g_\nu(\phi) \frac{1}{k_0 r (n_i^2 - n_{\text{eff}}^2)} \begin{cases} k_0 r n_{\text{eff}} u_i [C_i J'_\nu(u_i r) + D_i N'_\nu(u_i r)] - \\ \quad n_i^2 \nu / \eta_0 [A_i J_\nu(u_i r) + B_i N_\nu(u_i r)] & n_i > n_{\text{eff}} \\ k_0 r n_{\text{eff}} w_i [C_i I'_\nu(w_i r) + D_i K'_\nu(w_i r)] - \\ \quad n_i^2 \nu / \eta_0 [A_i I_\nu(w_i r) + B_i K_\nu(w_i r)] & n_i < n_{\text{eff}} \end{cases} \quad (3.4c)$$

$$h_\phi(r, \phi) = f_\nu(\phi) \frac{1}{k_0 r (n_i^2 - n_{\text{eff}}^2)} \begin{cases} -k_0 n_{\text{eff}} \nu [C_i J_\nu(u_i r) + D_i N_\nu(u_i r)] + \\ \quad u_i r n_i^2 / \eta_0 [A_i J'_\nu(u_i r) + B_i N'_\nu(u_i r)] & n_i > n_{\text{eff}} \\ -k_0 n_{\text{eff}} \nu [C_i I_\nu(w_i r) + D_i K_\nu(w_i r)] + \\ \quad w_i r n_i^2 / \eta_0 [A_i I'_\nu(w_i r) + B_i K'_\nu(w_i r)] & n_i < n_{\text{eff}} \end{cases} \quad (3.4d)$$

Therefore, for each layer, there are four constants to be determined, thus we need four equations to solve for this system. Those four equations are given by the continuity of $e_z(r, \phi)$,

3.2.2 The layer-by-layer method

For this method, we arbitrarily set $A_1 = 1$ and $C_1 = \alpha$. Using the continuity equations at $r = r_1$, we then compute the values of A_2 , B_2 , C_2 , and D_2 , as function of α . Using those four constants, we calculate $e_z(r_2)$ and $h_z(r_2)$. Then, from the continuity equations, we can obtain the four constants for the next layer, A_3 , B_3 , C_3 , and D_3 , still as function of α . We propagate the constants like this up to the layer before the last (the layer before the cladding).

From the continuity equations of $e_z(r)$ and $h_z(r)$ at $r = r_{N-1}$ (the last layer interface), we get the values of the last two constants, B_N and D_N . From the found constants of the last two layers, we compute the values of $e_\phi(r)$ and $h_\phi(r)$ when $r \rightarrow r_{N-1}$:

$$e_\phi(r_{N-1}^-) - e_\phi(r_{N-1}^+) = c_{11} + c_{12}\alpha \quad (3.8a)$$

$$h_\phi(r_{N-1}^-) - h_\phi(r_{N-1}^+) = c_{21} + c_{22}\alpha \quad (3.8b)$$

where \mathbf{c} is a 2×2 matrix of appropriate coefficients. If the continuity is respected, both equations should be equal to zero. It is respected when:

$$\begin{vmatrix} c_{11} & c_{12} \\ c_{21} & c_{22} \end{vmatrix} = c_{11}c_{22} - c_{12}c_{21} = 0 \quad (3.9)$$

Therefore, n_{eff} is a solution to a fiber mode if (3.9) is zero. The algorithm is summarized in Algorithm 3.2. To simplify code writing, we use $\alpha = j$, and we perform all the calculations using complex numbers. The COEFFICIENTS function returns a 4×4 matrix of coefficients, such as:

$$\begin{bmatrix} a_{11} & a_{12} & & \\ & & a_{23} & a_{24} \\ a_{31} & a_{32} & a_{33} & a_{34} \\ a_{41} & a_{42} & a_{43} & a_{44} \end{bmatrix} \begin{bmatrix} A_i \\ B_i \\ C_i \\ D_i \end{bmatrix} = \begin{bmatrix} e_z(r) \\ h_z(r) \\ e_\phi(r) \\ h_\phi(r) \end{bmatrix} \quad (3.10)$$

where A_i, \dots, D_i are the constants for the i^{th} layer, and e_z, \dots, h_ϕ are the field values at inner (r_{i-1}) or outer (r_i) radius of the layer. At $r = r_{i-1}$, field values are known, and a linear solver is used to find constant values. At $r = r_i$, field values are obtained by multiplying the coefficients by the known constants of the current layer. Please note that the coefficient matrix is equivalent to the sliding (like a stairway) diagonal of (3.7). Those coefficients are found using (3.3) and (3.4).

Not only is this function numerically more stable than the matrix method, it is also faster, especially when the number of layer N grows. $4(N-1) \ 4 \times 4$ determinants would need to be solved, compared to a $4(N-1) \times 4(N-1)$ determinant for the matrix method. For TE and TM modes, the function is similar, but simpler, as $e_z = 0, h_\phi = 0$ for TE modes, and $h_z = 0, e_\phi = 0$ for TM modes. Therefore, we only need to ensure continuity on two components instead of four. We no longer need the α variable, and all the systems become 2×2 instead of 4×4 .

Algorithm 3.2 Layer-by-layer method

```

1: function CHARFUNC( $n_{\text{eff}}, \nu$ , family,  $k_0, \mathbf{n}, \mathbf{r}$ )
2:   if family = TE then
3:      $A_1, B_1, C_1, D_1 \leftarrow 0, 0, 1, 0$ 
4:   else if family = TM then
5:      $A_1, B_1, C_1, D_1 \leftarrow 1, 0, 0, 0$ 
6:   else ▷ HE and EH modes
7:      $A_1, B_1, C_1, D_1 \leftarrow 1, 0, j, 0$ 
8:   end if
9:   for  $i = 1, N - 2$  do ▷ Inner layers
10:     $\mathbf{a} \leftarrow \text{COEFFICIENTS}(n_{\text{eff}}, \nu$ , family,  $k_0, n_i, r_i)$ 
11:     $e_z, h_z, e_\phi, h_\phi \leftarrow \mathbf{a} \cdot [A_i, B_i, C_i, D_i]^T$ 
12:     $\mathbf{a} \leftarrow \text{COEFFICIENTS}(n_{\text{eff}}, \nu$ , family,  $k_0, n_{i+1}, r_i)$ 
13:     $A_{i+1}, B_{i+1}, C_{i+1}, D_{i+1} \leftarrow \text{SOLVE}(\mathbf{a}, [e_z, h_z, e_\phi, h_\phi]^T)$  ▷  $4 \times 4$  determinant
14:  end for
15:   $i \leftarrow N - 1$  ▷ Last layer
16:   $\mathbf{a} \leftarrow \text{COEFFICIENTS}(n_{\text{eff}}, \nu$ , family,  $k_0, n_i, r_i)$ 
17:   $e_z, h_z, e_\phi, h_\phi \leftarrow \mathbf{a} \cdot [A_i, B_i, C_i, D_i]^T$ 
18:   $w \leftarrow k_0(n_{\text{eff}}^2 - n_N^2)^{1/2}$ 
19:   $B_N, D_N \leftarrow e_z/K_\nu(wr_i), h_z/K_\nu(wr_i)$ 
20:   $\mathbf{a} \leftarrow \text{COEFFICIENTS}(n_{\text{eff}}, \nu$ , family,  $k_0, n_N, r_i)$ 
21:   $e_\phi^N, h_\phi^N \leftarrow \mathbf{a} \cdot [0, B_N, 0, D_N]^T$ 
22:   $\mathbf{c} \leftarrow \begin{bmatrix} \Re(e_\phi - e_\phi^N) & \Im(e_\phi - e_\phi^N) \\ \Re(h_\phi - h_\phi^N) & \Im(h_\phi - h_\phi^N) \end{bmatrix}$ 
23:  return  $|\mathbf{c}|$  ▷ Determinant of matrix  $\mathbf{c}$ 
24: end function

```

3.3 Optimizing the search for n_{eff}

The **for** loop at line 3 of Algorithm 3.1 hides the fact we need to try all possible values of the real valued parameter n_{eff} , from the highest refractive index of the fiber to the refractive index of the cladding, until we find a value of n_{eff} that, passed to CHARFUNC, returns zero. Furthermore, as we saw in the previous section, the evaluation of CHARFUNC requires us to solve a number of linear systems, proportional to the number of layers in the fiber. Finally, we have to repeat the whole procedure for all the possible values of ν , and possibly for different wavelengths or different fiber parameters. Therefore, the quest for fiber modes can be very computationally intensive, and special cares need to be taken in optimizing the function. In the following subsections, we will present a few optimization strategies we used for our simulation software.

3.3.1 Finding the roots

Finding the roots of the characteristic function is not a trivial task, because the function has discontinuities. While there exists algorithms to find roots of well behaved functions, there is

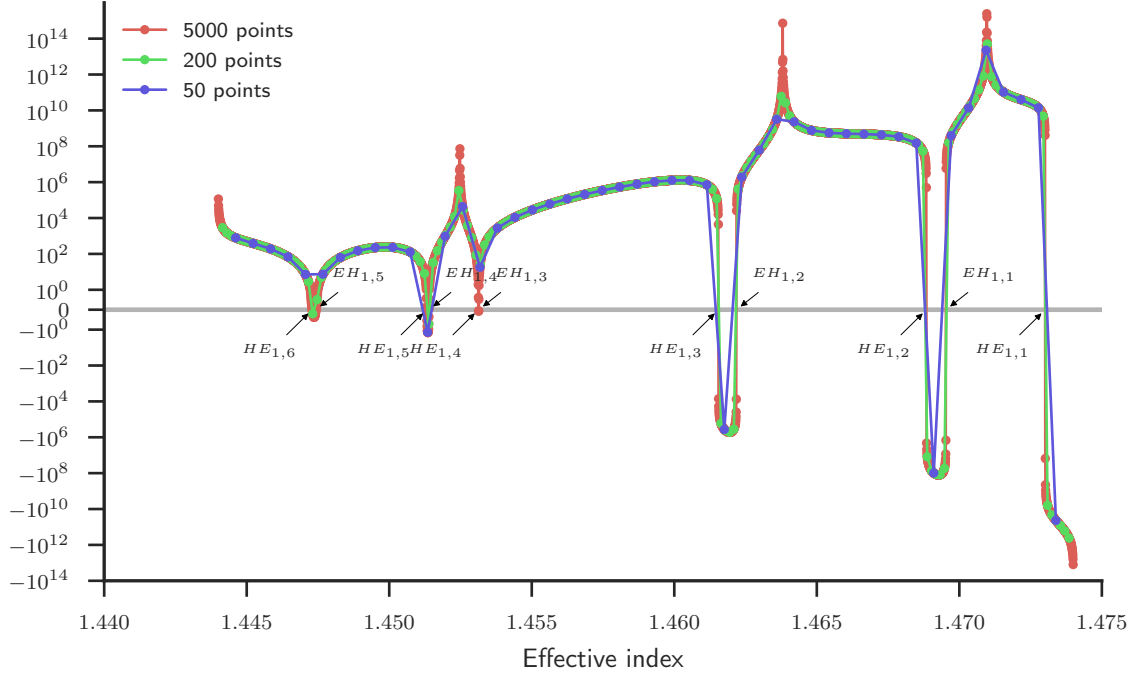


Figure 3.1: Example of a characteristic function, for a three layers fiber with $r_1 = 10 \mu\text{m}$, $n_1 = 1.474$, $r_2 = 20 \mu\text{m}$, $n_2 = 1.454$, and $n_3 = 1.444$. Wavelength is 1550 nm and $\nu = 1$. Scale is linear between -1 and 1, and logarithmic elsewhere, to clearly see the function.

no known algorithm that guarantee finding all roots of a discontinuous function.

If we want to plot the characteristic function, we should evaluate it at specific intervals. Then we would see where the function is crossing zero. However, the choice of the interval (or, in other words, the number of points we evaluate) is critical. Evaluating too many points would require unnecessary computing power, but if the interval is too large, there is the risk to fail to identify some zeros. This is especially true for multilayered fibers. In that case, the characteristic function has many discontinuities, and can suddenly go up and down. As an example, we plotted on Fig. 3.1, the characteristic function for $\nu = 2$, at 1550 nm, of a three layer step-index fiber with $r_1 = 10 \mu\text{m}$, $n_1 = 1.474$, $r_2 = 20 \mu\text{m}$, $n_2 = 1.454$, and $n_3 = 1.444$. Each time the function crosses zero, we have the solution for a guided mode. To clearly see the zeros, without losing the extrema of the function, we choose a hybrid vertical scale, that is linear between -1 and 1, and logarithmic elsewhere. In blue, we see the function plotted using 50 points. As we can see, two sets of roots are missed, near 1.453 and near 1.447. In we increase the number of points to 200 (in green), we find the two roots near 1.447, but we still miss the roots near 1.453. It is only when we plotted the function using 5000 points that the roots near 1.453 were detected. This illustrates how easily a pair of roots can be skipped. When it occurs, all the following modes are incorrectly tagged.

The algorithm we chose to find the roots of the characteristic function is inspired by the graphical representation of the function. First, we evaluate the function at specific intervals. When two successive points are of different sign, it means there is either a zero, or a discontinuity between the two points. If the function seems continuous between the two points, we use the Brent algorithm [119] to find the precise value of the zero. That algorithm is guaranteed to find a zero between two points, if those two points are of opposite sign and the function is continuous between those points.

The number of discontinuities in the characteristic equation can be greatly reduced by avoiding divisions by zero as much as possible. For instance, the characteristic function for scalar modes in weakly guiding fibers could be coded as:

$$uJ_{\ell-1}(ur_1)K_{\ell}(wr_1) + wK_{\ell-1}(wr_1)J_{\ell}(ur_1) \quad (3.11)$$

which has the same roots than (1.41), but is continuous over the n_{eff} search interval. However, in the case of multilayered fibers, avoiding discontinuities can be much more difficult.

The root finding algorithm is detailed in Algorithm 3.3. This is a more detailed and more accurate version of Algorithm 3.1. The FINDROOTS function takes as parameters the mode parameters, a wavelength, the fiber parameters, and the number of points to evaluate (np). It returns all the roots of the characteristic function, sorted by n_{eff} .

Algorithm 3.3 Roots of the characteristic function

```

1: function FINDROOTS( $\nu$ , family,  $\lambda$ ,  $\mathbf{n}$ ,  $\mathbf{r}$ ,  $np$ )
2:    $k_0 \leftarrow 2\pi/\lambda$ 
3:    $\delta \leftarrow (\max \mathbf{n} - n_N)/np$ 
4:    $\Omega, k \leftarrow \emptyset, 0$  ▷ To store results
5:    $n_{\text{eff}} \leftarrow \max \mathbf{n}$ 
6:    $r_1 \leftarrow \text{CHARFUNC}(n_{\text{eff}}, \nu, \text{family}, k_0, \mathbf{n}, \mathbf{r})$ 
7:   for  $i \leftarrow 2, np$  do
8:      $n_{\text{eff}} \leftarrow n_{\text{eff}} - \delta$ 
9:      $r_i \leftarrow \text{CHARFUNC}(n_{\text{eff}}, \nu, \text{family}, k_0, \mathbf{n}, \mathbf{r})$ 
10:    if  $\text{sgn } r_{i-1} \neq \text{sgn } r_i$  then
11:       $r_z, n_z \leftarrow \text{BRENTQ}(\text{CHARFUNC}, n_{\text{eff}}, n_{\text{eff}} + \delta)$ 
12:      if  $|r_{i-1}| > |r_z| < |r_i|$  then ▷ To avoid discontinuities
13:         $k \leftarrow k + 1$ 
14:         $\Omega_k \leftarrow n_z$  ▷  $k^{\text{th}}$  root of CHARFUNC
15:      end if
16:    end if
17:  end for
18:  return  $\Omega$ 
19: end function

```

3.3.2 Restricting the bounds

To find the list of guided modes in a given fiber at a given wavelength, we need to find the roots of the characteristic function, for each value of ν . For instance, if we find three roots when $\nu = 1$, it means $\text{HE}_{1,1}$, $\text{EH}_{1,1}$, and $\text{HE}_{1,2}$ modes are supported. If no roots are found for a given value of ν , it means no modes with that ν parameter are supported. Therefore, to prove that a mode is not supported, we have to test all possible values of n_{eff} , from the highest refractive index in the fiber, down to the refractive index of the cladding.

When we know the cutoff wavelength of a mode, we can already know whether this mode is supported or not at a given wavelength, since it will be guided only if the wavelength is lower than the cutoff wavelength. Therefore, a lot of unnecessary calculations can be avoided, because we can now search for modes we know are supported. We can stop the iteration in the root finding algorithm as soon as we found the last supported mode. However, we usually only know cutoff wavelengths for a few specific fiber profiles (those with $N \leq 3$ for instance). Without mode cutoff, the only solution is to search for all possible values of n_{eff} .

It is usually less computer intensive to solve for the scalar modes. While this approximation is not accurate outside the weakly guiding approximation, it can serve as a starting point for finding the vector modes. Indeed, if a scalar solution $\text{LP}_{\ell,m}$ is found, it means that at least one – and possibly all – of the underlying vector modes are also supported. The effective index of the vector modes can be more or less diverging from the effective index found from the scalar solution, depending on the refractive index contrast of the fiber, and depending on the proximity of the mode with its cutoff wavelength. However, that effective index could be used as a starting point for the search of vector modes effective indexes.

The mode with the highest refractive index is called the fundamental mode. In most cases, the fundamental mode is the $\text{HE}_{1,1}$ mode. However, this is not necessarily always the case [120]. If we know the effective index of the fundamental mode, we can restrict the n_{eff} search interval, because we know that the effective index of the other modes will always be smaller than the effective index of the fundamental mode.

Similarly, in many fiber designs, modes of the same family and with the same m parameter can often be sorted by their ν parameter. However, we have not found any evidence that this is always the case. Therefore, this criteria must be used with extreme caution.

It is often needed to plot the effective index as function of the wavelength. A good strategy in that case is to start by the lowest wavelength. This is for two reasons. First, we know that if a mode is not guided at a wavelength λ , it will not be guided at wavelengths higher than λ . Therefore, after finding the modes for the first wavelength, we can restrict the search at higher wavelengths for the modes found at the previous wavelength. The second reason is that the effective index of a mode decreases as the wavelength increases. Therefore, if we already know

the effective index of a given mode at a lower wavelength, we know that the effective index of that mode will be lower than that value (but probably close) at a higher wavelength.

Similarly, we know that increasing the index difference between the guiding layer and the cladding, or increasing the guiding layer radius, will increase the number of supported modes. Therefore, in the case of a simulation where we vary only one fiber parameter through iterations, we can start from the fiber design with the highest number of supported modes, and use the results as a starting point for the next iteration, similarly to what we do when simulating multiple wavelengths.

3.3.3 Parallelizing the algorithm

There are cases where, even after optimizing the fiber mode solver as much as we can, it is still too slow for our needs. For instance, in the context of a fiber design process, we could want to run a multidimensional optimizer, based on the fiber parameters. The cost function would be based on the number of supported modes, on the effective indexes of those modes, or even on parameters like group index or dispersion, that requires the evaluation of the effective index for many closed spaced points. In this kind of context, it can be useful to take advantage of the many processors of today's computers.

The principle of parallelization is to separate a single process into subprocesses that are independent as possible. For instance, if we have to solve for the modes in different fiber designs, we could launch a different process per design, and each process would perform the mode solving simultaneously. However, if the different designs are related, as we explained in previous section, the parallelization would prevent us to take advantage of that optimization.

In the case of a single fiber, but with multiple wavelengths to test, we could solve for a different wavelength on each process. Again, this would prevent us to take advantage of some possible optimizations. In the extreme case where many fiber designs and many wavelengths need to be simulated, we could even separate both wavelengths and fiber designs on different processes, but still at the price of not taking advantage of all possible computational savings. In theory, this would be the fastest option, but only in the case we have unlimited computer resources available.

If we consider that the solutions for each value of ν are independent, we could also assign a different value of ν on each process. Then we could take advantage of the knowledge of the solutions for different wavelengths or different fiber profiles. However, there are still some issues to consider, if we do not know in advance what are the ν values that provide solutions. Furthermore, the number of solutions for lower values of ν will generally be higher than for higher values of ν , which could cause an unbalance between the amount of work for each process. Especially, there would be no performance gain if most simulations lead to single mode solutions.

The point is that there is not a single unique solution that will provide the fastest performance for all cases. It depends on the nature and the size of the problem, and on the used computer architecture (number of processors, available memory, etc.) Figure 3.2 compares the performance of different parallelization and optimization strategies. In this illustration, the fastest strategy seems to be when we fully parallelize the problem (g). However, this is only true in the case we have enough processors to run all simulations simultaneously. Suppose we have eight processors instead of nine: the last simulation would need to wait for an available processor, and the resulting simulation time would be two times longer. In that case, using strategy (e) or (f) would be faster. Furthermore, the strategy (g) consumes as much computing power (represented as the area of the blocks) as the non-optimized sequential algorithm, illustrated in (a).

3.4 Computing the electromagnetic fields

Once we solved for the mode n_{eff} , calculating the electromagnetic fields is straightforward. All we need is to substitute the right values into (3.3) and (3.4), for a given transverse position (r, ϕ) . The radial position r tells us in which fiber layer we are, and thus we can choose the right set of constants A_i, \dots, D_i . However, the layer-by-layer method gives us those constants as function of a parameter α that is still unknown. We get it from (3.8):

$$\alpha = -\frac{c_{11}}{c_{12}} = -\frac{c_{21}}{c_{22}} \quad (3.12)$$

We can then compute the six components of $\mathbf{e}(r, \phi)$ and $\mathbf{h}(r, \phi)$. The obtained values are arbitrary, based on the choice of $A_1 = 1$ we made in the algorithm. The convention is usually to normalize the fields to get a unitary power flow [17]. Thus, the normalization constant is given by:

$$\frac{1}{2} \left| \int_{A_\infty} \mathbf{e} \times \mathbf{h}^* \cdot \hat{\mathbf{z}} dA \right| = \frac{1}{2} \left| \int_0^{2\pi} \int_0^\infty (e_r h_\phi - e_\phi h_r) r dr d\phi \right| \quad (3.13)$$

where the asterisk denotes the complex conjugate.

$\mathbf{e}(r, \phi)$ and $\mathbf{h}(r, \phi)$ are the envelope of the electromagnetic fields, and up to now were real values. If we append to them the complex exponential from (1.9), we now get the time and propagation dependencies of the fields, and the \mathbf{E} and \mathbf{H} fields now are complex. The modulus gives the field intensity, while the angle gives the phase of the rapidly oscillating signal.

Using that complete definition of the fields, it becomes possible to build OAM fields. We know that OAM modes are made of even and odd degeneracies of the vector modes. The difference between even and odd modes is given by the definition we give to the $f_\nu(\phi)$ and $g_\nu(\phi)$ functions, (1.25) for even modes, and (1.26) for odd modes. The radial orientation of the field is arbitrary – in fact we align the coordinates system to get either min or max value at $\phi = 0$ – but the relative orientation of even and odd fields is important. Therefore, an equivalent way to define even and odd modes is to always use the even definition of the $f_\nu(\phi)$

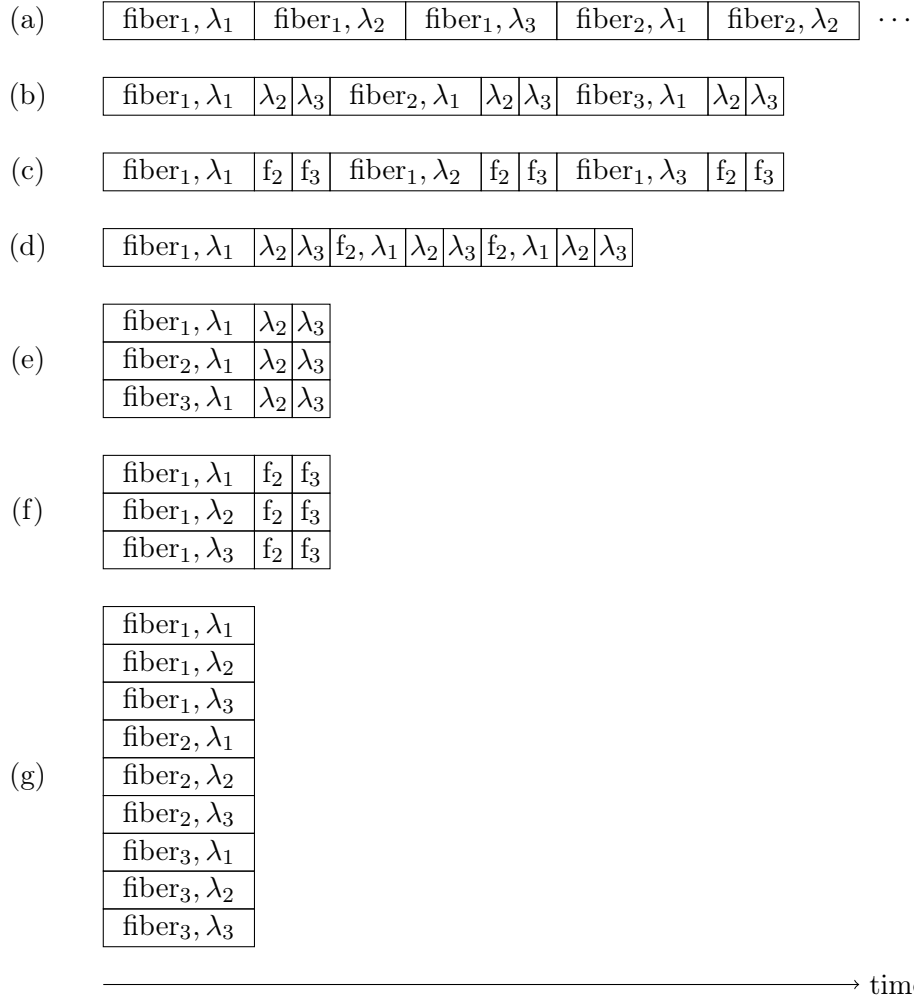


Figure 3.2: Optimization and parallelization of the algorithm. As an example, we illustrate a problem with three wavelengths and three (related) fiber profiles. (a) Unoptimized sequential execution; (b) Wavelength-optimized sequential execution; (c) Fiber-optimized sequential execution; (d) Wavelength- and fiber-optimized sequential execution; (e) Optimized parallel execution (one fiber per process); (f) Optimized parallel execution (one wavelength per process); (g) Fully parallelized execution. Cases (a) – (d) are sequential, while (e) – (g) are parallel. The total width of the boxes represents the execution time. Superposed boxes represent parallel processes executed simultaneously on different processors. Total area of the boxes represent used computing power.

and $g_\nu(\phi)$ functions, but to add a $\pi/2$ factor of rotation for even modes. The OAM field definition is then:

$$\mathbf{E}(r, \phi, z, t) \pm j\mathbf{E}\left(r, \phi \pm \frac{\pi}{2}, z, t\right) \quad (3.14a)$$

$$\mathbf{H}(r, \phi, z, t) \pm j\mathbf{H}\left(r, \phi \pm \frac{\pi}{2}, z, t\right) \quad (3.14b)$$

Using the resulting field, it is easy to verify that the intensity is a perfectly symmetric doughnut, and that the phase has an azimuthal dependency. It is also possible, by varying either the z or the t parameter, to observe the rotation of the polarization and the rotation of the polarization plane. Furthermore, it becomes possible to simulate the effects of a non-perfect phase difference or of unbalanced mode components on the resulting fields, similarly to what was done in [121].

The polarization is the direction of the electric field vectors. While this direction is in 3D space, we usually can use the projection of the polarization on the transverse plane, as the longitudinal component is usually negligible. The transverse polarization angle is given by:

$$\arctan\left(\frac{e_\phi(r, \phi)}{e_r(r, \phi)}\right) + \phi \quad (3.15)$$

It is often useful to get the fields in Cartesian coordinates. The transformation simply is a rotation of the coordinate system by a factor of ϕ :

$$\begin{bmatrix} e_x(r, \phi) \\ e_y(r, \phi) \end{bmatrix} = \begin{bmatrix} \cos(\phi) & -\sin(\phi) \\ \sin(\phi) & \cos(\phi) \end{bmatrix} \cdot \begin{bmatrix} e_r(r, \phi) \\ e_\phi(r, \phi) \end{bmatrix} \quad (3.16)$$

Part II

The modal map: a design tool

Chapter 4

Cutoff of ring-core fibers

4.1 Definition of ring-core fiber

Ring-core fiber (RCF), also known as annular core fiber, or M-type fiber, is a kind of step-index three-layer fiber, where the refractive index of the center is similar to the refractive index of the cladding ($n_1 = n_3$), and where the refractive index of the ring is higher than the refractive index of the cladding ($n_2 > n_3$) (see Figure 4.1).

This kind of fiber is of renewed interest because of applications in SDM [14] and optical sensing [122]. In particular, it appears well suited for transmitting OAM modes [1, 40, 95, 121], because its refractive index profile closely matches that of the annular intensity profile of OAM beams. RCF is also being investigated for few-mode transmission of LP modes [123–126], as RCF can be tailored to minimize differential group delay (DGD).

To the best of our knowledge, the analytical description of modal cutoffs in RCF have been limited to LP modes under the weakly guiding approximation [127–129]. In light of the recent advances in high-index contrast waveguides and the emerging interest in OAM-guiding fibers, a full vectorial description of RCF is necessary. Therefore, we derived the solution of the modal cutoffs for the vector modes of RCFs, without any approximations [6].

Please beware that the notation used here differs from the notation in [6], for consistency reasons with the next chapter. Particularly, we use r_1 and r_2 instead of a and b , for the radii, and the roles of n_1 and n_2 are inverted.

4.1.1 Normalized notation

In RCF, in contrast to SSIF, we have two fiber geometry parameters, namely r_1 and r_2 . By defining $\rho \triangleq r_1/r_2$, we can normalize our parameters in a similar way to that done in SSIF. In this way, the cutoff condition can be expressed in terms of the normalized frequency V and

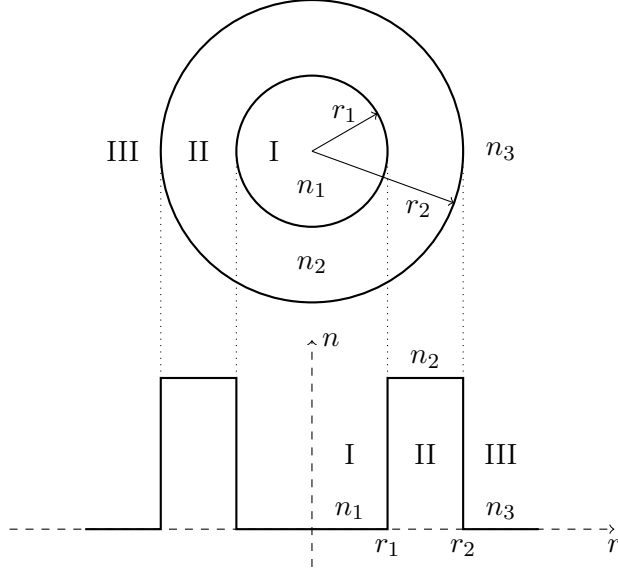


Figure 4.1: Ring-core fiber geometry (top view, and profile).

the ratio ρ using this equivalent notation:

$$V = k_0 r_2 \sqrt{n_2^2 - n_1^2} \quad (4.1a)$$

$$\rho V = k_0 r_1 \sqrt{n_2^2 - n_1^2} \quad (4.1b)$$

4.2 Derivation of the characteristic equation for vector modes

The modal solutions for RCF are found by solving Maxwell's equations, as we did in Chapter 1 for standard step-index fiber. Because we deal with step-index fiber, we can express $e_z(r)$ and $h_z(r)$ components as function of Bessel functions, as in (1.17) and (1.21):

$$e_z(r) = \begin{cases} C_1 I_\nu(wr) & r \leq r_1 \\ A_1 J_\nu(ur) + A_2 N_\nu(ur) & r_1 < r \leq r_2 \\ C_2 K_\nu(wr) & r > r_2 \end{cases} \quad (4.2a)$$

$$h_z(r) = \begin{cases} D_1 I_\nu(wr) & r \leq r_1 \\ B_1 J_\nu(ur) + B_2 N_\nu(ur) & r_1 < r \leq r_2 \\ D_2 K_\nu(wr) & r > r_2 \end{cases} \quad (4.2b)$$

where parameters u and w are defined as:

$$u^2 = n_2^2 k_0^2 - \beta^2 \quad (4.3a)$$

$$w^2 = \beta^2 - n_1^2 k_0^2 \quad (4.3b)$$

and A_1, \dots, D_2 are constants to be determined.

Radial and tangential components are found using (1.12):

$$e_r(r) = \begin{cases} -\frac{1}{w^2} \left[C_1 \beta w I'_\nu(wr) - D_1 \nu \eta_0 \frac{k_0}{r} I_\nu(wr) \right] & r \leq r_1 \\ \frac{1}{u^2} \left[\beta u (A_1 J'_\nu(ur) + A_2 N'_\nu(ur)) - \nu \eta_0 \frac{k_0}{r} (B_1 J_\nu(ur) + B_2 N_\nu(ur)) \right] & r_1 < r \leq r_2 \\ -\frac{1}{w^2} \left[C_2 \beta w K'_\nu(wr) - D_2 \nu \eta_0 \frac{k_0}{r} K_\nu(wr) \right] & r > r_2 \end{cases} \quad (4.4)$$

$$e_\phi(r) = \begin{cases} -\frac{1}{w^2} \left[C_1 \frac{\beta}{r} \nu I_\nu(wr) - D_1 w \eta_0 k_0 I'_\nu(wr) \right] & r \leq r_1 \\ \frac{1}{u^2} \left[\frac{\beta}{r} \nu (A_1 J_\nu(ur) + A_2 N_\nu(ur)) - w \eta_0 k_0 (B_1 J'_\nu(ur) + B_2 N'_\nu(ur)) \right] & r_1 < r \leq r_2 \\ -\frac{1}{w^2} \left[C_2 \frac{\beta}{r} \nu K_\nu(wr) - D_2 w \eta_0 k_0 K'_\nu(wr) \right] & r > r_2 \end{cases} \quad (4.5)$$

$$h_r(r) = \begin{cases} -\frac{1}{w^2} \left[D_1 \beta w I'_\nu(wr) - C_1 \nu \frac{k_0 n_1^2}{\eta_0 r} I_\nu(wr) \right] & r \leq r_1 \\ \frac{1}{u^2} \left[\beta u (B_1 J'_\nu(ur) + B_2 N'_\nu(ur)) - \nu \frac{k_0 n_2^2}{\eta_0 r} (A_1 J_\nu(ur) + A_2 N_\nu(ur)) \right] & r_1 < r \leq r_2 \\ -\frac{1}{w^2} \left[D_2 \beta w K'_\nu(wr) - C_2 \nu \frac{k_0 n_1^2}{\eta_0 r} K_\nu(wr) \right] & r > r_2 \end{cases} \quad (4.6)$$

$$h_\phi(r) = \begin{cases} -\frac{1}{w^2} \left[-D_1 \frac{\beta}{r} \nu I_\nu(wr) + C_1 w \frac{k_0 n_1^2}{\eta_0} I'_\nu(wr) \right] & r \leq r_1 \\ \frac{1}{u^2} \left[-\frac{\beta}{r} \nu (B_1 J_\nu(ur) + B_2 N_\nu(ur)) + u \frac{k_0 n_2^2}{\eta_0} (A_1 J'_\nu(ur) + A_2 N'_\nu(ur)) \right] & r_1 < r \leq r_2 \\ -\frac{1}{w^2} \left[-D_2 \frac{\beta}{r} \nu K_\nu(wr) + C_2 w \frac{k_0 n_1^2}{\eta_0} K'_\nu(wr) \right] & r > r_2 \end{cases} \quad (4.7)$$

To find the values of the eight constants, we ensure continuity of the e_z , h_z , e_ϕ , and h_ϕ components of the fields, at $r = r_1$ and $r = r_2$. First, we isolate constants C_1 , C_2 , D_1 , and D_2 from (4.2). Then, we write the four continuity equations for e_ϕ and h_ϕ . By rearranging the terms, this leads to:

$$\left(\frac{1}{u^2} + \frac{1}{w^2} \right) \frac{\nu \beta}{r_1^2} \left[A_1 J_\nu(ur_1) + A_2 N_\nu(ur_1) \right] = k_0 \left\{ \left[B_1 \frac{J'_\nu(ur_1)}{ur_1} + B_2 \frac{N'_\nu(ur_1)}{ur_1} \right] + \frac{I'_\nu(ur_1)}{(wr_1) I_\nu(wr_1)} \left[B_1 J_\nu(ur_1) + B_2 N_\nu(ur_1) \right] \right\} \quad (4.8a)$$

$$\left(\frac{1}{u^2} + \frac{1}{w^2} \right) \frac{\nu \beta}{r_1^2} \left[B_1 J_\nu(ur_1) + B_2 N_\nu(ur_1) \right] = k_0 \left\{ n_2^2 \left[A_1 \frac{J'_\nu(ur_1)}{ur_1} + A_2 \frac{N'_\nu(ur_1)}{ur_1} \right] + \frac{I'_\nu(ur_1)}{(wr_1) I_\nu(wr_1)} n_1^2 \left[A_1 J_\nu(ur_1) + A_2 N_\nu(ur_1) \right] \right\} \quad (4.8b)$$

$$\left(\frac{1}{u^2} + \frac{1}{w^2}\right) \frac{\nu\beta}{r_2^2} \left[A_1 J_\nu(ur_2) + A_2 N_\nu(ur_2) \right] = k_0 \left\{ \left[B_1 \frac{J'_\nu(ur_2)}{ur_2} + B_2 \frac{N'_\nu(ur_2)}{ur_2} \right] + \frac{K'_\nu(wr_2)}{(wr_2)K_\nu(wr_2)} \left[B_1 J_\nu(ur_2) + B_2 N_\nu(ur_2) \right] \right\} \quad (4.8c)$$

$$\left(\frac{1}{u^2} + \frac{1}{w^2}\right) \frac{\nu\beta}{r_2^2} \left[B_1 J_\nu(ur_2) + B_2 N_\nu(ur_2) \right] = k_0 \left\{ n_2^2 \left[A_1 \frac{J'_\nu(ur_2)}{ur_2} + A_2 \frac{N'_\nu(ur_2)}{ur_2} \right] + \frac{K'_\nu(wr_2)}{(wr_2)K_\nu(wr_2)} n_1^2 \left[A_1 J_\nu(ur_2) + A_2 N_\nu(ur_2) \right] \right\} \quad (4.8d)$$

The modal characteristic equation is obtained by putting those equation in matrix form, and by ensuring the (4×4) determinant is zero. This operation is straightforward using a computer and numerical methods. However, the corresponding analytical expression, that we need for finding the cutoff expression, would be so long and complicated that it would be of little practical use.

4.3 Cutoffs of RCF

The modal cutoff frequencies are obtained when $\beta \rightarrow n_1 k_0$ and $w \rightarrow 0$. However, this cannot be evaluated directly, because of the discontinuity in the K_ν function. Therefore, we need to use asymptotic expansions (A.26). As we will see, it is very important to use the first two terms of the series, because the first term will cancel out during the development of the equations. Otherwise, we would obtain the trivial solution that, at cutoff, $\mathbf{E} = \mathbf{H} = 0$.

We need to handle three cases separately: when $\nu = 0$ (TE and TM modes), when $\nu = 1$ ($\text{HE}_{1,m}$ modes), and when $\nu \geq 2$ ($\text{HE}_{\nu,m}$ and $\text{EH}_{\nu,m}$ modes). To simplify the equations, some observations can be made on the properties of the electromagnetic fields near cutoff. We know that above cutoff, the electromagnetic wave is guided within the ring layer of the fiber. Below cutoff, the electromagnetic wave no longer is guided, and the optical fiber can be seen as an infinite medium for propagation, the ring core being a simple defect running through this material; the electromagnetic field is like TEM, and $e_z = h_z = 0$. Therefore, as a mode approaches cutoff, its e_z and h_z components approach zero. We have observed that for HE modes e_z and h_z approach zero more quickly at r_1 than at r_2 , while for EH modes the opposite is true.

Figure 4.2 shows normalized squared $e_z(r)$ for a few selected modes, near cutoff. It allows us to see the different behavior of intensity for EH modes near r_1 and HE modes near r_2 . For the simulation, we used the following parameters: $r_1 = 4 \mu\text{m}$, $r_2 = 10 \mu\text{m}$, $n_1 = 1.444$, $n_2 = 1.474$, and we chose the wavelength 4 nm below cutoff. On the figure, we can see that the longitudinal intensity of HE modes (blue / purple lines) is zero when $r = r_1 = 4 \mu\text{m}$, while the longitudinal intensity of EH modes (green lines) is zero when $r = r_2 = 10 \mu\text{m}$.

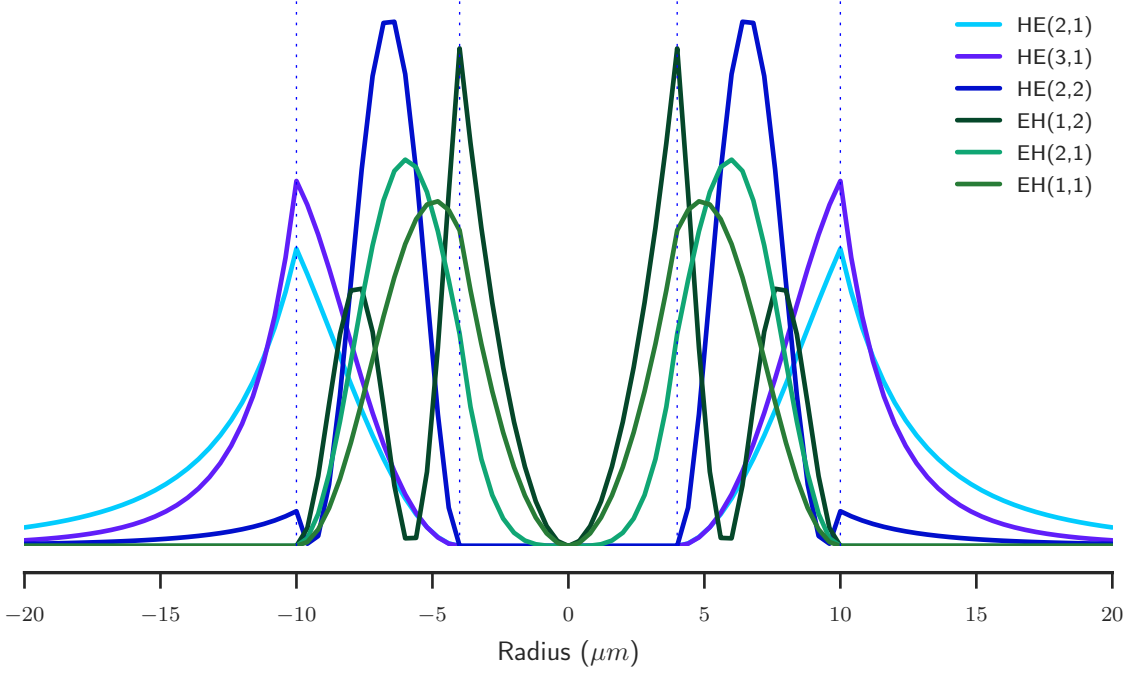


Figure 4.2: Normalized $e_z^2(r)$ of some modes, near cutoff. The vertical dashed lines indicate layer boundaries.

4.3.1 Cutoff of TE and TM modes

TE and TM modes have $\nu = 0$. Therefore the left-hand part in (4.8) is zero. After evaluating the limits when $w \rightarrow 0$ using (A.25) and (A.26), we get:

$$B_1 \left[-\frac{J_1(ur_1)}{ur_1} + \frac{J_0(ur_1)}{2} \right] + B_2 \left[-\frac{N_1(ur_1)}{ur_1} + \frac{N_0(ur_1)}{2} \right] = 0 \quad (4.9a)$$

$$A_1 \left[-n_2^2 \frac{J_1(ur_1)}{ur_1} + n_1^2 \frac{J_0(ur_1)}{2} \right] + A_2 \left[-n_2^2 \frac{N_1(ur_1)}{ur_1} + n_1^2 \frac{N_0(ur_1)}{2} \right] = 0 \quad (4.9b)$$

$$B_1 J_0(ur_2) + B_2 N_0(ur_2) = 0 \quad (4.9c)$$

$$A_1 J_0(ur_2) + A_2 N_0(ur_2) = 0 \quad (4.9d)$$

We know that for TE modes, $e_z = 0$. This implies that $A_1 = A_2 = 0$, because of (4.2a). Therefore, only (4.9a) and (4.9c) remain. We set the 2×2 determinant to zero, and after applying Bessel recurrence identities, it gives:

$$J_0(ur_2)N_2(ur_1) - N_0(ur_2)J_2(ur_1) = 0 \quad (4.10)$$

This is the cutoff expression for TE modes in RCF fiber.

The development for TM modes is similar, with $h_z = 0$, $B_1 = B_2 = 0$. We set the determinant

of (4.9b) and (4.9d) to zero, to obtain:

$$\left[n_1^2 \frac{J_0(ur_1)}{2} - n_2^2 \frac{J_1(ur_1)}{ur_1} \right] N_0(ur_2) - \left[n_1^2 \frac{N_0(ur_1)}{2} - n_2^2 \frac{N_1(ur_1)}{ur_1} \right] J_0(ur_2) = 0 \quad (4.11)$$

After multiplying by $2/n_2^2$ and applying Bessel recurrence identities, we obtain the cutoff expression for TM modes:

$$J_0(ur_2)N_2(ur_1) - N_0(ur_2)J_2(ur_1) = \left(\frac{n_1^2}{n_2^2} - 1 \right) [J_0(ur_2)N_0(ur_1) - J_0(ur_1)N_0(ur_2)] \quad (4.12)$$

As we can see, cutoffs of TE and TM modes are no longer similar to one another in RCF, as they were with SSIF.

4.3.2 Cutoff of $\text{HE}_{1,m}$ modes

For $\text{HE}_{1,m}$ modes, we have $\nu = 1$. Furthermore, $e_z(r_1) = h_z(r_1) = 0$ at cutoff, because this is an HE mode, as we explained before. Therefore, we get, from (4.2):

$$A_2 = -A_1 \frac{J_1(ur_1)}{N_1(ur_1)} \quad B_2 = -B_1 \frac{J_1(ur_1)}{N_1(ur_1)} \quad (4.13)$$

and from continuity equations, only (4.9c) and (4.9d) remain.

To simplify the notation, we introduce:

$$\mathcal{F}_\nu(ur_2) = J_\nu(ur_2) - \gamma N_\nu(ur_2) \quad (4.14)$$

with:

$$\gamma = \frac{J_\nu(ur_1)}{N_\nu(ur_1)} \quad (4.15)$$

Using this notation, (4.9c) and (4.9d) become:

$$\left(\frac{1}{u^2} + \frac{1}{w^2} \right) \frac{\beta}{r_2^2} A_1 \mathcal{F}_1(ur_2) = k_0 \left\{ B_1 \frac{\mathcal{F}'_1(ur_2)}{ur_2} + \frac{K'_1(wr_2)}{(wr_2)K_1(wr_2)} B_1 \mathcal{F}_1(ur_2) \right\} \quad (4.16a)$$

$$\left(\frac{1}{u^2} + \frac{1}{w^2} \right) \frac{\beta}{r_2^2} B_1 \mathcal{F}_1(ur_2) = k_0 \left\{ n_2^2 A_1 \frac{\mathcal{F}'_1(ur_2)}{ur_2} + \frac{K'_1(wr_2)}{(wr_2)K_1(wr_2)} n_1^2 A_1 \mathcal{F}_1(ur_2) \right\} \quad (4.16b)$$

Using asymptotic expansion from (A.26), and setting the determinant to zero, leads to the solution:

$$\mathcal{F}_1(ur_2) = 0 \quad (4.17)$$

Therefore, the cutoff expression of $\text{HE}_{1,m}$ modes in RCF is:

$$J_1(ur_2)N_1(ur_1) = J_1(ur_1)N_1(ur_2) \quad (4.18)$$

4.3.3 Cutoff of $\text{HE}_{\nu,m}$ modes

The difference between the development for $\text{HE}_{1,m}$ and $\text{HE}_{\nu,m}$ modes is the presence of ν in the left-hand part of the equations, and the asymptotic expansion that is different when $\nu \geq 2$. This leads to the following expression for the determinant:

$$\left(\frac{1}{u^2 r_2^2} + \frac{1}{w^2 r_2^2}\right)^2 \beta^2 \nu^2 \mathcal{F}_\nu^2(ur_2) = k_0^2 \left[\frac{\mathcal{F}'_\nu(ur_2)}{ur_2} - \left(\frac{\nu}{w^2 r_2^2} + \frac{1}{2(\nu-1)}\right) \mathcal{F}_\nu(ur_2) \right] \left[n_2^2 \frac{\mathcal{F}'_\nu(ur_2)}{ur_2} - n_1^2 \left(\frac{\nu}{w^2 r_2^2} + \frac{1}{2(\nu-1)}\right) \mathcal{F}_\nu(ur_2) \right] \quad (4.19)$$

The left-hand part of (4.19) can be expanded to the following, using (4.3):

$$\left(\frac{1}{u^2 r_2^2} + \frac{1}{w^2 r_2^2}\right)^2 \beta^2 \nu^2 \mathcal{F}_\nu^2(ur_2) = \left(\frac{\beta^2}{u^4 r_2^4} + \frac{\beta^2 + \beta^2}{u^2 r_2^2 w^2 r_2^2} + \frac{\beta^2}{w^4 r_2^4}\right) \nu^2 \mathcal{F}_\nu^2(ur_2) = \left(\frac{n_2^2 k_0^2 - u^2}{u^4 r_2^4} + \frac{n_2^2 k_0^2 - u^2 + w^2 + n_1^2 k_0^2}{u^2 r_2^2 w^2 r_2^2} + \frac{w^2 + n_1^2 k_0^2}{w^4 r_2^4}\right) \nu^2 \mathcal{F}_\nu^2(ur_2) = \left(\frac{n_2^2}{u^4 r_2^4} + \frac{n_1^2 + n_2^2}{u^2 r_2^2 w^2 r_2^2} + \frac{n_1^2}{w^4 r_2^4}\right) \nu^2 k_0^2 \mathcal{F}_\nu^2(ur_2) \quad (4.20)$$

The right-hand part of (4.19) becomes, after expansion:

$$n_2^2 k_0^2 \left[\frac{\mathcal{F}'_\nu(ur_2)}{ur_2} \right]^2 - (n_1^2 + n_2^2) k_0^2 \left[\frac{\nu}{w^2 r_2^2} + \frac{1}{2(\nu-1)} \right] \frac{\mathcal{F}'_\nu(ur_2)}{ur_2} \mathcal{F}_\nu(ur_2) + n_1^2 k_0^2 \left[\frac{\nu^2}{w^4 r_2^4} + \frac{\nu}{(\nu-1)w^2 r_2^2} + \frac{1}{4(\nu-1)^2} \right] \mathcal{F}_\nu^2(ur_2) \quad (4.21)$$

The term $n_1^2 \nu^2 k_0^2 \mathcal{F}_\nu(ur_2)/(w^4 r_2^4)$ is present on both sides of the equation, thus cancels out. We multiply the equation by $w^2 r_2^2$, and we evaluate the limit when $w \rightarrow 0$. Remaining terms are:

$$\frac{n_1^2 + n_2^2}{u^2 r_2^2} \nu^2 \mathcal{F}_\nu^2(ur_2) = -(n_1^2 + n_2^2) \nu \frac{\mathcal{F}'_\nu(ur_2)}{ur_2} \mathcal{F}_\nu(ur_2) + n_1^2 \frac{\nu}{(\nu-1)} \mathcal{F}_\nu^2(ur_2) \quad (4.22)$$

Derivative of $\mathcal{F}_\nu(ur_2)$ can be expanded using (A.14) and (A.15):

$$\mathcal{F}'_\nu(ur_2) = -\frac{\nu}{ur_2} \mathcal{F}_\nu(ur_2) + \mathcal{F}_{\nu-1}(ur_2) \quad (4.23)$$

Recurrence relations (A.8) and (A.9) also apply:

$$\mathcal{F}_{\nu-2}(ur_2) + \mathcal{F}_\nu(ur_2) = \frac{2(\nu-1)}{ur_2} \mathcal{F}_{\nu-1}(ur_2) \quad (4.24)$$

Applying (4.23) and (4.24) in (4.22), and with some reorganization, we get:

$$\mathcal{F}_\nu(ur_2) \left[\mathcal{F}_{\nu-2}(ur_2) + \frac{n_2^2 - n_1^2}{n_2^2 + n_1^2} \mathcal{F}_\nu(ur_2) \right] = 0 \quad (4.25)$$

$\mathcal{F}_\nu(ur_2)$ cannot be zero, because $e_z(r_2) \neq 0$ and $h_z(r_2) \neq 0$. Therefore, the cutoff expression for $\text{HE}_{\nu,m}$ modes, when $\nu \geq 2$, is given by:

$$\mathcal{F}_{\nu-2}(ur_2) = -\frac{n_2^2 - n_1^2}{n_2^2 + n_1^2} \mathcal{F}_\nu(ur_2) \quad (4.26)$$

that expands to:

$$J_{\nu-2}(ur_2)N_\nu(ur_1) - N_{\nu-2}(ur_2)J_\nu(ur_1) = -\frac{n_2^2 - n_1^2}{n_2^2 + n_1^2} [J_\nu(ur_2)N_\nu(ur_1) - N_\nu(ur_2)J_\nu(ur_1)] \quad (4.27)$$

4.3.4 Cutoff of $\text{EH}_{\nu,m}$ modes

Development of cutoff expressions for $\text{EH}_{\nu,m}$ modes is similar to the development for $\text{HE}_{\nu,m}$ modes, but with $e_z(r_2) = h_z(r_2) = 0$. Therefore, (4.9c) and (4.9d) are zero, and we take the determinant of (4.9a) and (4.9b). After applying the asymptotic expansion (A.25), this leads to:

$$\left(\frac{1}{u^2 r_1^2} + \frac{1}{w^2 r_1^2} \right)^2 \beta^2 \nu^2 \mathcal{F}_\nu^2(ur_1) = k_0^2 \left[\frac{\mathcal{F}'_\nu(ur_1)}{ur_1} + \left(\frac{\nu}{w^2 r_1^2} + \frac{1}{2(\nu-1)} \right) \mathcal{F}_\nu(ur_1) \right] \left[n_2^2 \frac{\mathcal{F}'_\nu(ur_1)}{ur_1} + n_1^2 \left(\frac{\nu}{w^2 r_1^2} + \frac{1}{2(\nu-1)} \right) \mathcal{F}_\nu(ur_1) \right] \quad (4.28)$$

where $\mathcal{F}_\nu(ur_1)$ is defined as previously, with

$$\gamma = \frac{J_\nu(ur_2)}{N_\nu(ur_2)} \quad (4.29)$$

In (4.28) the bracketed terms are a sum, while in (4.19) they are a difference. This leads to expanding the derivative of $\mathcal{F}_\nu(ur_1)$ with the opposite sign in (A.14) and (A.15). Finally, we get the cutoff expression for $\text{EH}_{\nu,m}$ modes:

$$\mathcal{F}_{\nu+2}(ur_1) = -\frac{n_2^2 - n_1^2}{n_2^2 + n_1^2} \mathcal{F}_\nu(ur_1) \quad (4.30)$$

that expands to:

$$J_{\nu+2}(ur_1)N_\nu(ur_2) - N_{\nu+2}(ur_1)J_\nu(ur_2) = -\frac{n_2^2 - n_1^2}{n_2^2 + n_1^2} [J_\nu(ur_1)N_\nu(ur_2) - N_\nu(ur_1)J_\nu(ur_2)] \quad (4.31)$$

Table 4.1 summarize cutoff equations for all modes in ring-core fibers, expressed as functions of normalized parameters ρ and V .

Table 4.1: Cutoff conditions for ring-core fibers

Mode	cutoff	
TE _{0,m}	$J_0(V)N_2(\rho V) - N_0(V)J_2(\rho V) = 0$	(4.10)
TM _{0,m}	$J_0(V)N_2(\rho V) - N_0(V)J_2(\rho V) =$ $\left(\frac{n_1^2}{n_2^2} - 1\right) [J_0(V)N_0(\rho V) - J_0(\rho V)N_0(V)]$	(4.12)
HE _{1,m}	$J_1(V)N_1(\rho V) = J_1(\rho V)N_1(V)$	(4.18)
HE _{ν,m}	$J_{\nu-2}(V)N_\nu(\rho V) - J_\nu(\rho V)N_{\nu-2}(V) =$ $- \frac{n_2^2 - n_1^2}{n_2^2 + n_1^2} [J_\nu(V)N_\nu(\rho V) - J_\nu(\rho V)N_\nu(V)]$	(4.27)
EH _{ν,m}	$J_{\nu+2}(\rho V)N_\nu(V) - J_\nu(V)N_{\nu+2}(\rho V) =$ $- \frac{n_2^2 - n_1^2}{n_2^2 + n_1^2} [J_\nu(\rho V)N_\nu(V) - J_\nu(V)N_\nu(\rho V)]$	(4.31)
LP _{ℓ,m}	$J_{\ell-1}(V)N_{\ell+1}(\rho V) - N_{\ell-1}(V)J_{\ell+1}(\rho V) = 0$	(4.33)

4.4 Numerical validation

To validate the cutoff expressions, we plot normalized propagation constant b (defined below) versus the normalized frequency V , for a few fiber parameters. Near cutoff, numerical calculation of the propagation constant requires very high precision, and becomes unstable; however, the prolongation of the curve of b versus V should reach zero at the cutoff frequency.

The V number for RCF is defined in Section 4.1.1. Normalized propagation constant is given by:

$$b = \frac{n_{\text{eff}}^2 - n_1^2}{n_2^2 - n_1^2} \quad (4.32)$$

It is zero at cutoff, and approaches one when $n_{\text{eff}} \rightarrow n_2$.

We simulated three different fiber profiles. The first simulation is with a fiber with a large core, but with a weak index contrast. In that case, the weakly guiding approximation applies, and modes are very close together within mode groups. The second simulation is with a stronger contrast; something similar to what we could get with a high-contrast silica fiber. The third simulation is with a silica tube, where the center and the cladding is air. In that case, the index contrast is very strong, and we clearly see the separation between the modes.

Simulation of the propagation constant was performed using the transfer matrix method [17, 118], one wavelength at a time. Using characteristic equation 4.8, we solved for β values that lead to a zero determinant. We assumed that the refractive indexes did not vary with wavelength, as it simplifies the simulation, while still allowing to verify our cutoff expressions. We computed the cutoff frequencies using the expressions found in the previous section (Table 4.1). Cutoffs are given by the zeros of those equations, and are plotted as vertical dashed lines on the graphs. Hence the asymptotic value of $b \rightarrow 0$ should correspond to our analytical prediction for validation.

4.4.1 Weakly guiding RCF

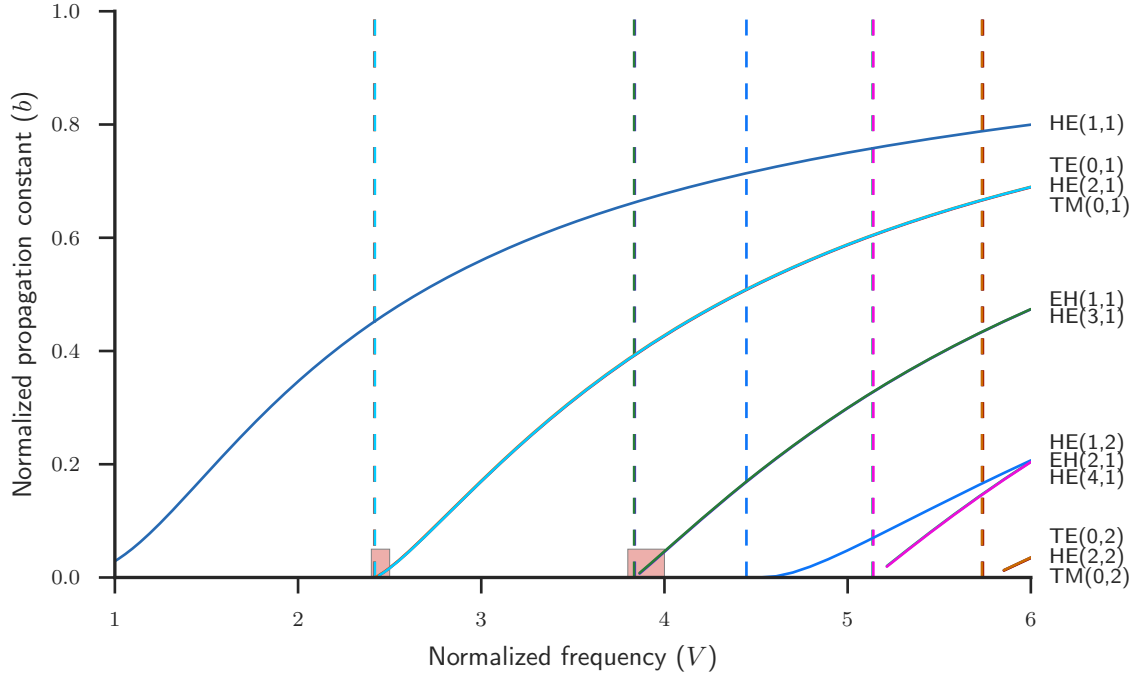
For the simulation we used the following parameters: $r_1 = 2 \mu\text{m}$, $r_2 = 8 \mu\text{m}$, $n_1 = 1.444$, $n_2 = 1.449$. Therefore, $\rho = 0.25$, the wavelength for $V = 1$ is 6045.46 nm, and the wavelength for $V = 6$ is 1007.58 nm. The index contrast is similar to what is found in SMF28TM, a typical weakly guiding fiber.

In Fig. 4.3 we plot in vertical lines the solutions for the V at cutoff for each of the modes, found via (4.10), (4.12), (4.18), (4.27), and (4.31). Curves give numerical solutions of b as a function of V . The first mode group, modes $\text{TE}_{0,1}$, $\text{HE}_{2,1}$, and $\text{TM}_{0,1}$, have propagation constants so close that their curves are indistinguishable. The same is true for the second mode group ($\text{EH}_{1,1}$ and $\text{HE}_{3,1}$), etc. This is not unexpected; for under the weakly guiding condition we expect the vector modes to group to form the LP modes. We see that the curves (found numerically) approach the vertical lines at $b = 0$, validating our equations for cutoff. We zoom in on two of these areas near $b = 0$. In Fig. 4.3(b) we can see three separate vertical lines, solutions for cutoff for each of the vector modes in the first mode group. While the numerical solutions of b versus V become unstable as $b \rightarrow 0$, the cutoff equations can predict even the small differences between the cutoff frequencies within the first mode group. Fig. 4.3(c) shows similar behavior for cutoff of the second mode group.

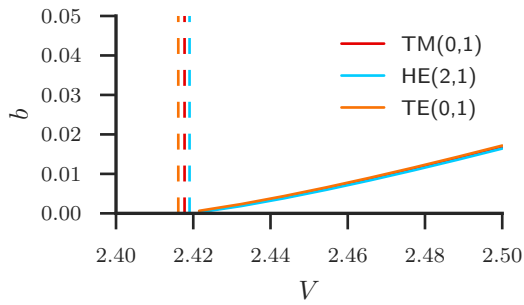
4.4.2 High contrast RCF

For the simulation we used the following parameters: $r_1 = 1 \mu\text{m}$, $r_2 = 4 \mu\text{m}$, $n_1 = 1.444$, $n_2 = 1.474$. Therefore, $\rho = 0.25$, the wavelength for $V = 1$ is 7436.06 nm, and the wavelength for $V = 6$ is 1239.34 nm. Chosen indexes for this example are similar to those found in a typical high contrast silica fiber.

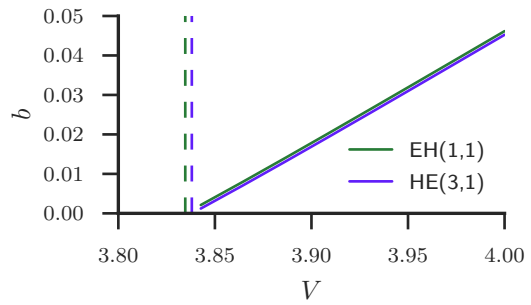
As we can see in Fig. 4.4, the curves for the propagation constant are similar to those of RCF with weak contrast, but the separation within modes of the same group is larger, as is the separation between cutoff frequencies. This is the expected behavior for fibers with higher contrast, as this refractive index contrast violates the weakly guiding condition. Again, the propagation curves approach the calculated cutoff values at $b = 0$, confirming the correctness of our cutoff expressions.



(a) Cutoffs of the twelve first modes

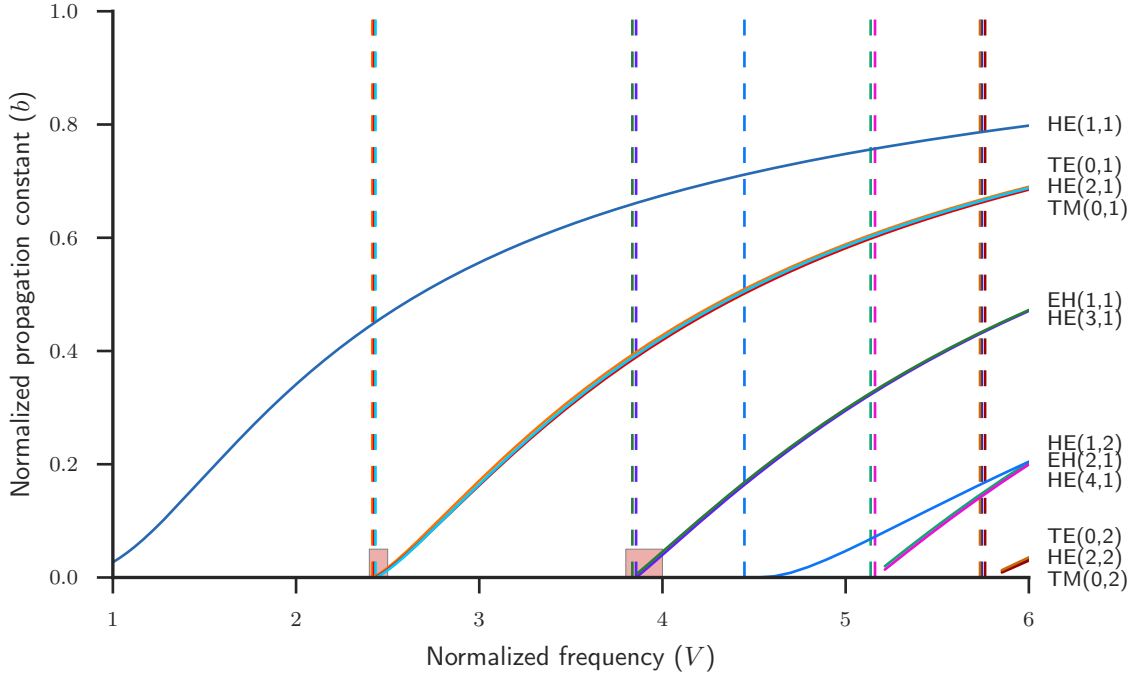


(b) Zoom on first mode group

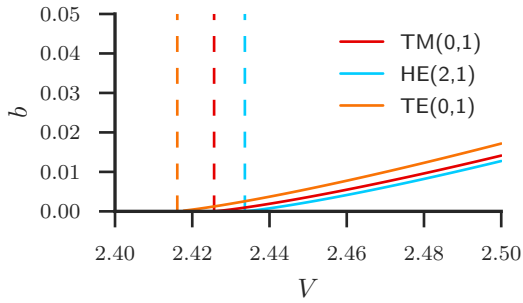


(c) Zoom on second mode group

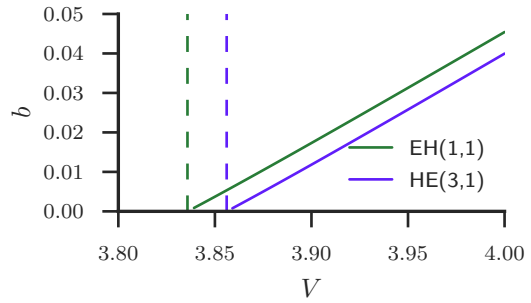
Figure 4.3: Cutoffs of a ring-core fiber with weak index contrast. Simulation parameters are: $r_1 = 2 \mu\text{m}$, $r_2 = 8 \mu\text{m}$, $n_1 = 1.444$, $n_2 = 1.449$. Subfigures (b) and (c) are zoom on the cutoff region of first and second mode groups, respectively, and shown as blue rectangles on subfigure (a).



(a) Cutoffs of the twelve first modes



(b) Zoom on first mode group



(c) Zoom on second mode group

Figure 4.4: Cutoffs of a ring-core fiber with a relatively high index contrast. Simulation parameters are: $r_1 = 1 \mu\text{m}$, $r_2 = 4 \mu\text{m}$, $n_1 = 1.444$, $n_2 = 1.474$. Subfigures (b) and (c) are zoom on the cutoff region of first and second mode groups, respectively, and shown as blue rectangles on subfigure (a).

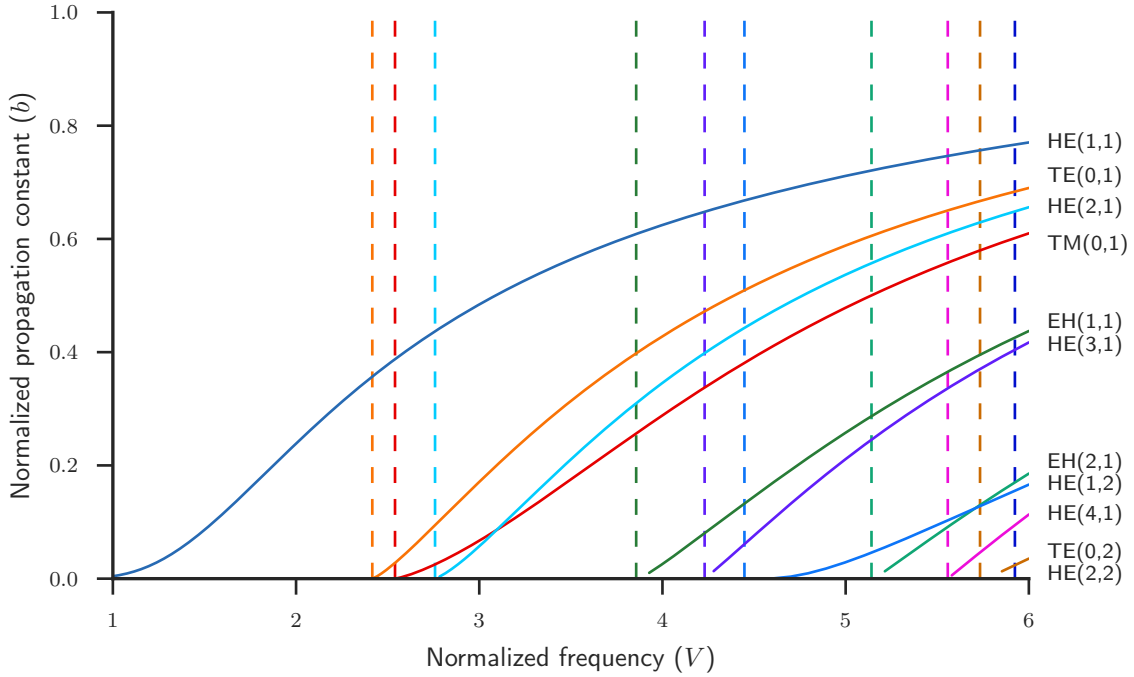


Figure 4.5: Cutoffs of a silica tube surrounded by air. Simulation parameters are: $r_1 = 0.25 \mu\text{m}$, $r_2 = 1 \mu\text{m}$, $n_1 = 1$, $n_2 = 1.444$.

4.4.3 Silica tube

For the simulation we used the following parameters: $r_1 = 0.25 \mu\text{m}$, $r_2 = 1 \mu\text{m}$, $n_1 = 1$, $n_2 = 1.444$. Therefore, $\rho = 0.25$, the wavelength for $V = 1$ is 6369.85 nm , and the wavelength for $V = 6$ is 1061.64 nm . This fiber could not be fabricated, because it would be too small and too fragile; it is there for comparison with the two previous examples, to illustrate what would happen with a very high index contrast. We kept the tube very small to keep wavelengths and V numbers similar to those in previous examples.

In this case, as we can see in Fig. 4.5, effective indexes clearly diverge from those of LP modes, but cutoff frequencies, calculated with our expressions, still are in agreement with simulated propagation constants.

In all three cases, cutoffs found match very well with numerically calculated cutoff frequencies. This gives us a high degree of confidence in the equations we found.

4.5 Asymptotic limits

Another way to validate expressions is to verify they converge to known solutions when we tend parameters to their limits. When $n_2 \rightarrow n_1$, we are in the weakly guiding regime. When

$r_1 \rightarrow 0$, RCF becomes SSIF. When $r_1 \rightarrow \infty$ and $r_2 \rightarrow \infty$, the RCF becomes a planar waveguide, curved onto itself.

4.5.1 Weakly guiding regime

Under the weakly guiding approximation, $(n_2^2 - n_1^2) \rightarrow 0$. We want to verify that expressions for all kind of modes reduce to the same form under the weakly guiding approximation. Furthermore, we want to verify that the expression obtained is the same as that given in [127, 128].

For TE modes, (4.10) remains the same, because it does not depend on the indexes of the fiber. For TM modes, the right-hand side of (4.12) becomes zero, and it becomes similar to (4.10). With $\ell = 1$, we can write:

$$J_{\ell-1}(ur_2)N_{\ell+1}(ur_1) - N_{\ell-1}(ur_2)J_{\ell+1}(ur_1) = 0 \quad (4.33)$$

Expression (4.18) for $\text{HE}_{1,m}$ modes is similar to (4.33), with $\ell = 0$, because of (A.6). With $\ell = \nu - 1$, expression (4.27) for $\text{HE}_{\nu,m}$ modes becomes like (4.33). Finally, with $\ell = \nu + 1$, expression (4.31) for $\text{EH}_{\nu,m}$ modes also becomes like (4.33).

Cutoff condition for scalar modes is given by (8) in [127], and in a very similar form in equation (13) of [128]. Using our notation, this equation is equivalent to:

$$\left[1 - \frac{\ell}{ur_1} \frac{J_\ell(ur_1)}{J'_\ell(ur_1)}\right] \left[\frac{\ell}{ur_2} \frac{N_\ell(ur_2)}{N'_\ell(ur_1)} + \frac{N'_\ell(ur_2)}{N'_\ell(ur_1)}\right] = \left[1 - \frac{\ell}{ur_1} \frac{N_\ell(ur_1)}{N'_\ell(ur_1)}\right] \left[\frac{\ell}{ur_2} \frac{J_\ell(ur_2)}{J'_\ell(ur_1)} + \frac{J'_\ell(ur_2)}{J'_\ell(ur_1)}\right] \quad (4.34)$$

While this seems rather complex, we will show it is equivalent to (4.33).

We first multiply both sides by $J'_\ell(ur_1)N'_\ell(ur_1)$:

$$\left[J'_\ell(ur_1) - \frac{\ell}{ur_1} J_\ell(ur_1)\right] \left[\frac{\ell}{ur_2} N_\ell(ur_2) + N'_\ell(ur_2)\right] = \left[N'_\ell(ur_1) - \frac{\ell}{ur_1} N_\ell(ur_1)\right] \left[\frac{\ell}{ur_2} J_\ell(ur_2) + J'_\ell(ur_2)\right] \quad (4.35)$$

Then we use (A.14) and (A.15) to transform all the derivatives:

$$\left[\frac{\ell}{ur_1} J_\ell(ur_1) - J_{\ell+1}(ur_1) - \frac{\ell}{ur_1} J_\ell(ur_1)\right] \left[\frac{\ell}{ur_2} N_\ell(ur_2) + N_{\ell-1}(ur_2) - \frac{\ell}{ur_2} N_\ell(ur_2)\right] = \left[\frac{\ell}{ur_1} N_\ell(ur_1) - N_{\ell+1}(ur_1) - \frac{\ell}{ur_1} N_\ell(ur_1)\right] \left[\frac{\ell}{ur_2} J_\ell(ur_2) + J_{\ell-1}(ur_2) - \frac{\ell}{ur_2} J_\ell(ur_2)\right] \quad (4.36)$$

This simplifies to (4.33).

4.5.2 Approaching SSIF

When r_1 approaches zero, the center of the RCF collapses, and it becomes a SSIF. We already gave cutoff expression for SSIF in Section 1.6, Table 1.1. We will now show that the same expressions are obtained from cutoff equations of RCF, when $r_1 \rightarrow 0$. To evaluate the limits, (A.18), (A.20), and (A.21) are used.

For $TE_{0,m}$ modes:

$$J_0(ur_2) \left[-\frac{4}{\pi(ur_1)^2} \right] = N_0(ur_2) \left[\frac{(ur_1)^2}{8} \right] \quad (4.37)$$

We multiply both sides by $(ur_1)^2$; $J_0(ur_2) = 0$ remains, as in (1.44).

For $TM_{0,m}$ mode:

$$J_0(ur_2) \left[-\frac{4}{\pi(ur_1)^2} \right] - N_0(ur_2) \left[\frac{(ur_1)^2}{8} \right] = \left(\frac{n_1^2}{n_2^2} - 1 \right) \left[J_0(ur_2) \frac{2}{\pi} \ln(ur_1) - 1 \cdot N_0(ur_2) \right] \quad (4.38)$$

Again, we multiply both sides by $(ur_1)^2$; $J_0(ur_2) = 0$ remains, as in (1.44).

For $HE_{1,m}$ modes:

$$J_1(ur_2) \left[-\frac{2}{\pi(ur_1)} \right] = N_1(ur_2) \frac{(ur_1)}{2} \quad (4.39)$$

We multiply both sides by (ur_1) , to get $J_1(ur_2) = 0$, as in (1.45).

For $HE_{\nu,m}$ modes:

$$J_{\nu-2}(ur_2) \left[-\frac{(\nu-1)!}{\pi} \left(\frac{2}{ur_1} \right)^\nu \right] - N_{\nu-2}(ur_2) \left[\frac{1}{\nu!} \left(\frac{ur_1}{2} \right)^\nu \right] = -\frac{n_2^2 - n_1^2}{n_2^2 + n_1^2} \left\{ J_\nu(ur_2) \left[-\frac{(\nu-1)!}{\pi} \left(\frac{2}{ur_1} \right)^\nu \right] - N_\nu(ur_2) \left[\frac{1}{\nu!} \left(\frac{ur_1}{2} \right)^\nu \right] \right\} \quad (4.40)$$

We multiply both sides by $(ur_1)^\nu$:

$$J_{\nu-2}(ur_2) = -\frac{n_2^2 - n_1^2}{n_2^2 + n_1^2} J_\nu(ur_2) \quad (4.41)$$

We apply Bessel recurrence relation (A.8) to the left-hand side:

$$\frac{2(\nu-1)}{ur_2} J_{\nu-1}(ur_2) - J_\nu(ur_2) = -\frac{n_2^2 - n_1^2}{n_2^2 + n_1^2} J_\nu(ur_2) \quad (4.42)$$

which is equivalent to (1.46).

Finally, for $\text{EH}_{\nu,m}$ modes:

$$\begin{aligned} & \left[\frac{1}{(\nu+2)!} \left(\frac{ur_1}{2} \right)^{\nu+2} \right] N_\nu(ur_2) - \left[-\frac{(\nu+1)!}{\pi} \left(\frac{2}{ur_1} \right)^{\nu+2} \right] J_\nu(ur_2) = \\ & - \frac{n_2^2 - n_1^2}{n_2^2 + n_1^2} \left\{ \left[\frac{1}{\nu!} \left(\frac{ur_1}{2} \right)^\nu \right] N_\nu(ur_2) - \left[-\frac{(\nu-1)!}{\pi} \left(\frac{2}{ur_1} \right)^\nu \right] J_\nu(ur_2) \right\} \end{aligned} \quad (4.43)$$

We multiply both sides by $(ur_1)^{\nu+2}$; $J_\nu(ur_2) = 0$ remains, as in (1.47).

4.5.3 Approaching planar waveguide

When both r_1 and r_2 approach infinity, the curvature radius of the ring-core also approaches infinity, and therefore the ring-core fiber is just like a planar waveguide. In fact, we can see a ring-core fiber with a very thin ring, and a large radius, as a planar waveguide curved on itself. We will show that cutoff expressions of RCF lead to cutoff expression for a planar waveguide, when $r_1 \rightarrow \infty$ and $r_2 \rightarrow \infty$.

In a planar waveguide, only $\text{TE}_{0,m}$ and $\text{TM}_{0,m}$ modes exist. Cutoff expression is given by [16, Table 12-2]:

$$ud = m\pi \quad (4.44)$$

where $d = r_2 - r_1$. In [16], the expression given is $U = j\pi/2$, because in their notation, $j = m$, and $U = (d/2)u$. We will now replace Bessel functions in cutoff equations by their asymptotic expansions when the argument approaches infinity, as given by (A.27) and (A.28).

For $\text{TE}_{0,m}$ modes:

$$\begin{aligned} & \sqrt{\frac{2}{\pi ur_2}} \cos \left\{ ur_2 - \frac{\pi}{4} \right\} \sqrt{\frac{2}{\pi ur_1}} \sin \left\{ ur_1 - \frac{5\pi}{4} \right\} - \\ & \sqrt{\frac{2}{\pi ur_2}} \sin \left\{ ur_2 - \frac{\pi}{4} \right\} \sqrt{\frac{2}{\pi ur_1}} \cos \left\{ ur_1 - \frac{5\pi}{4} \right\} = 0 \end{aligned} \quad (4.45a)$$

We apply trigonometric addition formula (A.36):

$$\sin \left\{ ur_2 - \frac{\pi}{4} - ur_1 + \frac{5\pi}{4} \right\} = 0 \quad (4.45b)$$

$$\sin(ud + \pi) = 0 \quad (4.45c)$$

Therefore, ud is a multiple of π , and it leads to (4.44).

For $\text{TM}_{0,m}$ modes:

$$\begin{aligned} & \sqrt{\frac{2}{\pi ur_2}} \cos \left\{ ur_2 - \frac{\pi}{4} \right\} \sqrt{\frac{2}{\pi ur_1}} \sin \left\{ ur_1 - \frac{5\pi}{4} \right\} - \\ & \quad \sqrt{\frac{2}{\pi ur_2}} \sin \left\{ ur_2 - \frac{\pi}{4} \right\} \sqrt{\frac{2}{\pi ur_1}} \cos \left\{ ur_1 - \frac{5\pi}{4} \right\} = \\ & \quad \left(\frac{n_1^2}{n_2^2} - 1 \right) \left[\sqrt{\frac{2}{\pi ur_2}} \cos \left\{ ur_2 - \frac{\pi}{4} \right\} \sqrt{\frac{2}{\pi ur_1}} \sin \left\{ ur_1 - \frac{\pi}{4} \right\} - \right. \\ & \quad \left. \sqrt{\frac{2}{\pi ur_1}} \cos \left\{ ur_1 - \frac{\pi}{4} \right\} \sqrt{\frac{2}{\pi ur_2}} \sin \left\{ ur_2 - \frac{\pi}{4} \right\} \right] \end{aligned} \quad (4.46a)$$

$$\sin(ud + \pi) = \left(\frac{n_1^2}{n_2^2} - 1 \right) \sin(ud) \quad (4.46b)$$

$$\frac{n_1^2}{n_2^2} \sin(ud) = 0 \quad (4.46c)$$

Again, solution exists if ud is a multiple of π , and it leads to (4.44).

For $\text{HE}_{\nu,m}$ and $\text{EH}_{\nu,m}$ modes, development is similar, and still gives the same cutoff expression. Therefore, it is verified that when radius is large and the ring is thin, cutoff of all modes are similar to cutoff of a planar waveguide.

4.6 Approximation for cutoff of $\text{HE}_{1,m}$ modes

In [130], equations (9.5.27)–(9.5.29) give an asymptotic expansion of the s^{th} zero of the cross-product function

$$J_\nu(z)N_\nu(\lambda z) - J_\nu(\lambda z)N_\nu(z) \quad (4.47)$$

Using $z = \rho V_0$, $\lambda = 1/\rho$, $\nu = 1$, and $s = m - 1$, we can directly use this development to solve for the cutoff conditions of the $\text{HE}_{1,m}$ modes. The first term of the expansion becomes:

$$V = \frac{z}{\rho} \approx \frac{\gamma}{\rho} = \frac{s\pi}{\rho(\lambda - 1)} = \frac{(m-1)\pi}{1-\rho} \quad (4.48)$$

In a similar way, we can develop the other terms of the expansion as

$$\epsilon = \frac{p}{\rho\gamma} + \frac{q - p^2}{\rho\gamma^3} + \frac{r - 4pq + 2p^2}{\rho\gamma^5} + \dots \quad (4.49)$$

where

$$\begin{aligned} \gamma &= \frac{(m-1)\pi\rho}{1-\rho} & p &= \frac{3}{8}\rho \\ q &= -\frac{21}{128} \frac{(1-\rho^3)}{(1-\rho)} \rho & r &= \frac{1899}{5120} \frac{(1-\rho^5)}{(1-\rho)} \rho \end{aligned}$$

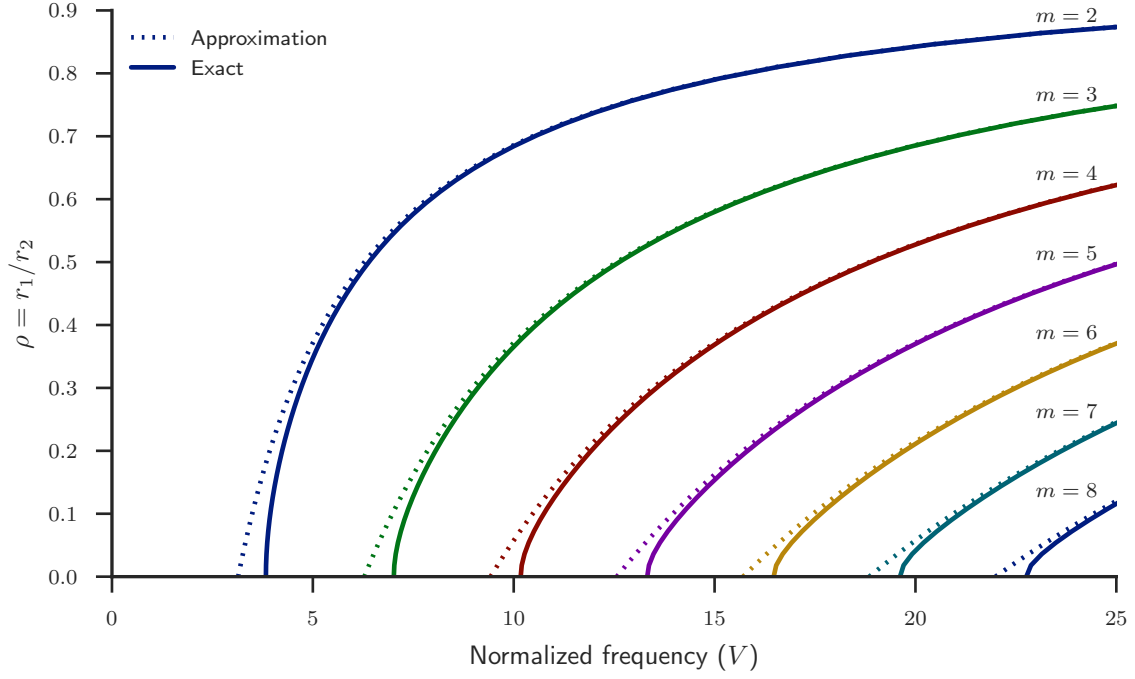


Figure 4.6: Approximated and exact cutoffs for $\text{HE}_{1,m}$ modes

Therefore, cutoff of $\text{HE}_{1,2}$ mode is approximated by

$$V = \frac{\pi}{1 - \rho} \quad (4.50)$$

and cutoff of other $\text{HE}_{1,m}$ modes are given by (4.48). This asymptotic expansion becomes unstable when $\rho \rightarrow 0$. However, this is not a problem, as when ρ is small, the fiber becomes like a SSIF, and cutoffs are given by the roots of $J_1(V)$ function. Figure 4.6 shows approximated and exact cutoffs for $\text{HE}_{1,m}$ modes, as function of the ρ parameter.

This approximation is useful to quickly determine how many radial orders (i.e., what is the maximum value for the m parameter) are supported for a given fiber design.

Chapter 5

Cutoff of three-layer fibers

5.1 The family of three-layer fibers

Three layer step-index fiber (3LSIF) is a simple extension of the extensively deployed single-core step-index fiber. This family of fibers includes double-clad fiber, W-type fiber [131], ring- or annular-core fiber [132], pedestal fiber, etc. These structures can be exploited for chromatic dispersion compensation [132], higher-order mode filtering, fiber amplifiers and lasers [133, 134], optical sensing, or orbital angular momentum (OAM) transmission [2, 50, 95].

We showed the development for the modal equations for step-index fibers with a single core and cladding – called standard step-index fiber (SSIF) throughout this thesis – in Chapter 1. Although adding another layer to the fiber only adds a combination of two Bessel functions to the expressions of the longitudinal electrical and magnetic fields, no exact equations have appeared for those fibers. The literature only provides approximations, typically for a specific kind of fiber profile. For instance, [131] gives approximate formulas for W-type fibers, but states that no analytical solution seems possible for the 4×4 determinant.

A more rigorous analysis of three-layer fibers is performed in [135]. While it gives solutions for the vector modes of those fibers, it does not address the calculation of cutoff frequencies. Knowledge of exact cutoffs of vector modes is important for numerically solving and identifying modes, and as a tool for designing fibers tailored for guiding a specific number of modes.

In the previous chapter, we developed the cutoff equations for ring-core fibers. However, RCF is just one of the five possible three-layer fiber layouts. The difference resides in the relative values of n_1 , n_2 , and n_3 . Figure 5.1 illustrates those five fiber profiles. The notation we use is the same than for RCF, in Fig. 4.1.

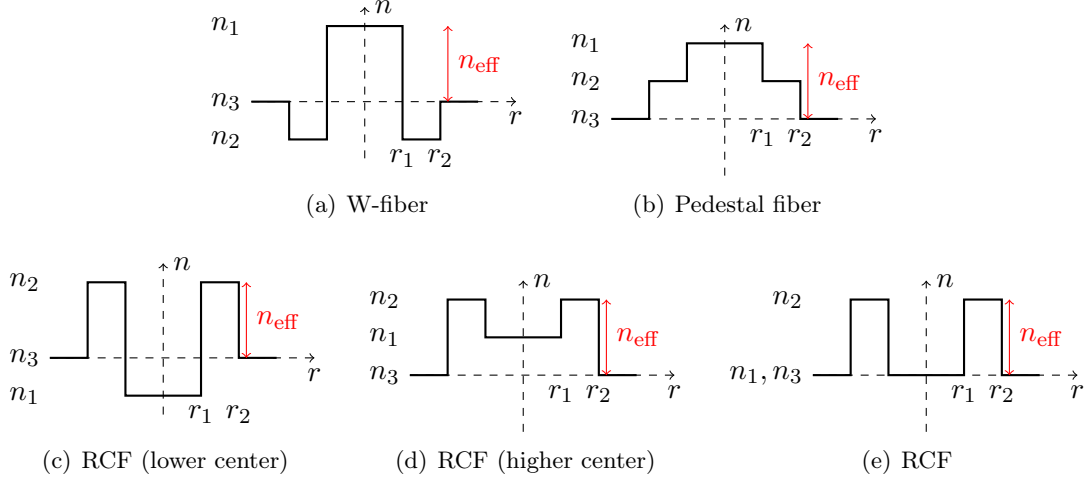


Figure 5.1: The five possible three-layer fiber profiles. (a) fiber with trench (W-fiber), (b) fiber with $n_1 > n_2 > n_3$, (c) – (e) ring-core fibers. The red arrow shows the possible range of n_{eff} that allows guided modes.

5.1.1 Normalized notation

We already defined the normalized frequency V for SSIF (1.22). In the case of multilayer fibers, we can use a similar normalized notation, if we replace n_{co} by n_{max} , the highest refractive index of the fiber layers, and r_1 by r_{N-1} , the radius of the last fiber layer, N being the total number of layers. As we can see, this is a generalized version of what we proposed for RCF (4.1). Defining a normalized frequency V allows all types of three-layer fiber to be easily compared with standard fiber.

In some cases, as we will see later, it is useful to define the V frequency with other choices of index and radius. This is acceptable, as it only changes the normalization constant, as long as the same definition of V is used when comparing two different fibers.

5.2 Derivation of the characteristic equation for vector modes

For RCF, in the previous chapter, it was well defined whether $e_z(r)$ and $h_z(r)$ were functions of ordinary Bessel functions $J_\nu(x)$ and $N_\nu(x)$, or functions of modified Bessel functions $I_\nu(x)$ and $K_\nu(x)$, depending on the layer to which r belonged. For the solution for 3LSIF, we now need a more generic way to express the fields, since there are five different configuration of

layers. We write $e_z(r)$ and $h_z(r)$ as:

$$e_z(r) = \begin{cases} A_1 J_\nu(\hat{u}_1 r) & r \leq r_1 \\ A_2 J_\nu(\hat{u}_2 r) + B_2 N_\nu(\hat{u}_2 r) & r_1 < r \leq r_2 \\ B_3 K_\nu(wr) & r > r_2 \end{cases} \quad (5.1a)$$

$$h_z(r) = \begin{cases} C_1 J_\nu(\hat{u}_1 r) & r \leq r_1 \\ C_2 J_\nu(\hat{u}_2 r) + D_2 N_\nu(\hat{u}_2 r) & r_1 < r \leq r_2 \\ D_3 K_\nu(wr) & r > r_2 \end{cases} \quad (5.1b)$$

where:

$$\hat{u}_1^2 = n_1^2 k_0^2 - \beta^2 \quad (5.2a)$$

$$\hat{u}_2^2 = n_2^2 k_0^2 - \beta^2 \quad (5.2b)$$

$$w^2 = \beta^2 - n_3^2 k_0^2 \quad (5.2c)$$

The hat over \hat{u}_1 and \hat{u}_2 is a reminder that this value can be either real or imaginary, depending on whether n_1 or n_2 is greater or less than n_{eff} . We also define:

$$u_1^2 = |n_1^2 k_0^2 - \beta^2| \quad u_2^2 = |n_2^2 k_0^2 - \beta^2| \quad (5.3)$$

without hat, as real values. Because of the relations between Bessel functions of complex arguments (A.31) and (A.32), we can show that

$$A J_\nu(ju_1) = A' I_\nu(u_1) \quad (5.4a)$$

$$B J_\nu(ju_2) + C N_\nu(ju_2) = B' I_\nu(u_2) + C' K_\nu(u_2) \quad (5.4b)$$

where A, B, C are appropriate real constants, and A', B', C' are appropriate (possibly complex) constants. Therefore, $J_\nu(\hat{u}r)$ is equivalent to either $J_\nu(ur)$ or $I_\nu(ur)$, whether \hat{u} is real or imaginary.

The radial dependency of azimuthal components, for each layer, is obtained from (1.12):

$$e_\phi(r) = \begin{cases} \frac{1}{\hat{u}_1^2} \left[\frac{\beta}{r} (-\nu A_1 J_\nu(\hat{u}_1 r)) - \eta_0 k_0 (\hat{u}_1 C_1 J'_\nu(\hat{u}_1 r)) \right] & r \leq r_1 \\ \frac{1}{\hat{u}_2^2} \left[\frac{\beta}{r} (-\nu [A_2 J_\nu(\hat{u}_2 r) + B_2 N_\nu(\hat{u}_2 r)]) - \eta_0 k_0 (\hat{u}_2 [C_2 J'_\nu(\hat{u}_2 r) + D_2 N'_\nu(\hat{u}_2 r)]) \right] & r_1 \leq r \leq r_2 \\ \frac{-1}{w^2} \left[\frac{\beta}{r} (-\nu B_3 K_\nu(wr)) - \eta_0 k_0 (w D_3 K'_\nu(wr)) \right] & r \geq r_2 \end{cases} \quad (5.5)$$

$$h_\phi(r) = \begin{cases} \frac{1}{\hat{u}_1^2} \left[\frac{\beta}{r} (\nu C_1 J_\nu(\hat{u}_1 r)) + \frac{1}{\eta_0} k_0 n_1^2 (\hat{u}_1 A_1 J'_\nu(\hat{u}_1 r)) \right] & r \leq r_1 \\ \frac{1}{\hat{u}_2^2} \left[\frac{\beta}{r} (\nu [C_2 J_\nu(\hat{u}_2 r) + D_2 N_\nu(\hat{u}_2 r)]) + \frac{1}{\eta_0} k_0 n_2^2 (\hat{u}_2 [A_2 J'_\nu(\hat{u}_2 r) + B_2 N'_\nu(\hat{u}_2 r)]) \right] & r_1 \leq r \leq r_2 \\ \frac{-1}{w^2} \left[\frac{\beta}{r} (\nu D_3 K_\nu(wr)) + \frac{1}{\eta_0} k_0 n_3^2 (w B_3 K'_\nu(wr)) \right] & r \geq r_2 \end{cases} \quad (5.6)$$

Ensuring continuity of the longitudinal fields at layer interfaces $r = r_1$ and $r = r_2$, we get the following four equations.

$$A_1 J_\nu(\hat{u}_1 r_1) = [A_2 J_\nu(\hat{u}_2 r_1) + B_2 N_\nu(\hat{u}_2 r_1)] \quad (5.7a)$$

$$C_1 J_\nu(\hat{u}_1 r_1) = [C_2 J_\nu(\hat{u}_2 r_1) + D_2 N_\nu(\hat{u}_2 r_1)] \quad (5.7b)$$

$$B_3 K_\nu(w r_2) = [A_2 J_\nu(\hat{u}_2 r_2) + B_2 N_\nu(\hat{u}_2 r_2)] \quad (5.7c)$$

$$D_3 K_\nu(w r_2) = [C_2 J_\nu(\hat{u}_2 r_2) + D_2 N_\nu(\hat{u}_2 r_2)] \quad (5.7d)$$

Similarly, the continuity of the azimuthal fields at layer interfaces $r = r_1$ and $r = r_2$ gives:

$$\begin{aligned} \frac{1}{\hat{u}_1^2} \left[\frac{\beta}{r_1} (-\nu A_1 J_\nu(\hat{u}_1 r_1)) - \eta_0 k_0 (\hat{u}_1 C_1 J'_\nu(\hat{u}_1 r_1)) \right] = \\ \frac{1}{\hat{u}_2^2} \left[\frac{\beta}{r_1} (-\nu [A_2 J_\nu(\hat{u}_2 r_1) + B_2 N_\nu(\hat{u}_2 r_1)]) - \eta_0 k_0 (\hat{u}_2 [C_2 J'_\nu(\hat{u}_2 r_1) + D_2 N'_\nu(\hat{u}_2 r_1)]) \right] \end{aligned} \quad (5.8a)$$

$$\begin{aligned} \frac{1}{\hat{u}_1^2} \left[\frac{\beta}{r_1} (\nu C_1 J_\nu(\hat{u}_1 r_1)) + \frac{1}{\eta_0} k_0 n_1^2 (\hat{u}_1 A_1 J'_\nu(\hat{u}_1 r_1)) \right] = \\ \frac{1}{\hat{u}_2^2} \left[\frac{\beta}{r_1} (\nu [C_2 J_\nu(\hat{u}_2 r_1) + D_2 N_\nu(\hat{u}_2 r_1)]) + \frac{1}{\eta_0} k_0 n_2^2 (\hat{u}_2 [A_2 J'_\nu(\hat{u}_2 r_1) + B_2 N'_\nu(\hat{u}_2 r_1)]) \right] \end{aligned} \quad (5.8b)$$

$$\begin{aligned} - \frac{1}{w^2} \left[\frac{\beta}{r_2} (-\nu B_3 K_\nu(w r_2)) - \eta_0 k_0 (w D_3 K'_\nu(w r_2)) \right] = \\ \frac{1}{\hat{u}_2^2} \left[\frac{\beta}{r_2} (-\nu [A_2 J_\nu(\hat{u}_2 r_2) + B_2 N_\nu(\hat{u}_2 r_2)]) - \eta_0 k_0 (\hat{u}_2 [C_2 J'_\nu(\hat{u}_2 r_2) + D_2 N'_\nu(\hat{u}_2 r_2)]) \right] \end{aligned} \quad (5.8c)$$

$$\begin{aligned} - \frac{1}{w^2} \left[\frac{\beta}{r_2} (\nu D_3 K_\nu(w r_2)) + \frac{1}{\eta_0} k_0 n_3^2 (w B_3 K'_\nu(w r_2)) \right] = \\ \frac{1}{\hat{u}_2^2} \left[\frac{\beta}{r_2} (\nu [C_2 J_\nu(\hat{u}_2 r_2) + D_2 N_\nu(\hat{u}_2 r_2)]) + \frac{1}{\eta_0} k_0 n_2^2 (\hat{u}_2 [A_2 J'_\nu(\hat{u}_2 r_2) + B_2 N'_\nu(\hat{u}_2 r_2)]) \right] \end{aligned} \quad (5.8d)$$

Using (5.7), we can eliminate constants A_1 , C_1 , B_3 , and D_3 . For simplicity, we also assume the constant η_0 is absorbed by C_2 , and D_2 . After some reorganization of the terms, we obtain the four modal equations for 3LSIF:

$$\begin{aligned} \left(\frac{1}{\hat{u}_1^2} - \frac{1}{\hat{u}_2^2} \right) \frac{\nu \beta}{r_1^2} [A_2 J_\nu(\hat{u}_2 r_1) + B_2 N_\nu(\hat{u}_2 r_1)] = \\ k_0 \left\{ \left[C_2 \frac{J'_\nu(\hat{u}_2 r_1)}{\hat{u}_2 r_1} + D_2 \frac{N'_\nu(\hat{u}_2 r_1)}{\hat{u}_2 r_1} \right] - \frac{J'_\nu(\hat{u}_1 r_1)}{(\hat{u}_1 r_1) J_\nu(\hat{u}_1 r_1)} [C_2 J_\nu(\hat{u}_2 r_1) + D_2 N_\nu(\hat{u}_2 r_1)] \right\} \end{aligned} \quad (5.9a)$$

$$\begin{aligned} \left(\frac{1}{\hat{u}_1^2} - \frac{1}{\hat{u}_2^2}\right) \frac{\nu\beta}{r_1^2} [C_2 J_\nu(\hat{u}_2 r_1) + D_2 N_\nu(\hat{u}_2 r_1)] = \\ k_0 \left\{ n_2^2 \left[A_2 \frac{J'_\nu(\hat{u}_2 r_1)}{\hat{u}_2 r_1} + B_2 \frac{N'_\nu(\hat{u}_2 r_1)}{\hat{u}_2 r_1} \right] - \right. \\ \left. \frac{J'_\nu(\hat{u}_1 r_1)}{(\hat{u}_1 r_1) J_\nu(\hat{u}_1 r_1)} n_1^2 [A_2 J_\nu(\hat{u}_2 r_1) + B_2 N_\nu(\hat{u}_2 r_1)] \right\} \quad (5.9b) \end{aligned}$$

$$\begin{aligned} \left(\frac{1}{\hat{u}_2^2} + \frac{1}{w^2}\right) \frac{\nu\beta}{r_2^2} [A_2 J_\nu(\hat{u}_2 r_2) + B_2 N_\nu(\hat{u}_2 r_2)] = \\ - k_0 \left\{ \left[C_2 \frac{J'_\nu(\hat{u}_2 r_2)}{\hat{u}_2 r_2} + D_2 \frac{N'_\nu(\hat{u}_2 r_2)}{\hat{u}_2 r_2} \right] + \right. \\ \left. \frac{K'_\nu(w r_2)}{(w r_2) K_\nu(w r_2)} [C_2 J_\nu(\hat{u}_2 r_2) + D_2 N_\nu(\hat{u}_2 r_2)] \right\} \quad (5.9c) \end{aligned}$$

$$\begin{aligned} \left(\frac{1}{\hat{u}_2^2} + \frac{1}{w^2}\right) \frac{\nu\beta}{r_2^2} [C_2 J_\nu(\hat{u}_2 r_2) + D_2 N_\nu(\hat{u}_2 r_2)] = \\ - k_0 \left\{ n_2^2 \left[A_2 \frac{J'_\nu(\hat{u}_2 r_2)}{\hat{u}_2 r_2} + B_2 \frac{N'_\nu(\hat{u}_2 r_2)}{\hat{u}_2 r_2} \right] + \right. \\ \left. \frac{K'_\nu(w r_2)}{(w r_2) K_\nu(w r_2)} n_3^2 [A_2 J_\nu(\hat{u}_2 r_2) + B_2 N_\nu(\hat{u}_2 r_2)] \right\} \quad (5.9d) \end{aligned}$$

5.3 Cutoffs of 3LSIF

Below the cutoff the propagating wave is a transverse electro-magnetic (TEM) mode, thus at cutoff the longitudinal component of the electric and magnetic field approaches zero. This means that the radial component of the electrical field is proportional to the radial component of the magnetic field. Therefore at cutoff we can further simplify the system of equations using

$$\frac{B_i}{A_i} = \frac{D_i}{C_i} = -\gamma \quad (5.10)$$

and putting it in the $\mathcal{F}_\nu(\hat{u}r)$ function, that is now defined as:

$$\mathcal{F}_\nu(\hat{u}r) = \begin{cases} J_\nu(ur) - \gamma N_\nu(ur) & (\hat{u} \text{ real}) \\ I_\nu(ur) - \gamma K_\nu(ur) & (\hat{u} \text{ imaginary}) \end{cases} \quad (5.11)$$

Using $\mathcal{F}_\nu(\hat{u}r)$, we can then rewrite (5.9) as:

$$\begin{aligned} A_2 \left(\frac{1}{\hat{u}_1^2} - \frac{1}{\hat{u}_2^2}\right) \frac{\nu\beta}{r_1^2} [\mathcal{F}_\nu(\hat{u}_2 r_1)] \\ - C_2 k_0 \left\{ \left[\frac{\mathcal{F}'_\nu(\hat{u}_2 r_1)}{\hat{u}_2 r_1} \right] - \frac{J'_\nu(\hat{u}_1 r_1)}{(\hat{u}_1 r_1) J_\nu(\hat{u}_1 r_1)} [\mathcal{F}_\nu(\hat{u}_2 r_1)] \right\} = 0 \quad (5.12a) \end{aligned}$$

$$\begin{aligned}
& - A_2 k_0 \left\{ n_2^2 \left[\frac{\mathcal{F}'_\nu(\hat{u}_2 r_1)}{\hat{u}_2 r_1} \right] - \frac{J'_\nu(\hat{u}_1 r_1)}{(\hat{u}_1 r_1) J_\nu(\hat{u}_1 r_1)} n_1^2 \left[\mathcal{F}_\nu(\hat{u}_2 r_1) \right] \right\} \\
& \quad + C_2 \left(\frac{1}{\hat{u}_1^2} - \frac{1}{\hat{u}_2^2} \right) \frac{\nu \beta}{r_1^2} \left[\mathcal{F}_\nu(\hat{u}_2 r_1) \right] = 0 \quad (5.12b)
\end{aligned}$$

$$\begin{aligned}
& A_2 \left(\frac{1}{\hat{u}_2^2} + \frac{1}{u_3^2} \right) \frac{\nu \beta}{r_2^2} \left[\mathcal{F}_\nu(\hat{u}_2 r_2) \right] \\
& \quad + C_2 k_0 \left\{ \left[\frac{\mathcal{F}'_\nu(\hat{u}_2 r_2)}{\hat{u}_2 r_2} \right] + \frac{K'_\nu(u_3 r_2)}{(u_3 r_2) K_\nu(u_3 r_2)} \left[\mathcal{F}_\nu(\hat{u}_2 r_2) \right] \right\} = 0 \quad (5.12c)
\end{aligned}$$

$$\begin{aligned}
& A_2 k_0 \left\{ n_2^2 \left[\frac{\mathcal{F}'_\nu(\hat{u}_2 r_2)}{\hat{u}_2 r_2} \right] + \frac{K'_\nu(u_3 r_2)}{(u_3 r_2) K_\nu(u_3 r_2)} n_3^2 \left[\mathcal{F}_\nu(\hat{u}_2 r_2) \right] \right\} \\
& \quad + C_2 \left(\frac{1}{\hat{u}_2^2} + \frac{1}{u_3^2} \right) \frac{\nu \beta}{r_2^2} \left[\mathcal{F}_\nu(\hat{u}_2 r_2) \right] = 0 \quad (5.12d)
\end{aligned}$$

We can see that (5.12a) and (5.12b) are related to $r = r_1$, while (5.12c) and (5.12d) are related to $r = r_2$. We need to solve for A_2 and C_2 . Modal solutions exist when the determinant is zero for both set of equations. This leads to the following two equations:

$$\begin{aligned}
& \left[\frac{1}{(\hat{u}_1 r_1)^2} - \frac{1}{(\hat{u}_2 r_1)^2} \right]^2 \nu^2 \beta^2 \mathcal{F}_\nu^2(\hat{u}_2 r_1) = \\
& \quad k_0^2 \left[\frac{\mathcal{F}'_\nu(\hat{u}_2 r_1)}{(\hat{u}_2 r_1)} - \frac{J'_\nu(\hat{u}_1 r_1)}{(\hat{u}_1 r_1) J_\nu(\hat{u}_1 r_1)} \mathcal{F}_\nu(\hat{u}_2 r_1) \right] \\
& \quad \left[n_2^2 \frac{\mathcal{F}'_\nu(\hat{u}_2 r_1)}{(\hat{u}_2 r_1)} - n_1^2 \frac{J'_\nu(\hat{u}_1 r_1)}{(\hat{u}_1 r_1) J_\nu(\hat{u}_1 r_1)} \mathcal{F}_\nu(\hat{u}_2 r_1) \right] \quad (5.13a)
\end{aligned}$$

$$\begin{aligned}
& \left[\frac{1}{(\hat{u}_2 r_2)^2} + \frac{1}{(w r_2)^2} \right]^2 \nu^2 \beta^2 \mathcal{F}_\nu^2(\hat{u}_2 r_2) = \\
& \quad k_0^2 \left[\frac{\mathcal{F}'_\nu(\hat{u}_2 r_2)}{(\hat{u}_2 r_2)} + \frac{K'_\nu(w r_2)}{(w r_2) K_\nu(w r_2)} \mathcal{F}_\nu(\hat{u}_2 r_2) \right] \\
& \quad \left[n_2^2 \frac{\mathcal{F}'_\nu(\hat{u}_2 r_2)}{(\hat{u}_2 r_2)} + n_3^2 \frac{K'_\nu(w r_2)}{(w r_2) K_\nu(w r_2)} \mathcal{F}_\nu(\hat{u}_2 r_2) \right] \quad (5.13b)
\end{aligned}$$

Inside those two equations, two unknowns remain: the β propagation constant, and the γ constant hidden inside the $\mathcal{F}_\nu(\hat{u}r)$ function. Recall that (5.13) only is valid at cutoff, because of the definition of γ .

Substituting the asymptotic expansion (A.26) into (5.13b), it becomes similar to (4.19), and we perform the same simplifications that we did for RCF equations. After evaluation of the limit, the remaining terms are:

$$\frac{n_2^2 + n_3^2}{(\hat{u}_2 r_2)^2} \nu^2 k_0^2 \mathcal{F}_\nu^2(\hat{u}_2 r_2) = -k_0^2 (n_2^2 + n_3^2) \nu \frac{\mathcal{F}'_\nu(\hat{u}_2 r_2)}{(\hat{u}_2 r_2)} \mathcal{F}_\nu(\hat{u}_2 r_2) + k_0^2 n_3^2 \frac{\nu}{(\nu - 1)} \mathcal{F}_\nu^2(\hat{u}_2 r_2) \quad (5.14)$$

After some reorganization, (5.14) becomes

$$\mathcal{F}_\nu(\hat{u}_2 r_2) \left[(n_2^2 + n_3^2) \frac{2(\nu - 1)}{(\hat{u}_2 r_2)} \left(\mathcal{F}'_\nu(\hat{u}_2 r_2) + \frac{\nu}{(\hat{u}_2 r_2)} \mathcal{F}_\nu(\hat{u}_2 r_2) \right) - 2n_3^2 \mathcal{F}_\nu(\hat{u}_2 r_2) \right] = 0 \quad (5.15)$$

It is possible to demonstrate, using Bessel recurrence relations, that:

$$\frac{2(\nu - 1)}{(\hat{u}_2 r_2)} \left(\mathcal{F}'_\nu(\hat{u}_2 r_2) + \frac{\nu}{(\hat{u}_2 r_2)} \mathcal{F}_\nu(\hat{u}_2 r_2) \right) = \mathcal{F}_{\nu-2}(\hat{u}_2 r_2) + \text{sgn}(\hat{u}_2^2) \mathcal{F}_\nu(\hat{u}_2 r_2) \quad (5.16)$$

where sgn is the sign function. Therefore, (5.15) simplifies to:

$$\mathcal{F}_\nu(\hat{u}_2 r_2) \left[\text{sgn}(\hat{u}_2^2) \frac{n_2^2 - n_3^2}{n_2^2 + n_3^2} \mathcal{F}_\nu(\hat{u}_2 r_2) + \mathcal{F}_{\nu-2}(\hat{u}_2 r_2) \right] = 0 \quad (5.17)$$

One possible solution for (5.17) is $\mathcal{F}_\nu(\hat{u}_2 r_2) = 0$. It implies that $e_z(r_2) = 0$, and it is related to solutions for $\text{TE}_{0,m}$, $\text{TM}_{0,m}$, $\text{EH}_{\nu,m}$, and $\text{HE}_{1,m}$ modes, as well for $\text{LP}_{\ell,m}$ modes. The other possible solution for (5.17) is when the expression inside the brackets is zero, and it is related to solutions for $\text{HE}_{\nu,m}$ modes, when $\nu \geq 2$.

Using (5.13a) and (5.17), we will now deduce cutoff expressions for each kind of mode, in each possible three-layer fiber layout.

5.3.1 Cutoff of $\text{TE}_{0,m}$ and $\text{TM}_{0,m}$ modes

Having $\mathcal{F}_\nu(\hat{u}_2 r_2) = 0$ implies that

$$\gamma = \begin{cases} \frac{J_\nu(u_2 r_2)}{N_\nu(u_2 r_2)} & (\hat{u}_2 \text{ real}) \\ \frac{I_\nu(u_2 r_2)}{K_\nu(u_2 r_2)} & (\hat{u}_2 \text{ imaginary}) \end{cases} \quad (5.18)$$

With $\nu = 0$, (5.13a) becomes:

$$\left[\frac{\mathcal{F}'_0(\hat{u}_2 r_1)}{(\hat{u}_2 r_1)} + \frac{\text{sgn}(\hat{u}_1) J_1(\hat{u}_1 r_1)}{(\hat{u}_1 r_1) J_0(\hat{u}_1 r_1)} \mathcal{F}_0(\hat{u}_2 r_1) \right] \left[n_2^2 \frac{\mathcal{F}'_0(\hat{u}_2 r_1)}{(\hat{u}_2 r_1)} + n_1^2 \frac{\text{sgn}(\hat{u}_1) J_1(\hat{u}_1 r_1)}{(\hat{u}_1 r_1) J_0(\hat{u}_1 r_1)} \mathcal{F}_0(\hat{u}_2 r_1) \right] = 0 \quad (5.19)$$

The expression in the first pair of brackets is zero for TE modes, and the expression in the second pair of brackets is zero for TM modes. We can now expand (5.19) for each fiber layout (according to Fig. 5.1).

Fiber profile (a)

With this layout, \hat{u}_1 is real, and \hat{u}_2 is imaginary. Therefore, $J_\nu(\hat{u}_1 r_1) = J_\nu(u_1 r_1)$,

$$\mathcal{F}_0(\hat{u}_2 r_1) = I_0(u_2 r_1) - \frac{I_0(u_2 r_2)}{K_0(u_2 r_2)} K_0(u_2 r_1) \quad (5.20a)$$

and

$$\frac{\mathcal{F}'_\nu(\hat{u}_2 r_1)}{\hat{u}_2 r_1} = -\frac{I_1(u_2 r_1)}{u_2 r_1} - \frac{I_0(u_2 r_2)}{K_0(u_2 r_2)} \frac{K_1(u_2 r_1)}{u_2 r_1} \quad (5.20b)$$

Using Bessel recurrence relations, we have:

$$\frac{I_1(u_2 r_1)}{u_2 r_1} = \frac{1}{2} [I_0(u_2 r_1) - I_2(u_2 r_1)] \quad (5.21a)$$

$$\frac{K_1(u_2 r_1)}{u_2 r_1} = \frac{1}{2} [K_2(u_2 r_1) - K_0(u_2 r_1)] \quad (5.21b)$$

$$\frac{J_1(u_1 r_1)}{u_1 r_1 J_0(u_1 r_1)} = \frac{1}{2} \left[\frac{J_2(u_1 r_1)}{J_0(u_1 r_1)} + 1 \right] \quad (5.21c)$$

The expression for $\text{TE}_{0,m}$ modes becomes:

$$-\frac{I_1(u_2 r_1)}{u_2 r_1} - \frac{I_0(u_2 r_2)}{K_0(u_2 r_2)} \frac{K_1(u_2 r_1)}{u_2 r_1} + \frac{J_1(\hat{u}_1 r_1)}{(\hat{u}_1 r_1) J_0(\hat{u}_1 r_1)} \left[I_0(u_2 r_1) - \frac{I_0(u_2 r_2)}{K_0(u_2 r_2)} K_0(u_2 r_1) \right] = 0$$

$$- [I_0(u_2 r_1) - I_2(u_2 r_1)] - \frac{I_0(u_2 r_2)}{K_0(u_2 r_2)} [K_2(u_2 r_1) - K_0(u_2 r_1)] + \left[\frac{J_2(u_1 r_1)}{J_0(u_1 r_1)} + 1 \right] \left[I_0(u_2 r_1) - \frac{I_0(u_2 r_2)}{K_0(u_2 r_2)} K_0(u_2 r_1) \right] = 0$$

$$J_0(u_1 r_1) [K_2(u_2 r_1) I_0(u_2 r_2) - I_2(u_2 r_1) K_0(u_2 r_2)] - J_2(u_1 r_1) [I_0(u_2 r_1) K_0(u_2 r_2) - K_0(u_2 r_1) I_0(u_2 r_2)] = 0 \quad (5.22)$$

Similarly, for $\text{TM}_{0,m}$ modes:

$$-\frac{n_2^2}{u_2 r_1} \left[I_1(u_2 r_1) + \frac{I_0(u_2 r_2)}{K_0(u_2 r_2)} K_1(u_2 r_1) \right] + n_1^2 \frac{J_1(u_1 r_1)}{u_1 r_1 J_0(u_1 r_1)} \left[I_0(u_2 r_1) - \frac{I_0(u_2 r_2)}{K_0(u_2 r_2)} K_0(u_2 r_1) \right] = 0$$

$$\frac{J_0(u_1 r_1)}{u_2 r_1} n_2^2 [I_1(u_2 r_1) K_0(u_2 r_2) + K_1(u_2 r_1) I_0(u_2 r_2)] - \frac{J_1(u_1 r_1)}{u_1 r_1} n_1^2 [I_0(u_2 r_1) K_0(u_2 r_2) - K_0(u_1 r_2) I_0(u_2 r_2)] = 0 \quad (5.23)$$

Fiber profiles (b) and (d)

Fiber profile (b) and (d) are similar at cutoff, because in both cases, \hat{u}_1 and \hat{u}_2 are real. Therefore:

$$\mathcal{F}_0(\hat{u}_2 r_1) = J_0(u_2 r_1) - \frac{J_0(u_2 r_2)}{N_0(u_2 r_2)} N_0(u_2 r_1) \quad (5.24a)$$

and

$$\frac{\mathcal{F}'_\nu(\hat{u}_2 r_1)}{\hat{u}_2 r_1} = -\frac{J_1(u_2 r_1)}{u_2 r_1} + \frac{J_0(u_2 r_2)}{N_0(u_2 r_2)} \frac{N_1(u_2 r_1)}{u_2 r_1} \quad (5.24b)$$

Using Bessel recurrence relations, we have:

$$\frac{J_1(u_2 r_1)}{u_2 r_1} = \frac{1}{2} [J_0(u_2 r_1) + J_2(u_2 r_1)] \quad (5.25a)$$

$$\frac{N_1(u_2 r_1)}{u_2 r_1} = \frac{1}{2} [N_0(u_2 r_1) + N_2(u_2 r_1)] \quad (5.25b)$$

The expression for TE_{0,m} modes becomes:

$$\begin{aligned} & -\frac{J_1(u_2 r_1)}{u_2 r_1} + \frac{J_0(u_2 r_2)}{N_0(u_2 r_2)} \frac{N_1(u_2 r_1)}{u_2 r_1} + \frac{J_1(\hat{u}_1 r_1)}{(\hat{u}_1 r_1) J_0(\hat{u}_1 r_1)} \left[J_0(u_2 r_1) - \frac{J_0(u_2 r_2)}{N_0(u_2 r_2)} N_0(u_2 r_1) \right] = 0 \\ & - [J_0(u_2 r_1) + J_2(u_2 r_1)] + \frac{J_0(u_2 r_2)}{N_0(u_2 r_2)} [N_0(u_2 r_1) + N_2(u_2 r_1)] + \\ & \quad \left[\frac{J_2(u_1 r_1)}{J_0(u_1 r_1)} + 1 \right] \left[J_0(u_2 r_1) - \frac{J_0(u_2 r_2)}{N_0(u_2 r_2)} N_0(u_2 r_1) \right] = 0 \\ & J_0(u_1 r_1) [N_2(u_2 r_1) J_0(u_2 r_2) - J_2(u_2 r_1) N_0(u_2 r_2)] + \\ & \quad J_2(u_1 r_1) [J_0(u_2 r_1) N_0(u_2 r_2) - N_0(u_2 r_1) J_0(u_2 r_2)] = 0 \quad (5.26) \end{aligned}$$

Similarly, for TM_{0,m} modes:

$$\begin{aligned} & n_2^2 \frac{1}{u_2 r_1} \left[-J_1(u_2 r_1) + \frac{J_0(u_2 r_2)}{N_0(u_2 r_2)} N_1(u_2 r_1) \right] + \\ & \quad n_1^2 \frac{J_1(u_1 r_1)}{u_1 r_1 J_0(u_1 r_1)} \left[J_0(u_2 r_1) - \frac{J_0(u_2 r_2)}{N_0(u_2 r_2)} N_0(u_2 r_1) \right] = 0 \\ & \frac{J_0(u_1 r_1)}{u_2 r_1} n_2^2 [J_1(u_2 r_1) N_0(u_2 r_2) - N_1(u_2 r_1) J_0(u_2 r_2)] - \\ & \quad \frac{J_1(u_1 r_1)}{u_1 r_1} n_1^2 [J_0(u_2 r_1) N_0(u_2 r_2) - N_0(u_1 r_2) J_0(u_2 r_2)] = 0 \quad (5.27) \end{aligned}$$

Fiber profile (c)

With this layout, \hat{u}_1 is imaginary, and \hat{u}_2 is real. Therefore, $J_\nu(\hat{u}_1 r_1) = I_\nu(u_1 r_1)$, and $\mathcal{F}_0(\hat{u}_2 r_1)$ and $\mathcal{F}'_0(\hat{u}_2 r_1)$ are given respectively by (5.24a) and (5.24b).

Using Bessel recurrence relations, we have:

$$\frac{I_1(u_1 r_1)}{u_1 r_1 I_0(u_1 r_1)} = \frac{1}{2} \left[-\frac{I_2(u_1 r_1)}{I_0(u_1 r_1)} + 1 \right] \quad (5.28)$$

The expression for TE_{0,m} modes becomes:

$$\begin{aligned}
& -\frac{J_1(u_2r_1)}{u_2r_1} + \frac{J_0(u_2r_2)}{N_0(u_2r_2)} \frac{N_1(u_2r_1)}{u_2r_1} + \frac{I_1(\hat{u}_1r_1)}{(\hat{u}_1r_1)I_0(\hat{u}_1r_1)} \left[J_0(u_2r_1) - \frac{J_0(u_2r_2)}{N_0(u_2r_2)} N_0(u_2r_1) \right] = 0 \\
& - [J_0(u_2r_1) + J_2(u_2r_1)] + \frac{J_0(u_2r_2)}{N_0(u_2r_2)} [N_0(u_2r_1) + N_2(u_2r_1)] + \\
& \quad \left[-\frac{I_2(u_1r_1)}{I_0(u_1r_1)} + 1 \right] \left[J_0(u_2r_1) - \frac{J_0(u_2r_2)}{N_0(u_2r_2)} N_0(u_2r_1) \right] = 0 \\
& I_0(u_1r_1) [N_2(u_2r_1)J_0(u_2r_2) - J_2(u_2r_1)N_0(u_2r_2)] - \\
& \quad I_2(u_1r_1) [J_0(u_2r_1)N_0(u_2r_2) - N_0(u_2r_1)J_0(u_2r_2)] = 0 \quad (5.29)
\end{aligned}$$

Similarly, for TM_{0,m} modes:

$$\begin{aligned}
& n_2^2 \frac{1}{u_2r_1} \left[-J_1(u_2r_1) + \frac{J_0(u_2r_2)}{N_0(u_2r_2)} N_1(u_2r_1) \right] + \\
& \quad n_1^2 \frac{I_1(u_1r_1)}{u_1r_1 I_0(u_1r_1)} \left[J_0(u_2r_1) - \frac{J_0(u_2r_2)}{N_0(u_2r_2)} N_0(u_2r_1) \right] = 0 \\
& \frac{I_0(u_1r_1)}{u_2r_1} n_2^2 [J_1(u_2r_1)N_0(u_2r_2) - N_1(u_2r_1)J_0(u_2r_2)] - \\
& \quad \frac{I_1(u_1r_1)}{u_1r_1} n_1^2 [J_0(u_2r_1)N_0(u_2r_2) - N_0(u_1r_2)J_0(u_2r_2)] = 0 \quad (5.30)
\end{aligned}$$

5.3.2 Cutoff of EH_{ν,m} and HE_{1,m} modes

We rewrite (5.13a) as a quadratic equation:

$$\left[\frac{\mathcal{F}'_\nu(\hat{u}_2r_1)}{(\hat{u}_2r_1)} \right]^2 + \kappa_1 \frac{\mathcal{F}'_\nu(\hat{u}_2r_1)}{(\hat{u}_2r_1)} \mathcal{F}_\nu(\hat{u}_2r_1) + \kappa_2 [\mathcal{F}_\nu(\hat{u}_2r_1)]^2 = 0 \quad (5.31)$$

where

$$\kappa_1 = -\frac{n_1^2 + n_2^2}{n_2^2} \left[\frac{J'_\nu(\hat{u}_1r_1)}{(\hat{u}_1r_1)J_\nu(\hat{u}_1r_1)} \right] \quad (5.32)$$

$$\begin{aligned}
\kappa_2 = & \frac{n_1^2}{n_2^2} \left[\frac{J'_\nu(\hat{u}_1r_1)}{(\hat{u}_1r_1)J_\nu(\hat{u}_1r_1)} \right]^2 - \\
& \nu^2 \frac{n_3^3}{n_2^2} \left[\frac{1}{(\hat{u}_1r_1)^2} - \frac{1}{(\hat{u}_2r_1)^2} \right]^2 \quad (5.33)
\end{aligned}$$

Roots of (5.31) are given by

$$\frac{\mathcal{F}'_\nu(\hat{u}_2r_1)}{(\hat{u}_2r_1)} = \frac{1}{2} \left[-\kappa_1 \pm \sqrt{\kappa_1^2 - 4\kappa_2} \right] \mathcal{F}_\nu(\hat{u}_2r_1) \quad (5.34)$$

The sign in (5.34) can be + or -, depending on whether we are looking for EH or for HE modes, and also depending on the type of fiber profile. We used numerical simulations to determine whether it should be + or -. Expanding the $\mathcal{F}_\nu(\hat{u}_2 r_1)$ functions in (5.34) using the γ value from (5.18), we obtain the cutoff equations for each fiber profile.

When \hat{u}_2 is real, (5.34) expands to:

$$\begin{aligned} \frac{1}{u_2 r_1} \left[J'_\nu(u_2 r_1) - \frac{J_\nu(u_2 r_2)}{N_\nu(u_2 r_2)} N'_\nu(u_2 r_1) \right] &= \\ \frac{1}{2} \left[-\kappa_1 \pm \sqrt{\kappa_1^2 - 4\kappa_2} \right] \left[J_\nu(u_2 r_1) - \frac{J_\nu(u_2 r_2)}{N_\nu(u_2 r_2)} N_\nu(u_2 r_1) \right] & \\ \frac{1}{u_2 r_1} \left[\frac{\nu}{u_2 r_1} J_\nu(u_2 r_1) - J_{\nu+1}(u_2 r_1) - \frac{J_\nu(u_2 r_2)}{N_\nu(u_2 r_2)} \left(\frac{\nu}{u_2 r_1} N_\nu(u_2 r_1) - N_{\nu+1}(u_2 r_1) \right) \right] &= \\ \frac{1}{2} \left[-\kappa_1 \pm \sqrt{\kappa_1^2 - 4\kappa_2} \right] \left[J_\nu(u_2 r_1) - \frac{J_\nu(u_2 r_2)}{N_\nu(u_2 r_2)} N_\nu(u_2 r_1) \right] & \\ J_{\nu+1}(u_2 r_1) N_\nu(u_2 r_2) - N_{\nu+1}(u_2 r_1) J_\nu(u_2 r_2) &= \\ \Delta^\pm [J_\nu(u_2 r_1) N_\nu(u_2 r_2) - N_\nu(u_2 r_1) J_\nu(u_2 r_2)] & \quad (5.35) \end{aligned}$$

where:

$$\Delta^\pm = u_2 r_1 \left[\frac{\nu}{(u_2 r_1)^2} + \frac{\kappa_1 \pm \sqrt{\kappa_1^2 - 4\kappa_2}}{2} \right] \quad (5.36)$$

Similarly, when \hat{u}_2 is imaginary, (5.34) expands to:

$$\begin{aligned} -\frac{1}{u_2 r_1} \left[I'_\nu(u_2 r_1) - \frac{I_\nu(u_2 r_2)}{K_\nu(u_2 r_2)} K'_\nu(u_2 r_1) \right] &= \\ \frac{1}{2} \left[-\kappa_1 \pm \sqrt{\kappa_1^2 - 4\kappa_2} \right] \left[I_\nu(u_2 r_1) - \frac{I_\nu(u_2 r_2)}{K_\nu(u_2 r_2)} K_\nu(u_2 r_1) \right] & \\ -\frac{1}{u_2 r_1} \left[\frac{\nu}{u_2 r_1} I_\nu(u_2 r_1) + I_{\nu+1}(u_2 r_1) - \frac{I_\nu(u_2 r_2)}{K_\nu(u_2 r_2)} \left(\frac{\nu}{u_2 r_1} K_\nu(u_2 r_1) - K_{\nu+1}(u_2 r_1) \right) \right] &= \\ \frac{1}{2} \left[-\kappa_1 \pm \sqrt{\kappa_1^2 - 4\kappa_2} \right] \left[I_\nu(u_2 r_1) - \frac{I_\nu(u_2 r_2)}{K_\nu(u_2 r_2)} K_\nu(u_2 r_1) \right] & \\ I_{\nu+1}(u_2 r_1) K_\nu(u_2 r_2) + K_{\nu+1}(u_2 r_1) I_\nu(u_2 r_2) &= \\ \Delta^\pm [-I_\nu(u_2 r_1) K_\nu(u_2 r_2) + K_\nu(u_2 r_1) I_\nu(u_2 r_2)] & \quad (5.37) \end{aligned}$$

Fiber profile (a)

With this layout, \hat{u}_1 is real, and \hat{u}_2 is imaginary. Therefore, (5.34) expands to (5.37). Δ^- is associated with solutions to EH $_{\nu,m}$ modes, and Δ^+ is associated with solutions to HE $_{1,m}$ modes.

Fiber profile (b)

With this layout, both \hat{u}_1 and \hat{u}_2 are real. Therefore, (5.34) expands to (5.35). Δ^+ is associated with solutions to $\text{EH}_{\nu,m}$ modes, and Δ^- is associated with solutions to $\text{HE}_{1,m}$ modes.

Fiber profile (c)

With this layout, \hat{u}_1 is imaginary, and \hat{u}_2 is real. Therefore, (5.34) expands to (5.35). Δ^- is associated with solutions to $\text{EH}_{\nu,m}$ modes, and Δ^+ is associated with solutions to $\text{HE}_{1,m}$ modes.

Fiber profile (d)

With this layout, both \hat{u}_1 and \hat{u}_2 are real. Therefore, (5.34) expands to (5.35). Δ^+ is associated with solutions to $\text{EH}_{\nu,m}$ modes, and Δ^- is associated with solutions to $\text{HE}_{1,m}$ modes.

5.3.3 Cutoff of $\text{HE}_{\nu,m}$ modes

For HE modes (with $\nu \geq 2$), $e_z(r_1) = 0$. We get the value of γ from (5.34):

$$J'_\nu(\hat{u}_2 r_1) - \gamma N'_\nu(\hat{u}_2 r_1) = \frac{\hat{u}_2 r_1}{2} \left[-\kappa_1 \pm \sqrt{\kappa_1^2 - 4\kappa_2} \right] [J_\nu(\hat{u}_2 r_1) - \gamma N_\nu(\hat{u}_2 r_1)] \quad (5.38)$$

We expand the derivatives:

$$\begin{aligned} \frac{\nu}{\hat{u}_2 r_1} J_\nu(\hat{u}_2 r_1) - \text{sgn}(\hat{u}_2^2) J_{\nu+1}(\hat{u}_2 r_1) - \gamma \left[\frac{\nu}{\hat{u}_2 r_1} N_\nu(\hat{u}_2 r_1) - N_{\nu+1}(\hat{u}_2 r_1) \right] = \\ \frac{\hat{u}_2 r_1}{2} \left[-\kappa_1 \pm \sqrt{\kappa_1^2 - 4\kappa_2} \right] [J_\nu(\hat{u}_2 r_1) - \gamma N_\nu(\hat{u}_2 r_1)] \end{aligned} \quad (5.39)$$

and apply the recurrence relations:

$$\Delta^\pm J_\nu(\hat{u}_2 r_1) - \text{sgn}(\hat{u}_2^2) J_{\nu+1}(\hat{u}_2 r_1) = \gamma [\Delta^\pm N_\nu(\hat{u}_2 r_1) - N_{\nu+1}(\hat{u}_2 r_1)] \quad (5.40)$$

to obtain:

$$\gamma = \begin{cases} \frac{J_\nu(u_2 r_1) \Delta^\pm - J_{\nu+1}(u_2 r_1)}{N_\nu(u_2 r_1) \Delta^\pm - N_{\nu+1}(u_2 r_1)} & (\hat{u}_2 \text{ real}) \\ \frac{I_\nu(u_2 r_1) \Delta^\pm + I_{\nu+1}(u_2 r_1)}{K_\nu(u_2 r_1) \Delta^\pm - K_{\nu+1}(u_2 r_1)} & (\hat{u}_2 \text{ imaginary}) \end{cases} \quad (5.41)$$

From (5.17) we know that

$$\text{sgn}(\hat{u}_2^2) \frac{n_2^2 - n_3^2}{n_2^2 + n_3^2} \mathcal{F}_\nu(\hat{u}_2 r_2) + \mathcal{F}_{\nu-2}(\hat{u}_2 r_2) = 0 \quad (5.42)$$

Putting (5.41) into (5.42), we obtain cutoffs for $\text{HE}_{\nu,m}$ modes when $\nu \geq 2$. Numerical experiments tell us that sign in Δ^\pm must be + for fiber profiles (a), (b), and (c); it is - for fiber profile (d).

5.3.4 Cutoff of LP _{ℓ,m} modes

The weakly guiding approximation implies that $n_1^2/n_3^2 \approx n_2^2/n_3^2 \approx 1$. Under this approximation, we can simplify (5.13a) to:

$$\pm \left[\frac{1}{(\hat{u}_1 r_1)^2} - \frac{1}{(\hat{u}_2 r_1)^2} \right] (\ell - 1) \mathcal{F}_{\ell-1}(\hat{u}_2 r_1) = \frac{\mathcal{F}'_{\ell-1}(\hat{u}_2 r_1)}{(\hat{u}_2 r_1)} - \frac{J'_{\ell-1}(\hat{u}_1 r_1)}{(\hat{u}_1 r_1) J_{\ell-1}(\hat{u}_1 r_1)} \mathcal{F}_{\ell-1}(\hat{u}_2 r_1) \quad (5.43)$$

where $\ell = \nu + 1$, for LP _{ℓ,m} modes.

By choosing the negative sign, the left-hand side of the equation cancels out with terms in the right hand-side (after expansion of the derivative of the Bessel functions). Remaining terms are:

$$\frac{J_{\ell-1}(\hat{u}_1 r_1)}{(\hat{u}_2 r_1)} \mathcal{F}_{\ell}(\hat{u}_2 r_1) = \frac{J_{\ell}(\hat{u}_1 r_1)}{(\hat{u}_1 r_1)} \mathcal{F}_{\ell-1}(\hat{u}_2 r_1) \quad (5.44)$$

We expand $\mathcal{F}_{\ell}(\hat{u}_2 r_1)$ for each fiber profile, using γ from (5.18), to get cutoffs of LP modes.

Cutoff expressions for all fiber profiles are summarized in Tables 5.1—5.4.

5.4 Numerical validation

To validate our expressions, we use the same methodology as that in Chapter 4. For each profile, we calculate the normalized propagation constant as a function of normalized frequency, and ensure the value of V given by our analytical expressions is close to the V value obtained by extrapolating numerically obtained modal solutions near the cutoff of each mode. We also ensure that the mode order, given by (3.1), is respected. Each test profile is identified by a letter corresponding to the illustration in Fig. 5.1. Fiber dimensions and refractive indexes are summarized in Table 5.5. We deliberately choose unrealistic parameters in order to get a reasonable number of modes; parameters were also chosen to assure a large separation between the modes, to clearly see the different cutoff frequencies.

For multilayer fibers, the normalized propagation constant is defined as:

$$b = \frac{n_{\text{eff}}^2 - n_{\text{cl}}^2}{n_{\text{max}}^2 - n_{\text{cl}}^2} \quad (5.45)$$

where $n_{\text{cl}} = n_3$ in the case of 3LSIF. Simulation results are shown on Fig. 5.2—5.5.

5.5 Continuity between fiber profiles

By varying n_1 and n_2 parameters, it is possible to go through the different kinds of fiber profiles. Furthermore, there should be a continuity in the cutoff when we vary the index to go from one kind of fiber profile to another kind of fiber profile. One way to verify this would be

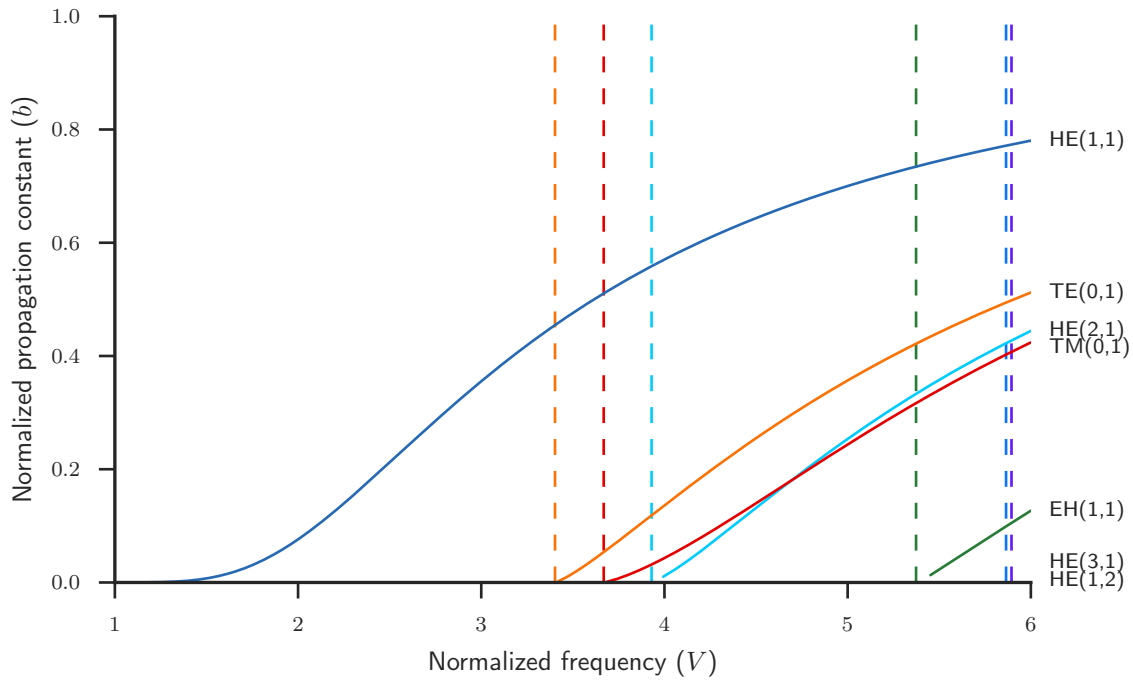


Figure 5.2: Cutoffs of first modes for fiber profile (a). Simulation parameters: $r_1 = 3 \mu\text{m}$, $r_2 = 4 \mu\text{m}$, $n_1 = 2.0$, $n_2 = 1.3$, $n_3 = 1.45$.

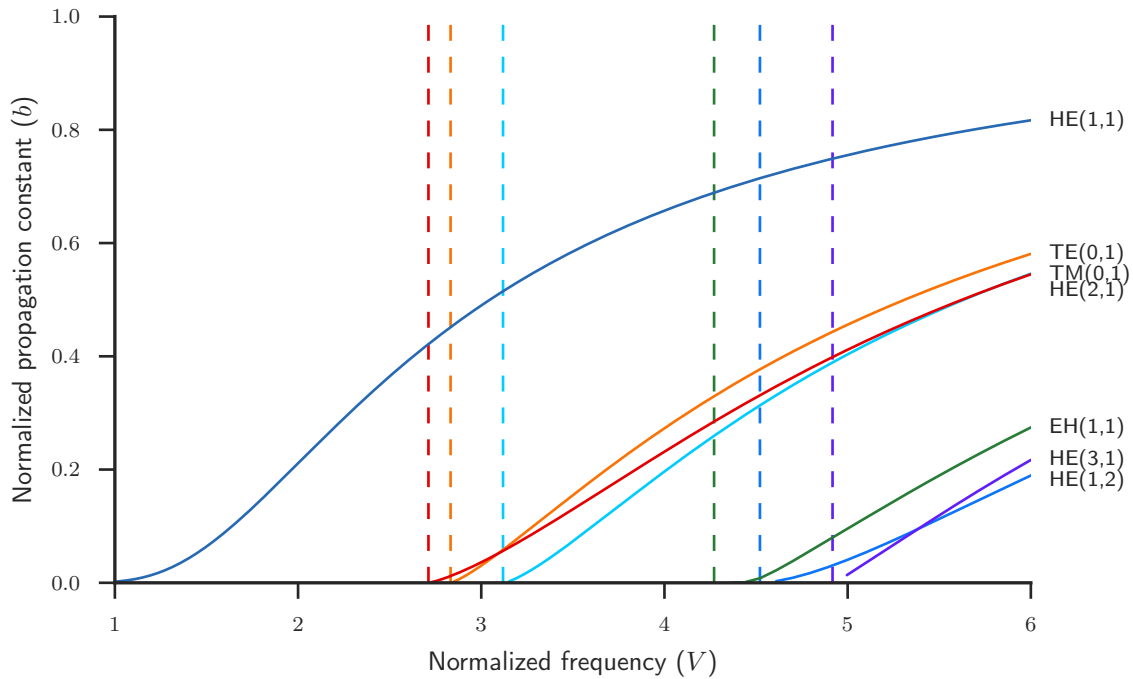


Figure 5.3: Cutoffs of first modes for fiber profile (b). Simulation parameters: $r_1 = 3 \mu\text{m}$, $r_2 = 4 \mu\text{m}$, $n_1 = 2.0$, $n_2 = 1.7$, $n_3 = 1.45$.

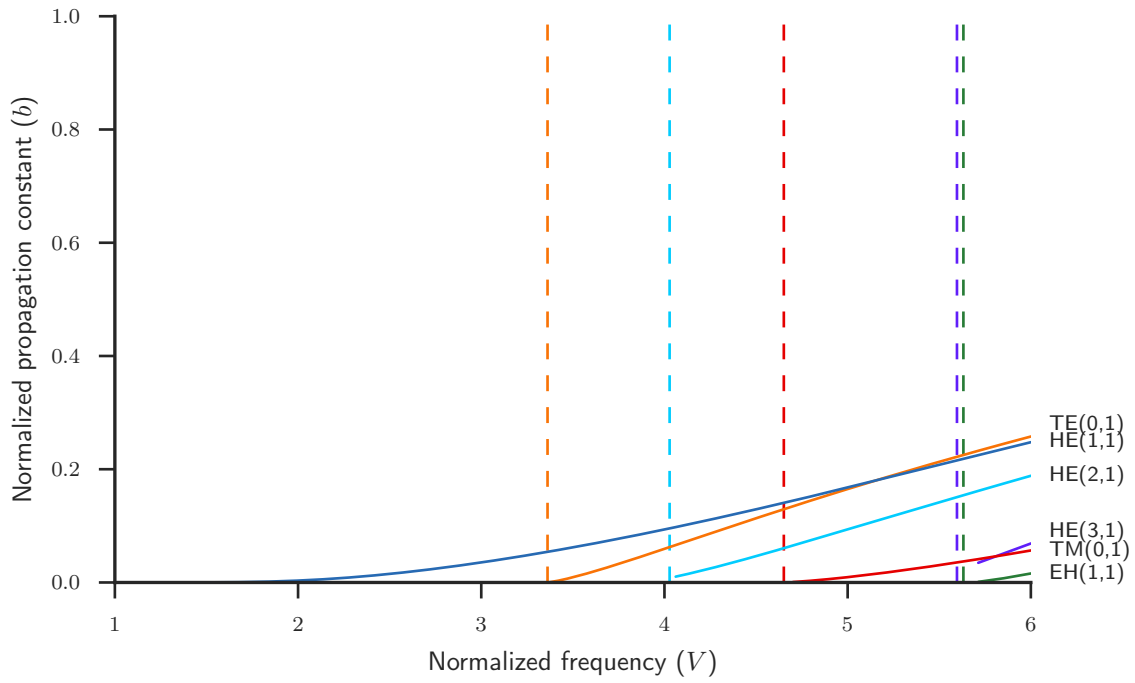


Figure 5.4: Cutoffs of first modes for fiber profile (c). Simulation parameters: $r_1 = 3 \mu\text{m}$, $r_2 = 4 \mu\text{m}$, $n_1 = 1.3$, $n_2 = 2.0$, $n_3 = 1.45$.

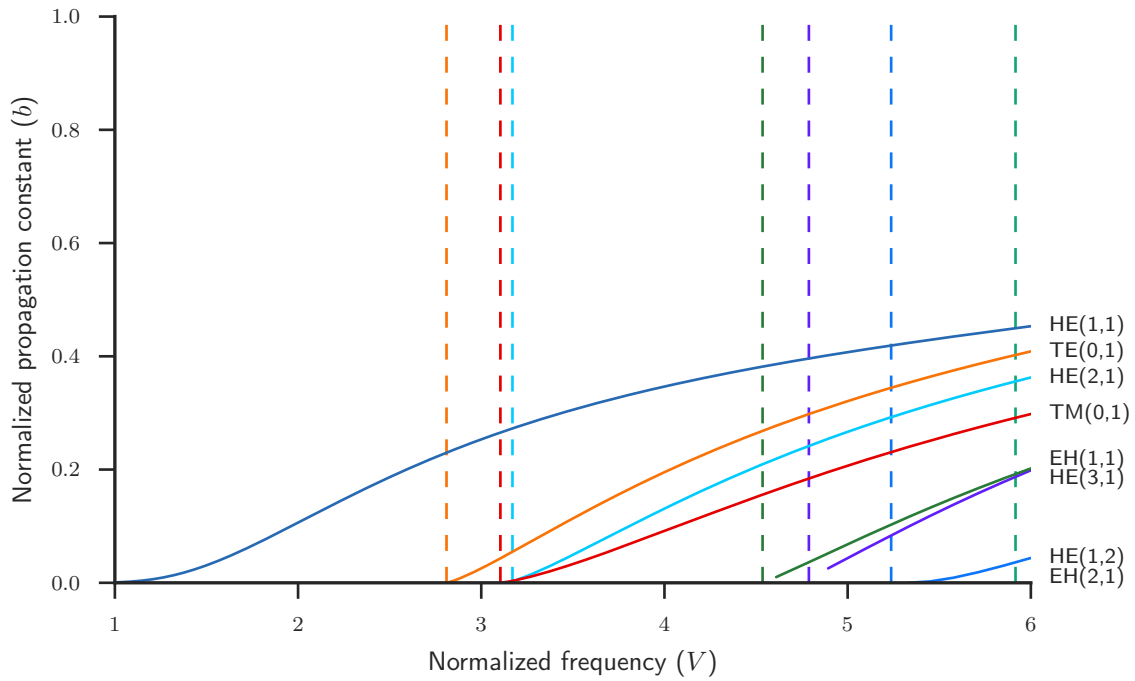


Figure 5.5: Cutoffs of first modes for fiber profile (d). Simulation parameters: $r_1 = 3 \mu\text{m}$, $r_2 = 4 \mu\text{m}$, $n_1 = 1.7$, $n_2 = 2.0$, $n_3 = 1.45$.

Table 5.1: Cutoff equations for fiber profile (a) (W-type fiber)

$\text{TE}_{0,m}$	$J_0(u_1 r_1) [K_2(u_2 r_1) I_0(u_2 r_2) - I_2(u_2 r_1) K_0(u_2 r_2)] =$ $J_2(u_1 r_1) [I_0(u_2 r_1) K_0(u_2 r_2) - K_0(u_2 r_1) I_0(u_2 r_2)]$
$\text{TM}_{0,m}$	$\frac{J_0(u_1 r_1)}{u_2 r_1} n_2^2 [I_1(u_2 r_1) K_0(u_2 r_2) + K_1(u_2 r_1) I_0(u_2 r_2)] =$ $\frac{J_1(u_1 r_1)}{u_1 r_1} n_1^2 [I_0(u_2 r_1) K_0(u_2 r_2) - K_0(u_2 r_1) I_0(u_2 r_2)]$
$\text{EH}_{\nu,m}$	$I_{\nu+1}(u_2 r_1) K_\nu(u_2 r_2) + K_{\nu+1}(u_2 r_1) I_\nu(u_2 r_2) =$ $[-I_\nu(u_2 r_1) K_\nu(u_2 r_2) + K_\nu(u_2 r_1) I_\nu(u_2 r_2)] \Delta^-$
$\text{HE}_{1,m}$	$I_2(u_2 r_1) K_1(u_2 r_2) + K_2(u_2 r_1) I_1(u_2 r_2) =$ $[-I_1(u_2 r_1) K_1(u_2 r_2) + K_1(u_2 r_1) I_1(u_2 r_2)] \Delta^+$
$\text{HE}_{\nu,m}$	$I_{\nu-2}(u_2 r_2) - \gamma K_{\nu-2}(u_2 r_2) =$ $\frac{n_2^2 - n_3^2}{n_3^2 + n_2^2} [I_\nu(u_2 r_2) - \gamma K_\nu(u_2 r_2)] \quad \gamma = \frac{I_\nu(u_2 r_1) \Delta^+ + I_{\nu+1}(u_2 r_1)}{K_\nu(u_2 r_1) \Delta^+ - K_{\nu+1}(u_2 r_1)}$
$\text{LP}_{\ell,m}$	$\frac{J_{\ell-1}(u_1 r_1)}{u_2 r_1} [I_\ell(u_2 r_1) K_{\ell-1}(u_2 r_2) + K_\ell(u_2 r_1) I_{\ell-1}(u_2 r_2)] =$ $\frac{J_\ell(u_1 r_1)}{u_1 r_1} [I_{\ell-1}(u_2 r_1) K_{\ell-1}(u_2 r_2) - K_{\ell-1}(u_2 r_1) I_{\ell-1}(u_2 r_2)]$

to show that cutoff expressions transform to known forms when we evaluate limits on given parameters. For example, we could show that expressions for fiber profile (d) transform to expressions for RCF when $n_1 \rightarrow n_3$.

However, performing such rigorous proofs would be tedious. We will rather prove the continuity of the expressions by fixing two refractive indexes in a fiber profile, and varying the third to go through the different profiles. By plotting the cutoff frequency as a function of that varying index, we will show that the obtained cutoff is continuous as we reach limits between the different profiles.

There are two possible simulation to run: one with n_1 fixed and n_2 varying, and the other for n_2 fixed and n_1 varying. In both cases, we will simulate a fiber with $r_1 = 4 \mu\text{m}$ and $r_2 = 6 \mu\text{m}$. The cladding will be $n_3 = 1.4$, the fixed index will be 1.6, and the other index will vary between 1.2 and 1.8.

Table 5.2: Cutoff equations for fiber profile (b)

TE _{0,m}	$J_0(u_1r_1) [J_2(u_2r_1)N_0(u_2r_2) - N_2(u_2r_1)J_0(u_2r_2)] =$ $J_2(u_1r_1) [J_0(u_2r_1)N_0(u_2r_2) - N_0(u_2r_1)J_0(u_2r_2)]$
TM _{0,m}	$\frac{J_0(u_1r_1)}{u_2r_1} n_2^2 [J_1(u_2r_1)N_0(u_2r_2) - N_1(u_2r_1)J_0(u_2r_2)] =$ $\frac{J_1(u_1r_1)}{u_1r_1} n_1^2 [J_0(u_2r_1)N_0(u_2r_2) - N_0(u_2r_1)J_0(u_2r_2)]$
EH _{ν,m}	$J_{ν+1}(u_2r_1)N_ν(u_2r_2) - N_{ν+1}(u_2r_1)J_ν(u_2r_2) =$ $[J_ν(u_2r_1)N_ν(u_2r_2) - N_ν(u_2r_1)J_ν(u_2r_2)] \Delta^+$
HE _{1,m}	$J_2(u_2r_1)N_1(u_2r_2) - N_2(u_2r_1)J_1(u_2r_2) =$ $[J_1(u_2r_1)N_1(u_2r_2) - N_1(u_2r_1)J_1(u_2r_2)] \Delta^-$
HE _{ν,m}	$J_{ν-2}(u_2r_2) - \gamma N_{ν-2}(u_2r_2) =$ $\frac{n_3^2 - n_2^2}{n_3^2 + n_2^2} [J_ν(u_2r_2) - \gamma N_ν(u_2r_2)] \quad \gamma = \frac{J_ν(u_2r_1)\Delta^+ - J_{ν+1}(u_2r_1)}{N_ν(u_2r_1)\Delta^+ - N_{ν+1}(u_2r_1)}$
LP _{ℓ,m}	$\frac{J_{ℓ-1}(u_1r_1)}{u_2r_1} [J_ℓ(u_2r_1)N_{ℓ-1}(u_2r_2) - N_ℓ(u_2r_1)J_{ℓ-1}(u_2r_2)] =$ $\frac{J_ℓ(u_1r_1)}{u_1r_1} [J_{ℓ-1}(u_2r_1)N_{ℓ-1}(u_2r_2) - N_{ℓ-1}(u_2r_1)J_{ℓ-1}(u_2r_2)]$

When n_2 is fixed

We fix n_2 , and vary n_1 from lower to higher index, we successively go through fiber profiles (c), (e), (d), SSIF, and (b). Results are shown on Fig. 5.6.

We can divide this graph into five different regions. When $n_1 < n_3$, we have a fiber profile of type (c). At $n_1 = n_3 = 1.4$, we have a ring-core fiber profile (type (e)). When n_1 is between n_3 and n_2 , we have a fiber profile of type (d). When $n_1 = n_2 = 1.6$, we have a simple single-core step-index profile. Finally, when $n_1 > n_2$, we have a fiber profile of type (b). To generate this plot, we defined V as $k_0r_2\sqrt{n_2^2 - n_3^2}$. This is needed in order to maintain one definition of V across the different fiber types.

Many observations can be made from this figure. First, since the cutoff values for each of the five regions are obtained using different equations, the continuity of each line confirms the continuity of each function; each fiber profile approaches the next type.

At $n_1 = n_2 = 1.6$, we have a standard fiber. As expected, cutoff of the TE_{0,1} mode is at 2.405

Table 5.3: Cutoff equations for fiber profile (c)

$\text{TE}_{0,m}$	$I_0(u_1 r_1) [N_2(u_2 r_1) J_0(u_2 r_2) - J_2(u_2 r_1) N_0(u_2 r_2)] =$ $I_2(u_1 r_1) [J_0(u_2 r_1) N_0(u_2 r_2) - N_0(u_2 r_1) J_0(u_2 r_2)]$
$\text{TM}_{0,m}$	$\frac{I_0(u_1 r_1)}{u_2 r_1} n_2^2 [J_1(u_2 r_1) N_0(u_2 r_2) - N_1(u_2 r_1) J_0(u_2 r_2)] =$ $\frac{I_1(u_1 r_1)}{u_1 r_1} n_1^2 [J_0(u_2 r_1) N_0(u_2 r_2) - N_0(u_2 r_1) J_0(u_2 r_2)]$
$\text{EH}_{\nu,m}$	$J_{\nu+1}(u_2 r_1) N_\nu(u_2 r_2) - N_{\nu+1}(u_2 r_1) J_\nu(u_2 r_2) =$ $[J_\nu(u_2 r_1) N_\nu(u_2 r_2) - N_\nu(u_2 r_1) J_\nu(u_2 r_2)] \Delta^-$
$\text{HE}_{1,m}$	$J_2(u_2 r_1) N_1(u_2 r_2) - N_2(u_2 r_1) J_1(u_2 r_2) =$ $[J_1(u_2 r_1) N_1(u_2 r_2) - N_1(u_2 r_1) J_1(u_2 r_2)] \Delta^+$
$\text{HE}_{\nu,m}$	$J_{\nu-2}(u_2 r_2) - \gamma N_{\nu-2}(u_2 r_2) =$ $\frac{n_3^2 - n_2^2}{n_3^2 + n_2^2} [J_\nu(u_2 r_2) - \gamma N_\nu(u_2 r_2)] \quad \gamma = \frac{J_\nu(u_2 r_1) \Delta^+ - J_{\nu+1}(u_2 r_1)}{N_\nu(u_2 r_1) \Delta^+ - N_{\nu+1}(u_2 r_1)}$
$\text{LP}_{\ell,m}$	$\frac{I_{\ell-1}(u_1 r_1)}{u_2 r_1} [J_\ell(u_2 r_1) N_{\ell-1}(u_2 r_2) - N_\ell(u_2 r_1) J_{\ell-1}(u_2 r_2)] =$ $\frac{I_\ell(u_1 r_1)}{u_1 r_1} [J_{\ell-1}(u_2 r_1) N_{\ell-1}(u_2 r_2) - N_{\ell-1}(u_2 r_1) J_{\ell-1}(u_2 r_2)]$

and cutoff of the $\text{EH}_{1,1}$ is at 3.832, the first roots of $J_0(x)$ and $J_1(x)$, as given in Table 1.2. We also see that at this value, $\text{TE}_{0,1}$ and $\text{TM}_{0,1}$ modes have the same cutoff. This crossing between TE and TM modes is possible, even if both modes are $\nu = 0$, because there is no ordering condition between TE and TM modes. However, we can conclude that, for fibers of type (c), (d), and (e), $\text{TE}_{0,m} > \text{TM}_{0,m}$ (in terms of n_{eff}), while $\text{TE}_{0,m} < \text{TM}_{0,m}$ for fibers of type (b). Modes $\text{EH}_{1,1}$ and $\text{HE}_{1,2}$ also have the same cutoff as they do in standard fibers (as it is the case for all $\text{EH}_{1,m}$ and $\text{HE}_{1,m+1}$ modes). However, they do not cross, because we need to maintain the relation $\text{HE}_{\nu,m} > \text{EH}_{\nu,m} > \text{HE}_{\nu,m+1}$. This is why there are discontinuities of the first derivative of the cutoff for those modes when we enter the $n_1 > n_2$ region.

When n_1 is fixed

We fix n_1 , and vary n_2 from lower to higher index, we successively go through fiber profiles (a), SSIF, (b), SSIF, and (d). Results are shown on Fig. 5.7.

We can separate Fig. 5.7 into five different regions. When $n_2 < n_3$, we have a fiber profile of type (a). At $n_2 = n_3 = 1.4$, we have a standard fiber, with the core radius equal to r_1 . When

Table 5.4: Cutoff equations for fiber profile (d)

TE _{0,m}	$J_0(u_1 r_1) [J_2(u_2 r_1) N_0(u_2 r_2) - N_2(u_2 r_1) J_0(u_2 r_2)] =$ $J_2(u_1 r_1) [J_0(u_2 r_1) N_0(u_2 r_2) - N_0(u_2 r_1) J_0(u_2 r_2)]$
TM _{0,m}	$\frac{J_0(u_1 r_1)}{u_2 r_1} n_2^2 [J_1(u_2 r_1) N_0(u_2 r_2) - N_1(u_2 r_1) J_0(u_2 r_2)] =$ $\frac{J_1(u_1 r_1)}{u_1 r_1} n_1^2 [J_0(u_2 r_1) N_0(u_2 r_2) - N_0(u_2 r_1) J_0(u_2 r_2)]$
EH _{ν,m}	$J_{ν+1}(u_2 r_1) N_ν(u_2 r_2) - N_{ν+1}(u_2 r_1) J_ν(u_2 r_2) =$ $[J_ν(u_2 r_1) N_ν(u_2 r_2) - N_ν(u_2 r_1) J_ν(u_2 r_2)] \Delta^+$
HE _{1,m}	$J_2(u_2 r_1) N_1(u_2 r_2) - N_2(u_2 r_1) J_1(u_2 r_2) =$ $[J_1(u_2 r_1) N_1(u_2 r_2) - N_1(u_2 r_1) J_1(u_2 r_2)] \Delta^-$
HE _{ν,m}	$J_{ν-2}(u_2 r_2) - \gamma N_{ν-2}(u_2 r_2) =$ $\frac{n_3^2 - n_2^2}{n_3^2 + n_2^2} [J_ν(u_2 r_2) - \gamma N_ν(u_2 r_2)] \quad \gamma = \frac{J_ν(u_2 r_1) \Delta^- - J_{ν+1}(u_2 r_1)}{N_ν(u_2 r_1) \Delta^- - N_{ν+1}(u_2 r_1)}$
LP _{ℓ,m}	$\frac{J_{ℓ-1}(u_1 r_1)}{u_2 r_1} [J_ℓ(u_2 r_1) N_{ℓ-1}(u_2 r_2) - N_ℓ(u_2 r_1) J_{ℓ-1}(u_2 r_2)] =$ $\frac{J_ℓ(u_1 r_1)}{u_1 r_1} [J_{ℓ-1}(u_2 r_1) N_{ℓ-1}(u_2 r_2) - N_{ℓ-1}(u_2 r_1) J_{ℓ-1}(u_2 r_2)]$

Table 5.5: Dimensions and indexes of test profiles

	r_1	r_2	n_1	n_2	n_3
(a)			2.0	1.3	
(b)	3 μm	4 μm	2.0	1.7	1.45
(c)			1.3	2.0	
(d)			1.7	2.0	

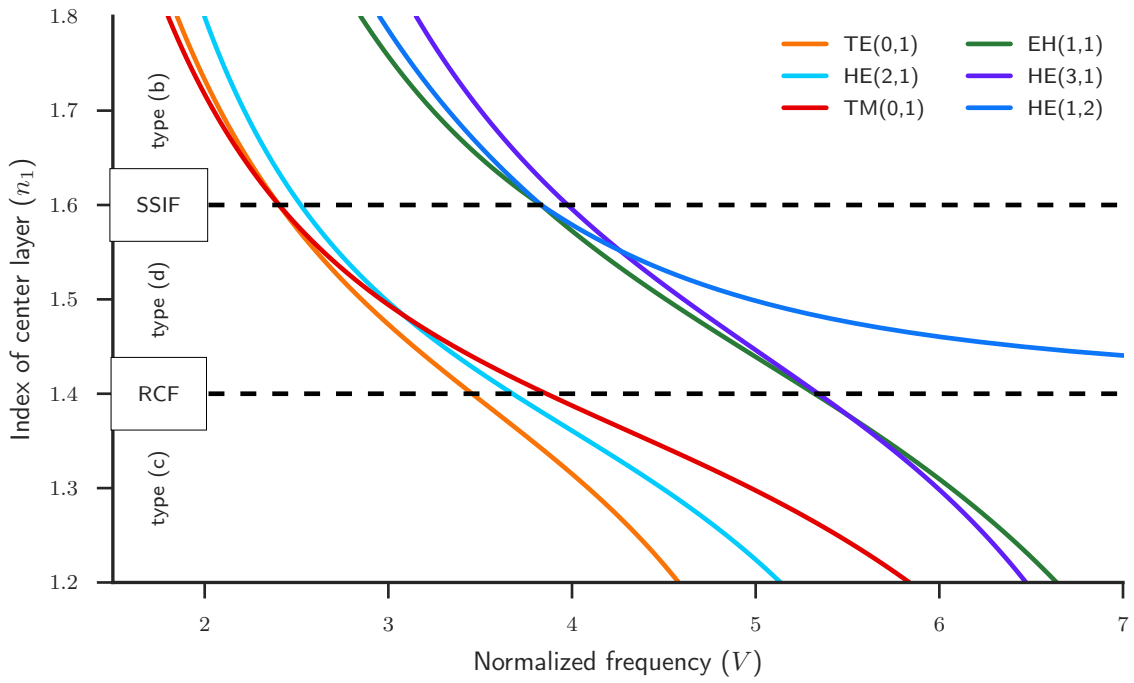


Figure 5.6: V at cutoff as a function of the index of the center layer, in three-layer step-index fiber. Simulation parameters: $r_1 = 4 \mu\text{m}$, $r_2 = 5 \mu\text{m}$, $n_2 = 1.6$, $n_3 = 1.4$.

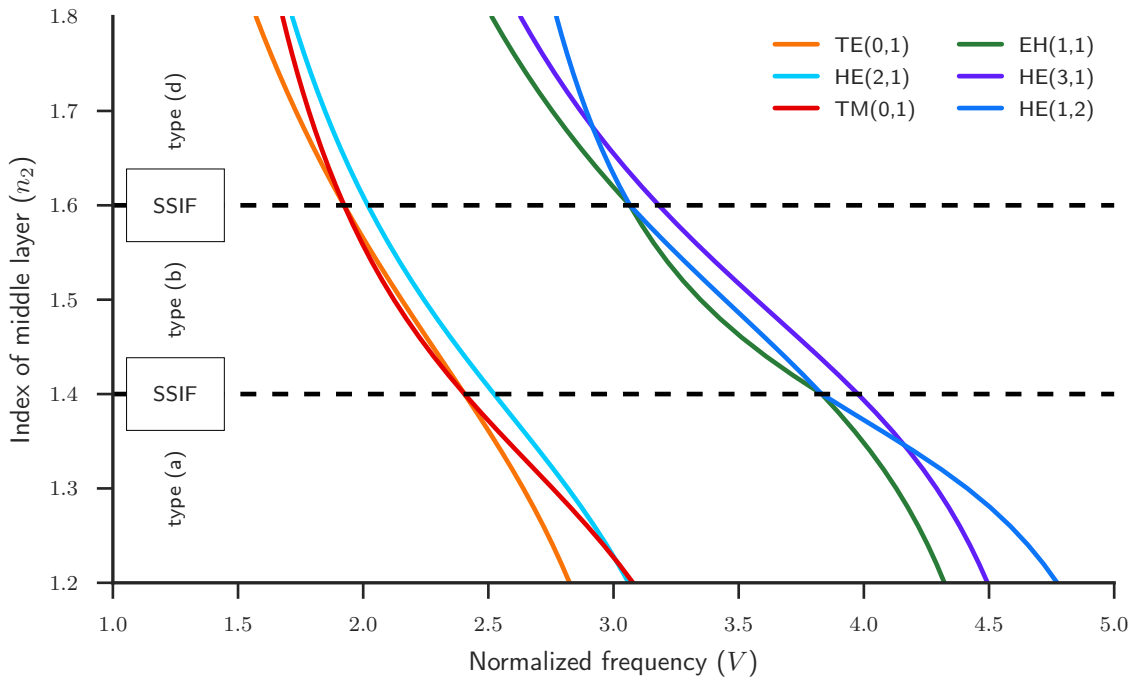


Figure 5.7: V at cutoff as a function of the index of the intermediate layer, in three-layer step-index fiber. Simulation parameters: $r_1 = 4 \mu\text{m}$, $r_2 = 5 \mu\text{m}$, $n_1 = 1.6$, $n_3 = 1.4$.

n_2 is between 1.4 and 1.6, we have a fiber profile of type (b). When $n_1 = n_2 = 1.6$, we have a standard fiber, with the core radius equal to r_2 . Finally, when $n_2 > n_1$, we have a fiber profile of type (d). Here, we defined V as $k_0 r_1 \sqrt{n_1^2 - n_3^2}$, for reasons similar to what we explained before.

Both $n_2 = 1.4$ and $n_2 = 1.6$ correspond to standard fiber, the only difference being the radius of the core. However, in Fig. 5.7, only at $n_2 = 1.4$ can we see the expected values of V for standard fiber mode cutoffs. This is an effect of the normalization (because we used r_1 value instead of r_2 to calculate V), and this is necessary to see the continuity of the cutoffs. Multiplying V by r_2/r_1 brings back the expected value of V at $n_2 = 1.4$.

Here again we see $TE_{0,m}$ and $TM_{0,m}$ modes crossing, and their inversion in type (b) fibers. We also see $EH_{1,m}$ and $HE_{1,m+1}$ modes having the same cutoff in standard fiber, and their particularities in type (b) fibers. Therefore, the properties of mode cutoffs of each fiber type are consistent, whether we vary n_1 or n_2 .

Asymptotic limit for LP modes

For $LP_{\ell,m}$ modes, we can easily obtain the cutoff expression for RCF, from the generic cutoff expression for 3LSIF (5.44). 3LSIF transforms to RCF when \hat{u}_2 is real, and $n_1 \rightarrow n_3$. At cutoff, it means that $\hat{u}_1 \rightarrow 0$.

Using the asymptotic expansion (A.21), we obtain:

$$\frac{2\ell \mathcal{F}_\ell(u_2 r_1)}{u_2 r_1} + \mathcal{F}_{\ell-1}(u_2 r_1) = 0 \quad (5.46)$$

Using Bessel recurring relations (A.8), this becomes, after simplification and expansion of the $\mathcal{F}_{\ell+1}(u_2 r_1)$ function

$$J_{\ell+1}(u_2 r_1) N_{\ell-1}(u_2 r_2) = J_{\ell-1}(u_2 r_2) N_{\ell+1}(u_2 r_1) \quad (5.47)$$

because $\gamma = \frac{J_{\ell-1}(u_2 r_2)}{N_{\ell-1}(u_2 r_2)}$. This is exactly the same expression as (4.33) found in Chapter 4.

Chapter 6

The modal map

6.1 Counting the number of dimensions

The design of SSIF is quite simple. Only three parameters characterize this kind of fiber: the refractive index of the core (n_{co}), the refractive index of the cladding (n_{cl}), and the radius of the core (r_1). The wavelength of the transmitted light (λ) is important to determine the supported modes. However, most of those parameters are predetermined. For instance, in telecommunications, wavelength usually is around 1550 nm, and cladding is made of silica ($n_{\text{cl}} \approx 1.444$). Remaining parameters can be included in one normalized parameter, the normalized frequency V , defined in (1.22). This V number includes both the radius r_1 , and the refractive indexes, that we often express as numerical aperture:

$$NA = \sqrt{n_{\text{co}}^2 - n_{\text{cl}}^2} \quad (6.1)$$

In the case of RCF, one more dimension is added: the inner radius of the ring-core. As we saw in Section 4.1.1, we still can use an equivalent V number defined for RCF (4.1), but we also define the ρ parameter as the ratio between inner and outer ring-core radius. With those normalized parameters:

$$ur_1 = \rho V \quad \text{and} \quad ur_2 = V \quad (6.2)$$

where $\rho = r_1/r_2$.

In the more generic case of 3LSIF, the refractive index in the center of the fiber is no longer the same as the refractive index of the cladding; thus an additional parameter is needed to describe the fiber. We now define the normalized frequency from the equivalent SSIF fiber that would envelope the 3LSIF, as we saw in Section 5.1.1. We can still use the same ρ parameter as defined for RCF. Additionally, we need a third normalized parameter, the ratio between u_1 and u_2 parameters:

$$v = \begin{cases} u_2/u_1 & u_1 > u_2 \\ u_1/u_2 & u_1 < u_2 \end{cases} \quad (6.3)$$

Table 6.1: Normalized fiber parameter equivalences in 3LSIF. (a) W-type fiber (fiber with trench); (b) Pedestal fiber; (c) ring-core fiber with lower center; (d) ring-core fiber with higher center; (e) ring-core fiber (RCF). $\rho = r_1/r_2$; $v = \min(u_1, u_2)/\max(u_1, u_2)$.


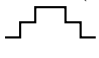

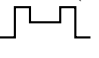

	Profile (a)	Profile (b)	Profile (c)	Profile (d)	Profile (e)
					
$u_1 r_1$	ρV	ρV	$\rho v V$	$\rho v V$	—
$u_1 r_2$	V	V	$v V$	$v V$	—
$u_2 r_1$	$\rho v V$	$\rho v V$	ρV	ρV	ρV
$u_2 r_2$	$v V$	$v V$	V	V	V

Table 6.2: Fiber parameters, as function of fiber profile. In this table, the generic definition is used for V and NA , where they are related to the highest index in the fiber.

Fiber profile	Scalar	Vector
	<i>weakly guiding</i>	
SSIF	V	V, NA
RCF	V, ρ	V, ρ, NA
3LSIF	V, ρ, v	V, ρ, v, NA
N layers	$u_1, r_1, u_2, \dots, u_{N-1}, r_{N-1}, w$	

Using those definitions, the V number is equivalent to the parameter $u_1 r_2$ in fiber profiles (a) and (b), and to the parameter $u_2 r_2$ in fiber profiles (c), (d), and (e), u_2 being equivalent to the parameter u of RCF. Relations for other parameters are given in Table 6.1. Parameter u_1 does not exist for fiber profile (e) (RCF), as it would be equivalent to parameter w . Parameter $u_1 r_2$ is not used in the modal equations, but is given here for completeness.

For each layer we add to the fiber profile, we need two supplementary parameters: one for the layer radius, the other for the layer index. Beyond three layers, the use of normalized parameters becomes unnecessarily complex, and we use $u_i r_i$ parameters directly. Table 6.2 summarizes parameters used to describe each kind of fiber.

6.2 Selecting number of modes

In the design of few-mode fiber (FMF), the first design target is probably the kind and the number of guided modes to support. The simplest case is to target a given number of LP modes in a SSIF. In that case, the number of modes only depends on the V number. We know that V is parametrized by the wavelength, the core radius, and the numerical aperture. However, as we already stated, wavelength and cladding index usually are fixed. Furthermore, for LP modes, we need a small index contrast between core and cladding, and thus a small NA . Therefore, the V number is mostly determined by the core radius.

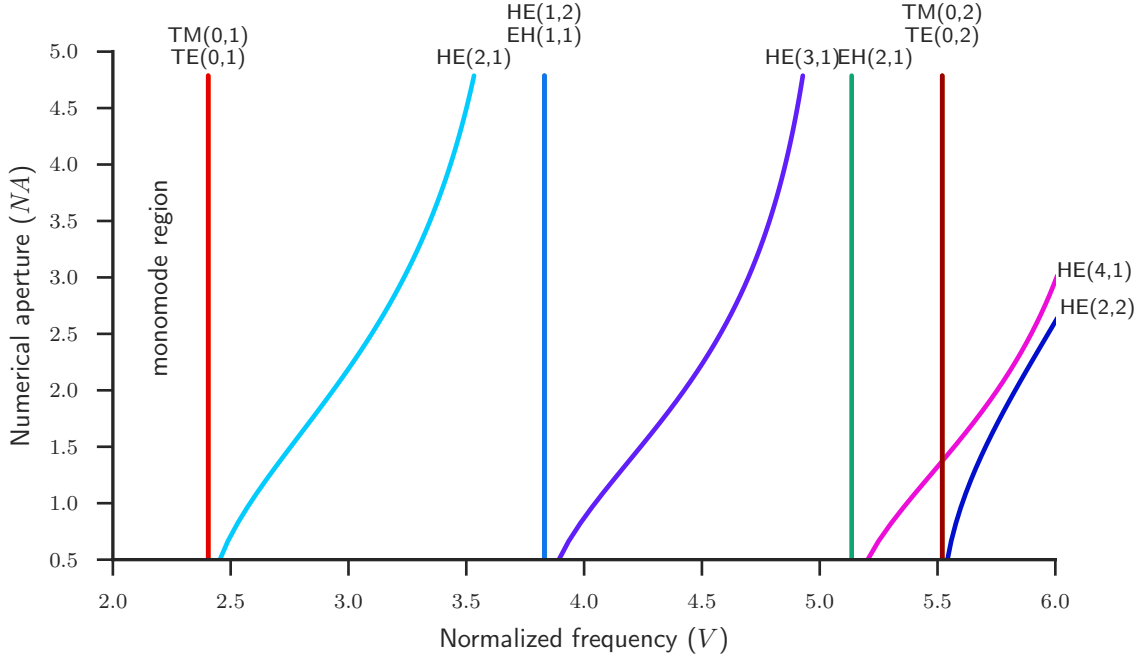


Figure 6.1: Mode cutoffs as function of NA , for SSIF. This graph is totally generic, as core radius is comprised in V , and indexes are comprised in NA .

In the case of vector modes, V number is no longer a sufficient criteria to determine the number of guided modes, because of the dependency on the refractive indexes that is present in the cutoff expression for $HE_{\nu,m}$ modes (1.46). This is illustrated on Fig. 6.1. On the figure, we see that the cutoff of most modes appears as a vertical line, as it is not affected by NA . However, cutoff of $HE_{\nu,m}$ modes vary as NA increases. This graph is totally generic, as core radius is comprised in V , and indexes are comprised in NA .

This figure introduces what we call a *modal map*. The cutoff lines define borders between regions. Each region corresponds to a number of guided modes, varying with the fiber parameters. For instance, the region where $V < 2.405$ is the region where the fiber is monomode. Between $V > 2.405$ and $V < 3.832$, the fiber is guiding $HE_{1,1}$ (which is guiding for all values of V), $TE_{0,1}$, and $TM_{0,1}$; it could also guide $HE_{2,1}$, depending on the numerical aperture. Other regions are defined similarly.

However, modal maps are of little practical use for SSIF, mainly because in telecommunication fibers, NA remains relatively small (below 0.3), and thus cutoff of $HE_{\nu,m}$ modes does not diverge tremendously from the cutoff of other modes. When V is large, we can estimate the number of supported vector modes using the simple relation [136]:

$$M \approx \frac{V^2}{2} \quad (6.4)$$

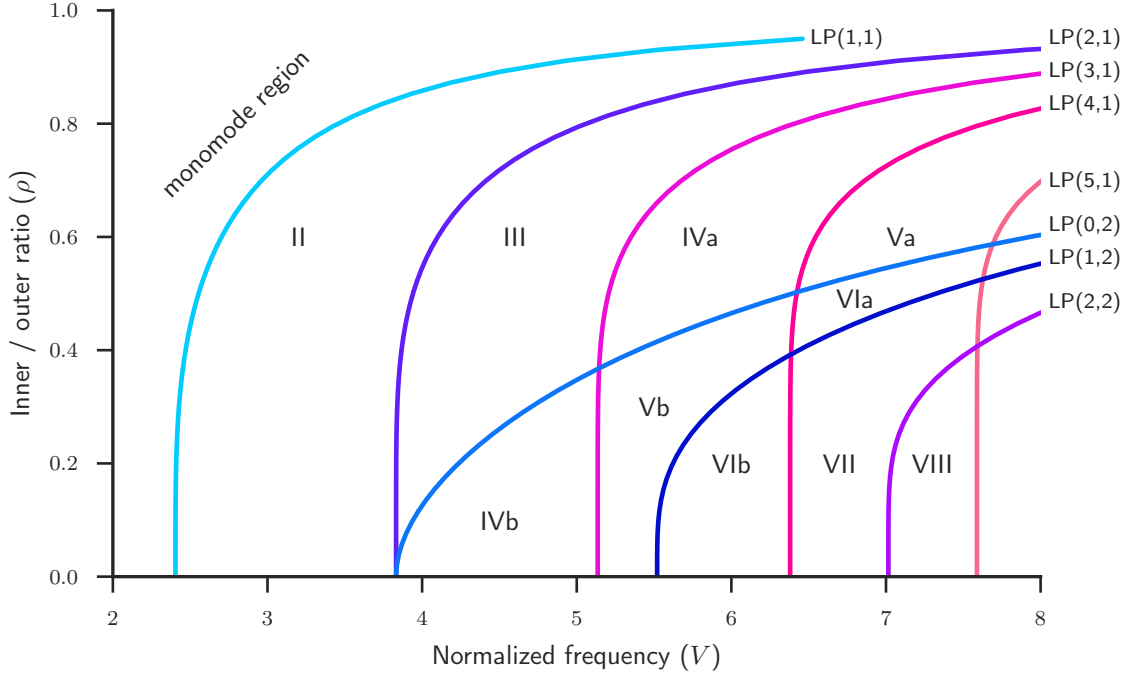


Figure 6.2: Modal map of LP modes in RCF. $n_1 = 1.444$; $n_2 = 1.494$; $NA = 0.38$.

Modal maps become a more interesting tool when we design RCF. Figure 6.2 shows the cutoff of $LP_{\ell,m}$ modes as function of ρ in RCF. For the simulation we used a cladding index n_1 of 1.444, and a ring index n_2 of 1.494; therefore $NA = 0.38$. The vertical axis can be seen as the thickness of the ring-core, and (for fixed indexes) the horizontal axis can be seen as the outer radius of the ring-core. Therefore, the modal map gives the number of supported modes as a function of the RCF geometry. When $\rho = 0$, we see the cutoffs of SSIF. The region above the cutoff of $LP_{1,1}$ mode is the monomode region. Other regions are labeled with the number of modes they support. For instance, region II is where both $LP_{0,1}$ and $LP_{1,1}$ are supported; region III supports $LP_{0,1}$, $LP_{1,1}$, and $LP_{2,1}$ modes; and so on. Regions IVa and IVb both support four modes, but the former supports $LP_{3,1}$, while the later supports $LP_{0,2}$. While SSIF are monomode only for $V < 2.405$, it is possible to design an RCF with $V > 2.405$ that is still single-mode, assuming ρ is high enough. This is one of the differences between SSIF and RCF.

We call the second index of the modes, the m parameter, the *radial order*, because it is related to the number of zeros in the radial dependency of the fields. When $m = 1$, we have only one spot or one ring of intensity in the mode. When $m = 2$, the mode has two concentric rings of intensity, and so on. The first mode with $m > 1$ is the $LP_{0,2}$ mode. From Fig. 6.2, we see that in a SSIF (i.e., at $\rho = 0$), the cutoff of $LP_{0,2}$ is the same as the cutoff of $LP_{2,1}$. Therefore, as soon as a SSIF supports more than $LP_{0,1}$ and $LP_{1,1}$ modes, it necessary supports $LP_{0,2}$

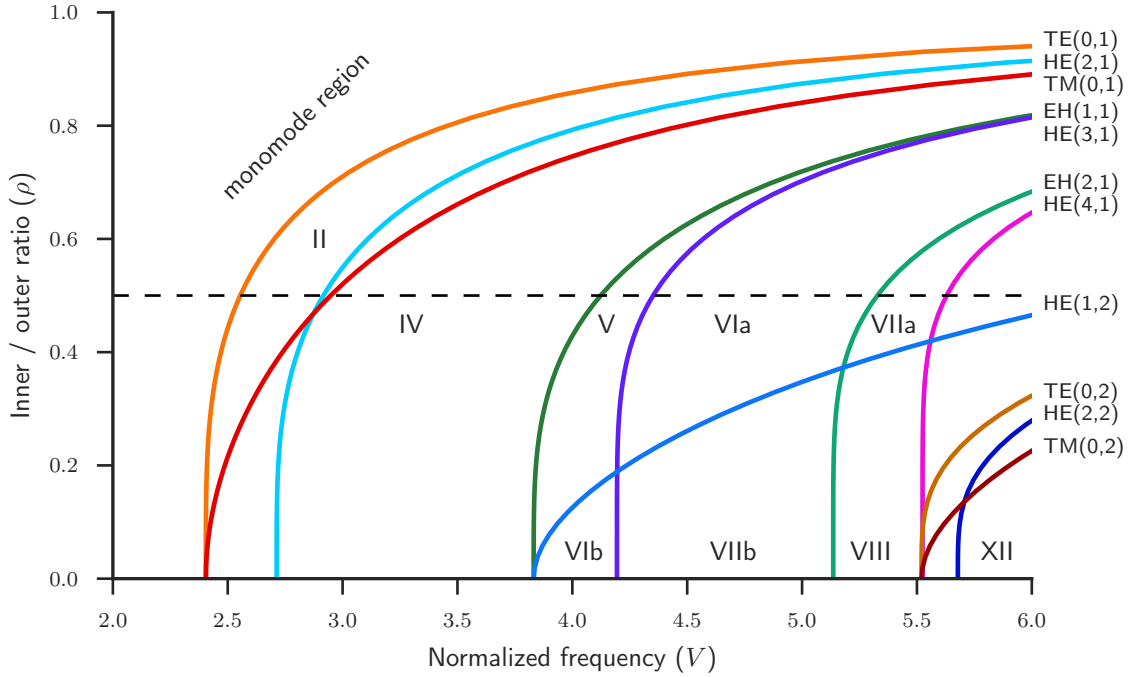


Figure 6.3: Modal map of vector modes in RCF, for fixed indexes. Cladding index $n_1 = 1.444$; ring index $n_2 = 2$.

mode, i.e., a mode of the second radial order. With RCF, by choosing the right value for the ρ parameter, it is possible to design a fiber supporting several modes of the first radial order, without supporting any second radial order mode.

Finding cutoff for the LP modes in RCF and vector modes for SSIF was already possible. With the cutoff equations developed in Chapter 4, we can now go further, and plot the modal map for vector modes in RCF. The vector mode map for RCF is a tridimensional map. However, if we fix one parameter, we can easily plot against the other. For example, Fig. 6.3 shows the modal map for a RCF with $n_1 = 1.444$ and $n_2 = 2$. The horizontal dashed line is where $\rho = 0.5$. Again, we tagged some regions with the number of supported vector modes.

Figure 6.4 shows the modal map for a RCF with $\rho = 0.5$ and $n_1 = 1.444$, where n_2 varies between 1.5 and 5.0. Therefore, the fiber dimensions are fixed, and the index of the ring-core is varying. The vertical axis is now n_2 , and this graph is like the third dimension of the previous figure, at the position indicated by the dashed line. This clearly shows which modes are most influenced by the index contrast (e.g. $HE_{\nu,m}$), and which modes are not (e.g. $HE_{1,m}$ and $TE_{0,m}$). The horizontal dashed lines on Fig. 6.3 and 6.4 represent equivalent parameters ($\rho = 0.5$ and $n_2 = 2$).

To see how cutoff varies as function of both ring index and thickness, we plotted on Fig. 6.5,

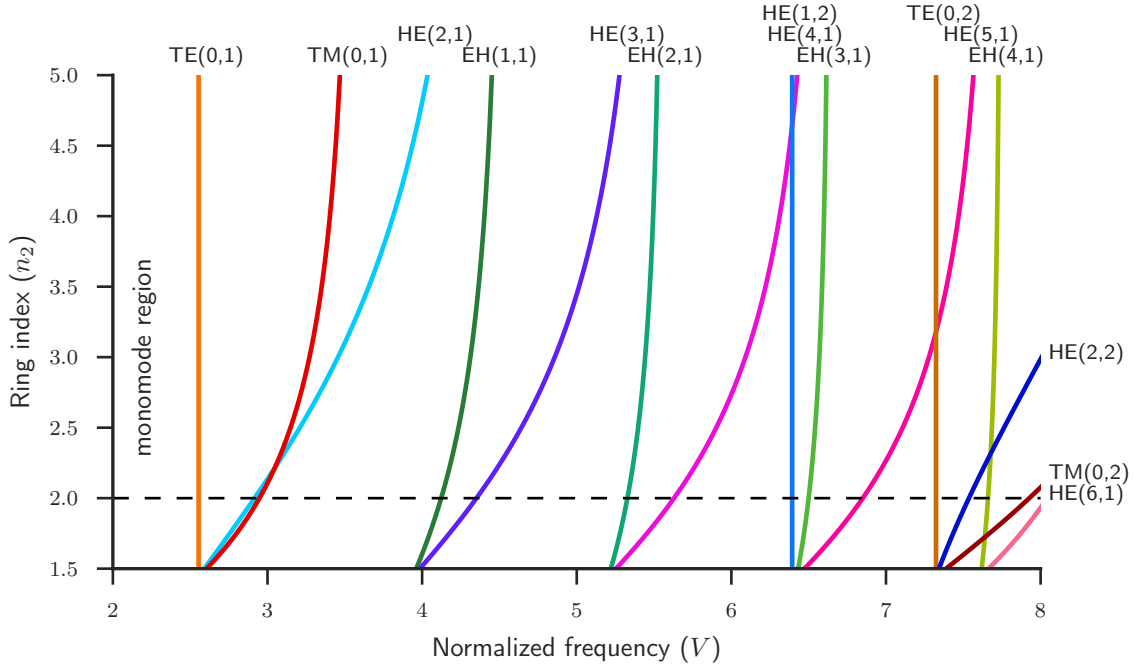


Figure 6.4: Modal map of vector modes in RCF, for fixed $\rho = 0.5$. Cladding index $n_1 = 1.444$.

the contours of the cutoff frequency V as a function of ρ and n_2 , for $\text{HE}_{2,1}$ mode, in a RCF with $n_1 = 1.444$. From this graph, we see that when ρ is small (i.e., the ring is thick), the cutoff is mostly influenced by the index contrast. However, when the ring is thin, it is ρ that most affects the cutoff value.

6.3 Targeting mode separation

In the design of fibers for the transmission of OAM modes, the number of supported modes is a necessary, but not a sufficient condition to produce a good fiber. Another criteria is the separation between the effective indexes of vector modes. While, for LP mode transmission, we want to minimize this separation to minimize group dispersion, for OAM modes, this is the opposite. We need to achieve a large effective index separation, to keep the OAM modes well separated, and to prevent the vector eigenmodes to couple into LP modes. The design of polarization maintaining fibers suggests a typical effective index separation of 1×10^{-4} [40]. To compute this separation, we need to find the effective index of all modes, for a given fiber at a given wavelength. We define Δn_{eff} as the difference between the effective indexes of two modes.

Figure 6.6 shows the effective index separation (Δn_{eff}) between the indicated mode pairs, as function of V . Each line has two color, associated with the two involved modes. For

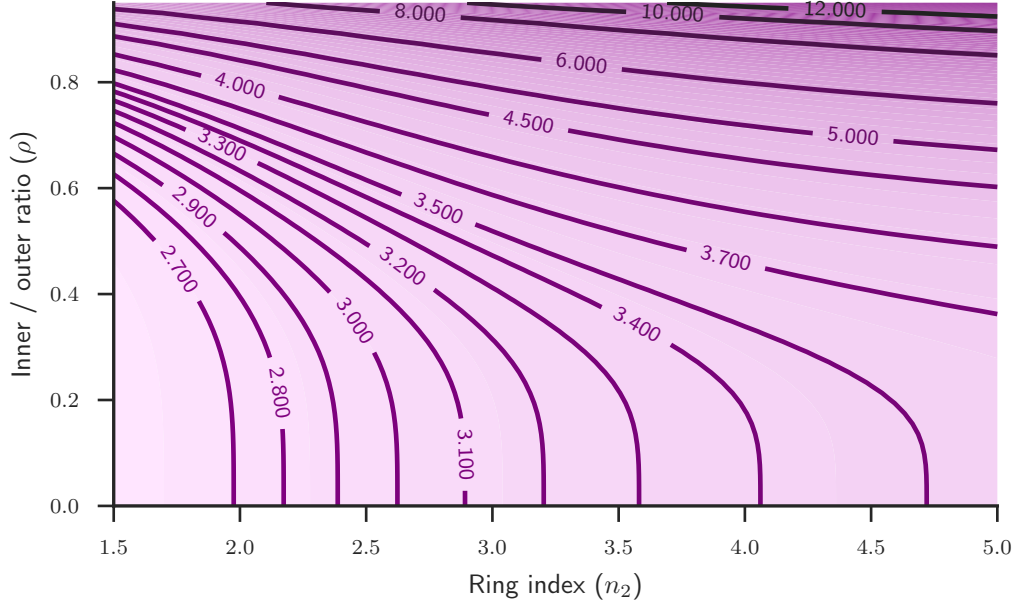


Figure 6.5: Contour plot of cutoff frequency V of $\text{HE}_{2,1}$ mode in RCF, as function of ρ and n_2 . Cladding index $n_1 = 1.444$.

this example, we chose the same parameters as those in the preceding examples ($\rho = 0.5$, $n_1 = 1.444$, $n_2 = 2$) and we plotted Δn_{eff} . We know that V is a function of wavelength, fiber dimensions, and fiber indexes. Therefore, on the graph, if we keep a fixed wavelength, V increases with core radius, as indexes are fixed. As V evolves, some modes become closer, while others have effective indexes that grow farther apart. For the design of OAM fibers, we would target the largest possible separation. In this example, we limited the range of V to only allow four supported modes, and there are six possible combinations. Adding only a few more supported modes, the graph would quickly become unreadable.

As considering all combinations of modes becomes too complex, a more practical approach is to consider the worse case, by considering the closest neighbor for each mode. This way, we know how separated a given mode is from the others. Figure 6.7 is similar to Fig. 6.6, but only shows the separation with the closest neighbor. For example, when V is small, only $\text{HE}_{1,1}$ and $\text{TE}_{0,1}$ are guided, with a given separation. When V increases, $\text{HE}_{2,1}$ and $\text{TM}_{0,1}$ begin to be guided, then $\text{EH}_{1,1}$, $\text{HE}_{3,1}$, and finally $\text{EH}_{2,1}$. The discontinuities we see on some lines (e.g. $\text{TE}_{0,1}$ and $\text{EH}_{1,1}$) occur when a closer mode suddenly begins to be guided. For instance, when $\text{TM}_{0,1}$ and $\text{HE}_{2,1}$ begin to be guided, $\text{TE}_{0,1}$ suddenly becomes closer to $\text{HE}_{2,1}$ than it was from $\text{HE}_{1,1}$; this is why there is a sudden drop in the line for the separation of $\text{TE}_{0,1}$. Similar behavior occurs for $\text{EH}_{1,1}$ when $\text{HE}_{3,1}$ begins to be guided. When we follow the line for a given mode, we know the distance to the closest mode. For instance, we know that near $V = 5$, $\text{HE}_{3,1}$ and $\text{EH}_{1,1}$ modes are very close. Around $V = 3.8$, all modes are more that 0.05

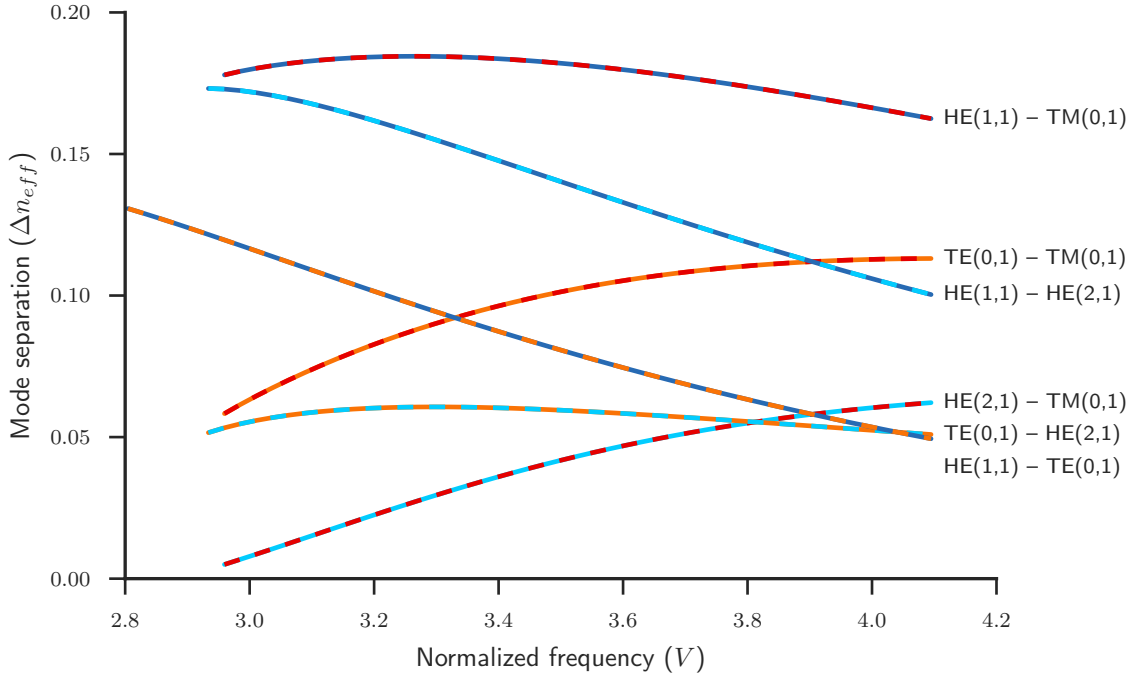


Figure 6.6: Effective index separation between modes in a RCF. Simulation parameters: $n_1 = 1.444$, $n_2 = 2$, $\rho = 0.5$.

apart.

This brings us to a third way to visualize mode separation. We define a new function that is the smallest separation between all the modes, for a given set of parameters. We can see this as a worse case, in the sense that no modes are closer than this value. Figure 6.8 shows the minimal effective index separation between all mode, for a RCF with $n_1 = 1.444$, $n_2 = 2$, and for three different values of ρ . For example, the green line ($\rho = 0.5$) corresponds to the lowest value among all the line on Fig. 6.7, for each value of V . By maximizing this function, we can target a fiber design with the best possible modal separation. However, as we can see, the minimal effective index separation is not a smooth function; it has many steps as the number of supported modes varies, or the closest modes change.

This minimal separation is closely related to the number of supported modes. As the number of guided modes increases, the minimal separation decreases. However, we do not clearly see what is the number of supported modes on Fig. 6.8. A better way is to combine the modal map and the minimal effective index separation. On top of the modal map, we plot the minimal effective index separation as a colormap. This is what we call the *augmented modal map*. Figure 6.9 shows an example of an augmented modal map, for a RCF with $n_1 = 1.444$ and $n_2 = 2$. We carefully adjusted the scale and the colors of the colormap to show how separation evolves within each region. This is why we plotted the colormap on a power scale instead of

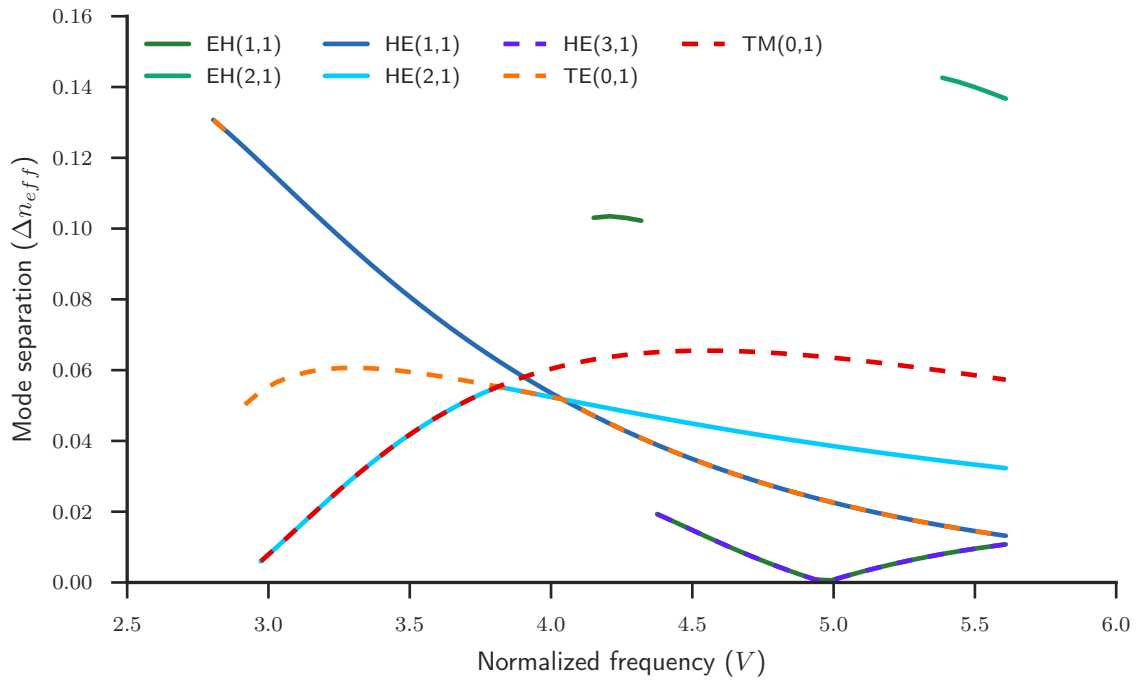


Figure 6.7: Smallest effective index separation between modes in a RCF. Simulation parameters: $n_1 = 1.444$, $n_2 = 2$, $\rho = 0.5$.

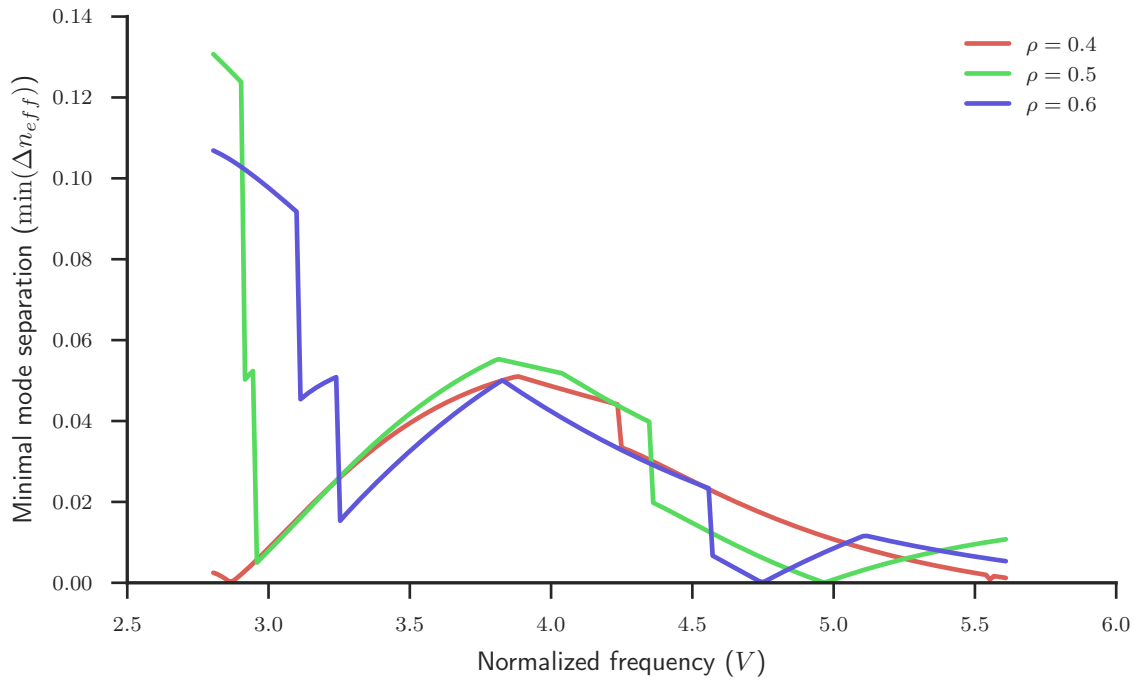


Figure 6.8: Minimal effective index separation in a RCF. Simulation parameters: $n_1 = 1.444$, $n_2 = 2$, $\rho = 0.5$.

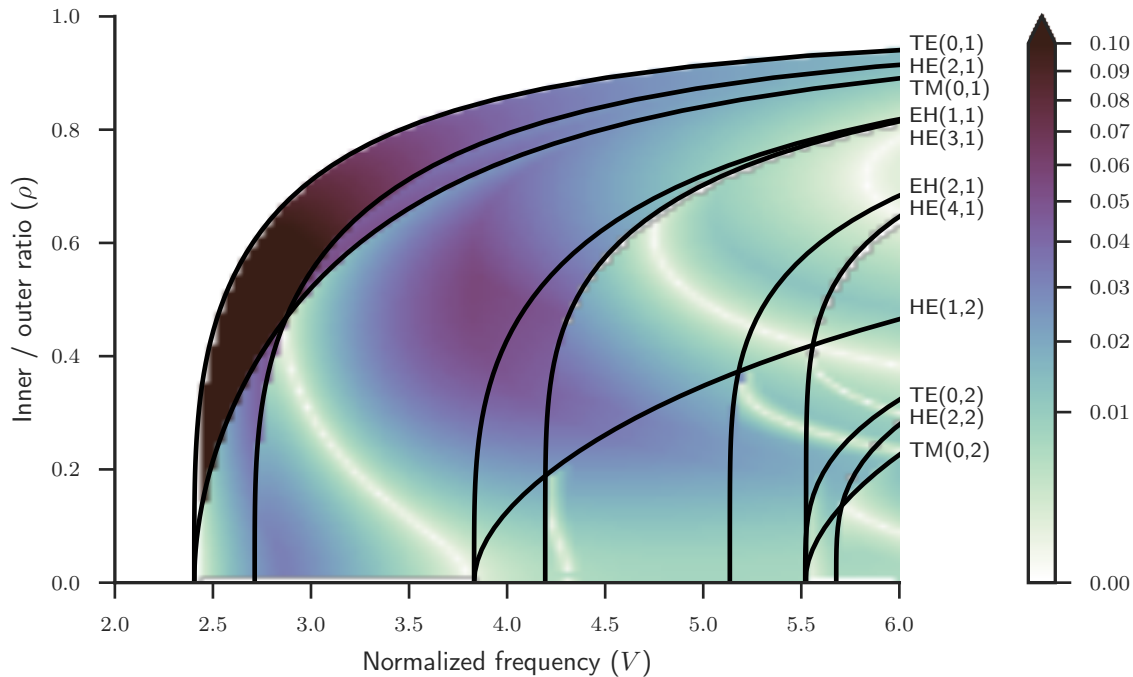


Figure 6.9: Augmented modal map for RCF with $n_1 = 1.444$ and $n_2 = 2$.

a linear scale. It is expected that the region where only two modes are supported exhibits a larger separation. This is why the two modes region, just below the cutoff of $TE_{0,1}$, is the darkest region. On some places, we see white lines. It corresponds to the parameters where the effective indexes of two modes are crossing. For instance, the white line in the four modes region, between cutoffs of $TM_{0,1}$ and $EH_{1,1}$ modes, is where the $HE_{2,1}$ and $TM_{0,1}$ effective indexes are crossing. This graph can be related to Fig. 6.8. For instance, if we draw an horizontal line at $\rho = 0.5$ on the augmented mode map, and if we follow the colormap along this line, we see it behaves exactly like the green line on Fig. 6.8. The separation is high when V is between 2.5 and 2.8, then it suddenly drops when $HE_{2,1}$ and $TM_{0,1}$ modes appear, then it progressively increases to reach a local maximum around 3.8; it decreases smoothly, with a little drop at $V = 4.4$ when $HE_{3,1}$ mode appears, to reach zero around $V = 5.0$; finally, it raises again. The same observation can be done for other values of ρ .

The augmented modal map is a useful tool, as it gives information about both the number of supported modes and the modal separation, in the same figure. However, it requires a lot of computational power to produce, because the effective index of every mode, for all combinations of parameters, need to be solved. A high resolution augmented modal map can potentially take hours to compute. Therefore, it is useful to choose well the range of fiber parameters before computing it. One way to do it to use the simpler modal map first (without the modal separation colormap) to choose the desired number of modes and to adjust the

range of parameters consequently. Then, a lower resolution colormap can be computed, to get a first insight about the modal separation. Finally, the higher resolution map can be computed, if the preliminary results are positive.

In Chapter 8, we will use the augmented modal map to design OAM fibers.

Part III

Fibers designed for OAM transmission

Chapter 7

Air-core annular fiber

7.1 Design of an OAM fiber

To avoid any confusion, we need to define how we count modes, information channels, and states, in optical fibers. The number of modes counts all polarizations and degeneracies as one mode, e.g. $\text{HE}_{1,1}$ is one mode. The number of states counts all degeneracies and polarizations, e.g. $\text{LP}_{1,1}$ has four different states (the symmetry axis of the field can be horizontal or vertical, and the polarization can be horizontal or vertical). Finally, the number of information bearing channels is the actual number of states we use to carry information.

Up to now, OAM fibers only supported a limited number of channels. For instance, the original vortex fiber [93] supports four information channels. The IPGIF support one more OAM mode, thus eight information channels [98]. And the air-core fiber from Gregg et al. [96] is multimode, but supports only up to twelve information channels.

Our goal is to design an OAM fiber that supports a higher number of channels. We also want to use as many states as possible as information channels, i.e., all OAM modes should be usable as information channels. It was already demonstrated that, to support OAM modes, the fiber must exhibit 1) good effective index separation between vector modes (the true eigenmodes of the fiber), to minimize modal coupling and degeneracy into LP modes, and 2) a fiber profile that matches the doughnut shaped OAM fields [40].

To obtain good mode separation, we must have a high contrast in refractive indexes of the fiber materials; in this way we violate the weakly guiding approximation under which LP modes are formulated. In particular, there must be great separation between the effective indexes of $\text{HE}_{\ell+1,m}$ and $\text{EH}_{\ell-1,m}$ modes, otherwise those modes would couple into $\text{LP}_{\ell,m}$ modes, and we would lose the OAM states during propagation. Design of polarization-maintaining fibers suggests that an effective index separation on the order of 1×10^{-4} between the modes in a group will preclude LP mode formation [40]. This is an order of magnitude greater separation than typically found in conventional fibers. However, this number should be seen as a rule of

Table 7.1: Index constraints for air-core annular fiber

Layer	Material	Refractive index	Molar concentration
I	Air	1.0	
II	SiO ₂ + GeO ₂	1.444 – 1.474	Up to 20%
III	SiO ₂ + P ₂ O ₅ + F	1.437 – 1.444	Up to 1.5%
IV	SiO ₂	1.444	

thumb; this is not a hard limit. In [95], they transmitted OAM modes over 2m of fiber with an effective index separation around 0.6×10^{-4} .

The refractive index contrast is limited by material constraints, and by the fabrication process. To achieve maximum contrast, a hollow air-core was suggested [94], since air has an index of approximately 1, which is as far from that of doped silica that we can achieve. In this design, the modes are traveling inside a doped ring-core, not inside the air core. This is different from PCF fibers that are also called air-core fibers, but where the light travels inside the air, guided by a photonic bandgap [137].

The fiber designed in [95] supports a large number of vector modes, but only a few of them are separated enough (in terms of effective index) to be able to transmit OAM modes. Hence only three OAM modes, supporting twelve information bearing channels, can effectively be used. In contrast, we want to design a fiber supporting fewer vector modes in total, but where all those vector modes can be used as a basis for OAM modes. All modes must have an effective index that resides between the refractive index of the cladding and the maximum refractive index of the fiber. A fiber having fewer vector modes allows them to be more separated (in terms of effective index), as the space of possible effective indexes is exploited by all supported modes. This is achieved by carefully adjusting the width of the doped region in the fiber to limit the total number of supported vector modes. We include an external layer of material having a refractive index lower than the cladding, a trench, to increase the contrast of the refractive indexes, and to limit the number of higher order modes.

Figure 7.1 shows the targeted design. We call this design *air-core annular fiber* (ACF), as the center of the fiber is air, but the fiber really is an annular (or ring-core) fiber, since this is the second layer that is guiding the modes. In this design, n_1 is the refractive index of air, and n_4 is the refractive index of silica. n_2 , n_3 , r_1 , r_2 , and r_3 are parameters to be determined. We target a fiber with 125 μm cladding diameter, for compatibility with standard fiber connectors. Indexes for n_2 and n_3 are limited by material constraints. Table 7.1 gives what are approximately the possible index ranges at 1550 nm, without facing manufacturing troubles.

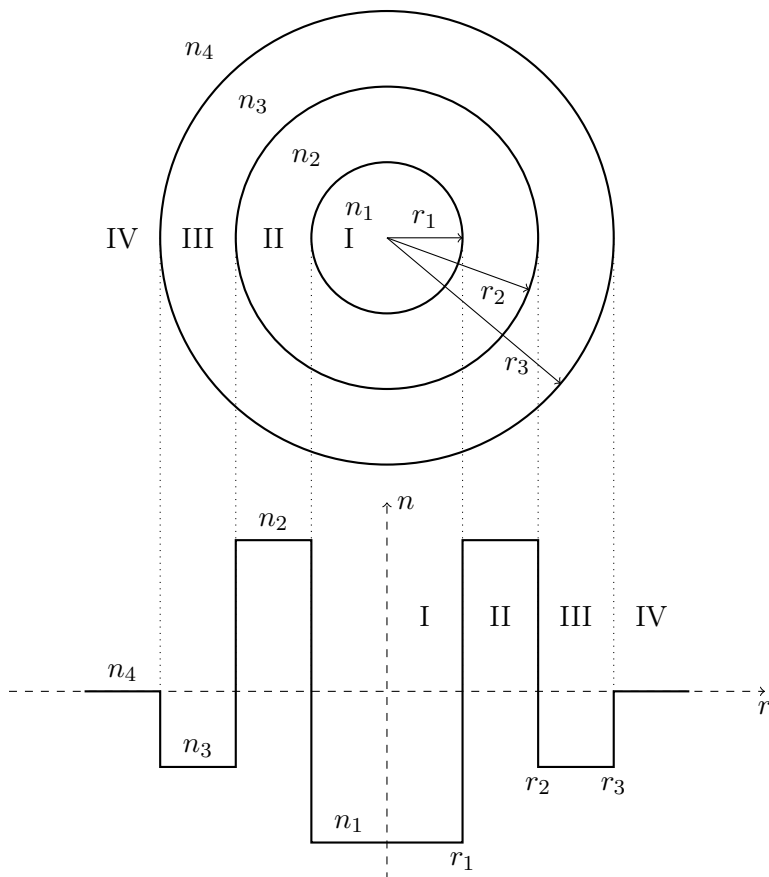


Figure 7.1: Air-core annular fiber geometry (top view, and profile).

7.2 Modeling and simulation

Finding the right fiber profile is a complex optimization problem. Usually, a higher index contrast will allow a higher effective index separation. However, a higher number of modes will decrease the effective index separation, since more modes will be packed in the same possible range of effective indexes. Therefore, the number of supported modes needs to be controlled by the thickness of the second layer. To achieve our design goal, a tradeoff must be performed between the number of supported modes, and the effective index separation.

As we explained in Chapter 6, there are many possible ways to examine the effective index separation. The simplest optimization is to maximize the minimal effective index separation. However, for a given fiber design, there could be a pair of modes that are closer than another pair, and that design would be rejected even if all other modes were well separated. Another possible optimization would be to maximize the average of the minimal effective index separation of each mode. But it is possible that this optimization favors a design with some very well separated modes, and some other modes that are very close. The point is that the ideal fiber profile does not exist. Simulation and optimization tools can help us in the choice of the

Table 7.2: Parameters of designed air-core annular fiber

	Radius (μm)	Molar concentration (%)	Index (1550 nm)	Index (657.6 nm)
Layer 1	9.2	—	1.000	1.000
Layer 2	11.6	22.5	1.480	1.493
Layer 3	15.6	1.1	1.439	1.451
Cladding	62.5	—	1.444	1.456

right design, but the final choice is always a compromise.

The simulation themselves were performed using the transfer-matrix method [118]. This method allows quick and accurate calculation of the effective index of each mode. While using fixed indexes for each layer would be sufficient to calculate the effective index of each mode, we rather used wavelength dependent indexes, calculated from the Sellmeier equation [138]. This allows us to get the effective indexes as function of the wavelength, and to estimate other modal parameters, such as group index and dispersion. The exact formulas we use are given in Appendix B.

The optimization itself was performed by sweeping through the range of possible parameters. The final design was chosen due to the good balance between the number of supported modes and the separation of the effective indexes, with a good tolerance to imperfections introduced into the index profile during the fabrication process.

Table 7.2 summarizes chosen parameters. Indexes are calculated from the given molar concentration. 1550 nm is the wavelength we intend to use for the experiments, while 657.6 nm is the wavelength used by the refractometer. This will allow us to compare the values from the design with the fabricated fiber. As we will see, we overestimated the capacity to dope the second layer; this is why the concentration of GeO_2 is higher in the design than what we now use as maximum possible concentration.

On Fig. 7.2 we plot the effective index as a function of the wavelength, over the C-band. We see that 20 vector modes are supported by the fiber, at 1550 nm. Therefore, 18 modes could serve as a basis for 10 OAM modes ($\ell = 0$ to 9), or 36 OAM states. Table 7.3 lists effective index, as well as minimal effective index separation, for each supported mode, at 1550 nm. As we can see, all modes are separated by 1×10^{-4} or more; the closest modes being $\text{TE}_{0,1}$ and $\text{HE}_{1,1}$. A special characteristic of this fiber design is that the mode with the highest effective index is $\text{TE}_{0,1}$, and not $\text{HE}_{1,1}$.

7.3 Fiber fabrication

The optical fiber was fabricated at our laboratory at COPL, equipped with modified chemical vapor deposition (MCVD) for preform fabrication and two drawing towers for fiber pulling.

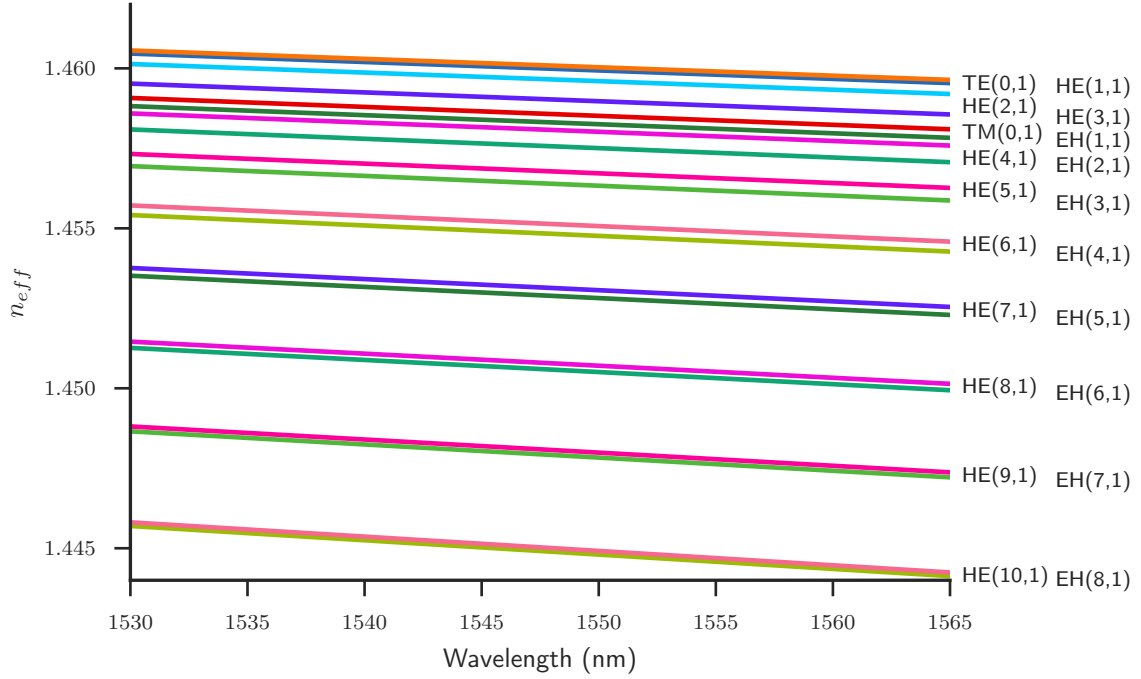


Figure 7.2: Effective index as function of wavelength, for designed ACF. Fiber design parameters are given in Table 7.2.

Table 7.3: Effective indexes and effective index separations, at 1550 nm, for designed ACF.

Mode	n_{eff}	Δn_{eff}	Mode	n_{eff}	Δn_{eff}
TE _{0,1}	1.459 90	9.956×10^{-5}	HE _{6,1}	1.454 91	3.078×10^{-4}
HE _{1,1}	1.459 80	9.956×10^{-5}	EH _{4,1}	1.454 60	3.078×10^{-4}
HE _{2,1}	1.459 47	3.364×10^{-4}	HE _{7,1}	1.452 89	2.475×10^{-4}
HE _{3,1}	1.458 83	4.595×10^{-4}	EH _{5,1}	1.452 64	2.475×10^{-4}
TM _{0,1}	1.458 38	2.633×10^{-4}	HE _{8,1}	1.450 52	1.985×10^{-4}
EH _{1,1}	1.458 11	2.382×10^{-4}	EH _{6,1}	1.450 32	1.985×10^{-4}
HE _{4,1}	1.457 87	2.382×10^{-4}	HE _{9,1}	1.447 78	1.549×10^{-4}
EH _{2,1}	1.457 36	5.139×10^{-4}	EH _{7,1}	1.447 63	1.549×10^{-4}
HE _{5,1}	1.456 57	3.897×10^{-4}	HE _{10,1}	1.444 69	1.131×10^{-4}
EH _{3,1}	1.456 18	3.897×10^{-4}	EH _{8,1}	1.444 58	1.131×10^{-4}

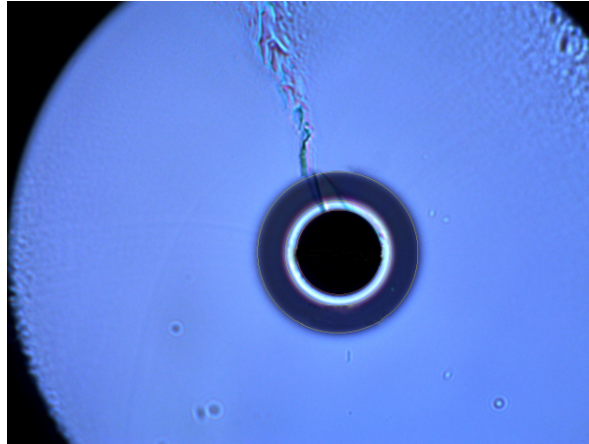


Figure 7.3: Optical microscope photograph of the end of the air-core annular fiber. [Credit: Steeve Morency.]

Figure 7.3 shows a photograph of one end of the fiber. The cladding diameter is around $125\ \mu\text{m}$, as in conventional fiber. The fiber preform was fabricated via MCVD in two steps. We formed the first layer by incorporating adequate concentrations of SiO_2 , P_2O_5 and F. This was followed by a deposit ring layer of SiO_2 and GeO_2 to produce a step-index profile. Finally, the result was partially collapsed to produce the glass preform. The hollow core diameter is controlled during the fiber drawing process to achieve the target value.

The refractive index profile was measured directly on the fabricated fiber, using a refracted near-field analyzer (Exfo NR-9200HR), and is shown in Fig. 7.4. We have four measurements, for both ends of the 2 km fiber, on two different axis. The 1.48 index we see in the center and exterior of the fiber is the index of the matching oil used for the measurement. However, the center of the fiber really is a hollow tube, and its index is 1 when the fiber is surrounded by air. The spatial resolution of the instrument is $\leq 0.4\ \mu\text{m}$. This is why the steps between the different refractive indexes are a little rounded. We can observe that refractive index is a little higher at the start of the fiber than at the end.

Fabricating a silica fiber with a very high refractive index contrast is difficult, because of the large stress that appears at the core cladding interface during fiber fabrication. Figure 7.5 compares the designed index profile with measured values. On this figure, we clearly see that the maximum index of the real fiber is lower than what was expected: around 1.487 at the start of the fiber, and 1.484 at the end. Fiber dimensions are very close to the design at the fiber start, but a little smaller at fiber end.

Based on the measured refractive index profile, we created a new numerical model for the fiber. Parameters of this model are summarized on Table 7.4. We used ten small steps to mimic the gradients of the trench. This new fiber profile is illustrated on Fig. 7.6. We ran the simulator against this new model, to get the number of supported modes, and associated

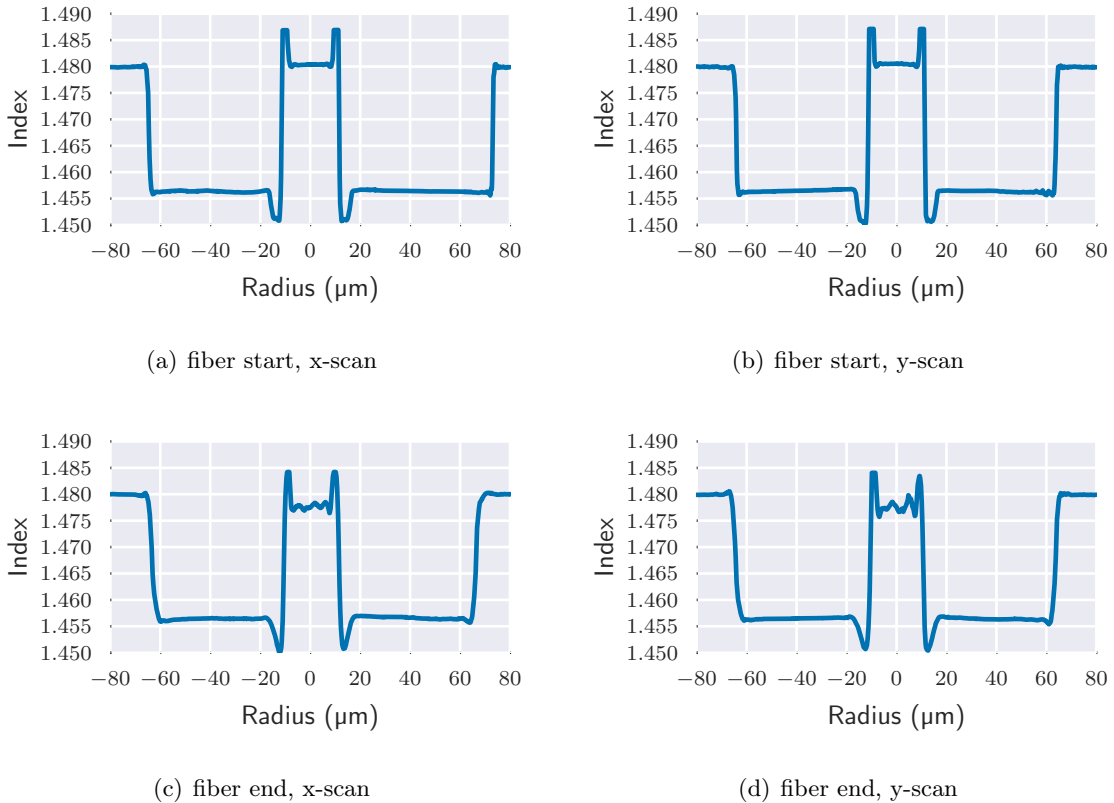


Figure 7.4: Refractive index measurement of the air-core annular fiber, at 657.6 nm. Measurements performed by Stéphane Gagnon.

Table 7.4: Parameters of air-core annular fiber model.

	Radius (μm)	Molar concentration (%)	Index (1550 nm)	Index (657.6 nm)
Layer 1	9.1	—	1.000	1.000
Layer 2	11.3	19.2	1.475	1.487
Layer 3	16.2	1.3	1.438	1.450
Cladding	62.5	—	1.444	1.456

effective indexes. Results are summarized on Figure 7.7 and in Table 7.5. From this new simulation, we expect the ACF to support 16 vector modes, or 8 OAM modes ($\ell = 0$ to $\ell = 7$, for a total of 28 OAM states).

7.4 Exciting OAM modes in ACF

To excite OAM modes in ACF, we use a setup similar to what is described in [93], generating the OAM beam in free-space using a SLM, before coupling the OAM beam into the fiber. However, we faced an unexpected problem: lower-order OAM beams are thicker than the thin $2\mu\text{m}$ ring where the modes propagate in our fiber, because, in free-space, the ratio between

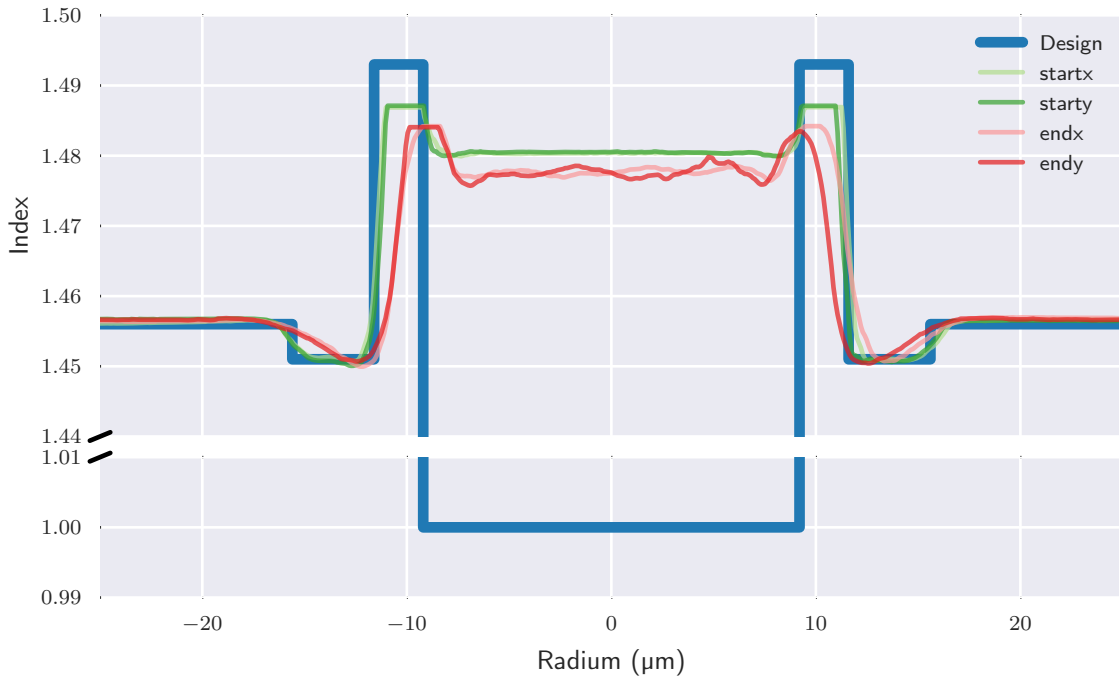


Figure 7.5: Comparison between ACF design and realized fiber profiles.

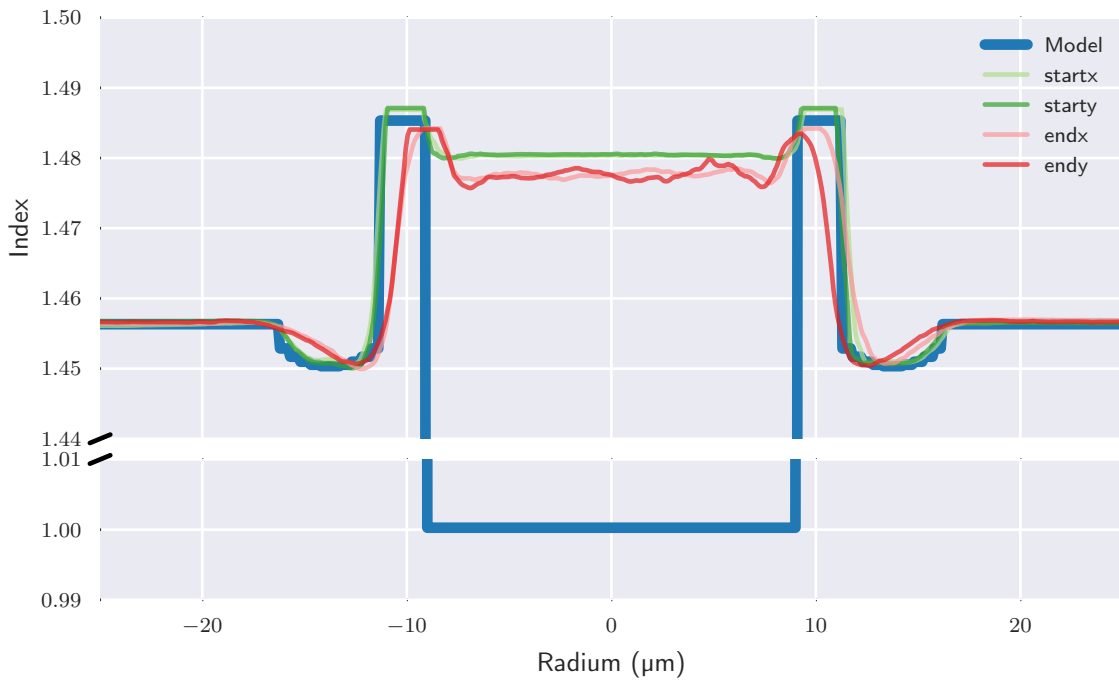


Figure 7.6: Comparison between realized fiber profiles and ACF model.

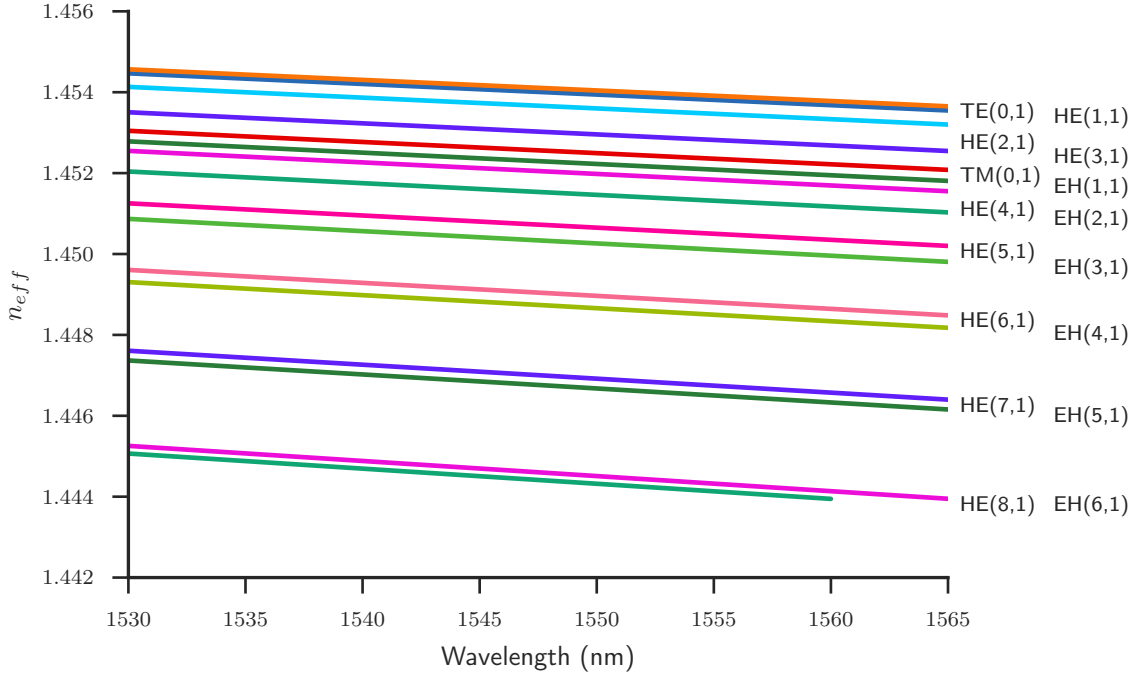


Figure 7.7: Effective index as function of wavelength, for ACF model. Fiber model parameters are given in Table 7.4.

Table 7.5: Effective indexes and effective index separations, at 1550 nm, for ACF model.

Mode	n_{eff}	Δn_{eff}	Mode	n_{eff}	Δn_{eff}
TE _{0,1}	1.453 91	1.019×10^{-4}	HE _{5,1}	1.450 50	3.911×10^{-4}
HE _{1,1}	1.453 81	1.019×10^{-4}	EH _{3,1}	1.450 11	3.911×10^{-4}
HE _{2,1}	1.453 47	3.443×10^{-4}	HE _{6,1}	1.448 80	3.058×10^{-4}
HE _{3,1}	1.452 82	4.644×10^{-4}	EH _{4,1}	1.448 50	3.058×10^{-4}
TM _{0,1}	1.452 36	2.693×10^{-4}	HE _{7,1}	1.446 74	2.424×10^{-4}
EH _{1,1}	1.452 09	2.496×10^{-4}	EH _{5,1}	1.446 50	2.424×10^{-4}
HE _{4,1}	1.451 84	2.496×10^{-4}	HE _{8,1}	1.444 32	1.900×10^{-4}
EH _{2,1}	1.451 32	5.192×10^{-4}	EH _{6,1}	1.444 13	1.900×10^{-4}

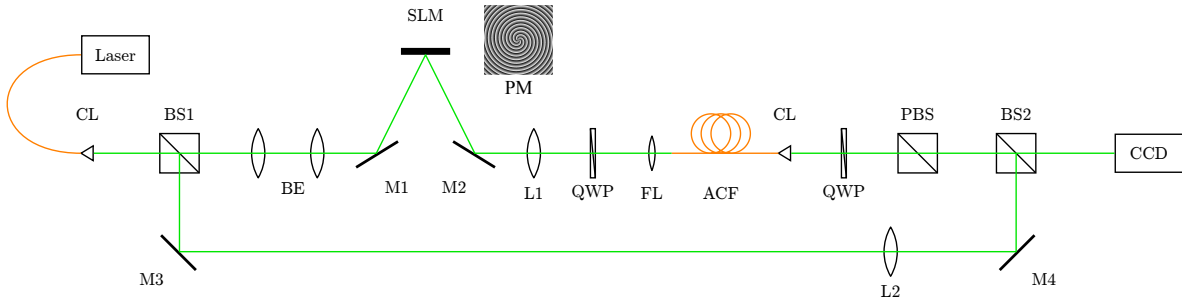


Figure 7.8: Experimental setup for the generation and the transmission of OAM through air-core annular fiber. CL: fiber collimator; BS: non-polarizing beam-splitter; BE: beam expander; M: mirror; SLM: spatial light modulator; PM: phase mask; L: lens; QWP: quarter wave plate; FL: focusing lens; ACF: air-core fiber; PBS: polarizing beam splitter; CCD: ccd camera.

inner and outer radius of the doughnut beam is a function of the topological charge ℓ [139]:

$$\mathbf{E}(x, y) \propto (x \cdot jy)^{|\ell|} \exp \left\{ - \left(\frac{x^2 + y^2}{w^2} \right) \right\} \quad (7.1)$$

where w is the Gaussian beam radius at focus. Dr. Pravin Vaity solved the coupling problem using what we call a *perfect vortex beam*, an OAM beam where both inner and outer radius can be controlled [140].

Figure 7.8 shows the experimental setup for coupling of a perfect OAM beam with different topological charges into air-core annular fiber. The beam from a semiconductor laser with a single mode fiber patch cord is collimated by a collimating lens. The beam is split in two parts. A single perfect OAM mode is generated per the method described in the previous section. As the SLM requires linearly polarized light, a quarter wave plate converts the beam to right or left circularly polarized light, before it is coupled into the fiber. At the output of the fiber, a quarter wave plate and a polarizing beam splitter are used to bring the beam back to linear polarization. Finally, the beam is interfered with the second part of the incident beam, to get the characteristic spiral pattern that allows the identification of OAM beams.

In Fig. 7.9 and 7.10, we present experimental results after propagation of OAM modes in 85 cm of our air-core fiber. We excited and observed nine different OAM orders ($\ell = 1$ to 9), as well as the fundamental mode. The presence of OAM in the generated modes is confirmed through interferometry. The number of spiral arms is equal to the topological charge of the mode. We also confirmed excitation of both positive and negative order OAM modes, in both right- and left- circular polarization, confirming that a total of 36 information bearing modes, with topological charges from $\ell = 0$ to $\ell = 9$, are supported by this ACF. Unfortunately, we were not able to transmit OAM modes over a longer fiber span, due to the high insertion losses we faced. Experimental manipulations were performed by Dr. Pravin Vaity.

Experiments demonstrated that the number of supported modes in the air-core annular fiber is greater than what was expected from simulation (two more OAM modes than expected).

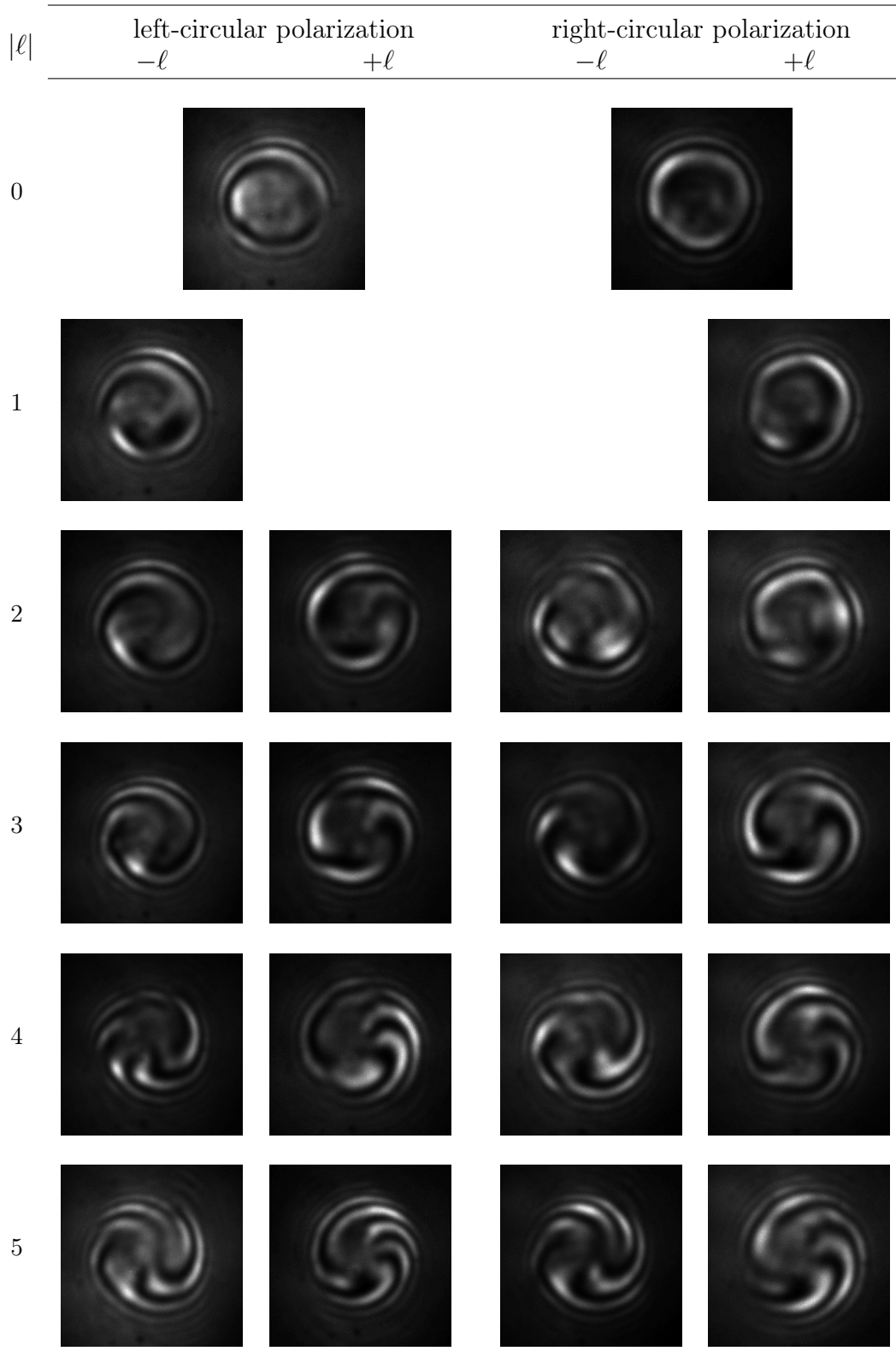


Figure 7.9: OAM beam interference with Gaussian beam, after transmission in fiber ($\ell = 0$ to 5). [Credit: Pravin Vaity.]

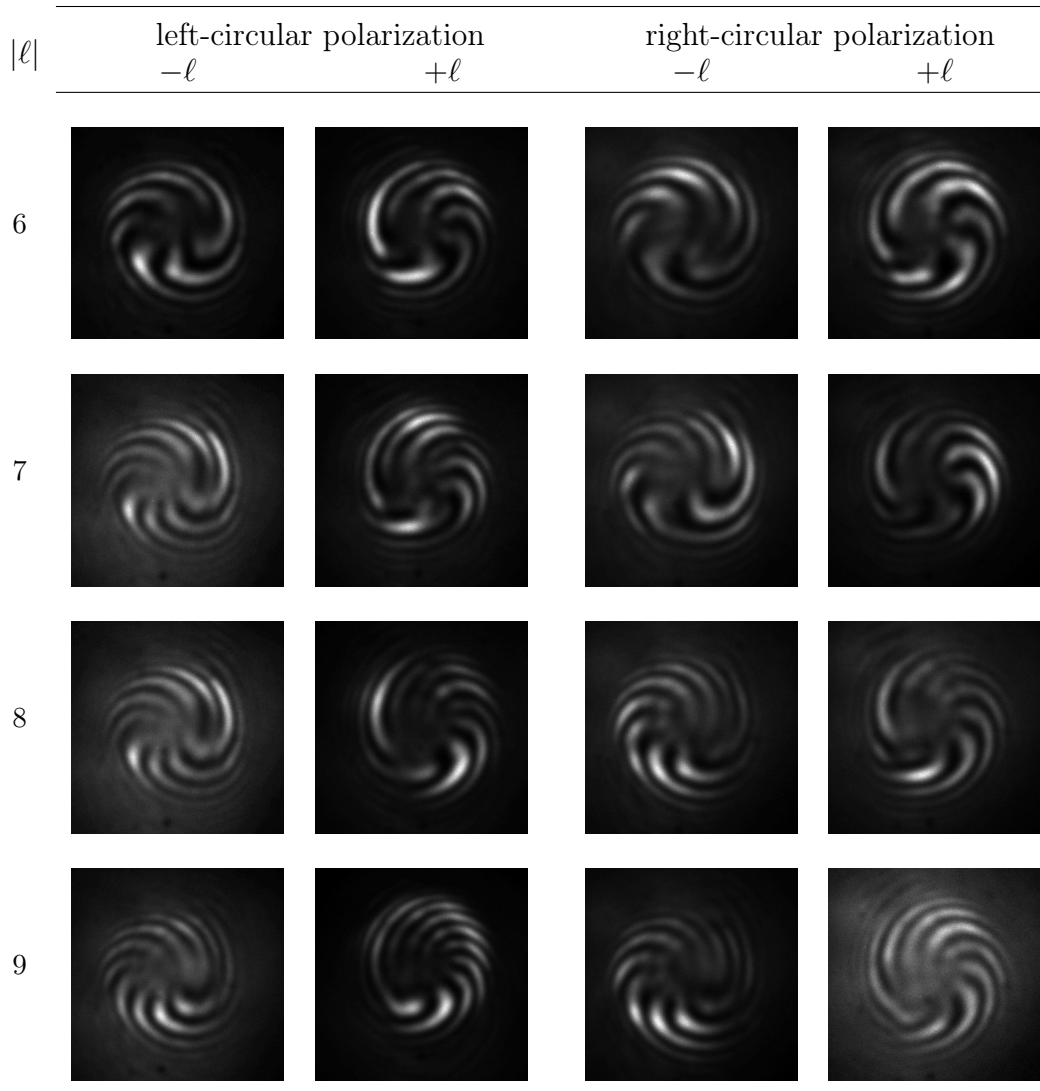


Figure 7.10: OAM beam interference with Gaussian beam, after transmission in fiber ($\ell = 6$ to 9). [Credit: Pravin Vaity.]

However, the fiber was very short, and we suspect these higher modes are less stable and slowly leaking, because we consistently observed heightened sensitivity to fiber perturbations for modes $\text{OAM}_{8,1}$ and $\text{OAM}_{9,1}$. Therefore, the number of observed modes is consistent with predictions.

We proposed a fiber profile able to guide a large number of OAM modes. Such fiber could have applications in short-reach telecommunications, or in any field where the transmission of different OAM modes through optical fiber could be useful. We proposed a novel way of shaping OAM beams, to form perfect vortex beams that can match annular fiber profiles. This kind of beam shaping is necessary because conventional free-space OAM beams usually do not match the profile of annular-core fibers. Using perfect OAM beam generation, we now have

a tool that gives the freedom of being able to couple OAM beams with any desired annular fiber profile. Finally, we successfully demonstrated the transmission of OAM modes through a special designed fiber. To the best of our knowledge, this is the highest reported number of OAM modes transmitted through an optical fiber.

Chapter 8

A family of ring-core fibers

We know that, to support OAM modes, the fiber must exhibit 1) large effective index separation between vector modes to minimize intermodal coupling between OAM modes and to avoid degeneracy into LP modes, and 2) a fiber profile that is compatible with the doughnut shaped OAM fields. Those two characteristics lead to the choice of a fiber design with an annular profile, or a ring-core fiber (RCF), with a high index contrast [84].

The fiber proposed in Chapter 7 had both those characteristics. However, it was designed using iterative search through numerical simulations, without a theoretical model to justify the optimality of the chosen parameters. Thus it is difficult to compare experimental results obtained using this fiber with an analytical model to explain them. To get a deeper understanding of the OAM modes in optical fibers, we decided to design a simpler fiber. The goal is not to propose a better fiber than the one proposed in the preceding chapter, but to obtain a fiber that will be easier to describe using theoretical models.

For ease of both analysis and fabrication, we target the design, production, and characterization of a simple step-index, ring-core profile (RCF). While more complex profiles, e.g., with graded index [98], with hollow core [95], or with a trench of lower index in the cladding [2], could potentially improve fiber performance, their design cannot be tackled as easily analytically. Our interest is twofold: first system performance, but also greater understanding of parameter impact on performance in the transition from design to fabrication. We have a theoretical basis to relate step-index parameters to fiber characteristics such as number of supported modes and their relative effective index separation. By concentrating on step-index RCF we can relate measured fiber characteristics to design parameters in a straightforward manner.

8.1 Choice of fiber parameters

In the design of an optical fiber, many parameters need to be determined. Some parameter values are imposed by physical constraints, e.g., the use of a silica cladding, or a given fiber fabrication process. Other parameter values are determined by the characteristics we want to achieve. We must also take into account the potential impact of fiber imperfections induced by the fabrication process.

Because fiber preform produced by the modified chemical vapor deposition (MCVD) process is the costliest part of fiber fabrication, we adopt a novel technique to sweep parameters of a family of OAM fibers at comparable cost to a single fiber fabrication. The family of fibers could be created by drawing five different fibers from a single preform. By changing the drawing speed at several points in the fiber drawing, we will create fibers with different diameters. As no couplers or definite diameters currently exist for OAM-transmitting fibers, we thought this would incur no greater experimental difficulty, as a free-space coupling system must be used in any case. This was a mistake. A better approach would be to etch the fiber preform to achieve a standard 125 μm fiber diameter, for each drawn fiber.

The ratio between the inner and outer radius of the core will remain constant, but each fiber will have different modal characteristics. In theory, one fiber will be superior to the other (the true design target), however variations during the fabrication of the fiber could favor a neighboring target value. More importantly, we will produce many closely related fiber specimens, facilitating experimental comparisons and inferences for our design process.

The first design goal to be set is the number of modes we want our fiber to support. The fundamental mode ($\text{HE}_{1,1}$ or $\text{LP}_{0,1}$) is always present and can be used for multiplexing, however, it is not really an OAM mode as it cannot carry orbital angular momentum (topological charge is zero). The first OAM modes are $\text{OAM}_{\pm 1,1}$, based on the $\text{HE}_{2,1}$ vector mode. The second set of OAM modes is $\text{OAM}_{\pm 2,1}$ composed of $\text{HE}_{3,1}$ or $\text{EH}_{1,1}$ modes. We elected to target three fibers supporting $\text{OAM}_{\pm 1,1}$ modes and two fibers supporting both $\text{OAM}_{\pm 1,1}$ and $\text{OAM}_{\pm 2,1}$ modes. The family of fibers we design will then have three fibers supporting four information channels, and two fibers supporting eight information channels.

The RCF profile was illustrated in Chapter 4, on Fig. 4.1. We target a specific ratio $\rho = r_1/r_2$ constant across fibers, a value used for the production of the preform. The external cladding diameter Φ_{clad} must be between 80 μm and 200 μm , otherwise the fiber would be too fragile. The value of n_1 is determined by the refractive index of the silica cladding. The refractive index of the ring-core can be varied by adjusting the composition of the glass. Finally, to favor the transmission of OAM modes, we will target a refractive index separation Δn_{eff} only slightly above a 1×10^{-4} threshold. This was demonstrated to reliably support OAM modes [40, 95]. All these criteria are summarized in Table 8.1.

Table 8.1: List of design criteria for RCF family.

Parameter	Target
#1 Number of information channels (number of OAM modes)	
– Fibers 1, 2, 3	4 (2)
– Fibers 4, 5	8 (3)
#2 Inner / outer core radius ratio $\rho = r_1/r_2$	fixed
#3 Cladding diameter	$80 \mu\text{m} \leq \Phi_{\text{clad}} \leq 200 \mu\text{m}$
#4 Minimum effective index separation	$\Delta n_{\text{eff}} \geq 1 \times 10^{-4}$

Table 8.2: RCF fiber index parameters.

Wavelength	λ	657.6 nm	1550 nm
Cladding (silica)	n_1	1.456	1.444
Ring core (SiO_2GeO_2)	n_2	1.487	1.474
Molar fraction of GeO_2 in SiO_2	X		0.20
Refractive index contrast	Δn		0.030

A high refractive index contrast favors the separation of the effective indexes of the modes [2, 95, 98]. However, material constraints must be considered, as too high GeO_2 doping causes the glass to break. We therefore fix n_2 to the highest possible value we can reach without compromising the integrity of the preform. This value will be $\Delta n = n_2 - n_1 = 0.03$ at $\lambda = 1550 \text{ nm}$. This corresponds to a 20% molar fraction of GeO_2 in SiO_2 . We neglect the presence of any other materials, such as phosphorus, that might be present in the doped silica. Material indexes are modeled using formulas presented in Appendix B. The fiber refractive index parameters used in our simulations are summarized in Table 8.2.

Having fixed refractive indexes n_1 and n_2 , the choice of inner and outer radii r_1 and r_2 remains, as it will determine the number of guided modes supported by the fiber, and the minimal distance Δn_{eff} between the effective indexes of the supported modes.

In Chapter 4, we developed cutoff equations for RCF. In Chapter 6, we presented the modal map, a tool to help in fiber design. We will now use this tool to design our family of fibers. In Fig. 8.1, we plot an augmented modal map, using the fiber parameters determined so far. Regions delimited by cutoff curves give us the number of guided modes supported by a given fiber design.

Consider the four regions delimited by the black cutoff curves. The white region (labeled I) is where parameters lead to a monomode fiber. This region is separated from the next region by the cutoffs for $\text{TE}_{0,1}$, $\text{TM}_{0,1}$, and $\text{HE}_{2,1}$ modes (curves are superimposed). In the next region (II), fiber supports $\text{OAM}_{\pm 1,1}$ mode, and Δn_{eff} is the minimal separation between $\text{TE}_{0,1}$, $\text{TM}_{0,1}$, and $\text{HE}_{2,1}$ modes. Then we have the cutoffs of $\text{EH}_{1,1}$ and $\text{HE}_{3,1}$ modes (curves tightly spaced).

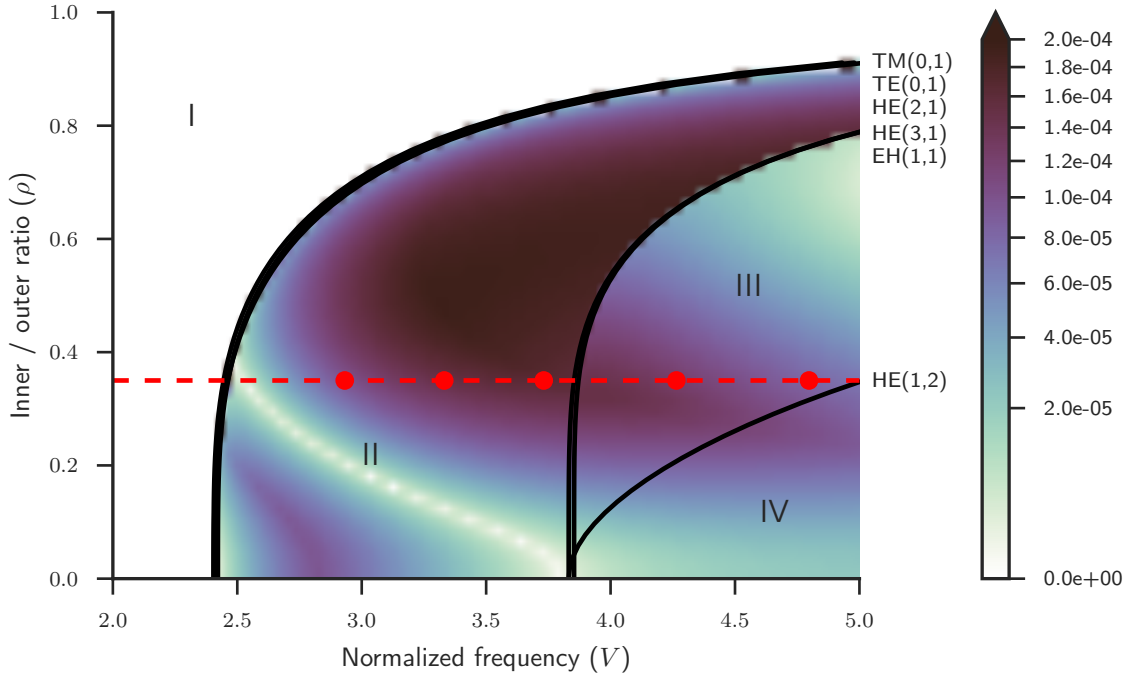


Figure 8.1: Augmented modal map, as function of core radius ratio ρ and normalized frequency V . Horizontal red dashed line is the chosen ρ parameter, while dots indicate chosen fiber parameters. For the simulation, $n_1 = 1.444$ and $n_2 = 1.474$.

The third region (III) corresponds to fibers supporting both $\text{OAM}_{\pm 1,1}$ and $\text{OAM}_{\pm 2,1}$ modes. In that region Δn_{eff} refers to the minimum mode separation within both families. Finally, at bottom right we have the cutoff of $\text{HE}_{1,2}$ mode; the region under that line (IV) also includes all other modes and $\text{HE}_{1,2}$. We want to avoid that region, because modes with higher radial order (i.e., with $m \geq 2$) are more difficult to multiplex and demultiplex. The $m = 1$ solution with a single intensity ring have been the focus of data transmission demonstrations as they are easier to manipulate, given the paucity of components available today for OAM. There is the added complication of finding a design that avoids crosstalk between modes of different radial order, since modes with $m > 1$ have effective indexes with a different slope, resulting in effective index curves that cross at some wavelengths, thereby causing Δn_{eff} to become very small.

The goal is to choose a fixed value of ρ (the ordiant) along which five values of V (the abscissa), so as to obtain five targeted fibers with large Δn_{eff} , preferably above our threshold of 1×10^{-4} , i.e., as dark as possible in the colormap and avoiding lighter colors. We also want to avoid modes with m parameter greater than one, otherwise the fiber would support modes having concentric rings of intensity in their fields. Finally, it is desirable to have fiber parameters that are significantly away from cutoff, as modes near cutoff are less tolerant to fiber imperfections. The set of five fibers, once fabricated, will allow us to compare the simulated

Table 8.3: Geometry of the designed RCF fibers (rounded to the second decimal).

Fiber	r_1	r_2	Φ_{clad}	V (1550 nm)
1	0.86 μm	2.44 μm	110 μm	2.9318
2	0.97 μm	2.78 μm	125 μm	3.3316
3	1.09 μm	3.11 μm	140 μm	3.7314
4	1.24 μm	3.56 μm	160 μm	4.2644
5	1.40 μm	4.00 μm	180 μm	4.7975

Table 8.4: Effective indexes of the modes in RCFs (at 1550 nm).

Fiber	HE _{1,1}	TE _{0,1}	HE _{2,1}	TM _{0,1}	EH _{1,1}	HE _{3,1}
1	1.4584	1.4480	1.4478	1.4477	—	—
2	1.4601	1.4515	1.4513	1.4511	—	—
3	1.4615	1.4544	1.4543	1.4541	—	—
4	1.4630	1.4576	1.4575	1.4573	1.4474	1.4473
5	1.4643	1.4601	1.4600	1.4598	1.4514	1.4513

characteristics with measured fiber properties. The first three should support the LP_{1,1} mode group (OAM_{1,1}) and the two last ones should also support the LP_{2,1} mode group (OAM_{2,1}). Taking the goals as described, we chose a design illustrated in Fig. 8.1 by a horizontal red dashed line at the selected value of $\rho = 0.35$. Five dots for the V values selected correspond to the five values of r_1 and r_2 indicated in Table 8.3. Fiber 1 has the smallest cladding diameter, while fiber 5 has the thickest.

8.2 Simulation of modal properties

Effective indexes of the different modes are numerically calculated using the transfer-matrix method [118]. Results are summarized in Table 8.4. We also plot, in Fig. 8.2, normalized propagation constant as a function of normalized frequency for all the guided modes. In this figure, vertical dotted lines indicate V for the different fibers when $\lambda = 1550$ nm. For the transmission of OAM modes, we are interested in the separation between the effective indexes within a mode group (Δn_{eff}). We target this separation to be as large as possible, and at least 1×10^{-4} (criteria #4). The calculated effective index separations are given in Table 8.5, and plotted on Fig. 8.3. As we can see, our design criteria is respected for three fiber designs, but not for fiber 1 and fiber 5. This will allow us to test the stability of OAM modes vis-à-vis our threshold of 1×10^{-4} .

We saw in Chapter 1, that the group velocity is related to the first derivative of the effective index (1.49). The derivative of the effective index is calculated, using five-points stencil (see Section A.4), to obtain the group index (1.50). On Fig. 8.4, we plot the group index as function of the core radius, for our RCF design (19% GeO₂ doping in the ring-core), at 1550 nm. In

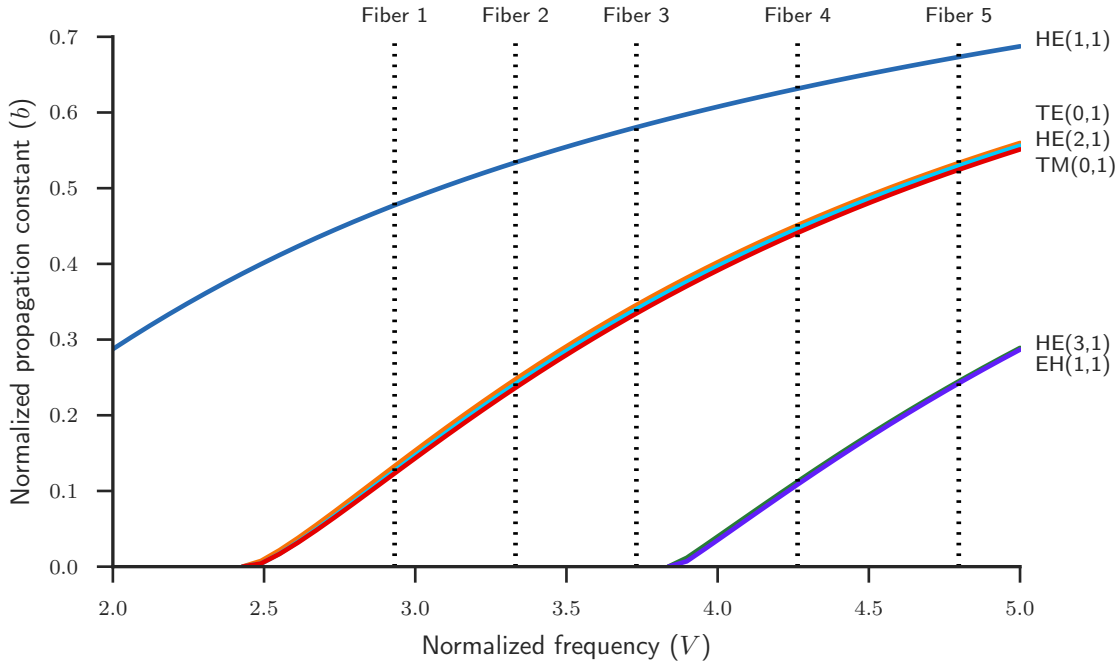


Figure 8.2: Normalized propagation constant as function of normalized frequency, in RCF. $\lambda = 1550$ nm, $\rho = 0.35$, $n_1 = 1.444$, $n_2 = 1.474$.

Table 8.5: Effective index separation within mode groups (at 1550 nm).

Fiber	TE _{0,1} -HE _{2,1}	HE _{2,1} -TM _{0,1}	EH _{1,1} -HE _{3,1}
1	1.9475×10^{-4}	9.8276×10^{-5}	—
2	1.8798×10^{-4}	1.4943×10^{-4}	—
3	1.6817×10^{-4}	1.6715×10^{-4}	—
4	1.4076×10^{-4}	1.6484×10^{-4}	1.2135×10^{-4}
5	1.1757×10^{-4}	1.5067×10^{-4}	8.0648×10^{-5}

this case, we no longer can use the V number for the x -axis, as group index is influenced differently by wavelength and by core radius. Plotting it as function of the core radius is the only way to display all five fibers on the same graph. Group index values for the five RCF are summarized in Table 8.6.

8.3 Fiber fabrication

The optical fibers were fabricated in-house with modified chemical vapor deposition (MCVD) and fiber drawing facilities. Two steps were used in order to produce the correct preform geometry. First, adequate concentrations of SiO₂ and GeO₂ were deposited to produce the ring core layer, followed by a deposit of SiO₂ to match the index profile cladding. Finally, the

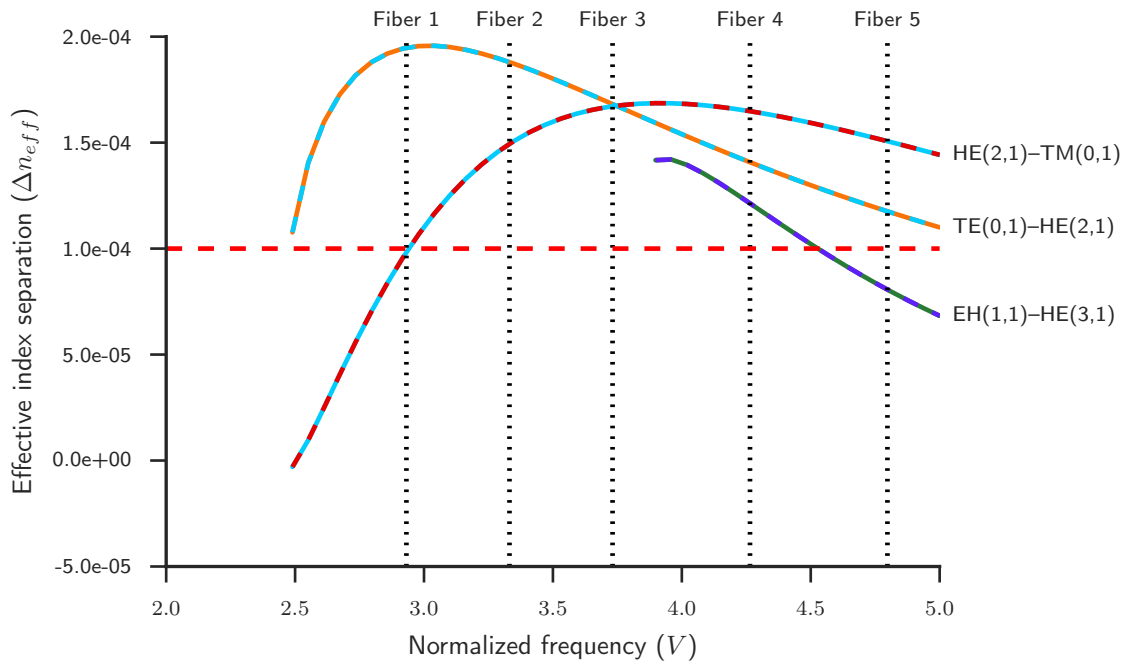


Figure 8.3: Effective index separation, in RCF. $\lambda = 1550 \text{ nm}$, $\rho = 0.35$, $n_1 = 1.444$, $n_2 = 1.474$.

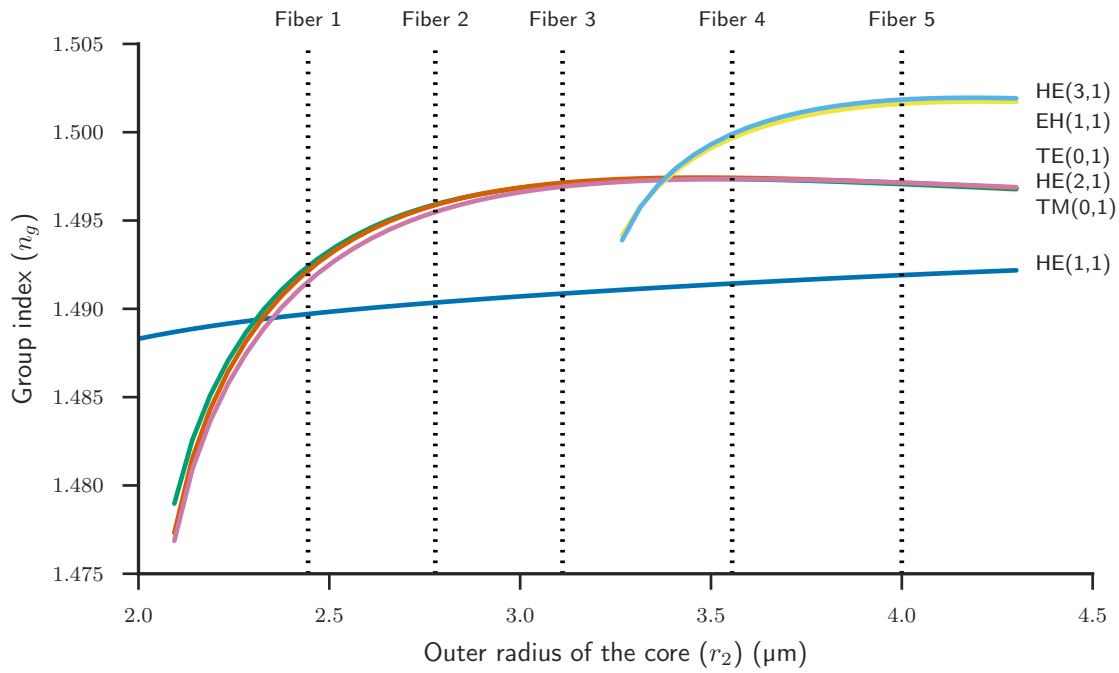


Figure 8.4: Group index of RCF, as function of outer radius of the ring-core (r_2). $\lambda = 1550 \text{ nm}$, $\rho = 0.35$, $n_1 = 1.444$, $n_2 = 1.474$.

Table 8.6: Group indexes of the modes in RCFs (at 1550 nm).

Fiber	HE _{1,1}	TE _{0,1}	HE _{2,1}	TM _{0,1}	EH _{1,1}	HE _{3,1}
1	1.4897	1.4924	1.4922	1.4915	—	—
2	1.4904	1.4959	1.4959	1.4955	—	—
3	1.4909	1.4971	1.4971	1.4969	—	—
4	1.4914	1.4973	1.4974	1.4974	1.4997	1.4999
5	1.4919	1.4971	1.4971	1.4971	1.5016	1.5019

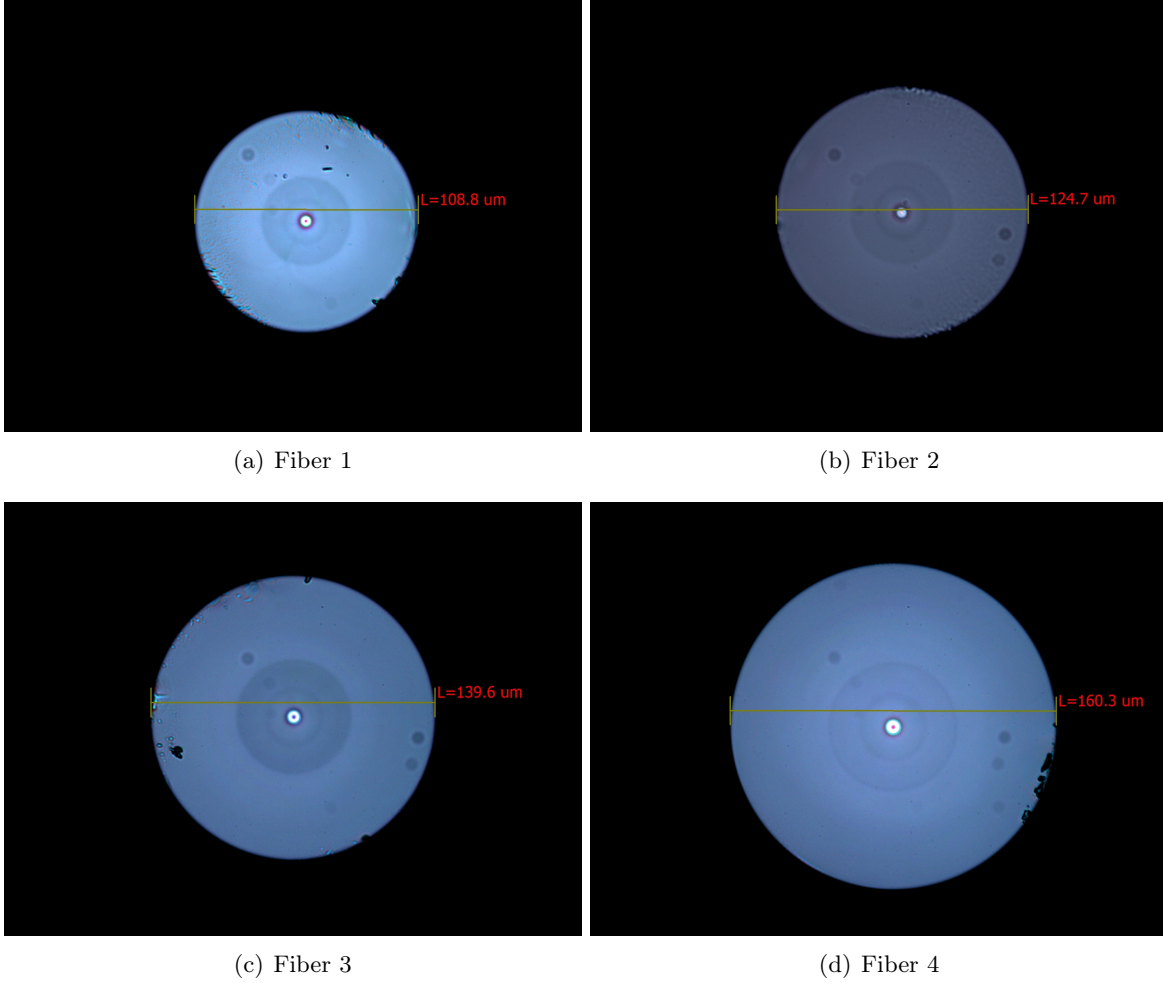


Figure 8.5: Optical microscope photographs of RCFs [Credit: Steeve Morency].

tube was collapsed to produce the glass preform. The ring-core diameter was controlled during the fiber drawing process to achieve the desired geometry of the fiber. Figure 8.5 shows optical microscope photographs of the fiber ends, for RCF fibers 1 to 4 (we did not take photograph of fiber 5). Measured diameter is displayed. The ring-core is the bright circle in the middle of the fiber.

The fiber refractive index profile (RIP) of fibers 2, 3, and 4 was measured using an EXFO NR-9200 refractometer, operating at 657.6 nm. On Fig. 8.6, we plotted the measured profiles (orange), compared the the designed profile (green). We only show the measurement for the center of the fiber ($|r| < 10 \mu\text{m}$) to clearly see the profile of the ring-core. As we can see, the fabricated fiber is a relatively good match to the designed profile, but the step transitions are smoother than expected. This could be caused by the fabrication process; it is also possible that the $0.4 \mu\text{m}$ spatial resolution of the RIP profiler exaggerates this smoothness.

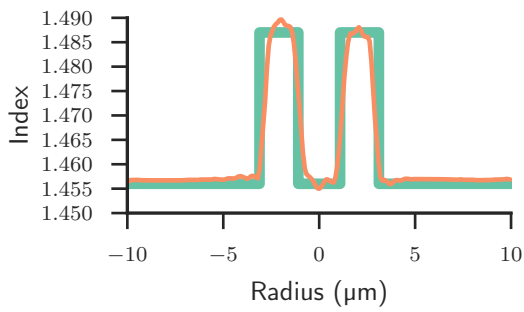
We successfully transmitted OAM modes through the fabricated fibers, generating OAM modes in free-space using a spatial light modulator (SLM), and coupling the OAM beam into the fiber. The ring intensity profile was measured, as well as an interference pattern confirming the characteristic OAM spiral form. Representative measurements for fiber 2, after transmission through 2 m, are presented in Fig. 8.7. The intensity profile is not as perfectly ring-shaped for all fiber samples, especially when transmitting over a longer distance, because of the coupling between modes. However, in all cases, including transmissions between 1 and 1.5 km, we could visualize the spiral interference pattern, confirming the presence of the launched OAM modes. Coupling into RCF4 and RCF5 was particularly challenging due to the size of fiber (poor match with available bare fiber adapters) and, in the case of RCF5, its brittleness.

8.4 Effective index measurement

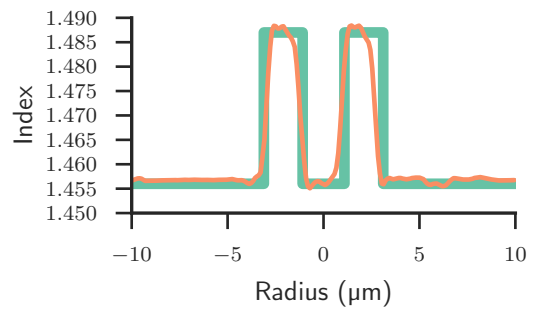
To verify calculated values for effective index, we wrote a weak FBG on the fibers, then we analyzed the reflectogram, using the method described in [141]. The designed grating length is 40 mm with a tanh shape apodization (coefficient $s = 4$), and the mask period is $\Lambda_{\text{PM}} = 1070 \text{ nm}$. For each fiber design, we measured the Bragg reflection on three different samples, and we averaged the wavelength positions of the reflection peaks. A sample reflectogram is given on Fig. 8.8. Figure 8.9 was generated by taking reflectograms for all five fibers (including that shown in Fig. 8.8), scaling each reflectogram so that the peak values appear similar, and plotting them along a common x -axis. The y -axis remains roughly in dB and relative heights within a reflectogram are noteworthy, however absolute heights from reflectogram to reflectogram convey no information. FBG writing and reflection measurements were performed by Dr. Lixian Wang.

On fibers 1 and 3, we measured four different peaks on the second mode group, instead of the three expected peaks. We suspect the two central peaks to be the result of birefringence, caused by fiber imperfections. Therefore, we considered the average between the wavelengths of those two peaks as the reflection wavelength of the $\text{HE}_{2,1}$ mode.

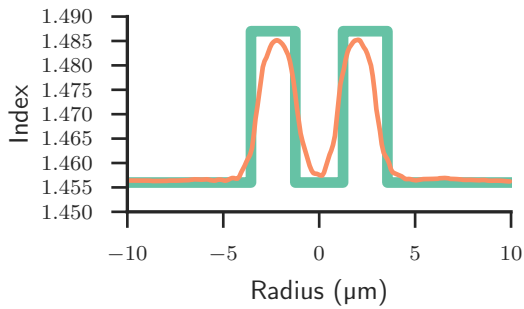
We cannot rely on the absolute measured n_{eff} values, as many parameters can shift this value, e.g., fiber stress during FBG writing and temperature when performing the measurement.



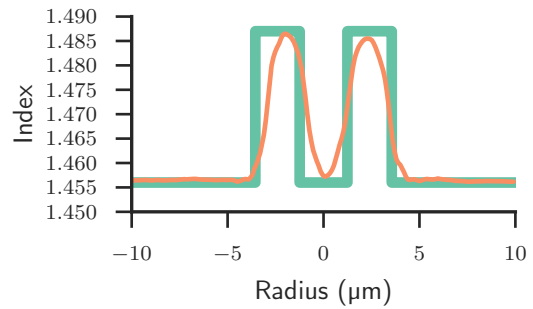
(a) fiber 2, x-scan



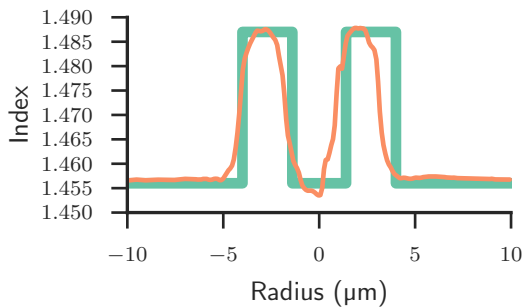
(b) fiber 2, y-scan



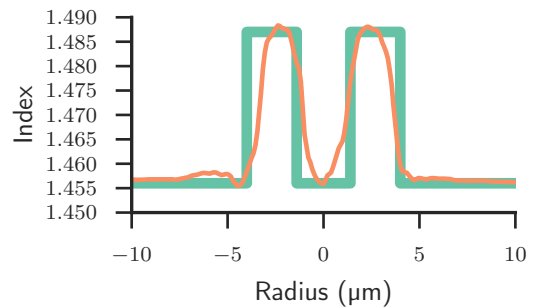
(c) fiber 3, x-scan



(d) fiber 3, y-scan



(e) fiber 4, x-scan



(f) fiber 4, y-scan

Figure 8.6: Refractive index measurement of ring-core fibers, at 657.6 nm. Measurements performed by Patrick LaRochelle.

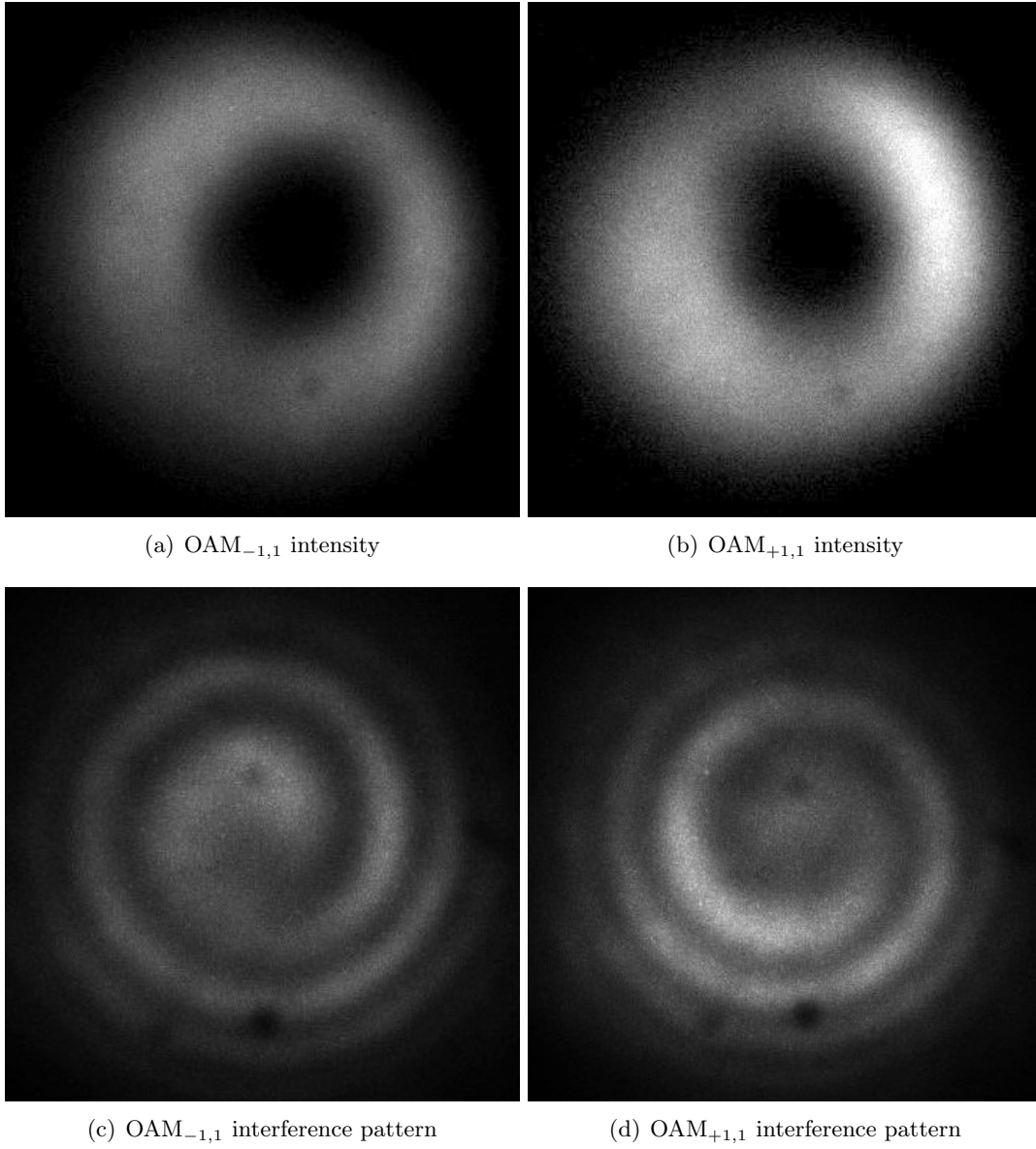


Figure 8.7: Output intensity profiles after 2 m transmission of OAM mode in ring-core fiber 2 [Credit: Pravin Vaity].

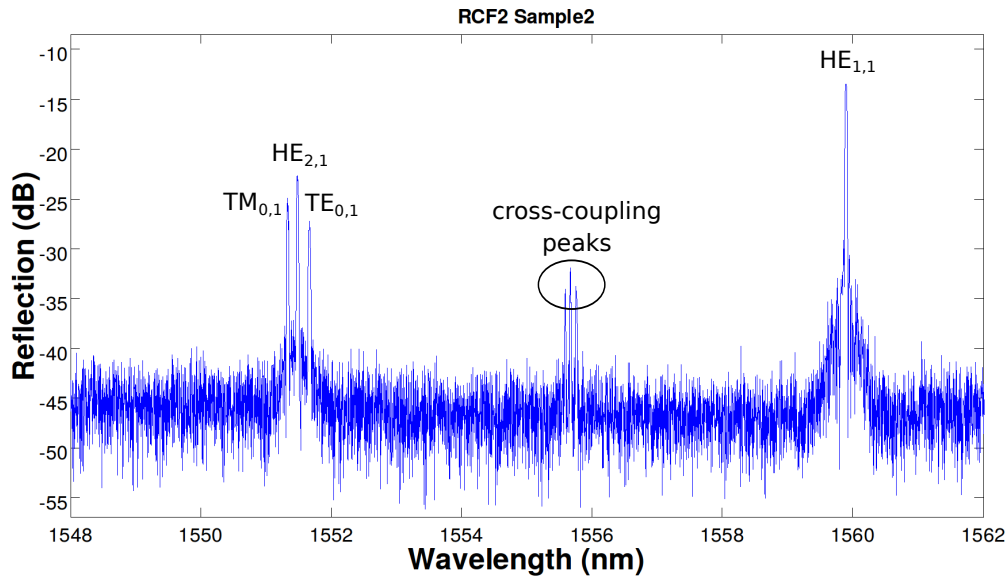


Figure 8.8: FBG reflectogram for RCF 2 (sample 2). Measures performed by Lixian Wang.

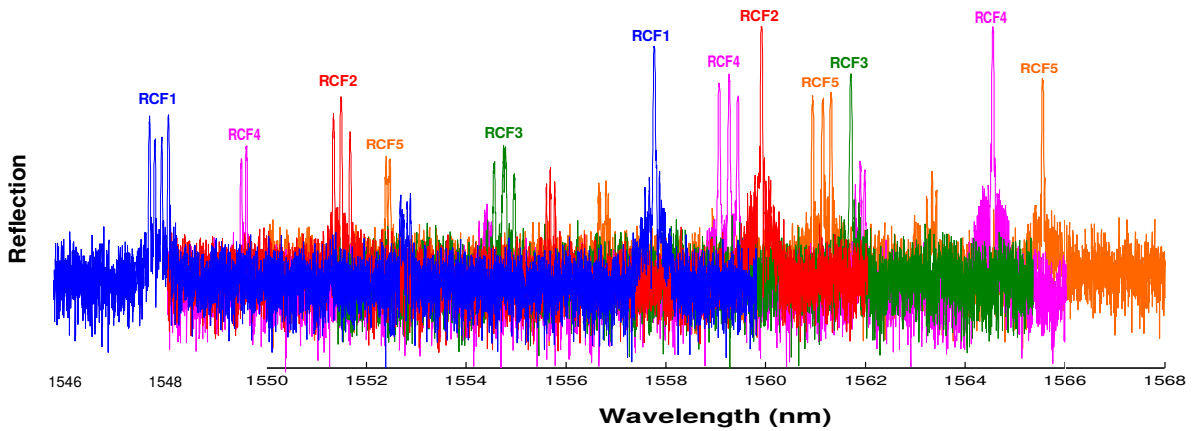


Figure 8.9: Superimposed FBG reflectogram for all RCFs. This allows comparison of reflection wavelengths for the different fibers. All reflectogram were vertically aligned and scaled to fit the graph, hence absolute heights from reflectogram to reflectogram convey no information. Measurement performed by Lixian Wang.

Table 8.7: Δn_{eff} measured values (using FBG), compared to calculated values.

		TE _{0,1} – HE _{2,1}	HE _{2,1} – TM _{0,1}	EH _{1,1} – HE _{3,1}
Fiber 1	measured Δn_{eff}	1.83×10^{-4}	1.62×10^{-4}	
	simulated Δn_{eff}	1.89×10^{-4}	0.94×10^{-4}	
	absolute error	0.65×10^{-5}	6.83×10^{-5}	
	relative difference	3.56%	42.13%	
Fiber 2	measured Δn_{eff}	1.68×10^{-4}	1.41×10^{-4}	
	simulated Δn_{eff}	1.83×10^{-4}	1.45×10^{-4}	
	absolute error	1.52×10^{-5}	0.40×10^{-5}	
	relative difference	9.09%	2.82%	
Fiber 3	measured Δn_{eff}	1.79×10^{-4}	1.92×10^{-4}	
	simulated Δn_{eff}	1.64×10^{-4}	1.61×10^{-4}	
	absolute error	1.54×10^{-5}	3.07×10^{-5}	
	relative difference	8.62%	16.00%	
Fiber 4	measured Δn_{eff}	1.66×10^{-4}	1.85×10^{-4}	0.95×10^{-4}
	simulated Δn_{eff}	1.38×10^{-4}	1.60×10^{-4}	1.18×10^{-4}
	absolute error	2.83×10^{-5}	2.44×10^{-5}	2.27×10^{-5}
	relative difference	17.07%	13.21%	23.83%
Fiber 5	measured Δn_{eff}	1.54×10^{-4}	1.91×10^{-4}	0.71×10^{-4}
	simulated Δn_{eff}	1.15×10^{-4}	1.47×10^{-4}	0.79×10^{-4}
	absolute error	3.86×10^{-5}	4.45×10^{-5}	0.74×10^{-5}
	relative difference	25.13%	23.24%	10.42%

However, since we expect the effective indexes of all modes to shift together, we can compare the measured effective index separation within mode groups (Δn_{eff}) with the predicted values. Results are summarized in Table 8.7. The relative difference is given by the absolute error divided by the measured Δn_{eff} . As we can see, there is some variation between measured and simulated values. However, this variation always is at the fifth or the sixth decimal of the effective index. We compare very small values, and the difference can be attributed to both non-ideal fabricated fiber – e.g., longitudinal variation of the index profile along the fiber, core ellipticity (i.e., form birefringence), any bends of the fiber, and environmental variations (moving air, temperature, etc.) – and measurement errors.

8.5 Group index measurement

The group index (n_g) is relative to the propagation speed of a pulse, for a given mode in a given fiber. It is related to the group velocity (v_g), and can be measured from the time it

Table 8.8: Lengths of ring-core fibers used for time-of-flight experiment.

Fiber	RCF1	RCF2	RCF3	RCF4	RCF5
Length (m)	1500	1580	1500	1130	1170

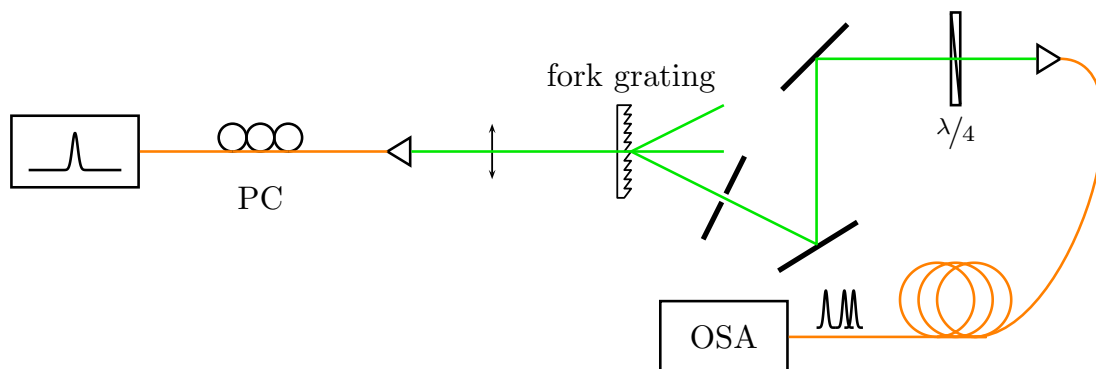


Figure 8.10: Experimental setup for TOF using fork-grating.

takes for a pulse (T_g) to be transmitted through a given length of fiber (L).

$$n_g = \frac{c}{v_g} = \frac{cT_g}{L} \quad (8.1)$$

However, directly measuring the velocity of a pulse can be complex. We rather send a train of pulses through a length of fiber, and we synchronize the output on an oscilloscope. This way, we can precisely measure the delay between two pulses (ΔT_g), to get the relative group index (Δn_g).

For the experiment, we sent a 40 ps optical pulse that repeats every 51.2 ns, through a fiber sample. The length of each fiber sample is summarized in Table 8.8, and was determined by the availability of each fiber. Because the SLM is sensible to high peak power, we used a fork grating, imprinted in a glass plate, to generate OAM modes that we coupled into the fiber. This was necessary to get enough power at the end of the fiber. By adjusting the position of the fiber relatively to the incident beam, it was possible to excite the different modes of the fiber altogether. Finally, a quarter wave-plate allowed to favor either OAM $_{\pm 1,1}$ (HE $_{2,1}$), or TE $_{0,1}$ and TM $_{0,1}$ modes. Experimental setup is illustrated on Fig. 8.10.

Experiment results are plotted on Fig 8.11, for input with linear polarization. The horizontal axis is the time scale; the zero on this axis is arbitrary as it is related to the synchronization of the oscilloscope. Vertical axis is in logarithmic scale, and gives the read voltage. We did not displayed the voltage values, as this is also arbitrary. The important data from those figures is the relative timing between the peaks.

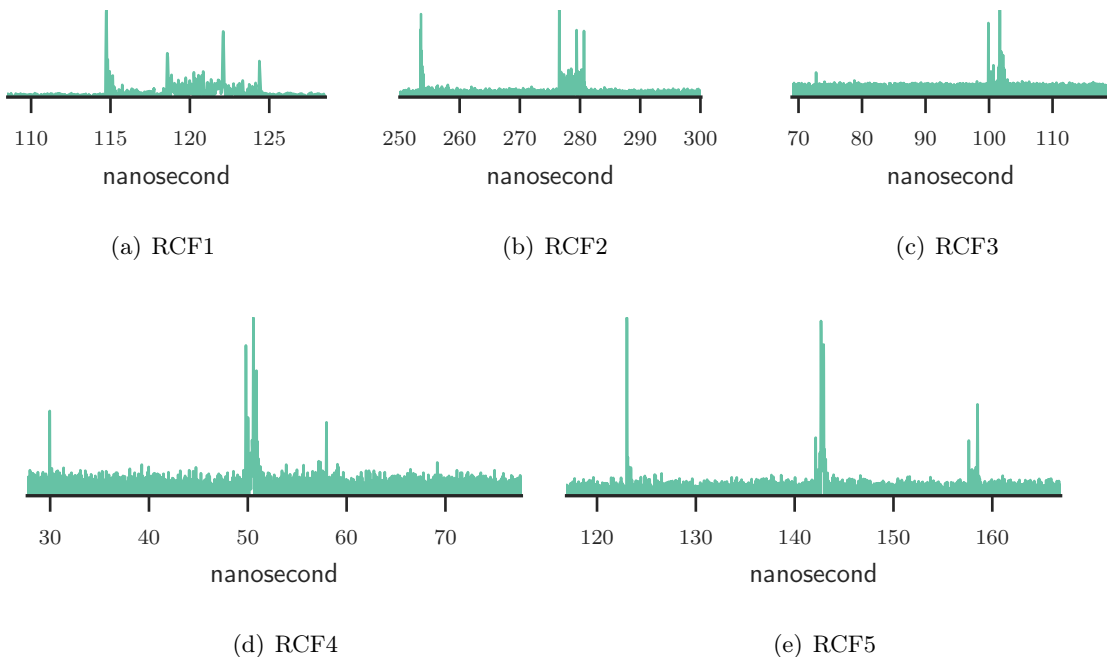


Figure 8.11: Time-of-flight experiment results, using linear polarization, for all RCFs.

Table 8.9: Measured values for TOF experiment in RCF1

Peak	T_g (ns)	ΔT_g (ns)	$\Delta n_g \cdot 10^3$	Value (mV)
<i>noise</i>				74.453
Peak 1	114.737	—	—	206.225
Peak 2	118.575	3.839	0.728	89.872
Peak 3	122.097	7.360	1.397	121.353
Peak 4	124.378	9.641	1.829	84.453

Changing the polarization from right-circular to left-circular, or to linear, modifies the relative power of each peak. However, the position of the peaks remains stable. Usually, linear polarization allows to see peaks for all the vector modes. Tables 8.9–8.13 give measured values (time and voltage), for each RCF, the voltage being the maximum red value within the different input polarizations. Noise value is the median value among the data. Finally, given time delay and group index are relative to the first measured peak.

The values we want to compare with simulations are the values in the fourth column of Tables 8.9–8.13 (Δn_g). From the simulated group indexes of Table 8.4, we compute the relative group indexes in Table 8.14. On Table 8.15, we compare simulated values with measured ones. The value is the difference between simulated and measured Δn_g , while the percentage is the difference relative to simulated value.

As it was for effective index measurements, measured group index values are different than

Table 8.10: Measured values for TOF experiment in RCF2

Peak	T_g (ns)	ΔT_g (ns)	$\Delta n_g \cdot 10^3$	Value (mV)
<i>noise</i>				15.273
Peak 1	253.581	—	—	36.371
Peak 2	276.548	22.967	4.358	38.764
Peak 3	279.442	25.861	4.907	43.580
Peak 4	280.651	27.070	5.136	33.787

Table 8.11: Measured values for TOF experiment in RCF3

Peak	T_g (ns)	ΔT_g (ns)	$\Delta n_g \cdot 10^3$	Value (mV)
<i>noise</i>				23.097
Peak 1	72.765	—	—	30.544
Peak 2	99.896	27.131	5.148	46.052
Peak 3	101.703	28.938	5.491	59.975
Peak 4	102.387	29.621	5.620	41.532

Table 8.12: Measured values for TOF experiment in RCF4

Peak	T_g (ns)	ΔT_g (ns)	$\Delta n_g \cdot 10^3$	Value (mV)
<i>noise</i>				87.617
Peak 1	29.956	—	—	113.806
Peak 2	49.810	19.853	3.767	186.508
Peak 3	50.579	20.623	3.913	242.673
Peak 4	50.872	20.916	3.969	203.291
Peak 5	57.184	27.228	5.166	110.430
Peak 6	57.954	27.998	5.312	115.208

Table 8.13: Measured values for TOF experiment in RCF5

Peak	T_g (ns)	ΔT_g (ns)	$\Delta n_g \cdot 10^3$	Value (mV)
<i>noise</i>				21.459
Peak 1	123.033	—	—	50.010
Peak 2	142.130	19.096	3.623	31.987
Peak 3	142.667	19.634	3.725	40.459
Peak 4	142.936	19.902	3.776	34.975
Peak 5	157.624	34.591	6.563	26.918
Peak 6	158.503	35.470	6.730	27.604

Table 8.14: Relative group indexes ($\Delta n_g \cdot 10^3$) of the modes in RCFs (at 1550 nm).

Fiber	TE _{0,1}	HE _{2,1}	TM _{0,1}	EH _{1,1}	HE _{3,1}
1	2.707	2.453	1.835	—	—
2	5.567	5.531	5.138	—	—
3	6.232	6.276	6.062	—	—
4	5.913	5.986	5.918	8.239	8.470
5	5.153	5.229	5.237	9.706	9.938

Table 8.15: Group index difference between simulation and measurement ($\cdot 10^3$)

Fiber	TE _{0,1}	HE _{2,1}	TM _{0,1}	EH _{1,1}	HE _{3,1}
1	0.881 (33%)	1.053 (43%)	1.112 (60%)	—	—
2	0.434 (8%)	0.623 (11%)	0.782 (15%)	—	—
3	0.739 (12%)	0.650 (10%)	0.902 (15%)	—	—
4	2.007 (34%)	2.021 (34%)	2.153 (36%)	3.074 (37%)	3.158 (37%)
5	1.537 (30%)	1.505 (29%)	1.464 (28%)	3.137 (32%)	3.210 (32%)

what we obtained from simulation. We suspect that the difference between the measured refractive index profile, which is smoother, and the step-index profile we used for simulations is the main culprit for this difference. However, the time of flight experiment confirms the expected number of supported modes for each fiber. Comparing Fig. 8.11 with Fig. 8.4, we can see that measured group indexes follow the same qualitative behavior than what we got in simulation. For instance, group indexes for the first mode group are getting closer as the fiber diameter increases; group indexes of the first mode group are closer to group index of fundamental mode in fiber 1 than they are in the other fibers; first mode group is almost at the same distance from fundamental mode and second mode group in fiber 5, while it is closer to second mode group in fiber 4.

8.6 Discussion

Our simulations show that as expected the lower the number of supported modes, the easier it is to design a fiber with a large effective index separation within mode groups. We can see this in Fig. 8.1, where the darker area (corresponding to $\Delta n_{\text{eff}} \geq 1 \times 10^4$) is more extensive for the region supporting only the first OAM mode (region II), than it is for the region supporting more OAM modes (region III).

We fabricated one fiber preform which we used to engineer the family of five different fibers in a single drawing run. The measured RIP shows a relatively good agreement between targeted and realized profiles. The fact that all fibers but fiber 2 have unusual cladding diameters led to unexpected challenges.

Experimental manipulations also highlighted the impact of the core dimensions on OAM coupling from free-space to fiber. Several lenses were tested via trial and error to achieve good coupling of the free-space OAM beam with the RCF. The inner / outer core radius ratio ρ also is important. In free-space OAM beams, this ratio is a function of topological charge; it is lower for lower order OAM modes [2]. Therefore, the ideal coupling setup on a given fiber is different for each mode, and a tradeoff is needed when simultaneously coupling all OAM modes. A commercial OAM system will use multiplexers whose efficiency may ultimately also vary with ρ , however these technologies are still under research [34, 51, 142].

Measurements on effective index performed using FBG, and measurements on group index performed using time of flight, confirmed that the fabricated fibers support the expected number of modes. We also observed high birefringence on fibers 1 and 3, probably caused by imperfections induced to the fibers during the fabrication process. As the measurement of effective index difference Δn_{eff} requires very precise values, our conclusions are limited to confirming that the effective index *separation* within mode groups is higher than 1×10^{-4} for most of the modes, as expected.

We proposed the design of a family of five ring-core fibers, using the modal map developed in Chapter 6. We proposed a novel way of producing those five different fibers from a single preform, to reduce production costs. We took advantage of the similarities and the differences among those five fibers to better understand how the dimensions of a ring-core with a fixed ρ parameter influence the modal characteristics of the fiber. Experimental manipulations of the fabricated fibers allowed us to confirm that the modal behavior of the fabricated fibers is similar to what was predicted by simulation, and therefore increased our degree of confidence in simulation results. It confirmed that, considering the expected tolerances on fiber fabrication, it is possible to fabricate OAM ring-core fibers that are in accordance with the theoretical models. It also revealed some challenges that were not obvious from simulations, giving us new design constraints to consider when fabricating RCF. We confirmed that our design targets were reached, and we have a good knowledge of the modal characteristics of each fabricated fiber.

Conclusion

The use of the orbital angular momentum of light to encode data channels is a tangible solution to increase the capacity of optical fiber links and to address the need for a higher data bandwidth. This was established by some proof-of-concept systems [93]. However, we lacked tools and models to easily design optical fibers tailored for the transmission of OAM modes. The creation of such tools was addressed in this thesis.

In Part I, we summarized the notions of guided optics, physics, and computer science we needed to design OAM fibers. Bringing together ideas from these various fields allowed us to master OAM fiber design presented in the balance of the thesis.

In Part II, we developed cutoff equations for three-layer fibers. Three-layer fibers, especially ring-core fibers, are the basic building blocks for OAM fibers. By knowing the cutoff equations, we can more easily predict the number of modes supported by a given fiber design, and it allows to focus on the design parameters needed to support a given number of modes. Using this information, we proposed a tool to help in fiber design, the *modal map*.

Finally, in Part III, we proposed two different OAM fiber designs. The fibers were designed with the help of numerical simulations. Then they were fabricated, and we performed measurements to confirm the accuracy of our numerical models.

Obviously, there is no perfect OAM fiber design. It is always a tradeoff between the number of supported modes, their purity, and their stability. There are also many constraints, on fiber material and geometry, on the fabrication process, and on the coupling with the multiplexer and the demultiplexer stages. For instance, a larger number of supported modes can lead to more coupling between the modes. A fiber core that is too small can make the light difficult to couple. An index contrast that is too large can lead to unwanted elliptical polarization. Hopefully, the comprehension of the characteristics needed to design a good OAM fiber is slowly evolving [84]. The tools we proposed help in the process of choosing the right design parameters, for a given application.

At the end of this thesis, many questions remain open. This is not unexpected, since we explored only some specific aspects of a new and vast topic. Significant effort is already underway on related topics, like designing better OAM fibers, designing OAM multiplexers

and demultiplexers, both using free-space optics and using integrated photonic, and studying the performance of OAM communication systems. We conclude by raising some open topics that could be developed by future work.

8.7 Openings for future work

8.7.1 The simulation software

In Chapter 3, we presented the numerical methods needed to solve for fiber modes and other related properties. We wrote a simulation software based on those numerical methods, and on the algorithms we developed. We used this software to perform all the simulations in this thesis. The simulation software is publicly available on GitHub*, and we hope that other developers and researchers will continue to use it, and to improve it.

Among the possible improvements for the software, one aspect is the speed of the simulator. Best simulation enables enable the user to quickly see the effects on the fiber properties when he modifies fiber parameters, especially when the fiber design is complex. When we profiled the code, we realized that the bottleneck of our solver is computing the Bessel functions, and solving for the linear systems. In Algorithm 3.2, each time the COEFFICIENTS function is called, two Bessel functions and two Bessel function derivatives need to be evaluated. In theory, it could be performed in parallel on different processes. Similarly, the 4×4 linear solver could easily be parallelized to take advantage of multiple processors. However, those tasks by themselves execute very quickly; it is the number of times those functions are called that makes them slow down calculation. The overhead required by the parallelization of those functions would be higher than the resulting gain.

However, there exists a device able to perform thousands of operations simultaneously, the graphics processing unit (GPU), also know as general purpose GPU (GPGPU) in our case of interest. To be effectively used, a GPU needs to perform the same operations simultaneously, on different data sets. To efficiently use the GPU, we unroll the **for** loop at line 7 of Algorithm 3.3. Each cell of the GPU evaluates the CHARFUNC function for a specific value of n_{eff} , simultaneously. When a change of sign is detected between two consecutive values of n_{eff} , we can repeat the evaluation, but between the two n_{eff} values that lead to a sign change. We repeat the procedure until the interval between consecutive values of n_{eff} is small enough to reach the wanted precision. Since all n_{eff} values are evaluated simultaneously, the time required to find all the roots of the characteristic function is equivalent to only a few calls to the function. Obviously, the number of points to evaluate needs to be carefully adjusted to the GPU used, to get optimal performance. Implementing this kind of algorithm could potentially dramatically increase the performances of the mode solve.

*<https://github.com/cbrunet/fibermodes>

Another possible improvement for the mode solver would be to generalize it for other kinds of fiber. At Present, we only solve for modes of step-index fibers. However, it could be possible to also solve for graded-index fibers, by using a fourth order Runge-Kutta to numerically solve the coupled differential equations of the modes [17]. All we need in that case are the analytical expressions for the refractive index and its derivative. Therefore, it could be possible to implement solvers for common gradient functions, as parabolic or as super-Gaussian functions.

8.7.2 The cutoff equations

In Chapters 4 and 5, we found analytical expressions for the cutoff of three-layer fibers. The generalization of those equations for more than three layers is probably intractable, except for some very specific fiber geometries. However, the mathematical tricks we used to find the analytical expressions could be the inspiration for an algorithm, based on the layer-by-layer method and on the cutoff expressions for ring-core fibers, to numerically solve for the cutoff of any multi-layer fiber. While success is not certain, it would certainly worth exploring this avenue.

8.7.3 Improvements in fiber design

The first OAM fiber we designed, the air-core fiber, had modes that were stable over time (hours). However, they are sensitive to fiber bends, especially for lower order modes (OAM_{0,1} through OAM_{3,1}). This is consistent with observations from [97]. More simulations and measurements are needed on this fiber to better characterize performance and achieve a deeper understanding of OAM mode transmission. For instance, effective indexes could be measured using the reflectogram of a Bragg grating [143]. Bending and twist losses could be investigated more systematically experimentally, and compared to numerical simulations of these impairments. Our experiments were limited to a short length of fiber as we were not able to efficiently transmit the light on longer spans of fiber. We observed high loss in of our fiber, that we estimate to a few dB per meter, and we suspect spin-orbit coupling to be the cause of those losses [144, 145]. Losses must be reduced to be able to measure channel crosstalk using the fiber in an optical communications setup.

The spin-orbit coupling theory itself could be simplified and improved. We hope that a simple relation could be found to relate the parameters of a ring-core fiber with the ellipticity of the polarization of its supported OAM modes. This would allow to use it as a new parameter to optimize in the design process of OAM fibers.

A recent paper suggested that the spin-orbit coupling could be reduced by the use of a graded-index profile [146]. However, the design they proposed exhibits an index contrast that makes the fabrication of that fiber unpracticable. We think that a more realistic approach would be to design a ring-core graded-index fiber, similar to [126]. With sufficient effective index

separation of the modes, this fiber could potentially suffer less from spin-orbit coupling, and it could be easier to couple the light into the fiber.

When we experimented with the family of ring-core fibers presented in Chapter 8, we realized that while free-space coupling is used for advanced experimentation, simple characterization of power, etc. would be greatly facilitated if we could exploit telecom equipment and measurement systems made for 125 μm fibers. Furthermore, it could be possible to draw fibers with different core dimensions, but with the same cladding diameter, by etching the preform as needed, before fiber drawing. Were we to again fabricate a family of fibers from a single preform, this is the approach we would prefer.

8.8 Closing remarks

The orbital angular momentum is a fantastic property of the light, with a lot of potential applications. The use of the OAM for spatial-division multiplexing in optical communications is only a tiny subset of all those applications. We cannot predict yet if commercial communication systems will use OAM one day or not, neither we can know what form it will take (optical fibers, free-space optics, integrated circuits). We begin to have some OAM optical fibers, but we do not have a crystal ball yet.

One thing is certain, it is worth doing this research on OAM modes for telecommunications. History tells us that a many great discoveries were achieved when searching for something else: Teflon nonstick coating was discovered when attempting to create a new refrigerant; Fermat's last theorem is not really useful in itself, but it allowed the development of a lot of valuable mathematical tools; and three-layer step-index cutoff equations were discovered when trying to design and model OAM fibers.

Appendix A

Formulas

This appendix contains common formulas used throughout the thesis. It first introduces vector operators notation and definitions, and gives some related identities for these operators. Then it introduces the Bessel functions, and lists some Bessel function identities. Finally, it presents the five points stencil method used for the numerical estimation of the derivatives.

A.1 Vector operators and identities

\mathbf{F} is a vector field. φ is a scalar field.

A.1.1 Operators

Name	Notation	Definition	Definition
		(Cartesian coordinates)	(Cylindrical coordinates)
Vector field	\mathbf{F}	$F_x \hat{\mathbf{x}} + F_y \hat{\mathbf{y}} + F_z \hat{\mathbf{z}}$	$F_y \hat{\mathbf{r}} + F_\phi \hat{\phi} + F_z \hat{\mathbf{z}}$
Gradient	$\nabla \varphi$	$\frac{\partial \varphi}{\partial x} \hat{\mathbf{x}} + \frac{\partial \varphi}{\partial y} \hat{\mathbf{y}} + \frac{\partial \varphi}{\partial z} \hat{\mathbf{z}}$	$\frac{\partial \varphi}{\partial r} \hat{\mathbf{r}} + \frac{1}{r} \frac{\partial \varphi}{\partial \phi} \hat{\phi} + \frac{\partial \varphi}{\partial z} \hat{\mathbf{z}}$
Divergence	$\nabla \cdot \mathbf{F}$	$\frac{\partial F_x}{\partial x} + \frac{\partial F_y}{\partial y} + \frac{\partial F_z}{\partial z}$	$\frac{1}{r} \frac{\partial (r F_r)}{\partial r} + \frac{1}{r} \frac{\partial F_\phi}{\partial \phi} + \frac{\partial F_z}{\partial z}$
Curl	$\nabla \times \mathbf{F}$	$\left(\frac{\partial F_z}{\partial y} - \frac{\partial F_y}{\partial z} \right) \hat{\mathbf{x}} + \left(\frac{\partial F_x}{\partial z} - \frac{\partial F_z}{\partial x} \right) \hat{\mathbf{y}} + \left(\frac{\partial F_y}{\partial x} - \frac{\partial F_x}{\partial y} \right) \hat{\mathbf{z}}$	$\left(\frac{1}{r} \frac{\partial F_z}{\partial \phi} - \frac{\partial F_\phi}{\partial z} \right) \hat{\mathbf{r}} + \left(\frac{\partial F_r}{\partial z} - \frac{\partial F_z}{\partial r} \right) \hat{\phi} + \frac{1}{r} \left(\frac{\partial (r F_\phi)}{\partial r} - \frac{\partial F_r}{\partial \phi} \right) \hat{\mathbf{z}}$
Laplacian	$\nabla^2 \varphi$	$\frac{\partial^2 \varphi}{\partial x^2} + \frac{\partial^2 \varphi}{\partial y^2} + \frac{\partial^2 \varphi}{\partial z^2}$	$\frac{\partial^2 \varphi}{\partial r^2} + \frac{1}{r} \frac{\partial \varphi}{\partial r} + \frac{1}{r^2} \frac{\partial^2 \varphi}{\partial \phi^2} + \frac{\partial^2 \varphi}{\partial z^2}$
Vector Laplacian	$\nabla^2 \mathbf{F}$	$\nabla^2 F_x \hat{\mathbf{x}} + \nabla^2 F_y \hat{\mathbf{y}} + \nabla^2 F_z \hat{\mathbf{z}}$	$\left(\nabla^2 F_r - \frac{F_r}{r^2} - \frac{2}{r^2} \frac{\partial F_\phi}{\partial \phi} \right) \hat{\mathbf{r}} + \left(\nabla^2 F_\phi - \frac{F_\phi}{r^2} + \frac{2}{r^2} \frac{\partial F_r}{\partial \phi} \right) \hat{\phi} + \nabla^2 F_z \hat{\mathbf{z}}$

A.1.2 Identities

Curl of curl:

$$\nabla \times (\nabla \times \mathbf{F}) = \nabla(\nabla \cdot \mathbf{F}) - \nabla^2 \mathbf{F} \quad (\text{A.1})$$

Curl product rule:

$$\nabla \times (\varphi \mathbf{F}) = (\nabla \varphi) \times \mathbf{F} + \varphi \nabla \times \mathbf{F} \quad (\text{A.2})$$

Divergence product rule:

$$\nabla \cdot (\varphi \mathbf{F}) = (\nabla \varphi) \cdot \mathbf{F} + \varphi (\nabla \cdot \mathbf{F}) \quad (\text{A.3})$$

A.2 The Bessel functions

Linear combinations of Bessel functions of the first kind $J_\nu(ux)$ and of the second kind $N_\nu(ux)$ (also known as $Y_\nu(ux)$) are solutions to the differential equation:

$$\frac{d^2 y}{dx^2} + \frac{1}{x} \frac{dy}{dx} + \left(u^2 - \frac{\nu^2}{x^2} \right) y = 0 \quad (\text{A.4})$$

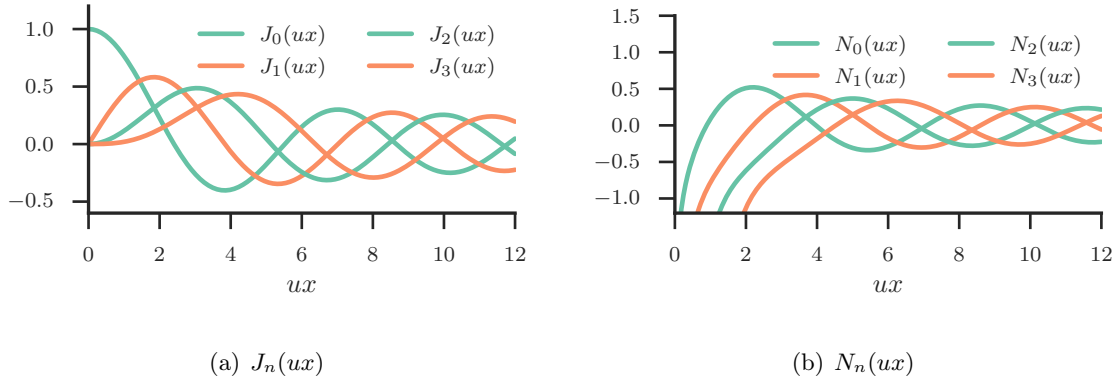


Figure A.1: Ordinary Bessel functions of first (a) and second (b) kind.

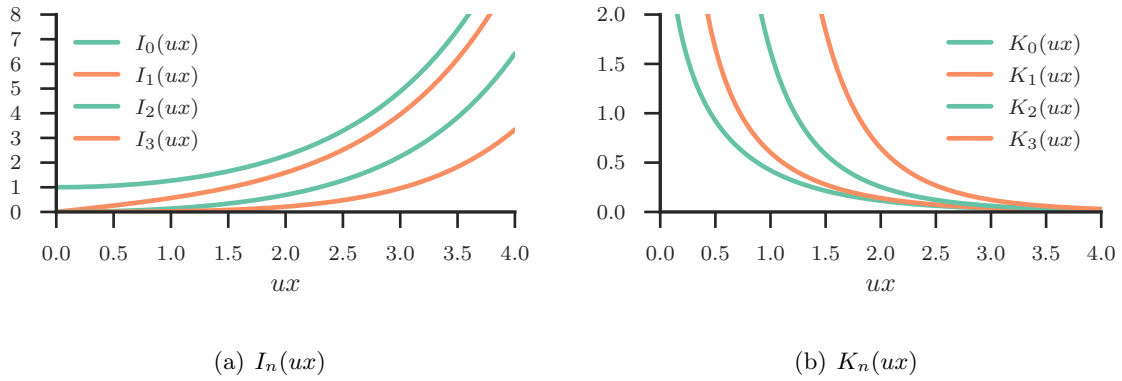


Figure A.2: Modified Bessel functions of first (a) and second (b) kind.

where ν is an integer, u and x are real numbers. ν is the order of the Bessel function, while ux is the argument. Those functions are illustrated on Fig. A.1.

Linear combinations of modified Bessel functions of the first kind $I_\nu(ux)$ and of the second kind $K_\nu(ux)$ are solutions to the differential equation:

$$\frac{d^2 y}{dx^2} + \frac{1}{x} \frac{dy}{dx} - \left(u^2 + \frac{\nu^2}{x^2} \right) y = 0 \quad (\text{A.5})$$

Those functions are illustrated on Fig. A.2.

Bessel functions are related to the modal solutions of cylindrical waveguides. Selected identities are given in the following section. More details and properties can be found in specialized literature, such as [130, chapter 9].

A.2.1 Selected Bessel function identities

The following identities were produced from [17, Appendix A].

Symmetry relations

$$J_{-\nu}(x) = (-1)^\nu J_\nu(x) \qquad N_{-\nu}(x) = (-1)^\nu N_\nu(x) \qquad (\text{A.6})$$

$$I_{-\nu}(x) = I_\nu(x) \qquad K_{-\nu}(x) = K_\nu(x) \qquad (\text{A.7})$$

Recurrence functions

$$J_{\nu+1}(x) = \frac{2\nu}{x} J_\nu(x) - J_{\nu-1} \qquad (\text{A.8})$$

$$N_{\nu+1}(x) = \frac{2\nu}{x} N_\nu(x) - N_{\nu-1} \qquad (\text{A.9})$$

$$I_{\nu+1}(x) = -\frac{2\nu}{x} I_\nu(x) + I_{\nu-1} \qquad (\text{A.10})$$

$$K_{\nu+1}(x) = \frac{2\nu}{x} K_\nu(x) + K_{\nu-1} \qquad (\text{A.11})$$

Derivative of Bessel functions

$$\frac{dJ_0(x)}{dx} = -J_1(x) \qquad \frac{dN_0(x)}{dx} = -N_1(x) \qquad (\text{A.12})$$

$$\frac{dI_0(x)}{dx} = I_1(x) \qquad \frac{dK_0(x)}{dx} = -K_1(x) \qquad (\text{A.13})$$

$$\frac{dJ_\nu(x)}{dx} = \pm \frac{\nu}{x} J_\nu(x) \mp J_{\nu\pm 1}(x) = \frac{1}{2} [J_{\nu-1}(x) - J_{\nu+1}(x)] \qquad (\text{A.14})$$

$$\frac{dN_\nu(x)}{dx} = \pm \frac{\nu}{x} N_\nu(x) \mp N_{\nu\pm 1}(x) = \frac{1}{2} [N_{\nu-1}(x) - N_{\nu+1}(x)] \qquad (\text{A.15})$$

$$\frac{dI_\nu(x)}{dx} = \pm \frac{\nu}{x} I_\nu(x) + I_{\nu\pm 1}(x) = \frac{1}{2} [I_{\nu-1}(x) + I_{\nu+1}(x)] \qquad (\text{A.16})$$

$$\frac{dK_\nu(x)}{dx} = \pm \frac{\nu}{x} K_\nu(x) - K_{\nu\pm 1}(x) = -\frac{1}{2} [K_{\nu-1}(x) + K_{\nu+1}(x)] \qquad (\text{A.17})$$

Asymptotic expansions

For $x \rightarrow 0$

$$J_0(x) \simeq 1 - \frac{x^2}{4} \qquad N_0(x) \simeq \left(\frac{2}{\pi}\right) \ln x \qquad (\text{A.18})$$

$$I_0(x) \simeq 1 + \frac{x^2}{4} \qquad K_0(x) \simeq -\ln x \qquad (\text{A.19})$$

$$J_1(x) \simeq \frac{x}{2} - \frac{x^3}{16} \qquad I_1(x) \simeq \frac{x}{2} + \frac{x^3}{16} \qquad (\text{A.20})$$

$$J_\nu(x) \simeq \frac{1}{\nu!} \left(\frac{x}{2}\right)^\nu \quad N_\nu(x) \simeq -\frac{(\nu-1)!}{\pi} \left(\frac{2}{x}\right)^\nu \quad (\text{A.21})$$

$$I_\nu(x) \simeq \frac{1}{\nu!} \left(\frac{x}{2}\right)^\nu \quad K_\nu(x) \simeq \frac{(\nu-1)!}{\pi} \left(\frac{2}{x}\right)^\nu \quad (\text{A.22})$$

$$\frac{xJ'_\nu(x)}{J_\nu(x)} \simeq \begin{cases} -\frac{x^2}{2} - \frac{x^4}{16} & \nu = 0 \\ \nu - \frac{x^2}{2(\nu+1)} & \nu > 0 \end{cases} \quad (\text{A.23})$$

$$\frac{xN'_\nu(x)}{N_\nu(x)} \simeq \begin{cases} \frac{1}{\ln x} & \nu = 0 \\ -1 - x^2 \ln x & \nu = 1 \\ -\nu + \frac{x^2}{2(\nu-1)} & \nu > 1 \end{cases} \quad (\text{A.24})$$

$$\frac{xI'_\nu(x)}{I_\nu(x)} \simeq \begin{cases} \frac{x^2}{2} - \frac{x^4}{16} & \nu = 0 \\ \nu + \frac{x^2}{2(\nu+1)} & \nu > 0 \end{cases} \quad (\text{A.25})$$

$$\frac{xK'_\nu(x)}{K_\nu(x)} \simeq \begin{cases} \frac{1}{\ln x} & \nu = 0 \\ -1 + x^2 \ln x & \nu = 1 \\ -\nu - \frac{x^2}{2(\nu-1)} & \nu > 1 \end{cases} \quad (\text{A.26})$$

For $x \rightarrow \infty$

$$J_\nu(x) \simeq \sqrt{\frac{2}{\pi x}} \cos \left\{ x - \frac{\pi}{2} \left(\nu + \frac{1}{2} \right) \right\} \quad (\text{A.27})$$

$$N_\nu(x) \simeq \sqrt{\frac{2}{\pi x}} \sin \left\{ x - \frac{\pi}{2} \left(\nu + \frac{1}{2} \right) \right\} \quad (\text{A.28})$$

$$I_\nu(x) \simeq \frac{\exp(x)}{\sqrt{2\pi x}} \left\{ 1 - \frac{4\nu^2 - 1}{8x} \right\} \quad (\text{A.29})$$

$$K_\nu(x) \simeq \sqrt{\frac{\pi}{2x}} \exp(-x) \left\{ 1 + \frac{4\nu^2 - 1}{8x} \right\} \quad (\text{A.30})$$

Complex argument

$$J_\nu(jx) = j^\nu I_\nu(x) \quad (\text{A.31})$$

$$N_\nu(jx) = j^{(\nu+1)} I_\nu(x) - \frac{2}{\pi} (-j)^\nu K_\nu(x) \quad (\text{A.32})$$

$$I_\nu(jx) = j^\nu J_\nu(x) \quad (\text{A.33})$$

$$K_\nu(jx) = \frac{\pi}{2} (-j)^\nu [jJ_\nu(x) - N_\nu(x)] \quad (\text{A.34})$$

A.3 Selected trigonometric identities

Euler's formula:

$$\exp(\pm jx) = \cos(x) \pm j \sin(x) \quad (\text{A.35})$$

Addition formula:

$$\sin(A \pm B) = \sin A \cos B \pm \cos A \sin B \quad (\text{A.36})$$

A.4 Stencil method for numerical estimation of the derivatives

The differentiation formula is given by [130, Table 25.2]:

$$\left. \frac{d^k f(x)}{dx^k} \right|_{x=x_0} \approx \frac{k!}{m!h^k} \sum_{i=0}^m A_i f(x_0 + (i - m/2)h) \quad (\text{A.37})$$

where $m + 1$ is the number of points used for the derivation, k is the order of the derivative, h is the distance between the points, and A_i are the coefficients, given in Table A.1.

Table A.1: Coefficients for five-point stencil ($m = 4$)

k	A_0	A_1	A_2	A_3	A_4
1	2	-16	0	16	-2
2	-1	16	-30	16	-1
3	-2	4	0	-4	2

Appendix B

Refractive index calculation

B.1 Refractive index of Air

In most cases, we can assume that the refractive index of Air is 1. However, for more precise calculations, we use the following formula [147], that is valid for dry air, at 15 °C, 101.325 kPa, and with 450 ppm CO₂ content, from 0.23 μm to 1.69 μm:

$$n - 1 = \frac{0.05792105}{238.0185 - \lambda^{-2}} + \frac{0.00167917}{57.362 - \lambda^{-2}} \quad (\text{B.1})$$

where λ is the wavelength, in μm.

B.2 Refractive index of silica

The refractive index of Fused silica (SiO₂), also known as Fused quartz, is given by the well known Sellmeier equation [138]:

$$n^2 - 1 = \frac{0.6961663\lambda^2}{\lambda^2 - 0.0684043^2} + \frac{0.4079426\lambda^2}{\lambda^2 - 0.1162414^2} + \frac{0.8974794\lambda^2}{\lambda^2 - 9.896161^2} \quad (\text{B.2})$$

where λ is the wavelength, in μm, and which is valid at 20 °C, from 0.21 μm to 3.71 μm.

B.3 Refractive index of doped silica

Refractive index of silica can be modified by the addition of other chemicals. The most common dopant is germania (GeO₂), used to increase the refractive index. The similarity between the Si and Ge elements allows to add a large proportion of germania to silica – up to 20%, and sometimes more – without breaking the cristaline structure of the glass. Another dopand, Fluorine, is used to lower the refractive index of silica.

Table B.1: Sellmeier coefficients, for silica [138] and germania [148].

	Silica	Germania
A_1	0.696 166 30	0.806 866 42
A_2	0.407 942 60	0.718 158 48
A_3	0.897 479 40	0.854 168 31
ℓ_1	0.068 404 30	0.068 972 606
ℓ_2	0.116 241 40	0.153 966 05
ℓ_3	9.896 161 0	11.821 931

Table B.2: Coefficients for Claussius-Mossotti interpolation

		$i = 1$	$i = 2$	$i = 3$
Silica	A_{si}	0.204 515 457 8	0.064 516 762 58	0.131 158 315 1
	z_{si} (μm)	0.061 308 073 20	0.110 885 984 8	8.964 441 861
Germania	B_i	-0.101 178 376 9	0.177 893 499 9	-0.106 417 958 1
Fluorine	B_i	-0.054 139 380 39	-0.178 858 882 4	-0.074 459 313 32

B.3.1 Silica doped with germania

The model we use is based on a simple linear relationship between the Sellmeier coefficients of silica and germania, proposed by Fleming [148]:

$$n^2 - 1 = \sum_{i=1}^3 \frac{[SA_i + X(GA_i - SA_i)] \lambda^2}{\lambda^2 - [S\ell_i + X(G\ell_i - S\ell_i)]^2} \quad (\text{B.3})$$

where SA_i , GA_i , $S\ell_i$, and $G\ell_i$ are Sellmeier coefficients of silica and Germania, given in Table B.1, X is the molar concentration of GeO_2 , and λ is the wavelength, in μm .

Another model, based on the Claussius-Mossotti interpolation, is given in [149]. However, that model tends to be less precise when germania concentration is high, as it is the case with OAM fibers; therefore we prefer Fleming's model.

B.3.2 Silica doped with Fluorine

For silica doped with Fluorine, [150] gives formulas only for $X = 1\%$ and $X = 2\%$ concentrations. To get a more generic formula, we use the Claussius-Mossotti interpolation from [149]. The formula is:

$$\frac{n^2 - 1}{n^2 + 2} = \sum_{i=1}^3 \frac{(A_{si} + XB_i) \lambda^2}{\lambda^2 - z_{si}^2} \quad (\text{B.4})$$

where X is the molar concentration of the dopant, and λ is the wavelength, in μm . Coefficients are given in Table B.2.

Bibliography

- [1] C. Brunet, B. Ung, Y. Messaddeq, S. LaRochelle, E. Bernier, and L. Rusch, “Design of an optical fiber supporting 16 oam modes,” in *Optical Fiber Communication Conference*. Optical Society of America, 2014, p. Th2A.24. [Online]. Available: <http://www.opticsinfobase.org/abstract.cfm?URI=OFC-2014-Th2A.24>
- [2] C. Brunet, P. Vaity, Y. Messaddeq, S. LaRochelle, and L. A. Rusch, “Design, fabrication and validation of an oam fiber supporting 36 states,” *Opt. Express*, vol. 22, no. 21, pp. 26 117–26 127, Oct. 2014. [Online]. Available: <http://www.opticsexpress.org/abstract.cfm?URI=oe-22-21-26117>
- [3] C. Brunet and L. A. Rusch, “System and method for optical fiber,” U.S. Patent 20 150 104 139, April, 2015. [Online]. Available: <http://www.freepatentsonline.com/y2015/0104139.html>
- [4] C. Brunet, P. Vaity, B. Ung, Y. Messaddeq, S. LaRochelle, and L. A. Rusch, “Design of a family of ring-core fiber for oam,” in *Optical Fiber Communication Conference*. Optical Society of America, 2015, p. M3D.1. [Online]. Available: <http://www.opticsinfobase.org/abstract.cfm?URI=OFC-2015-M3D.1>
- [5] C. Brunet, B. Ung, L. Wang, Y. Messaddeq, S. LaRochelle, and L. A. Rusch, “Design of a family of ring-core fibers for oam transmission studies,” *Opt. Express*, vol. 23, no. 8, pp. 10 553–10 563, Apr 2015. [Online]. Available: <http://www.opticsexpress.org/abstract.cfm?URI=oe-23-8-10553>
- [6] C. Brunet, B. Ung, P.-A. Bélanger, Y. Messaddeq, S. LaRochelle, and L. A. Rusch, “Vector mode analysis of ring-core fibers: Design tools for spatial division multiplexing,” *J. Lightwave Technol.*, vol. 32, no. 23, pp. 4046–4057, Dec. 2014.
- [7] C. Brunet, P.-A. Bélanger, and L. A. Rusch, “Exact expressions for vector mode cutoff in three-layer step-index fibers,” May 2015, submitted to IEEE Journal of Selected Topics in Quantum Electronics.

- [8] P. Vaity, C. Brunet, Y. Messaddeq, S. LaRochelle, and L. Rusch, "Exciting oam modes in annular-core fibers via perfect oam beams," in *Optical Communication (ECOC), 2014 European Conference on*, Sept 2014, pp. 1–3.
- [9] B. Ung, L. Wang, C. Brunet, P. Vaity, C. Jin, L. Rusch, Y. Messaddeq, and S. LaRochelle, "Inverse-parabolic graded-index profile for transmission of cylindrical vector modes in optical fibers," in *Optical Fiber Communication Conference*. Optical Society of America, 2014, p. Tu3K.4. [Online]. Available: <http://www.opticsinfobase.org/abstract.cfm?URI=OFC-2014-Tu3K.4>
- [10] R. Essiambre and R. Tkach, "Capacity trends and limits of optical communication networks," *Proceedings of the IEEE*, vol. 100, no. 5, pp. 1035–1055, May 2012.
- [11] D. J. Richardson, "Filling the light pipe," *Science*, vol. 330, no. 6002, pp. 327–328, 2010. [Online]. Available: <http://www.sciencemag.org/content/330/6002/327.short>
- [12] C. Shannon, "A mathematical theory of communication," *Bell System Technical Journal, The*, vol. 27, no. 3, pp. 379–423, July 1948.
- [13] S. Murshid, B. Grossman, and P. Narakorn, "Spatial domain multiplexing: A new dimension in fiber optic multiplexing," *Optics & Laser Technology*, vol. 40, no. 8, pp. 1030–1036, 2008. [Online]. Available: <http://www.sciencedirect.com/science/article/pii/S003039920800042X>
- [14] D. J. Richardson, J. M. Fini, and L. E. Nelson, "Space-division multiplexing in optical fibres," *Nat Photon*, vol. 7, no. 5, pp. 354–362, May 2013. [Online]. Available: <http://dx.doi.org/10.1038/nphoton.2013.94>
- [15] G. Li, N. Bai, N. Zhao, and C. Xia, "Space-division multiplexing: the next frontier in optical communication," *Adv. Opt. Photon.*, vol. 6, no. 4, pp. 413–487, Dec. 2014. [Online]. Available: <http://aop.osa.org/abstract.cfm?URI=aop-6-4-413>
- [16] A. W. Snyder and J. D. Love, *Optical waveguide theory*. Chapman and Hall, 1983.
- [17] J. Bures, *Guided Optics*, ser. Physics textbook. Wiley, 2009. [Online]. Available: <http://books.google.ca/books?id=8dcJ8L6ICwwC>
- [18] G. Agrawal, *Nonlinear Fiber Optics*, 4th ed., ser. Optics and Photonics. Academic Press, 2007. [Online]. Available: <http://books.google.ca/books?id=b5S0JqHMoxAC>
- [19] G. Keiser, *Optical Fiber Communications*. McGraw-Hill Education, 2010. [Online]. Available: <http://books.google.ca/books?id=9d2jQwAACAAJ>
- [20] L. Allen, M. W. Beijersbergen, R. J. C. Spreeuw, and J. P. Woerdman, "Orbital angular momentum of light and the transformation of laguerre-gaussian laser

- modes,” *Phys. Rev. A*, vol. 45, pp. 8185–8189, Jun. 1992. [Online]. Available: <http://link.aps.org/doi/10.1103/PhysRevA.45.8185>
- [21] G. Volpe and D. Petrov, “Generation of cylindrical vector beams with few-mode fibers excited by laguerre–gaussian beams,” *Optics Communications*, vol. 237, no. 1–3, pp. 89–95, 2004. [Online]. Available: <http://www.sciencedirect.com/science/article/pii/S0030401804003669>
- [22] Q. Zhan, “Cylindrical vector beams: from mathematical concepts to applications,” *Adv. Opt. Photon.*, vol. 1, no. 1, pp. 1–57, Jan 2009. [Online]. Available: <http://aop.osa.org/abstract.cfm?URI=aop-1-1-1>
- [23] M. V. Berry, “Paraxial beams of spinning light,” *SPIE Proceedings*, vol. 3487, pp. 6–11, Aug. 1998. [Online]. Available: [+http://dx.doi.org/10.1117/12.317704](http://dx.doi.org/10.1117/12.317704)
- [24] L. Allen, M. Padgett, and M. Babiker, “The orbital angular momentum of light,” in *Progress in Optics*, E. Wolf, Ed. Elsevier, 1999, vol. 39, ch. IV, pp. 291–372. [Online]. Available: <http://www.sciencedirect.com/science/article/pii/S0079663808703913>
- [25] J. Conry, R. Vyas, and S. Singh, “Polarization of orbital angular momentum carrying laser beams,” *J. Opt. Soc. Am. A*, vol. 30, no. 5, pp. 821–824, May 2013. [Online]. Available: <http://josaa.osa.org/abstract.cfm?URI=josaa-30-5-821>
- [26] S. Franke-Arnold, L. Allen, and M. Padgett, “Advances in optical angular momentum,” *Laser and Photonics Reviews*, vol. 2, no. 4, pp. 299–313, 2008. [Online]. Available: <http://dx.doi.org/10.1002/lpor.200810007>
- [27] L. Torres, Juan P. & Torner, Ed., *Twisted Photons: Applications of Light with Orbital Angular Momentum*. Wiley, 2011.
- [28] A. M. Yao and M. J. Padgett, “Orbital angular momentum: origins, behavior and applications,” *Adv. Opt. Photon.*, vol. 3, no. 2, pp. 161–204, Jun. 2011. [Online]. Available: <http://aop.osa.org/abstract.cfm?URI=aop-3-2-161>
- [29] W. Harm, S. Bernet, M. Ritsch-Marte, I. Harder, and N. Lindlein, “Adjustable diffractive spiral phase plates,” *Opt. Express*, vol. 23, no. 1, pp. 413–421, Jan 2015. [Online]. Available: <http://www.opticsexpress.org/abstract.cfm?URI=oe-23-1-413>
- [30] G. Gibson, J. Courtial, M. Padgett, M. Vasnetsov, V. Pas’ko, S. Barnett, and S. Franke-Arnold, “Free-space information transfer using light beams carrying orbital angular momentum,” *Opt. Express*, vol. 12, no. 22, pp. 5448–5456, Nov. 2004. [Online]. Available: <http://www.opticsexpress.org/abstract.cfm?URI=oe-12-22-5448>
- [31] Y. Li, J. Kim, and M. J. Escuti, “Orbital angular momentum generation and mode transformation with high efficiency using forkedpolarization gratings,”

- Appl. Opt.*, vol. 51, no. 34, pp. 8236–8245, Dec. 2012. [Online]. Available: <http://ao.osa.org/abstract.cfm?URI=ao-51-34-8236>
- [32] M. Beijersbergen, L. Allen, H. van der Veen, and J. Woerdman, “Astigmatic laser mode converters and transfer of orbital angular momentum,” *Optics Communications*, vol. 96, no. 1-3, pp. 123–132, 1993. [Online]. Available: <http://www.sciencedirect.com/science/article/pii/003040189390535D>
- [33] P. Genevieux, G. Labroille, J.-F. Morizur, C. Simonneau, G. Campbell, P. Lam, N. Treps, P. Brindel, R. Muller, J. Renaudier, M. Salsi, and G. Charlet, “3 modes transmission using hybrid separation with high mode selectivity and low losses spatial mode multiplexer,” in *Optical Communication (ECOC), 2014 European Conference on*, Sep. 2014, pp. 1–3.
- [34] G. Labroille, B. Denolle, P. Jian, P. Genevieux, N. Treps, and J.-F. Morizur, “Efficient and mode selective spatial mode multiplexer based on multi-plane light conversion,” *Opt. Express*, vol. 22, no. 13, pp. 15 599–15 607, Jun. 2014. [Online]. Available: <http://www.opticsexpress.org/abstract.cfm?URI=oe-22-13-15599>
- [35] G. Lazarev, A. Hermerschmidt, S. Krüger, and S. Osten, *LCOS Spatial Light Modulators: Trends and Applications*. Wiley-VCH Verlag GmbH & Co. KGaA, 2012, pp. 1–29. [Online]. Available: <http://dx.doi.org/10.1002/9783527648443.ch1>
- [36] A. Witkowska, S. G. Leon-Saval, A. Pham, and T. A. Birks, “All-fiber lp₁₁ mode converters,” *Opt. Lett.*, vol. 33, no. 4, pp. 306–308, Feb 2008. [Online]. Available: <http://ol.osa.org/abstract.cfm?URI=ol-33-4-306>
- [37] N. K. Viswanathan and V. V. G. Inavalli, “Generation of optical vector beams using a two-mode fiber,” *Opt. Lett.*, vol. 34, no. 8, pp. 1189–1191, Apr. 2009. [Online]. Available: <http://ol.osa.org/abstract.cfm?URI=ol-34-8-1189>
- [38] P. Z. Dashti, F. Alhassen, and H. P. Lee, “Observation of orbital angular momentum transfer between acoustic and optical vortices in optical fiber,” *Phys. Rev. Lett.*, vol. 96, p. 043604, Feb. 2006. [Online]. Available: <http://link.aps.org/doi/10.1103/PhysRevLett.96.043604>
- [39] R. Kumar, D. S. Mehta, A. Sachdeva, A. Garg, P. Senthilkumaran, and C. Shakher, “Generation and detection of optical vortices using all fiber-optic system,” *Optics Communications*, vol. 281, no. 13, pp. 3414–3420, 2008. [Online]. Available: <http://www.sciencedirect.com/science/article/pii/S003040180800240X>
- [40] S. Ramachandran, P. Kristensen, and M. F. Yan, “Generation and propagation of radially polarized beams in optical fibers,” *Opt. Lett.*, vol. 34, no. 16, pp. 2525–2527, Aug. 2009. [Online]. Available: <http://ol.osa.org/abstract.cfm?URI=ol-34-16-2525>

- [41] N. Bozinovic, S. Golowich, P. Kristensen, and S. Ramachandran, “Control of orbital angular momentum of light with optical fibers,” *Opt. Lett.*, vol. 37, no. 13, pp. 2451–2453, Jul. 2012. [Online]. Available: <http://ol.osa.org/abstract.cfm?URI=ol-37-13-2451>
- [42] L. Fang, H. Jia, H. Zhou, and B. Liu, “Generation of cylindrically symmetric modes and orbital-angular-momentum modes with tilted optical gratings inscribed in high-numerical-aperture fibers,” *J. Opt. Soc. Am. A*, vol. 32, no. 1, pp. 150–155, Jan. 2015. [Online]. Available: <http://josaa.osa.org/abstract.cfm?URI=josaa-32-1-150>
- [43] L. Fang and J. Wang, “Flexible generation/conversion/exchange of fiber-guided orbital angular momentum modes using helical gratings,” *Opt. Lett.*, vol. 40, no. 17, pp. 4010–4013, Sep 2015. [Online]. Available: <http://ol.osa.org/abstract.cfm?URI=ol-40-17-4010>
- [44] Y. Yan, J. Wang, L. Zhang, J.-Y. Yang, I. Fazal, N. Ahmed, B. Shamee, A. Willner, K. Birnbaum, J. Choi, B. Erkmen, and S. Dolinar, “New approach for generating and (de)multiplexing oam modes in a fiber coupler consisting of a central ring and four external cores,” in *Optical Communication (ECOC), 2011 37th European Conference and Exhibition on*, Sep. 2011, pp. 1–3.
- [45] Y. Yan, J. Wang, L. Zhang, J.-Y. Yang, I. M. Fazal, N. Ahmed, B. Shamee, A. E. Willner, K. Birnbaum, and S. Dolinar, “Fiber coupler for generating orbital angular momentum modes,” *Opt. Lett.*, vol. 36, no. 21, pp. 4269–4271, Nov. 2011. [Online]. Available: <http://ol.osa.org/abstract.cfm?URI=ol-36-21-4269>
- [46] Y. Yan, J.-Y. Yang, Y. Yue, M. R. Chitgarha, H. Huang, N. Ahmed, J. Wang, M. Tur, S. Dolinar, and A. Willner, “High-purity generation and power-efficient multiplexing of optical orbital angular momentum (oam) modes in a ring fiber for spatial-division multiplexing systems,” in *Conference on Lasers and Electro-Optics 2012*. Optical Society of America, 2012, p. JTh2A.58. [Online]. Available: <http://www.opticsinfobase.org/abstract.cfm?URI=QELS-2012-JTh2A.58>
- [47] Y. Yan, Y. Yue, H. Huang, J.-Y. Yang, M. R. Chitgarha, N. Ahmed, M. Tur, S. J. Dolinar, and A. E. Willner, “Efficient generation and multiplexing of optical orbital angular momentum modes in a ring fiber by using multiple coherent inputs,” *Opt. Lett.*, vol. 37, no. 17, pp. 3645–3647, Sep. 2012. [Online]. Available: <http://ol.osa.org/abstract.cfm?URI=ol-37-17-3645>
- [48] W. Gao, X. Hu, C. Mu, and P. Sun, “Generation of vector vortex beams with a small core multimode liquid core optical fiber,” *Opt. Express*, vol. 22, no. 9, pp. 11 325–11 330, May 2014. [Online]. Available: <http://www.opticsexpress.org/abstract.cfm?URI=oe-22-9-11325>

- [49] E. Karimi, B. Piccirillo, E. Nagali, L. Marrucci, and E. Santamato, "Efficient generation and sorting of orbital angular momentum eigenmodes of light by thermally tuned q-plates," *Applied Physics Letters*, vol. 94, no. 23, p. 231124, Jun. 2009.
- [50] C. R. Doerr, N. Fontaine, M. Hirano, T. Sasaki, L. Buhl, and P. Winzer, "Silicon photonic integrated circuit for coupling to a ring-core multimode fiber for space-division multiplexing," in *37th European Conference and Exposition on Optical Communications*. Optical Society of America, 2011, p. Th.13.A.3. [Online]. Available: <http://www.opticsinfobase.org/abstract.cfm?URI=ECOC-2011-Th.13.A.3>
- [51] N. K. Fontaine, C. R. Doerr, and L. Buhl, "Efficient multiplexing and demultiplexing of free-space orbital angular momentum using photonic integrated circuits," in *Optical Fiber Communication Conference*. Optical Society of America, 2012, p. OTu1I.2. [Online]. Available: <http://www.opticsinfobase.org/abstract.cfm?URI=OFC-2012-OTu1I.2>
- [52] T. Su, R. P. Scott, S. S. Djordjevic, N. K. Fontaine, D. J. Geisler, X. Cai, and S. J. B. Yoo, "Demonstration of free space coherent optical communication using integrated silicon photonic orbital angular momentum devices," *Opt. Express*, vol. 20, no. 9, pp. 9396–9402, Apr. 2012. [Online]. Available: <http://www.opticsexpress.org/abstract.cfm?URI=oe-20-9-9396>
- [53] B. Guan, R. P. Scott, N. K. Fontaine, T. Su, C. Ferrari, M. Cappuzzo, F. Klemens, B. Keller, M. Earnshaw, and S. J. B. Yoo, "Integrated optical orbital angular momentum multiplexing device using 3-d waveguides and a silica plc," in *CLEO: 2013*. Optical Society of America, 2013, p. CTu1L.4. [Online]. Available: http://www.opticsinfobase.org/abstract.cfm?URI=CLEO_SI-2013-CTu1L.4
- [54] C. Qin, B. Guan, R. P. Scott, R. Proietti, N. K. Fontaine, T. Su, C. Ferarri, M. Capuzzo, F. Clemens, B. Keller, M. Earnshaw, and S. Yoo, "Demonstration of orbital angular momentum state conversion using two hybrid 3d photonic integrated circuits," in *Optical Fiber Communication Conference*. Optical Society of America, 2014, p. Th4A.1. [Online]. Available: <http://www.opticsinfobase.org/abstract.cfm?URI=OFC-2014-Th4A.1>
- [55] B. Guan, R. P. Scott, C. Qin, N. K. Fontaine, T. Su, C. Ferrari, M. Cappuzzo, F. Klemens, B. Keller, M. Earnshaw, and S. J. B. Yoo, "Free-space coherent optical communication with orbital angular, momentum multiplexing/demultiplexing using a hybrid 3d photonic integrated circuit," *Opt. Express*, vol. 22, no. 1, pp. 145–156, Jan 2014. [Online]. Available: <http://www.opticsexpress.org/abstract.cfm?URI=oe-22-1-145>
- [56] X. Cai, J. Wang, M. J. Strain, B. Johnson-Morris, J. Zhu, M. Sorel, J. L. O'Brien, M. G. Thompson, and S. Yu, "Integrated compact optical vortex beam

- emitters,” *Science*, vol. 338, no. 6105, pp. 363–366, 2012. [Online]. Available: <http://www.sciencemag.org/content/338/6105/363.abstract>
- [57] H. Li, D. B. Phillips, X. Wang, Y.-L. D. Ho, L. Chen, X. Zhou, J. Zhu, S. Yu, and X. Cai, “Orbital angular momentum vertical-cavity surface-emitting lasers,” *Optica*, vol. 2, no. 6, pp. 547–552, Jun 2015. [Online]. Available: <http://www.osapublishing.org/optica/abstract.cfm?URI=optica-2-6-547>
- [58] G. C. G. Berkhout, M. P. J. Lavery, J. Courtial, M. W. Beijersbergen, and M. J. Padgett, “Efficient sorting of orbital angular momentum states of light,” *Physical Review Letters*, vol. 105, p. 153601, Oct. 2010. [Online]. Available: <http://link.aps.org/doi/10.1103/PhysRevLett.105.153601>
- [59] Z. Bouchal and R. Čelechovský, “Mixed vortex states of light as information carriers,” *New Journal of Physics*, vol. 6, no. 1, p. 131, 2004. [Online]. Available: <http://stacks.iop.org/1367-2630/6/i=1/a=131>
- [60] R. Čelechovský and Z. Bouchal, “Optical implementation of the vortex information channel,” *New Journal of Physics*, vol. 9, no. 9, p. 328, 2007. [Online]. Available: <http://stacks.iop.org/1367-2630/9/i=9/a=328>
- [61] Y. Awaji, N. Wada, and Y. Toda, “Demonstration of spatial mode division multiplexing using laguerre-gaussian mode beam in telecom-wavelength,” in *IEEE Photonics Society, 2010 23rd Annual Meeting of the*, Nov. 2010, pp. 551–552.
- [62] J. Wang, J.-Y. Yang, I. Fazal, N. Ahmed, Y. Yan, B. Shamee, A. Willner, K. Birnbaum, J. Choi, B. Erkmen, S. Dolinar, and M. Tur, “Demonstration of 12.8-bit/s/hz spectral efficiency using 16-qam signals over multiple orbital-angular-momentum modes,” in *Optical Communication (ECOC), 2011 37th European Conference and Exhibition on*, Sep. 2011, pp. 1–3.
- [63] ———, “25.6-bit/s/hz spectral efficiency using 16-qam signals over pol-muxed multiple orbital-angular-momentum modes,” in *Photonics Conference (PHO), 2011 IEEE*, Oct. 2011, pp. 587–588.
- [64] J. Wang, J.-Y. Yang, I. M. Fazal, N. Ahmed, Y. Yan, H. Huang, Y. Ren, Y. Yue, S. Dolinar, M. Tur, and A. E. Willner, “Terabit free-space data transmission employing orbital angular momentum multiplexing,” *Nat. Photon.*, vol. 6, no. 7, pp. 488–496, Jul. 2012. [Online]. Available: <http://dx.doi.org/10.1038/nphoton.2012.138>
- [65] I. M. Fazal, J. Wang, J.-Y. Yang, N. Ahmed, B. Shamee, Y. Yan, A. Willner, S. Dolinar, K. Birnbaum, B. Erkmen, and J. Choi, “Demonstration of 2-tbit/s data link using orthogonal orbital-angular-momentum modes and wdm,” in *Frontiers*

- in Optics*. Optical Society of America, 2011, p. FTuT1. [Online]. Available: <http://www.opticsinfobase.org/abstract.cfm?URI=FiO-2011-FTuT1>
- [66] Z. Wang, N. Zhang, and X.-C. Yuan, “High-volume optical vortex multiplexing and de-multiplexing for free-space optical communication,” *Opt. Express*, vol. 19, no. 2, pp. 482–492, Jan. 2011. [Online]. Available: <http://www.opticsexpress.org/abstract.cfm?URI=oe-19-2-482>
- [67] H. Huang, G. Xie, Y. Yan, N. Ahmed, Y. Ren, Y. Yue, D. Rogawski, M. Tur, B. Erkmen, K. Birnbaum, S. Dolinar, M. Lavery, M. Padgett, and A. E. Willner, “100 tbit/s free-space data link using orbital angular momentum mode division multiplexing combined with wavelength division multiplexing,” in *Optical Fiber Communication Conference/National Fiber Optic Engineers Conference 2013*. Optical Society of America, 2013, p. OTh4G.5. [Online]. Available: <http://www.opticsinfobase.org/abstract.cfm?URI=OFC-2013-OTh4G.5>
- [68] H. Huang, G. Xie, Y. Yan, N. Ahmed, Y. Ren, Y. Yue, D. Rogawski, M. J. Willner, B. I. Erkmen, K. M. Birnbaum, S. J. Dolinar, M. P. J. Lavery, M. J. Padgett, M. Tur, and A. E. Willner, “100 tbit/s free-space data link enabled by three-dimensional multiplexing of orbital angular momentum, polarization, and wavelength,” *Opt. Lett.*, vol. 39, no. 2, pp. 197–200, Jan. 2014. [Online]. Available: <http://ol.osa.org/abstract.cfm?URI=ol-39-2-197>
- [69] A. E. Willner, H. Huang, Y. Yan, Y. Ren, N. Ahmed, G. Xie, C. Bao, L. Li, Y. Cao, Z. Zhao, J. Wang, M. P. J. Lavery, M. Tur, S. Ramachandran, A. F. Molisch, N. Ashrafi, and S. Ashrafi, “Optical communications using orbital angular momentum beams,” *Adv. Opt. Photon.*, vol. 7, no. 1, pp. 66–106, Mar 2015. [Online]. Available: <http://aop.osa.org/abstract.cfm?URI=aop-7-1-66>
- [70] J. Wu, H. Li, and Y. Li, “Encoding information as orbital angular momentum states of light for wireless optical communications,” *Optical Engineering*, vol. 46, no. 1, pp. 019 701–019 701–5, 2007. [Online]. Available: [+http://dx.doi.org/10.1117/1.2431800](http://dx.doi.org/10.1117/1.2431800)
- [71] S. Gröblacher, T. Jennewein, A. Vaziri, G. Weihs, and A. Zeilinger, “Experimental quantum cryptography with qutrits,” *New J. Phys.*, vol. 8, no. 5, p. 75, 2006. [Online]. Available: <http://stacks.iop.org/1367-2630/8/i=5/a=075>
- [72] M. Mirhosseini, O. S. Magaña-Loaiza, M. N. O’Sullivan, B. Rodenburg, M. Malik, M. P. J. Lavery, M. J. Padgett, D. J. Gauthier, and R. W. Boyd, “High-dimensional quantum cryptography with twisted light,” *New Journal of Physics*, vol. 17, no. 3, p. 033033, 2015. [Online]. Available: <http://stacks.iop.org/1367-2630/17/i=3/a=033033>
- [73] M. Krenn, R. Fickler, M. Fink, J. Handsteiner, M. Malik, T. Scheidl, R. Ursin, and A. Zeilinger, “Communication with spatially modulated light through turbulent air

- across vienna,” *New Journal of Physics*, vol. 16, no. 11, p. 113028, 2014. [Online]. Available: <http://stacks.iop.org/1367-2630/16/i=11/a=113028>
- [74] C. Paterson, “Atmospheric turbulence and orbital angular momentum of single photons for optical communication,” *Phys. Rev. Lett.*, vol. 94, p. 153901, Apr. 2005. [Online]. Available: <http://link.aps.org/doi/10.1103/PhysRevLett.94.153901>
- [75] J. A. Anguita, M. A. Neifeld, and B. V. Vasic, “Turbulence-induced channel crosstalk in an orbital angular momentum-multiplexed free-space optical link,” *Appl. Opt.*, vol. 47, no. 13, pp. 2414–2429, May 2008. [Online]. Available: <http://ao.osa.org/abstract.cfm?URI=ao-47-13-2414>
- [76] G. A. Tyler and R. W. Boyd, “Influence of atmospheric turbulence on the propagation of quantum states of light carrying orbital angular momentum,” *Opt. Lett.*, vol. 34, no. 2, pp. 142–144, Jan. 2009. [Online]. Available: <http://ol.osa.org/abstract.cfm?URI=ol-34-2-142>
- [77] V. P. Aksenov, I. V. Izmailov, F. Y. Kanev, and B. N. Poizner, “Optical vortex detector as a basis for a data transfer system: Operational principle, model, and simulation of the influence of turbulence and noise,” *Optics Communications*, vol. 285, no. 6, pp. 905–928, 2012. [Online]. Available: <http://www.sciencedirect.com/science/article/pii/S0030401811011813>
- [78] I. Djordjevic, “Orbital angular momentum (oam) based ldpc-coded free-space optical communication,” in *IEEE Photonics Society, 2010 23rd Annual Meeting of the*, Nov. 2010, pp. 502–503.
- [79] B. Thidé, H. Then, J. Sjöholm, K. Palmer, J. Bergman, T. D. Carozzi, Y. N. Istomin, N. H. Ibragimov, and R. Khamitova, “Utilization of photon orbital angular momentum in the low-frequency radio domain,” *Phys. Rev. Lett.*, vol. 99, p. 087701, Aug. 2007. [Online]. Available: <http://link.aps.org/doi/10.1103/PhysRevLett.99.087701>
- [80] S. Mohammadi, L. Daldorff, J. Bergman, R. Karlsson, B. Thide, K. Forozesh, T. Carozzi, and B. Isham, “Orbital angular momentum in radio - a system study,” *Antennas and Propagation, IEEE Transactions on*, vol. 58, no. 2, pp. 565–572, Feb. 2010.
- [81] O. Edfors and A. Johansson, “Is orbital angular momentum (oam) based radio communication an unexploited area?” *Antennas and Propagation, IEEE Transactions on*, vol. 60, no. 2, pp. 1126–1131, Feb. 2012.
- [82] F. Tamburini, E. Mari, A. Sponselli, B. Thidé, A. Bianchini, and F. Romanato, “Encoding many channels on the same frequency through radio vorticity: first experimental test,” *New Journal of Physics*, vol. 14, no. 3, p. 033001, 2012. [Online]. Available: <http://stacks.iop.org/1367-2630/14/i=3/a=033001>

- [83] S. Ramachandran and P. Kristensen, “Optical vortices in fiber,” *Nanophotonics*, vol. 2, no. 5-6, pp. 455–474, Nov. 2013.
- [84] S. Ramachandran, P. Gregg, P. Kristensen, and S. E. Golowich, “On the scalability of ring fiber designs for oam multiplexing,” *Opt. Express*, vol. 23, no. 3, pp. 3721–3730, Feb. 2015. [Online]. Available: <http://www.opticsexpress.org/abstract.cfm?URI=oe-23-3-3721>
- [85] A. N. Alexeyev, T. A. Fadeyeva, and A. V. Volyar, “Optical vortices and the flow of their angular momentum in a multimode fiber,” *Semiconductor Physics, Quantum Electronics & Optoelectronics*, vol. 1, no. 1, pp. 82–89, 1998.
- [86] N. Bozinovic, P. Kristensen, and S. Ramachandran, “Long-range fiber-transmission of photons with orbital angular momentum,” in *CLEO:2011 - Laser Applications to Photonic Applications*. Optical Society of America, 2011, p. CTuB1. [Online]. Available: <http://www.opticsinfobase.org/abstract.cfm?URI=CLEO:SandI-2011-CTuB1>
- [87] ———, “Are orbital angular momentum (oam/vortex) states of light long-lived in fibers?” in *Laser Science*. Optical Society of America, 2011, p. LWL3. [Online]. Available: <http://www.opticsinfobase.org/abstract.cfm?URI=LS-2011-LWL3>
- [88] N. Bozinovic, S. Ramachandran, M. Brodsky, and P. Kristensen, “Record-length transmission of entangled photons with orbital angular momentum (vortices),” in *Frontiers in Optics*. Optical Society of America, 2011, p. PDPB1. [Online]. Available: <http://www.opticsinfobase.org/abstract.cfm?URI=FiO-2011-PDPB1>
- [89] I. B. Djordjevic, M. Arabaci, L. Xu, and T. Wang, “Spatial-domain-based multidimensional modulation for multi-tb/s serial optical transmission,” *Opt. Express*, vol. 19, no. 7, pp. 6845–6857, Mar. 2011. [Online]. Available: <http://www.opticsexpress.org/abstract.cfm?URI=oe-19-7-6845>
- [90] N. Bozinovic, Y. Yue, Y. Ren, M. Tur, P. Kristensen, A. Willner, and S. Ramachandran, “Orbital angular momentum (oam) based mode division multiplexing (mdm) over a km-length fiber,” in *ECOC Postdeadline Papers*, 2012.
- [91] Y. Ren, Y. Zhang, Y. Yue, N. Bozinovic, G. Xie, H. Huang, M. Tur, P. Kristensen, I. B. Djordjevic, S. Ramachandran, and A. E. Willner, “Efficient crosstalk mitigation of oam based 400-gbit/s qpsk data transmission in 1.1-km vortex fiber by using soft-decision ldpc codes,” in *CLEO: 2013*. Optical Society of America, 2013, p. CM2G.5. [Online]. Available: http://www.opticsinfobase.org/abstract.cfm?URI=CLEO_SI-2013-CM2G.5
- [92] Y. Yue, N. Bozinovic, Y. Ren, H. Huang, M. Tur, P. Kristensen, S. Ramachandran, and A. E. Willner, “1.6-tbit/s muxing, transmission and demuxing through 1.1-km of vortex fiber carrying 2 oam beams each with 10 wavelength channels,” in

- Optical Fiber Communication Conference/National Fiber Optic Engineers Conference 2013*. Optical Society of America, 2013, p. OTh4G.2. [Online]. Available: <http://www.opticsinfobase.org/abstract.cfm?URI=OFC-2013-OTh4G.2>
- [93] N. Bozinovic, Y. Yue, Y. Ren, M. Tur, P. Kristensen, H. Huang, A. E. Willner, and S. Ramachandran, “Terabit-scale orbital angular momentum mode division multiplexing in fibers,” *Science*, vol. 340, no. 6140, pp. 1545–1548, 2013. [Online]. Available: <http://www.sciencemag.org/content/340/6140/1545.abstract>
- [94] S. Golowich, P. Kristensen, N. Bozinovic, P. Gregg, and S. Ramachandran, “Fibers supporting orbital angular momentum states for information capacity scaling,” in *Proc. of FIO*. OSA, 2012, p. FW2D.2. [Online]. Available: <http://www.opticsinfobase.org/abstract.cfm?URI=FiO-2012-FW2D.2>
- [95] P. Gregg, P. Kristensen, S. Golowich, J. Olsen, P. Steinvurzel, and S. Ramachandran, “Stable transmission of 12 oam states in air-core fiber,” in *CLEO: 2013*. Optical Society of America, 2013, p. CTu2K.2. [Online]. Available: http://www.opticsinfobase.org/abstract.cfm?URI=CLEO_SI-2013-CTu2K.2
- [96] P. Gregg, P. Kristensen, and S. Ramachandran, “OAM stability in fiber due to angular momentum conservation,” in *CLEO: 2014*. Optical Society of America, 2014, p. SM2N.2. [Online]. Available: http://www.opticsinfobase.org/abstract.cfm?URI=CLEO_SI-2014-SM2N.2
- [97] —, “Conservation of orbital angular momentum in air-core optical fibers,” *Optica*, vol. 2, no. 3, pp. 267–270, Mar 2015. [Online]. Available: <http://www.opticsinfobase.org/optica/abstract.cfm?URI=optica-2-3-267>
- [98] B. Ung, P. Vaity, L. Wang, Y. Messaddeq, L. A. Rusch, and S. LaRochelle, “Few-mode fiber with inverse-parabolic graded-index profile for transmission of oam-carrying modes,” *Opt. Express*, vol. 22, no. 15, pp. 18 044–18 055, Jul. 2014. [Online]. Available: <http://www.opticsexpress.org/abstract.cfm?URI=oe-22-15-18044>
- [99] M. Zhu, W. Zhang, L. Xi, X. Tang, and X. Zhang, “A new designed dual-guided ring-core fiber for {OAM} mode transmission,” *Optical Fiber Technology*, vol. 25, pp. 58 – 63, 2015. [Online]. Available: <http://www.sciencedirect.com/science/article/pii/S1068520015001017>
- [100] Y. Awaji, N. Wada, Y. Toda, and T. Hayashi, “Propagation of laguerre-gaussian mode light through multi-core fiber at telecom wavelength,” in *CLEO:2011 - Laser Applications to Photonic Applications*. Optical Society of America, 2011, p. CThGG2. [Online]. Available: http://www.osapublishing.org/abstract.cfm?URI=CLEO_SI-2011-CThGG2

- [101] —, “World first mode/spatial division multiplexing in multi-core fiber using laguerre-gaussian mode,” in *Optical Communication (ECOC), 2011 37th European Conference and Exhibition on*, Sep. 2011, pp. 1–3.
- [102] Y. Awaji, N. Wada, and Y. Toda, “Observation of orbital angular momentum spectrum in propagating mode through seven-core fibers,” in *Conference on Lasers and Electro-Optics 2012*. Optical Society of America, 2012, p. JTu2K.3. [Online]. Available: http://www.osapublishing.org/abstract.cfm?URI=CLEO_AT-2012-JTu2K.3
- [103] S. Li and J. Wang, “A multi-ring multi-oam-mode fiber for high-density space-division multiplexing (7 rings x 22 oam modes),” in *Photonics Conference (IPC), 2013 IEEE*, Sept 2013, pp. 301–302.
- [104] —, “Multi-orbital-angular-momentum multi-ring fiber for high-density space-division multiplexing,” *Photonics Journal, IEEE*, vol. 5, no. 5, pp. 7 101 007–7 101 007, Oct 2013.
- [105] —, “A compact trench-assisted multi-orbital-angular-momentum multi-ring fiber for ultrahigh-density space-division multiplexing (19 rings x 22 modes),” *Sci. Rep.*, vol. 4, pp. –, Jan. 2014. [Online]. Available: <http://dx.doi.org/10.1038/srep03853>
- [106] —, “Supermode fiber for orbital angular momentum (oam) transmission,” *Opt. Express*, vol. 23, no. 14, pp. 18 736–18 745, Jul 2015. [Online]. Available: <http://www.opticsexpress.org/abstract.cfm?URI=oe-23-14-18736>
- [107] J. A. Carpenter, B. C. Thomsen, and T. D. Wilkinson, “Optical vortex based mode division multiplexing over graded-index multimode fibre,” in *Optical Fiber Communication Conference/National Fiber Optic Engineers Conference 2013*. Optical Society of America, 2013, p. OTh4G.3. [Online]. Available: <http://www.opticsinfobase.org/abstract.cfm?URI=OFC-2013-OTh4G.3>
- [108] A. Tatarczak, M. A. Usuga, and I. Tafur Monroy, “Oam-enhanced transmission for multimode short-range links,” *Proc. SPIE*, vol. 9390, pp. 93 900E–93 900E–7, 2015. [Online]. Available: <http://dx.doi.org/10.1117/12.2079795>
- [109] S. Murshid, B. Grossman, and P. Narakom, “Method and apparatus for spatial domain multiplexing in optical fiber communications,” US Patent 7 174 067 B2, Dec., 2007. [Online]. Available: <http://www.google.com/patents/US7174067>
- [110] S. Murshid and R. Biswas, “Analysis of spatially multiplexed helically propagating channels in step index optical waveguides,” in *Frontiers in Optics*. Optical Society of America, 2011, p. FTuT7. [Online]. Available: <http://www.opticsinfobase.org/abstract.cfm?URI=FiO-2011-FTuT7>

- [111] S. H. Murshid, H. P. Muralikrishnan, and S. P. Kozaitis, "Orbital angular momentum in four channel spatial domain multiplexing system for multi-terabit per second communication architectures," *Proc. of SPIE*, pp. 839 703–839 703–7, 2012. [Online]. Available: <http://dx.doi.org/10.1117/12.920812>
- [112] Y. Yan, Y. Yue, H. Huang, Y. Ren, N. Ahmed, A. Willner, and S. Dolinar, "Spatial-mode multicasting of a single 100-gbit/s orbital angular momentum (oam) mode onto multiple oam modes," in *European Conference and Exhibition on Optical Communication*. Optical Society of America, 2012, p. Th.2.D.1. [Online]. Available: <http://www.opticsinfobase.org/abstract.cfm?URI=ECEOC-2012-Th.2.D.1>
- [113] H. Huang, Y. Yue, Y. Yan, N. Ahmed, Y. Ren, and A. E. Willner, "Orbital-angular-momentum-based reconfigurable and "lossless" optical add/drop multiplexing of multiple 100-gbit/s channels," in *Optical Fiber Communication Conference/National Fiber Optic Engineers Conference 2013*. Optical Society of America, 2013, p. OTh4G.4. [Online]. Available: <http://www.opticsinfobase.org/abstract.cfm?URI=OFC-2013-OTh4G.4>
- [114] A. E. Willner, H. Huang, N. Ahmed, Y. Yue, and M. J. Willner, "Data switching in communication networks using orbital-angular-momentum multiplexing," in *Advanced Photonics for Communications*. Optical Society of America, 2014, p. PT1B.1. [Online]. Available: <http://www.opticsinfobase.org/abstract.cfm?URI=PS-2014-PT1B.1>
- [115] W. Gao, C. Mu, H. Li, Y. Yang, and Z. Zhu, "Parametric amplification of orbital angular momentum beams based on light-acoustic interaction," *Applied Physics Letters*, vol. 107, no. 4, pp. –, 2015. [Online]. Available: <http://scitation.aip.org/content/aip/journal/apl/107/4/10.1063/1.4927699>
- [116] S. Li, Q. Mo, X. Hu, C. Du, and J. Wang, "Controllable all-fiber orbital angular momentum mode converter," *Opt. Lett.*, vol. 40, no. 18, pp. 4376–4379, Sep 2015. [Online]. Available: <http://ol.osa.org/abstract.cfm?URI=ol-40-18-4376>
- [117] Q. Kang, P. Gregg, Y. Jung, E. Lim, S.-U. Alam, S. Ramachandran, and D. J. Richardson, "Amplification of 12 oam states in an air-core edf," in *Optical Fiber Communication Conference*. Optical Society of America, 2015, p. Tu3C.2. [Online]. Available: <http://www.osapublishing.org/abstract.cfm?URI=OFC-2015-Tu3C.2>
- [118] P. Yeh, A. Yariv, and E. Marom, "Theory of bragg fiber," *J. Opt. Soc. Am.*, vol. 68, no. 9, pp. 1196–1201, Sep 1978. [Online]. Available: <http://www.opticsinfobase.org/abstract.cfm?URI=josa-68-9-1196>
- [119] R. P. Brent, *Algorithms for minimization without derivatives*, N. Englewood Cliffs, Ed. Prentice-Hall, 1972.

- [120] J. Bures and X. Daxhelet, "Single-mode te₀₁ fibers," vol. 7134, 2008, pp. 71 342S–71 342S–8. [Online]. Available: <http://dx.doi.org/10.1117/12.803334>
- [121] Y. Yue, Y. Yan, N. Ahmed, J.-Y. Yang, L. Zhang, Y. Ren, H. Huang, K. Birnbaum, B. Erkmen, S. Dolinar, M. Tur, and A. Willner, "Mode properties and propagation effects of optical orbital angular momentum (oam) modes in a ring fiber," *Photonics Journal, IEEE*, vol. 4, no. 2, pp. 535–543, Apr. 2012.
- [122] P. Solarik, Z. Burian, I. Kasik, V. Matejec, J. Mrazek, and M. Hayer, "Dielectric annular core fiber for optical sensing," *Proc. SPIE*, vol. 6189, pp. 61 891R–61 891R–10, 2006. [Online]. Available: <http://dx.doi.org/10.1117/12.662286>
- [123] N. Fontaine, R. Ryf, M. Hirano, and T. Sasaki, "Experimental investigation of crosstalk accumulation in a ring-core fiber," in *Photonics Society Summer Topical Meeting Series, 2013 IEEE*, July 2013, pp. 111–112.
- [124] X. Jin, R. Li, D. O'Brien, and F. Payne, "Linearly polarized mode division multiplexed transmission over ring-index multimode fibres," in *Photonics Society Summer Topical Meeting Series, 2013 IEEE*, July 2013, pp. 113–114.
- [125] M. Kasahara, K. Saitoh, T. Sakamoto, N. Hanzawa, T. Matsui, K. Tsujikawa, and F. Yamamoto, "Design of three-spatial-mode ring-core fiber," *J. Lightwave Technol.*, vol. 32, no. 7, pp. 1337–1343, Apr 2014. [Online]. Available: <http://jlt.osa.org/abstract.cfm?URI=jlt-32-7-1337>
- [126] F. Feng, G. S. Gordon, X. Jin, D. O'Brien, F. Payne, Y. min Jung, Q. Kang, J. K. Sahu, S. U. Alam, D. J. Richardson, and T. D. Wilkinson, "Experimental characterization of a graded-index ring-core fiber supporting 7 lp mode groups," in *Optical Fiber Communication Conference*. Optical Society of America, 2015, p. Tu2D.3. [Online]. Available: <http://www.osapublishing.org/abstract.cfm?URI=OFC-2015-Tu2D.3>
- [127] B. C. Sarkar, P. K. Choudhury, and T. Yoshino, "On the analysis of a weakly guiding doubly clad dielectric optical fiber with an annular core," *Microwave and Optical Technology Letters*, vol. 31, no. 6, pp. 435–439, 2001. [Online]. Available: <http://dx.doi.org/10.1002/mop.10056>
- [128] J. Marcou and S. Février, "Comments on 'On the analysis of a weakly guiding doubly clad dielectric optical fiber with an annular core'," *Microwave and Optical Technology Letters*, vol. 38, no. 3, pp. 249–254, 2003. [Online]. Available: <http://dx.doi.org/10.1002/mop.11029>
- [129] M. Hautakorpi and M. Kaivola, "Modal analysis of m-type-dielectric-profile optical fibers in the weakly guiding approximation," *J. Opt. Soc. Am. A*, vol. 22, no. 6, pp. 1163–1169, Jun 2005. [Online]. Available: <http://josaa.osa.org/abstract.cfm?URI=josaa-22-6-1163>

- [130] M. Abramowitz and I. A. Stegun, *Handbook of mathematical functions with formulas, graphs, and mathematical tables*, ser. National Bureau of Standards Applied Mathematics Series. For sale by the Superintendent of Documents, U.S. Government Printing Office, Washington, D.C., 1964, vol. 55.
- [131] S. Kawakami and S. Nishida, “Characteristics of a doubly clad optical fiber with a low-index inner cladding,” *Quantum Electronics, IEEE Journal of*, vol. 10, no. 12, pp. 879–887, Dec. 1974.
- [132] R. S. Romaniuk, “Manufacturing and characterization of ring-index optical fibers,” *Optica Applicata*, vol. 31, no. 2, pp. 425–444, 2001.
- [133] E. Snitzer, H. Po, F. Hakimi, R. Tumminelli, and B. McCollum, “Double clad, offset core nd fiber laser,” in *Optical Fiber Sensors*. Optical Society of America, 1988, p. PD5. [Online]. Available: <http://www.opticsinfobase.org/abstract.cfm?URI=OFS-1988-PD5>
- [134] L. Zenteno, “High-power double-clad fiber lasers,” *Lightwave Technology, Journal of*, vol. 11, no. 9, pp. 1435–1446, Sep 1993.
- [135] C. Y. H. Tsao, D. N. Payne, and W. A. Gambling, “Modal characteristics of three-layered optical fiber waveguides: a modified approach,” *J. Opt. Soc. Am. A*, vol. 6, no. 4, pp. 555–563, Apr 1989. [Online]. Available: <http://josaa.osa.org/abstract.cfm?URI=josaa-6-4-555>
- [136] J. Gowar, *Optical Communication Systems*, ser. Eastern Economy Edition. Prentice-Hall of India, 1993. [Online]. Available: <https://books.google.ca/books?id=FYpIPgAACAAJ>
- [137] R. F. Cregan, B. J. Mangan, J. C. Knight, T. A. Birks, P. S. J. Russell, P. J. Roberts, and D. C. Allan, “Single-mode photonic band gap guidance of light in air,” *Science*, vol. 285, no. 5433, pp. 1537–1539, 1999. [Online]. Available: <http://www.sciencemag.org/content/285/5433/1537.abstract>
- [138] I. H. Malitson, “Interspecimen comparison of the refractive index of fused silica,” *J. Opt. Soc. Am.*, vol. 55, no. 10, pp. 1205–1208, Oct 1965. [Online]. Available: <http://www.opticsinfobase.org/abstract.cfm?URI=josa-55-10-1205>
- [139] J. E. Curtis and D. G. Grier, “Structure of optical vortices,” *Phys. Rev. Lett.*, vol. 90, p. 133901, Apr 2003. [Online]. Available: <http://link.aps.org/doi/10.1103/PhysRevLett.90.133901>
- [140] P. Vaity and L. Rusch, “Perfect vortex beam: Fourier transformation of a besell beam,” *Opt. Lett.*, vol. 40, no. 4, pp. 597–600, Feb. 2015. [Online]. Available: <http://ol.osa.org/abstract.cfm?URI=ol-40-4-597>

- [141] L. Wang, P. Vaity, B. Ung, Y. Messaddeq, L. A. Rusch, and S. LaRochelle, "Characterization of oam fibers using fiber bragg gratings," *Opt. Express*, vol. 22, no. 13, pp. 15 653–15 661, Jun. 2014. [Online]. Available: <http://www.opticsexpress.org/abstract.cfm?URI=oe-22-13-15653>
- [142] R. Scott, B. Guan, C. Qin, N. Fontaine, T. Su, C. Ferrari, M. Cappuzzo, F. Klemens, B. Keller, M. Earnshaw, and S. Yoo, "Free-space coherent optical communication demonstration using a 3d photonic integrated circuit device for orbital angular momentum multiplexing/demultiplexing," in *Optical Communication (ECOC 2013), 39th European Conference and Exhibition on*, Sept 2013, pp. 1–3.
- [143] L. Wang, B. Ung, P. Vaity, L. Rusch, Y. Messaddeq, and S. LaRochelle, "Characterization of optical fibers supporting oam states using fiber bragg gratings," in *CLEO: 2014*. Optical Society of America, 2014, p. SM2N.4. [Online]. Available: http://www.opticsinfobase.org/abstract.cfm?URI=CLEO_SI-2014-SM2N.4
- [144] S. E. Golowich, "Asymptotic theory of strong spin-orbit coupling in optical fiber," in *Frontiers in Optics 2013 Postdeadline*. Optical Society of America, 2013, p. FW6A.1. [Online]. Available: <http://www.opticsinfobase.org/abstract.cfm?URI=FiO-2013-FW6A.1>
- [145] S. Golowich, "Asymptotic theory of strong spin-orbit coupling in optical fiber," *Opt. Lett.*, vol. 39, no. 1, pp. 92–95, Jan. 2014. [Online]. Available: <http://ol.osa.org/abstract.cfm?URI=ol-39-1-92>
- [146] Z. Zhang, J. Gan, X. Heng, Y. Wu, Q. Li, Q. Qian, D. Chen, and Z. Yang, "Optical fiber design with orbital angular momentum light purity higher than 99.9%," *Opt. Express*, vol. 23, no. 23, pp. 29 331–29 341, Nov 2015. [Online]. Available: <http://www.opticsexpress.org/abstract.cfm?URI=oe-23-23-29331>
- [147] P. E. Ciddor, "Refractive index of air: new equations for the visible and near infrared," *Appl. Opt.*, vol. 35, no. 9, pp. 1566–1573, Mar 1996. [Online]. Available: <http://ao.osa.org/abstract.cfm?URI=ao-35-9-1566>
- [148] J. W. Fleming, "Dispersion in GeO₂–SiO₂ glasses," *Appl. Opt.*, vol. 23, no. 24, pp. 4486–4493, Dec 1984. [Online]. Available: <http://ao.osa.org/abstract.cfm?URI=ao-23-24-4486>
- [149] H. Sunak and S. Bastien, "Refractive index and material dispersion interpolation of doped silica in the 0.6–1.8 μm wavelength region," *Photonics Technology Letters, IEEE*, vol. 1, no. 6, pp. 142–145, June 1989.
- [150] J. W. Fleming and D. L. Wood, "Refractive index dispersion and related properties in fluorine doped silica," *Appl. Opt.*, vol. 22, no. 19, pp. 3102–3104, Oct 1983. [Online]. Available: <http://ao.osa.org/abstract.cfm?URI=ao-22-19-3102>